Evaluation of the mechanical properties and of the damage of polyethylenes subjected to oligo-cyclic stresses in relation to their microstructures

Hang Guo

To cite this version:

Hang Guo. Evaluation of the mechanical properties and of the damage of polyethylenes subjected to oligo-cyclic stresses in relation to their microstructures. Materials. Université de Lyon, 2021. English. NNT : 2021LYSEI020 . tel-03404167

HAL Id: tel-03404167
https://theses.hal.science/tel-03404167v1

Submitted on 26 Oct 2021

N°d'ordre NNT : 2021LYSEI020

THESE de DOCTORAT DE L'UNIVERSITE DE LYON
Opérée au sein de
INSA Lyon

Ecole Doctorale N° EDA 034
Matériaux de Lyon

Spécialité de doctorat : Matériaux
Discipline : Matériaux

Soutenue publiquement/à huis clos le **25/03/2021**, par :
Hang GUO

Evaluation des propriétés mécaniques et de l'endommagement de polyéthylènes soumis à des sollicitations oligo-cycliques en relation avec leurs microstructures

Devant le jury composé de :

Cantournet, Sabine	Directeur de Recherche	Mines ParisTech	Rapporteur
Laiarinandrasana, Lucien	Professeur	Mines ParisTech	Rapporteur
Govaert, Leon	Professeur	Eindhoven University of Technology	Examinateur
Gaucher, Valérie	Professeur	Université de Lille	Examinatrice
Rinaldi, Renaud	Maître de Conférences	INSA-Lyon	Co-encadrant
LAME, Olivier	Professeur	INSA-Lyon	Directeur de thèse
Broudin, Morgane	Ingénieur-Chercheur	EDF – R&D	Examinatrice

Laboratoire de recherche : MATEIS

Evaluation des propriétés mécaniques et de l'endommagement de polyéthylènes soumis à des sollicitations oligo-cycliques en relation avec leurs microstructures.

Résumé

En tant que représentant de la polyoléfine, le polyéthylène (PE) est l'un des thermoplastiques les plus populaires appliqués dans divers domaines industriels en raison de sa excellente performance mécanique. En particulier, en tant que matériau utilisé dans les systèmes de tuyauterie, le polyéthylène haute densité (PEHD) présente une grande résistance sismique.

En général, les essais oligo-cycliques consistant en un processus de chargement-déchargement répété et plastique, sont mis en place pour simuler des événements sismiques, et ainsi étudier les performances sismiques du matériau. Les performances mécaniques sont fortement liées à la microstructure et à la morphologie du PE.

Cette recherche vise à étudier les origines de la bonne résistance sismique des matériaux PEHD, les points d'investigation suivants sont principalement concernés: 1) les évolutions mécaniques et microstructurales y compris l'endommagement lors de la déformation oligo-cyclique. Et la corrélation macro-micro. 2) L'influence de la microstructure et de la morphologie du PEHD vierge sur les réponses mécaniques et les évolutions de la microstructure lors des essais oligo-cycliques. 3) Les différences de comportements mécaniques et de micro-mécanismes associés entre les matériaux d'origine et préchargés.

Mots-Clés: polyéthylène haute densité - essais oligo-cycliques - résistance sismique - évolutions mécaniques et microstructurales – corrélation macro-micro

Evaluation of the mechanical properties and of the damage of polyethylenes subjected to oligo-cyclic stresses in relation to their microstructures.

Abstract

As a representative of polyolefin, polyethylene (PE) is one of the most popular thermoplastics applied in various industrial domains due to its excellent mechanical performance. Particularly, as a material used in piping systems, high-density polyethylene (HDPE) shows a great seismic resistance.

Generally, oligo-cyclic tests consisting of repeated and plastic loading-unloading process, are set to simulate seismic events, thus investigate the seismic performance of the material. The mechanical performances are greatly related to the microstructure and morphology of PE.

This thesis aims to study the origins of the good seismic resistance of HDPE materials, the following points of investigation are mainly concerned: 1) the mechanical and microstructure evolutions including damage along with the oligo-cyclic deformation. And the macro-micro correlation. 2) The influence of pristine HDPE microstructure and morphology on the mechanical responses and associated microstructure evolutions during oligo-cyclic tests. 3)The differences of mechanical behaviors and associated micro-mechanisms between the original and pre-loaded materials.

Key words: high-density polyethylene - oligo-cyclic tests - seismic resistance - mechanical and microstructure evolutions - macro-micro correlation

Département FEDORA – INSA Lyon - Ecoles Doctorales

SIGLE	ECOLE DOCTORALE	NOM ET COORDONNEES DU RESPONSABLE
CHIMIE	**CHIMIE DE LYON** **https://www.edchimie-lyon.fr** Sec. : Renée EL MELHEM Bât. Blaise PASCAL, 3e étage secretariat@edchimie-lyon.fr	**M. Stéphane DANIELE** C2P2-CPE LYON-UMR 5265 Bâtiment F308, BP 2077 43 Boulevard du 11 novembre 1918 69616 Villeurbanne **directeur@edchimie-lyon.fr**
E.E.A.	**ÉLECTRONIQUE, ÉLECTROTECHNIQUE, AUTOMATIQUE** **https://edeea.universite-lyon.fr** Sec. : Stéphanie CAUVIN Bâtiment Direction INSA Lyon Tél : 04.72.43.71.70 secretariat.edeea@insa-lyon.fr	**M. Philippe DELACHARTRE** INSA LYON Laboratoire CREATIS Bâtiment Blaise Pascal, 7 avenue Jean Capelle 69621 Villeurbanne CEDEX Tél : 04.72.43.88.63 **philippe.delachartre@insa-lyon.fr**
E2M2	**ÉVOLUTION, ÉCOSYSTÈME, MICROBIOLOGIE, MODÉLISATION** **http://e2m2.universite-lyon.fr** Sec. : Sylvie ROBERJOT Bât. Atrium, UCB Lyon 1 Tél : 04.72.44.83.62 secretariat.e2m2@univ-lyon1.fr	**M. Philippe NORMAND** Université Claude Bernard Lyon 1 UMR 5557 Lab. d'Ecologie Microbienne Bâtiment Mendel 43, boulevard du 11 Novembre 1918 69 622 Villeurbanne CEDEX **philippe.normand@univ-lyon1.fr**
EDISS	**INTERDISCIPLINAIRE SCIENCES-SANTÉ** **http://ediss.universite-lyon.fr** Sec. : Sylvie ROBERJOT Bât. Atrium, UCB Lyon 1 Tél : 04.72.44.83.62 secretariat.ediss@univ-lyon1.fr	**Mme Sylvie RICARD-BLUM** Institut de Chimie et Biochimie Moléculaires et Supramoléculaires (ICBMS) - UMR 5246 CNRS - Université Lyon 1 Bâtiment Raulin - 2ème étage Nord 43 Boulevard du 11 novembre 1918 69622 Villeurbanne Cedex Tél : +33(0)4 72 44 82 32 **sylvie.ricard-blum@univ-lyon1.fr**
INFOMATHS	**INFORMATIQUE ET MATHÉMATIQUES** **http://edinfomaths.universite-lyon.fr** Sec. : Renée EL MELHEM Bât. Blaise PASCAL, 3e étage Tél : 04.72.43.80.46 infomaths@univ-lyon1.fr	**M. Hamamache KHEDDOUCI** Université Claude Bernard Lyon 1 Bât. Nautibus 43, Boulevard du 11 novembre 1918 69 622 Villeurbanne Cedex France Tél : 04.72.44.83.69 **hamamache.kheddouci@univ-lyon1.fr**
Matériaux	**MATÉRIAUX DE LYON** **http://ed34.universite-lyon.fr** Sec. : Yann DE ORDENANA Tél : 04.72.18.62.44 yann.de-ordenana@ec-lyon.fr	**M. Stéphane BENAYOUN** Ecole Centrale de Lyon Laboratoire LTDS 36 avenue Guy de Collongue 69134 Ecully CEDEX Tél : 04.72.18.64.37 **stephane.benayoun@ec-lyon.fr**
MEGA	**MÉCANIQUE, ÉNERGÉTIQUE, GÉNIE CIVIL, ACOUSTIQUE** **http://edmega.universite-lyon.fr** Sec. : Stéphanie CAUVIN Tél : 04.72.43.71.70 Bâtiment Direction INSA Lyon mega@insa-lyon.fr	**M. Jocelyn BONJOUR** INSA Lyon Laboratoire CETHIL Bâtiment Sadi-Carnot 9, rue de la Physique 69621 Villeurbanne CEDEX **jocelyn.bonjour@insa-lyon.fr**
ScSo	**ScSo*** **https://edsciencessociales.universite-lyon.fr** Sec. : Mélina FAVETON INSA : J.Y. TOUSSAINT Tél : 04.78.69.77.79 melina.faveton@univ-lyon2.fr	**M. Christian MONTES** Université Lumière Lyon 2 86 Rue Pasteur 69365 Lyon CEDEX 07 **christian.montes@univ-lyon2.fr**

*ScSo : Histoire, Géographie, Aménagement, Urbanisme, Archéologie, Science politique, Sociologie, Anthropologie

穷达皆由命，何劳发叹声。

但知行好事，莫要问前程。

Acknowledgement

As three years fly over, I still remember the first day that I came to MATEIS (group PVMH), the onset of my career of research. Thanks to many persons, I have not only learned a lot about the science and technique, but also obtained many unforgettable experiences and memories during the daily life.

I appreciate my supervisors at INSA, Olivier LAME and Renaud RINALDI for guiding the research, and change me from a layman to a “polymerist”. And because of their contribution, the thesis can be successfully finished in a good quality.

Then I appreciate all the supervisors in EDF involved in this project, Morgane BROUDIN, Sourour TAYAKOUT, Denis PONT, Nicolas ROBERT, Yves DENOS, Celine GAUDIN, Cyrielle FOREST, Yannick Nziakou DJOUGUELA, and Romain MAURIN. In particular, they remind me the importance of the industrial background of this thesis, and I really enjoy each discussion/meeting about the scientific and industrial problematics with them.

I’d also thank all the professors who attend to my defense as committee members: Prof. Leon GOVAERT, Prof. Valérie GAUCHER, Prof. Lucien LAIARINANDRASANA and Prof. Sabine CANTOURNET. Thanks for their patience to read my preliminary manuscript and provide me with the useful suggestions. Also, during the defense, it is my honor to make a deep discussion with them.

I wish to also appreciate my colleagues in MATEIS, in PVMH. The list is too long to present here as people come and go. However, it is undoubtably my pleasure to pass the three years with you together. I won’t forget the days that we spent in the coffee room, in the office, and also in the pubs.

Finally yet importantly, I am indebt to my family and friends. In this troubled time, I still feel together with you, and I got the energy and confidence from you to finish this work, to continue facing the challenges in the future.

General introduction and industrial background

As one of the low-carbon energy sources, nuclear power is widely applied to produce electricity. According to the data of the World Nuclear Association, until February 2020, about 440 nuclear power reactors operating in about 30 countries, and 55 reactors are under construction. In France, about 75% of the electricity comes from nuclear technology. The safety of nuclear power is thus one of the most important points that should be taken into account during the design and implementation of nuclear power plants. Particularly, the cooling system composed of the water pipelines assuring the arrival of water, which cools the reactor and the spent fuel storage pool, is very important for the safety of the nuclear center. Indeed, the loss of the cold source due to the damage of pipelines can lead to the melting of the reactor core and an important accident. Traditionally, the material used for water pipelines in nuclear center is limited to metallic materials, especially, steel. These materials show several disadvantages: on the one hand, several chemical degradations could be found in these materials. On the other hand, nuclear power plants typically have high seismic requirements, but these materials are normally not ductile enough to resist against the earthquakes. During the last decade, polyethylene (PE), more precisely, high-density polyethylene (HDPE) has been successfully approved as the material that can be used in the nuclear power plant piping system due to its excellent mechanical and chemical performances. Especially, the Polyethylene Piping System Integrated Technology ＆Engineering Center in Japan reported that the HDPE pipelines subjected to earthquakes remain almost non-damaged.

PE is generally considered as a model of semi-crystalline polymers due to its relatively simple chemical compositions. However, at meso- and micro- (nano) scales, the structure of PE can be very complex, it depends not only on the molecular characteristics but also on the crystallization conditions. The high ductility thus great resistance against the seism should be directly related to the microstructural properties of PE. The investigations on the macro-meso-micro correlations are thus important for understanding the origin of the great seismic performance of HDPE materials, and improving the material selection and processing of the HDPE piping system in the nuclear center.

The main aim of this PhD thesis is to investigate the following themes:

- The mechanical behavior and associated microstructure evolutions in HDPE materials during the earthquake.
- The damage assessment of the HDPE materials subjected to earthquake.
- The influence of the microstructure evolutions including damage on the post-seism mechanical properties of HDPEs.
- The influence of the pristine HDPE microstructures and morphologies (trigged via crystallization process) on the aforementioned three studies.

This manuscript consists of the following 7 chapters:

- Chapter 1: The bibliography concerning the microstructure of PE at different scales, the influence of crystallization conditions (thermal treatments) on the microstructure and morphology of PE, the mechanical behavior and deformation-induced microstructure evolutions of PE, the experimental test to simulate the seism (oligo-cyclic tests), the damage assessment in PE.

- Chapter 2: The sample preparation with different thermal treatments followed by microstructural and mechanical characterizations of the pristine (undeformed) PE samples by various experimental methods.
- Chapter 3: The characterization of microstructure evolutions along with the oligo-cyclic deformation in real-time. The cavitation and lamellae fragmentation are drawn special attentions.
- Chapter 4: The evaluation of the correlation between mechanical and microstructure changes under oligo-cyclic loading conditions
- Chapter 5: The post-cyclic characterization of the anisotropic microstructural and mechanical properties in the pre-loaded PE samples
- Chapter 6: The post-cyclic characterization of the local amorphous modulus in the pre-loaded PE samples
- Chapter 7: The general conclusions and perspectives.

1 Bibliography

1.1 Preamble

As a representative of polyolefin, polyethylene (*PE*) is one of the most popular thermoplastics which finds its application in various industrial domains due to the excellent mechanical performance. Particularly, as a material used in pipelines, high-density polyethylene (*HDPE*) shows a great seismic resistance. Indeed, the *Polyethylene Piping System Integrated Technology &Engineering Center* in Japan reported that the HDPE pipelines remain almost non-damaged after being subjected to earthquakes (from 2003 to 2016) [1]. In the literature, the investigations on the seismic performance of the materials were mainly at macroscale[2–6], few discussed about the microstructural origins. Therefore, this thesis aims to study the following topics:

- The microstructural origins of the high seismic resistance of HDPE materials;
- The microstructure/mechanical evolutions during the seismic events in HDPE materials;
- The damage assessment and post-seismic performance of the HDPE materials subjected to seism.

Therefore, the literatures about the following points should be firstly mentioned:

- The structure of PE at different scales;
- The crystallization process associated with the microstructural properties of PE;
- The experimental tests to simulate the seismic events;
- The deformation-induced microstructure evolutions in PE.
- The damage assessment in PE

1.2 Structure of polyethylene

1.2.1 Molecular structure

Polyethylene (*PE*) is considered as a model material of semi-crystalline polymers because of its simple chemical structure: a PE chain with a planar "*zig-zag*" conformation consists of carbon (*C*) backbone and each *C* atom is covalently attached with two hydrogen (*H*) atoms (shown in **Figure 2.1**)[7]. According to its density and branching level, PEs are generally classified into different grades: 1) high-density polyethylene (*HDPE*) has a low level of chain branching, 2) linear low-density polyethylene (*LLDPE*) has a larger number of short branches, 3) *LDPE* has a very high branching level. A schematic of the macromolecules of these three groups of PEs are drawn in **Figure 2.2.**

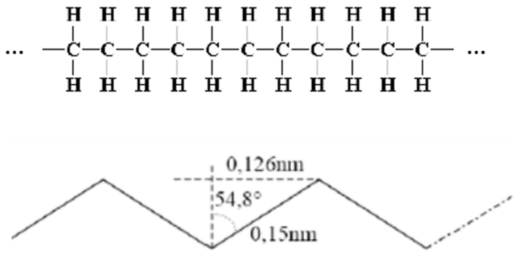

Figure 2.1: *Molecular structure of a PE long chain[8] (N.B. the bottom figure details the geometrical peculiarity of the C-C-C bond).*

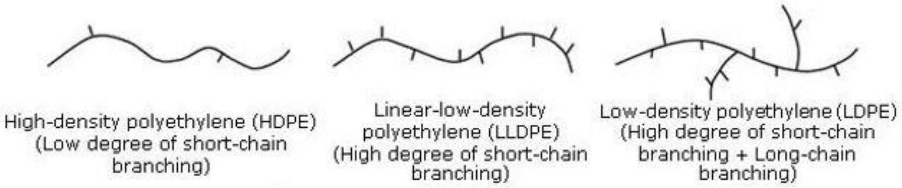

Figure 2.2: *Classification of PE according to density and branching level[9].*

The characterization of the length and branching of each molecular chain is impossible, therefore, the average characteristics of the molecular weight and branching distribution can be determined to statistically characterize the molecular structure of a polymer[9]. Normally, the molecular weights can be defined by three average values using respectively the equation (1-3) and commonly expressed in *g/mol*: 1) Number-Average Molecular Weight, 2) Weight-Average Molecular Weight and 3) Z-Average Molecular Weight. M_i and N_i are the molecular weight and the number of chains of the fraction i respectively. The $\bar{M}_w/\bar{M}_n$ ratio corresponds to the polydispersity index and describes the heterogeneity of sizes of molecules.

$$\bar{\mathrm{M}}_\mathrm{n} = \frac{\sum \mathrm{M_i N_i}}{\sum \mathrm{N_i}} \tag{1}$$

$$\bar{\mathrm{M}}_\mathrm{w} = \frac{\sum \mathrm{M_i^2 N_i}}{\sum \mathrm{M_i N_i}} \tag{2}$$

$$\bar{\mathrm{M}}_z = \frac{\sum \mathrm{M_i^3 N_i}}{\sum \mathrm{M_i^2 N_i}} \tag{3}$$

These molecular parameters can significantly influence the microstructure and morphology formed during the crystallization process thus the mechanical behavior at macroscale. In the section 1.3, the relation between molecular weight and chain motion during the crystallization is discussed. Particularly, in this PhD thesis, a special attention is drawn into $\bar{M}_w$, as this parameter is important for estimating the density of tie molecules using Brown’s model[10,11], which will be detailed in the following subsection 1.2.4.

1.2.2 Crystallographic structure

In the molten state, all the molecular chains of PE or other semi-crystalline polymers remain disordered. However, the decrease of temperature from the molten state can lead to the partial organization of molecular chain segments, this process being referred as the crystallization (see section 1.3). Once crystallized, the semi-crystalline polymer is composed of both the well-arranged chains in the crystalline phase and disordered chains in the amorphous phase.

The crystallographic structure is commonly described by a unit cell, which is the smallest repetitive arrangement of chain segments. Orthorhombic and monoclinic cells at scale of angstroms are mainly reported in PE. During a common crystallization process, the unit cell of PE is orthorhombic (**Figure 2.3a)**, the dimensions of the unit cell along the orthogonal main axis is different, and the cell density is about 1.003g/cm^3[9]. Upon uniaxial elongation, the orthorhombic cell can be transformed into the metastable monoclinic one (**Figure 2.3b)** whose density is about 0.997g/cm^3, which is close to the orthorhombic unit cell (less than 1% difference). In these two types of crystallographic structure, the *c*-axis is defined as the direction of the macromolecular chains.

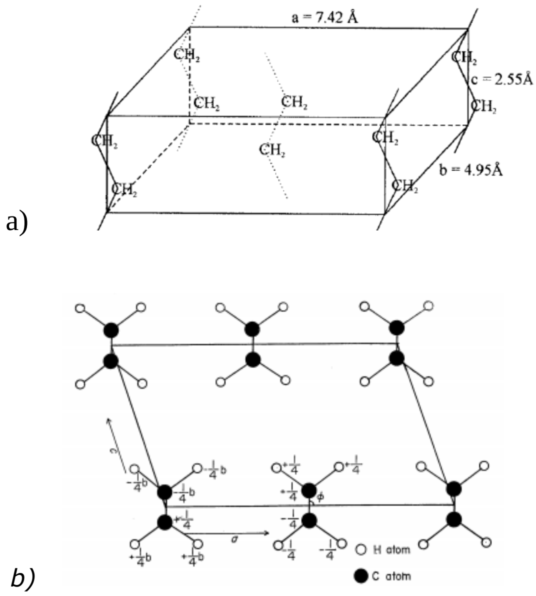

Figure 2.3: *Schematic of a) Orthorhombic unit cell[9] and b) Monoclinic unit cell of PE[12].*

1.2.3 Lamellar structure

During the crystallization, the growth of crystalline lamellae occurs along the *b*-axis as shown in **Figure 2.4**[9]**.** It implies that the chains normally fold over the surface of the so-called “lamella”. Some authors have observed that the lamellar structure is twisted using *AFM* (*Atomic force microscopy*)[13] and *X-ray* diffraction[14]. The surface stress [15,16] and consecutive formation of screw dislocations [17] during the crystallization are attempted to interpret the twisting behavior of the crystalline lamellae. The parameter L_c corresponds to the thickness of the crystalline lamellae. This microstructural dimension is known to directly affects the mechanical properties and can be measured by *SAXS* (*small angle X-ray scattering*) technique. Noticeably, the dimensions along the other two axes (namely *a* and *b*), which are much greater than that along the *c* direction, are rarely discussed in the literature, even though these geometrical features are also thought to potentially influence the mechanical behaviors of PE [8].

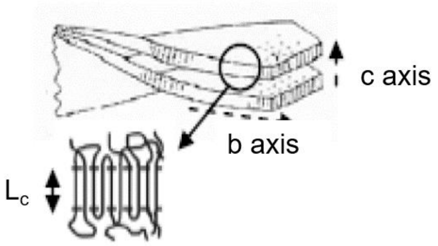

Figure 2.4: *Twisted lamellar structure[18].*

1.2.4 Interlamellar structure

At nanoscale, a semi-crystalline polymer is classically recognized as a two-layers composite structure: an amorphous phase separates the two neighboring crystalline lamellae. The total thickness of a single crystalline layer (L_c) and a single amorphous layer (L_a) is defined as the long period (L_p). This parameter describing the dimension of the repeated structure can be characterized by *SAXS* technique. Kavesh and Schultz [19] have found that the interlamellar amorphous phase has a relatively higher density (*0.9 g/cm*^{3}, estimated by linear extrapolation l to zero crystallinity) than the purely amorphous phase (*0.85g/cm*^{3}, estimated by extrapolation to room temperature) at room temperature. According to their research, an interphase, which has the density between the amorphous and crystalline phase should exist. Indeed, from the perfectly ordered crystalline phase to the disordered amorphous phase, the transition should not be sudden. **Figure 2.5** highlights the amorphous-interphase-crystalline structure of semi-crystalline polymers[20].

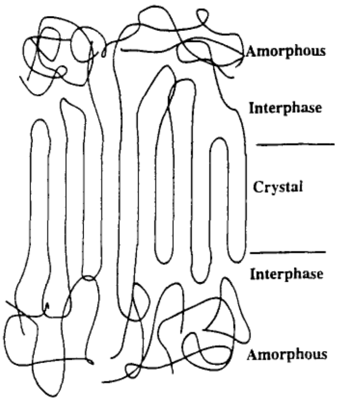

Figure 2.5: *Amorphous-interphase-crystalline structure[20].*

In both the amorphous phase and the interphase, several elements, such as tie molecules, entanglements and loops, allow the physical coupling with the crystalline phases (shown in **Figure 2.6**). Although these elements have different conformations, upon deformation, they contribute to transmit the stress between the neighboring crystalline/amorphous layers. Thus, they are altogether labeled as stress transmitters (STs)[8,18]. To our knowledge, no technique permits the direct quantification and discrimination between these 3 sub-categories. However, indirect evidences of the existence of these elements have been reported. For example, the research on crazing performed with transmission electron microscopy at the submicron scale, reported the need for some interlamellar molecular connections to ensure the fibrillary transformation at the crack tip. These fibrillary structures can continually transmit the stress, and benefit the resistance against crazing propagation[21–24]. Additionally, authors have reported that the natural draw ratio (λ_n) and neck width are two macroscopic mechanical indicators that can indirectly applied for the "quantification" of the density of stress transmitters. More precisely, the lower the natural draw ratio or the more diffuse the neck, the higher the density of STs[18,21,25].

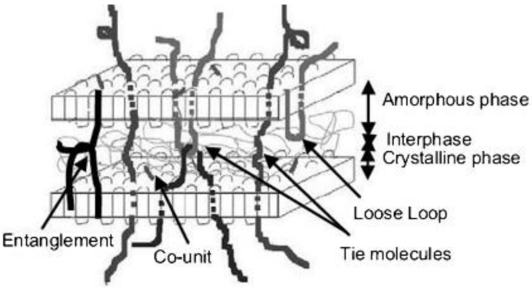

Figure 2.6: *Stress transmitters in semi-crystalline polymers.*

Moreover, Huang and Brown proposed a statistical model to evaluate the density of tie molecules[10,26]. They assumed that for a chain in the molten state to possibly form a tie molecule during crystallization, its end-to-end length (L) has to be larger than $2L_c+L_a$. Reminding that L_c and L_a are respectively the thicknesses of the crystalline and inter-lamellar layers (see 1.2.4), the inequality suggests that the chain can cross the two adjacent crystalline phases along c direction. $P(r)$ given by following equation (4) represents the probability for a chain which has an end-to-end length of r to form a tie molecule:

$$P(r) = ar^2\exp(-b^2r^2) \tag{4}$$

Where $b^2 = \frac{3}{2\bar{r}^2}$, $a = \frac{4b^3}{\pi^{0.5}}$ and $\bar{r} = (Dn'l^2)^{0.5}$. $\bar{r}$ is the root-mean-square value of the end-to-end length of a random chain. For PE, D equals 6.8 and defines the rigidity of chains, n' is the number of links that can be estimated by weight-average molecular weight $\bar{M}_w$ and l is the C-C bond length, whose value is 0.153 nm (see figure 2.1). The probability to form a tie molecule is finally given by equation (5). The correction factor *1/3* was introduced to account for the fact that the other two dimensions of lamella are much larger than the long period, so that only chain segments with their end-to-end vector normal to the crystalline lamellar surface can form tie molecules. It is worth mentioning that equation (5) is suitable for a monodisperse system. For a given molecular weight distribution, $n(M)$, the probability should be calculated using relation (6), where ndM corresponds to the number of molecular weights between M and $M+dM$ values.

$$P = \frac{1}{3}\frac{\int_{2L_c+L_a}^{\infty} r^2\exp(-b^2r^2)dr}{\int_0^{\infty} r^2\exp(-b^2r^2)dr} \tag{5}$$

$$\bar{P} = \frac{\int_0^{\infty} nPdM}{\int_0^{\infty} ndM} \tag{6}$$

The formation of tie molecules in different PEs are illustrated as **Figure 2.7.** Polymers crystallize from the melt in the form of chain folded lamellae whose thickness does not exceed a few tens of nanometers which is much smaller than the size of the random coil conformation in the melt. Several crystalline lamellae can grow within the sphere of gyration of chain as long as the chain molar weight is sufficiently high [21]. The formation of these elements is highly related to the initial molecular structure of polyethylene. The higher molecular weight enhances the probability of the formation of tie molecules. This relation is detailed in the following subsection 1.3.1.

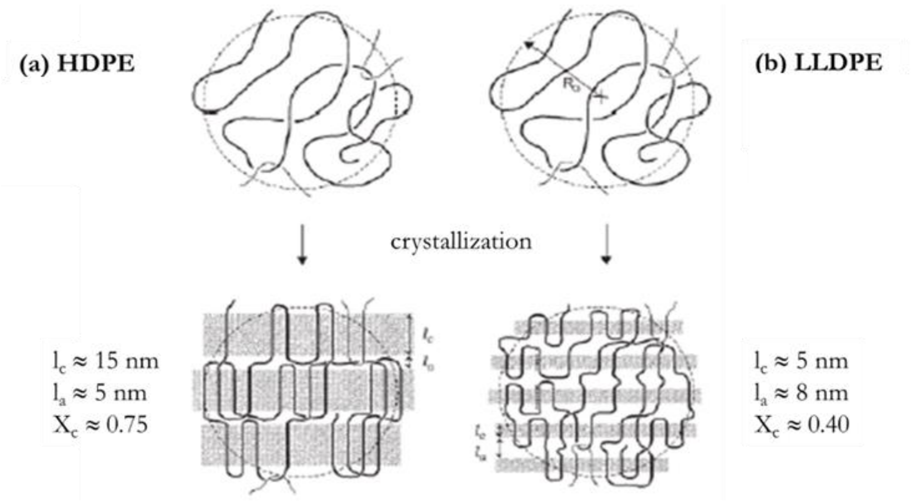

Figure 2.7: *Schematic of formation of tie molecules during crystallization (adapted from[21]).*

Yeh et al. modified the Brown's model by taking into account the formation of entanglements [27]. However, their model requires knowing the number of entanglements present in the amorphous phase. This quantity can be estimated in quenched PE, in which a large number of entanglements in the molten state prevail through rapid cooling but is unlikely to be established in PE solid samples subjected to isothermal treatment where significant disentanglement occurs during the crystallization.

It worth noting that, besides the aforementioned connections, the crystalline structure can also be percolated[18,28,29]. In the PhD thesis of Humbert et al.[18], the percolating path (traced in green) is observed by *AFM* (see **Figure 2.8**). Naturally, percolated crystalline networks can transmit the stress and then influence the mechanical properties of the PE.

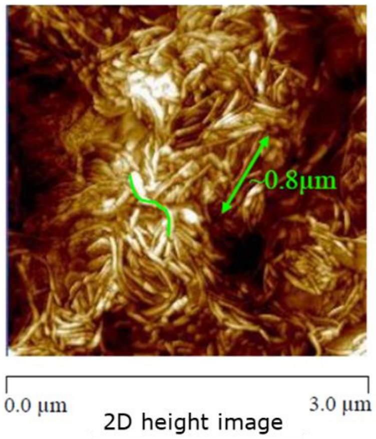

Figure 2.8: *Observation of percolated crystalline structure by AFM[18].*

1.2.5 Spherulitic structure

At mesoscale (the scale of several microns), super structures are aggregated by the crystalline lamellae, the major one being the spherulitic structure (shown as **Figure 2.9**). Such aggregate is formatted when the crystallinity of PE is higher than 35%[30]. In this PhD thesis, the investigations are all based on the HDPE with crystallinity much higher than the enounced critical value. Therefore, only the spherulite will be discussed at mesoscale. The aforementioned *b*-axis of lamella is considered as the radial direction of the spherulite, as highlighted in **Figure 2.9**, which is also the growing direction of the nucleus corresponding to the center of the spherulite. According to the research of Schultz[31], the size of spherulite depends on the nucleation behavior associated with the thermal history. On the one hand, upon fast cooling, the nucleation dominates so that a relatively larger number of spherulites can be formed. On the other hand, upon slow cooling, the number of nucleus tends to be lower, suggesting that the growth of crystallites dominates, resulting in relatively larger spherulites. Also, the associated crystallization mechanisms are displayed in the next section 1.3.

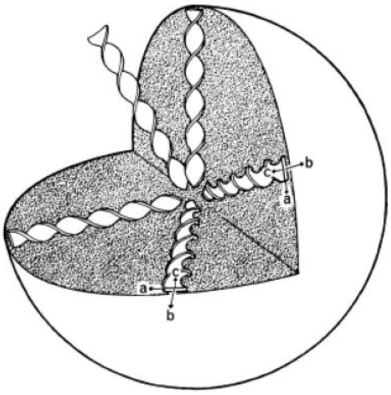

Figure 2.9: *Schematic of spherulitic structure[8].*

1.3 Crystallization of polyethylene

1.3.1 Mechanism of crystallization

In the molten state, the PE chains are orientated randomly and these disordered chains are entangled with the adjacent chains. In order to describe the global conformation of the randomly orientated chain, the concept of statistical sphere and radius of gyration (R_g) is applied (see **Figure 3.1**). R_g is calculated using the following equation (7), These parameters have been already listed in the subsection 1.2.4 for the Brown's model, where D is the rigidity of molecule (reminder: $D=6.8$ for PE), n' is the C-C link number and l is the length of the link. The radius of gyration is also related to the molecular weight M as shown in the following equation (8).

$$R_g{}^2 = \frac{1}{6}Dn'l^2 \tag{7}$$

$$R_g = aM^{0.5} \tag{8}$$

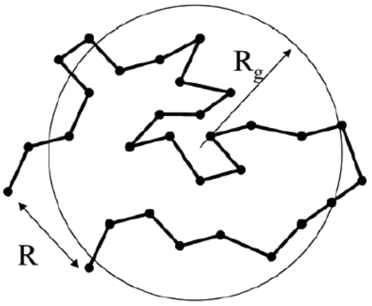

Figure 3.1: *Radius of gyration of the statistical sphere[32].*

In order to achieve the crystallization, sufficient mobility of the chains is required. One of the most common model to describe the mobility of chains is the theory of reptation proposed by De Gennes[33]. A polymer chain (P in **Figure 3.2a**) is trapped in a 3D networks with various defects (O in **Figure 3.2a**). The trajectory of the chains can be limited within an imaginary "tube". As shown in **Figure 3.2b**, the chain P cannot move sideways and is trapped in T. The molecular weight can directly affect the time of reptation. The higher the molecular weight, the longer time for the chain to be completely disengaged from its initial "tube".

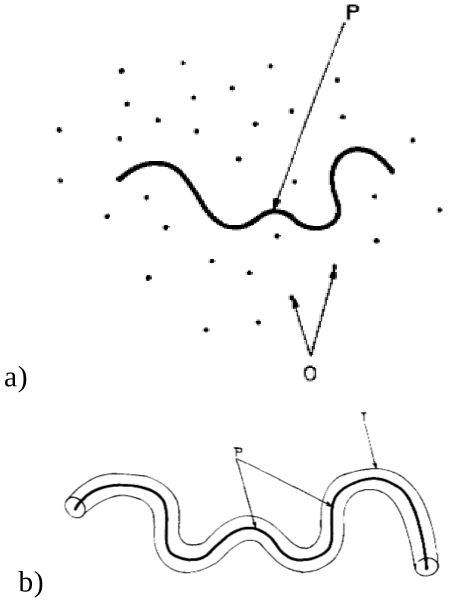

Figure 3.2: *a) Polymer chain P is free to move between the fixed obstacles O; (b) reptation of a chain P in an imaginary tube T[32].*

The crystallization initiates from the nucleation site, which can be homogeneous when the nucleus is formed directly from the melt, or heterogeneous when the nucleus is formed on the surface of an external agent or a crystal of the same polymer. The nucleus is shown in **Figure 3.3**: a segment of a chain is represented by a cuboid with the dimensions a_0, b_0, l. The free enthalpy for the formation of a nucleus can be calculated using relation (9).

$$\Delta\Phi = -V(\Delta G) + 2\sigma_e a_0 b_0 + 2\sigma(a_0 + b_0)l \tag{9}$$

Where V is the crystal volume, σ and σ_e are respectively the lateral and base surface energies. $\Delta G = \frac{\Delta h_f(\Delta T)}{T_f^0}$ and $\Delta T = T_f^0 - T_x$, Δh_f is the melting enthalpy and T_f^0 is the melting temperature of a perfect crystal and T_x is the isothermal crystallization temperature. Below a certain critical size, the nucleus is not thermodynamically stable and resolves on its own. Relation (10) corresponds to the stable thermodynamic conditions, the critical dimensions of the nucleus are thus expressed as shown in relation (11).

$$\frac{\partial\Phi}{\partial l} = 0; \frac{\partial\Phi}{\partial L} = 0 \tag{10}$$

$$l^* = \frac{2\sigma_e T_f^0}{\Delta h_f \Delta T}; L^* = \frac{4\sigma T_f^0}{\Delta h_f \Delta T} \tag{11}$$

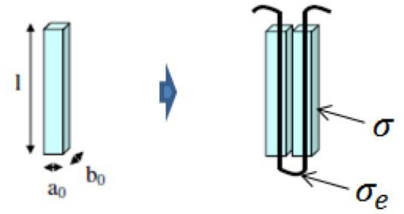

Figure 3.3: *Schematic and dimension of a nucleus[32].*

Lauritzen-Hoffman's theory describes the growth process by the successive deposits of chain segments on the lateral surfaces of the initial nucleus[34]. The initial thickness of the nucleus is thus kept constant in isothermal crystallization regime and defines the thickness of the crystals. Indeed, the growth and nucleation are two competing mechanisms taking place during the crystallization, and the prevalence of one with respect to the other depends on the temperature difference (supercooling) ΔT. Three regimes can be distinguished:

> Regime I: With a low ΔT, the nucleation is difficult. The segments tend to adhere to an existing nucleus and the chain is folded step by step. It is called as the mononucleate regime. Consequently, the crystals can be “very” thick.
>
> Regime II: With an intermediate ΔT, the chain folding rate and the nucleation rate are very close. Therefore, the filling of the layers and the creation of new layers take place simultaneously.
>
> Regime III: With a high ΔT, nucleation is very rapid and the filling of the layers becomes very slow. New nucleuses tend to appear even though the filling of previous layer is not completed. The crystals are thus smaller, and thinner.

The rate of crystal growth is also governed by the phenomenon of macromolecular chain reptation. According to Hoffman [34], there is a force of reptation, which pulls the molecule through a tube located in the melt, to fold it on the surface of the crystal, on the growth front. The reptating tube actually represents neighboring molecules in the melt. The overall crystallization rate is then a function of the rate of chain reptation. However, if the rate of crystallization is too fast, as in Regime III, reptation does not have time to operate, and only reptation of chain ends near the crystal surface can occur.

During a rapid change between the molten and solid states (Regime III), the radius of gyration R_g of the statistical sphere is almost not modified. All the entanglements existing in the melt are then retained and trapped in the amorphous phase[21]. During slow crystallization in regime I and II, the reptation phenomenon can favor the disentanglement[34]. The number of disentanglements depends on the molecular mass: the lower it is, the easier the reptation and therefore the greater the disentanglement.

1.3.2 Thermal treatments and influence on the microstructure

The crystallization conditions, as suggested in the previous paragraph, can be directly related to the thermal history: several thermal treatments (quenching, isothermal treatment, annealing etc.) are thus normally used to modify the original microstructure of polymers in order to adapt to the mechanical requirements. Two types of thermal treatments are mainly discussed in this section: Isothermal treatments and Quenching. Under certain conditions, these two thermal treatments can approximately correspond to the two extreme aforementioned regimes of crystallization I and III [8] [13]. The temperature profiles of these two processes are in **Figure 3.4**. The PE materials are firstly heated up to its molten state and then cooled down. During the quenching process requiring a fast cooling (see **Figure 3.4a**), the molten material can be crystalized in liquid nitrogen, cooling water or air, and, as evoked earlier, the crystallization occurs rapidly and incompletely. Ultimately, this process leads to thin crystallites, small spherulites and high density of stress transmitters[25,29]. Under isothermal treatment (**Figure 3.4b**), the crystallization process occurs at a fixed temperature that is a bit higher than the crystallizing one T_c. Consequently, the crystallization occurs slowly, the growth of crystallites dominates over nucleation, and the obtained crystallites and spherulites are thicker, and larger respectively. It worth noting that the duration of this process should be very long till the completion of crystallization. Moreover, due to the great arrangement of crystallites and disentanglement, the amount of remained stress transmitters is limited [35].

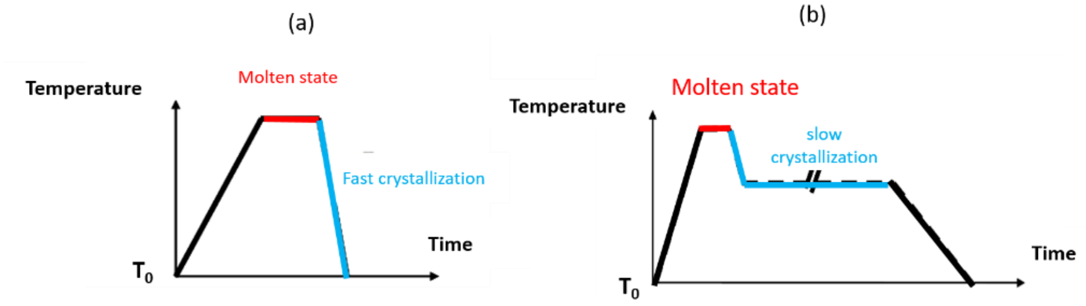

Figure 3.4: *Temperature profiles of a) quenching and b) isothermal treatment.*

1.4 Oligo-cyclic loading: simulate the seismic events

1.4.1 Overview: loading signal of seismic events

In the literature, the applied loading signals to simulate the seismic events can be different and complex[2,3,5,6,36]. However, all of these signals contain two major features: (i) the loading signal involves repeated loading-unloading process and the number of cycles is generally about a few tens. (ii) The cyclic deformation induces the plasticity (the imposed strain is beyond the yield point). As mentioned above, these aforementioned studies are mainly focused on the seismic responses of complicated structures at macroscale. However, in this thesis, the main attention is paid on the materials' response with the use of simple geometry but at microscale. To simplify the macro-micro correlation, only the uniaxial tensile deformation mode is further concerned.

1.4.2 Regimes of cyclic loading

Generally, the term "cyclic loading" designates the repetition of cycles of force (stress) or displacement (strain). The repetition of loading-unloading, even below the elastic limit of the constitutive material (high-cycle fatigue tests), can lead to the rupture of parts in service and be the cause of accidents like those that have occurred in the railway or aeronautical industry over the last 150 years[37]. The relationship between the maximum applied stress/strain (or stress/strain amplitude) and the lifetime of the material is generally used to describe the regime of cyclic loading[38–43]. Most commonly, the relationship between applied maximum stress (requiring stress-controlled mode) and lifetime is named as the S-N curve. As an example, **Figure 4.1** shows a classical S-N curve of a HDPE material[44].

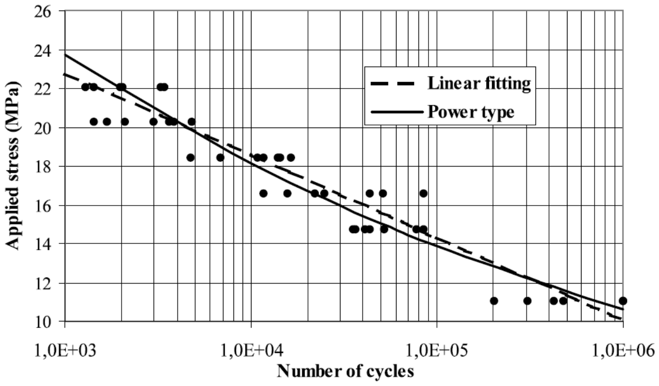

Figure 4.1: *S-N curve of a HDPE material[44]*

The cyclic failure modes of semi-crystalline thermoplastics are related to the imposed loading[39–41]. On the one hand, in the low cycle (oligo-cyclic) regime related to the high imposed stress[45–47] strain[48],or frequency[47,48], the failure of semi-crystalline polymer is caused by hysteretic heating of the sample. The heat generated during cyclic loading cannot be efficiently transferred to the surroundings due to the high dissipation (large hysteretic energy) and poor thermal conductivity of polymers, thus it induces the ductile failure (a large local plastic deformation)[41]. On the other hand, in the high cycle regime identified by a long fatigue life due to a low applied stress/strain and/or low frequency, commonly, the sample is thermally stable due to the balance between the hysteretic heating and the heat exchange with the environment (conduction, convection and radiation), the brittle failure due to the growth of cracks can be observed [40,41]. In a short-fiber reinforced thermoplastics for instance, the hysteretic energy is recognized as a criterion of lifetime[49]. The relation between lifetime N (defined as the total number of cycles), and steady dissipated energy Δ^* is expressed as equation (12). f is a parameter accounting for the mean stress effect, C and b are the material-related constant parameters [42,49,50].

$$\Delta^* = fCN^{-b} \tag{12}$$

1.4.3 Typical cyclic loading modes

In the literature, three typical cyclic loading modes are mainly employed for the cyclic tensile tests in semi-crystalline polymers:

- Stress-controlled mode[38,39,42,49,51–53]: the material is loaded between two fixed forces (stresses);
- Strain-controlled mode: the loading process is repeated between two displacements (strains)[54–56];

- Mixed mode: the material is loaded between the maximum-strain and the zero-force states[57–60].

Naturally, constant forces or displacements leading to the constant stresses or strains suggest a strong hypothesis regarding the evolution of the samples throughout the test.

The following **Figure 4.2a, b and c** display the cyclic stress-strain profiles for these three modes respectively. In particular, **Figure 4.2a** and **b** show the nominal stress-strain profiles for the polyamide, whereas the **Figure 4.2c** corresponds to the true stress-strain profile of an ultra-high molecular weight polyethylene. Whatever the cyclic loading mode, the semi-crystalline polymers show hysteresis phenomenon. Moreover, several mechanical indicators (modulus, stress/strain) change with increasing cycles.

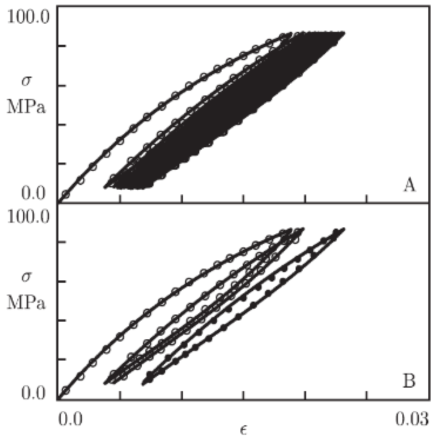

(a)

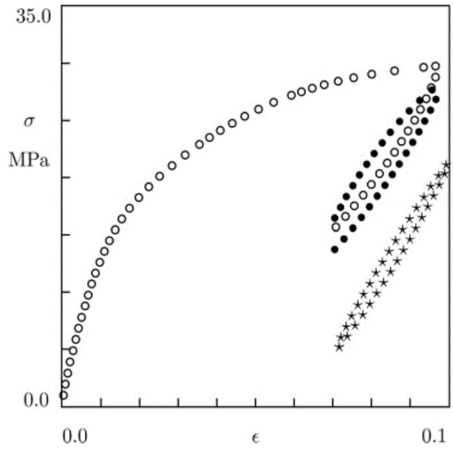

(b)

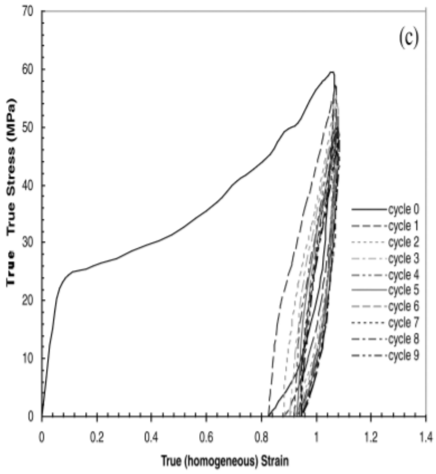

(c)

Figure 4.2: *a) Stress-controlled cyclic loading mode[53]; b) Strain-controlled cyclic loading mode[54]; c) Mixed cyclic loading mode[59]*

The stress-controlled mode is often applied for common high-cycle fatigue tests in the elastic regime. When the imposed force is high enough, it is possible to induce the plasticity, but the maximum applied strain cannot exceed the yield point, due to the further softening effect associated with necking initiation and propagation. It means that the plasticity involved per cycle is limited. Therefore, it is prone to induce the plasticity during the cyclic deformation on strain-controlled or mixed mode. However, during the strain-controlled cyclic test, it is possible to induce the compression during the unloading phase, which is not expected in the pure (cyclic) tensile characterizations. Ultimately, a special attention is drawn on the mixed-mode cyclic loading in this PhD thesis so that the disadvantages of other loading modes can be avoided. Also, it should mention that, under mixed-mode cyclic loading conditions, the first few cycles (especially the first one), involve the most important evolutions and strongly differ to other progressively saturated ones.

1.5 Deformation-induced microstructure evolutions and damage assessment in semi-crystalline polymers

1.5.1 Problematics

As enounced already, the main aim of this thesis is to evaluate the possible/potential seism-induced damage in the HDPE materials. Therefore, in this section, the related works in the literature focusing on the following subjects are mainly studied:

(i) What microstructure evolutions can be induced by deformation in semi-crystalline polymers?
(ii) Among these evolutions, which ones are related to the damage in semi-crystalline polymers?
(iii) What approaches have been used for characterizing the damage in semi-crystalline polymers?

(iv) Besides the damage, what other mechanical/microstructure evolutions are involved due to the deformation of semi-crystalline polymers?

1.5.2 Deformation-induced microstructure evolutions

1.5.2.1 Stress-strain relationship

The strain-induced microstructure evolutions including the damage has been fundamentally and widely evaluated by simple uniaxial tensile test. At macroscale, **Figure 5.1** demonstrates the classical nominal tensile stress-strain curve. At the onset of loading process, the visco-elastic deformation is recoverable. When the applied strain reaches the elastic limit (yield point), a drop of the axial stress appears accompanied with the necking initiation (strain localization). After a threshold value, named as natural draw ratio (λ_n) has been reached in the region where the neck was initiated, the plastic deformation stops in this region while neck propagates over the whole length of the sample at nearly constant engineering stress. At the end of the process, the whole sample is plastically deformed with a uniform draw ratio equal to λ_n. It is worth noting that the local strain in necked region can increase slightly due to the plastic creep[61–63].

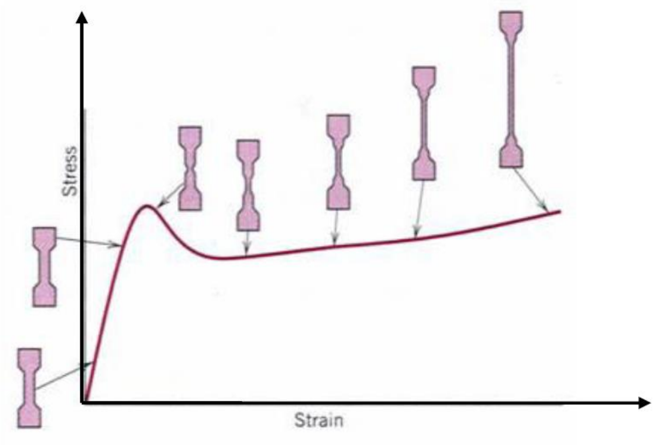

Figure 5.1: *Nominal stress-strain curve of HDPE under uniaxial simple tensile[8].*

1.5.2.2 Microstructure evolutions during the elastic deformation

In the visco-elastic regime, at lamellar scale, the deformation is mainly attributed to the amorphous phase due to its much lower modulus compared to the crystalline one. It worth noting that there is also the motion of crystallite without obvious shearing observed by WAXS in the elastic regime[35,64,65]. Three deformation modes are included are depicted in **Figure 5.2**: inter-lamellar shear (a), inter-lamellar separation (b) and lamella stack rotation (c)[66].

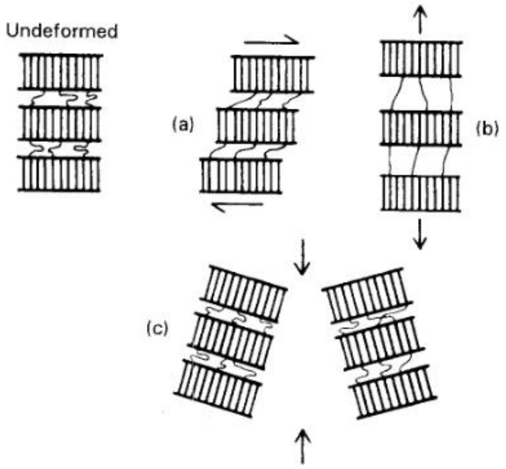

Figure 5.2: a) Inter-lamellar shear; b) inter-lamellar separation; c) stack rotation[66]

In addition, as shown in **Figure 5.3**, several researchers have found a negative volumetric strain at the onset of the elastic deformation and this phenomenon is reversible[67–69]. It is explained by the fact that during the inter-lamellar separation, the chains in the amorphous phase are oriented along the tensile direction[39]. This orientation can then induce densification of the amorphous phase, a slight crystallization, which provokes the negative volume deformation.

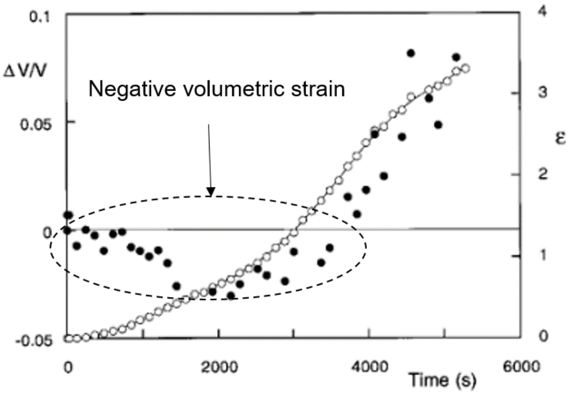

Figure 5.3: Volumetric and true axial strains, as a function of drawing time at 20°C [69].

1.5.2.3 Microstructure evolutions during the plastic deformation

During the softening/neck initiation phase, the shear (fragmentation) of the crystallites multiplies in an avalanche, and a macroscopic necking (strain localization) is initiated in the specimen. In addition, cavitation (generation of micro-voids) may be expected in some samples. The initial lamellar microstructure progressively transforms into small crystalline blocks, bridged by macromolecular chains. This phenomenon is called fibrillary transformation[70–76]. The melting/recrystallization mechanism is used to interpret the change of long periods during this transformation (as shown in **Figure 5.4**). Once the neck is fully propagated, the whole specimen is completely fibrillated, the material then begins to harden until rupture[18]. Besides these evolutions, a martensitic transformation was also observed in the crystalline phase[18,77–79], however, it is not the main object to investigate here.

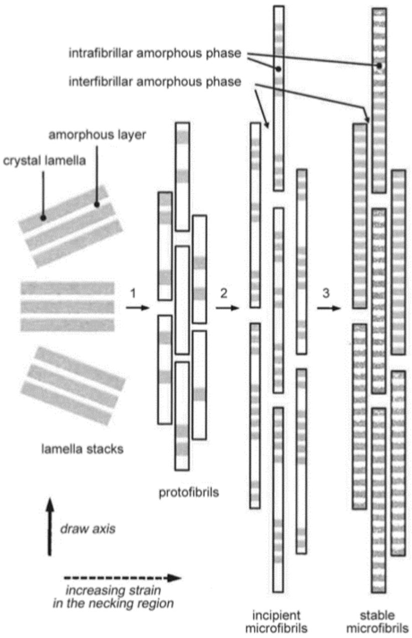

Figure 5.4: *schematic of fibrillar transformation[75].*

1.5.3 Damage assessment

The damage is considered as the deterioration of the material properties. In particular, in this thesis, the deterioration of mechanical properties draws a special attention. At microscale, in the literature, authors have attributed the damage in semi-crystalline polymers to some structural changes such as cavitation and fragmentation of lamellae. However, the macro-micro correlation is still controversial. The associated works are summarized in this subsection.

1.5.3.1 Cavitation

As mentioned above (subsection 1.4.2), the failure of semi-crystalline polymers can occur in both ductile and/or brittle manners. Various combinations of them are caused by cavitation/crazing phenomenon that finally leads to the macroscopic cracking[80]. At nanoscale, there is no internal structure in the nano-cavities, so they are unable to transmit the stress (just as the macroscopic crack).The assemblies of the elongated cavities separated by fibrils may resemble crazes [81]. According to the work of Castagnet et al.[82], in semi-crystalline polymers, the cavities firstly appear in the equatorial region of spherulite where the lamellae are normal to the loading direction, which favors the initiation of cavitation (by both uniaxial tensile and fatigue loadings). However, it is worth noting that the cavitation can also be expected in the polar region due to the lamellae fragmentation[83]. **Figure 5.5** shows the cavitation between the lamellae and further longitudinal coalescence[84]: (A) when films were strained along chain direction the increase in lamellae separation resulted in short craze-like cavities; (B) those cavities did not propagate laterally, because their growth was apparently arrested by shish crystal reinforcement. Eventually, the cavities coalesced, resulting in the growth of elongated voids between shish-kebabs and formation of the craze-like structures, which propagated parallel to the chain direction.

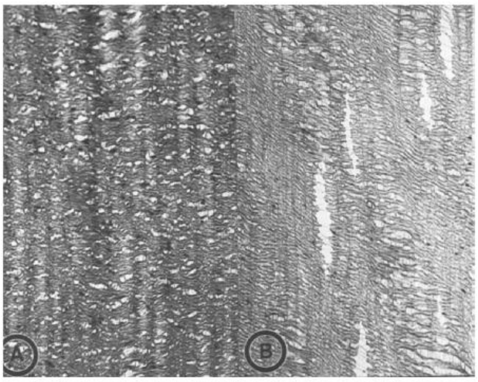

Figure 5.5: *Cavitation between lamellae and longitudinal coalescence*[84].

As for the micro-characterizations under fatigue loading conditions, Raphael et al.[85] performed X-ray tomography measurements to evidence that the cavitation-related fatigue damage in a polyamide (PA) progresses by intra-spherulitic failure in their equatorial plane (see **Figure 5.6**).

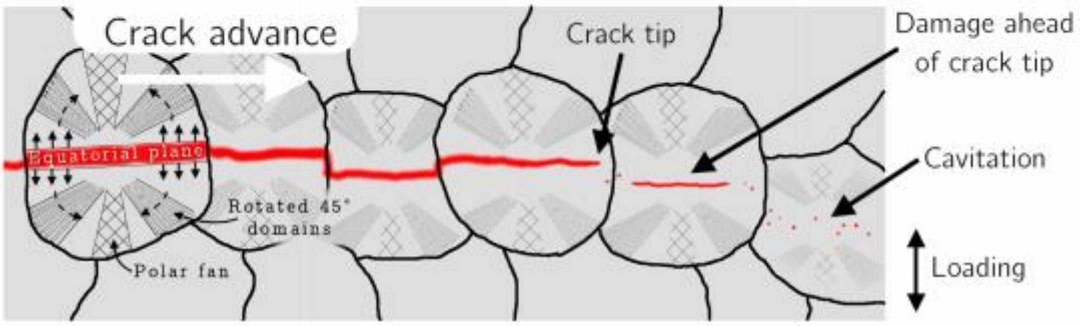

Figure 5.6: *Fatigue damage progression by intra-spherulitic failure in the equatorial plane*[85]

Mourglia-Seignobs et al.[38] also observed the microstructure evolutions in polyamide during stress-controlled fatigue tests in the vicinity of the fracture surface. Cryogenic fracture was conducted to obtain a transverse plane which was then observed using scanning electron microscopy (SEM) after metallization (**Figure 5.7**). Just underneath the final fracture surface, and up to 50 µm from the surface, cracks are observed. Up to 60 µm from the surface, crazes (or cracks bridged by polymer fibrils) are then observed. Beyond 60 µm, only cavities are observed. Moreover, the evolution of cavities (shown in **Figure 5.8**) were characterized using X-ray technique. The whole process is decomposed into three stages: 1) the nucleation of uncorrelated and foremost spherical cavities with sizes distributed between 10 and 100 nm, the number of cavities increases progressively; 2) the number of cavities decreases, whereas the size and anisotropy of the cavities increase. Defects become ellipsoidal cavities, elongated in the direction normal to the applied stress. 3) These cavities form the crazes observed by SEM. They suggested that the rupture of the material is the consequence of an accumulation of damage rather than the propagation of a single crack.

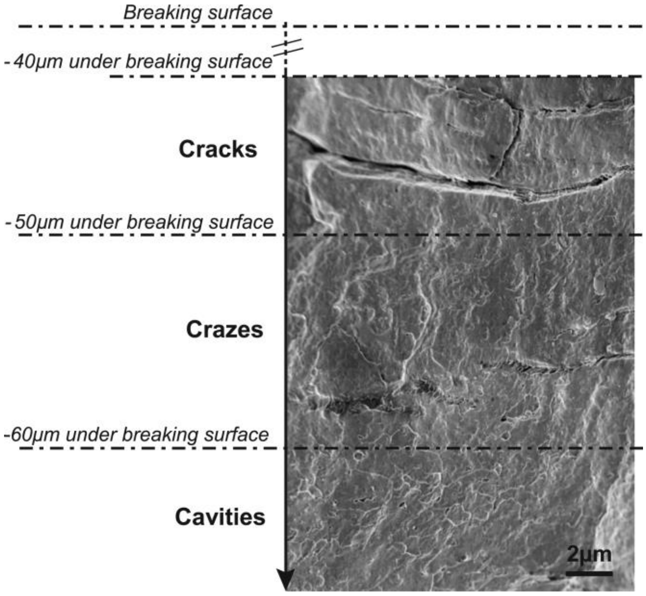

Figure 5.7: *Cryofracture in the direction parallel to the stress in neat PA after fatigue failure (SEM) [38].*

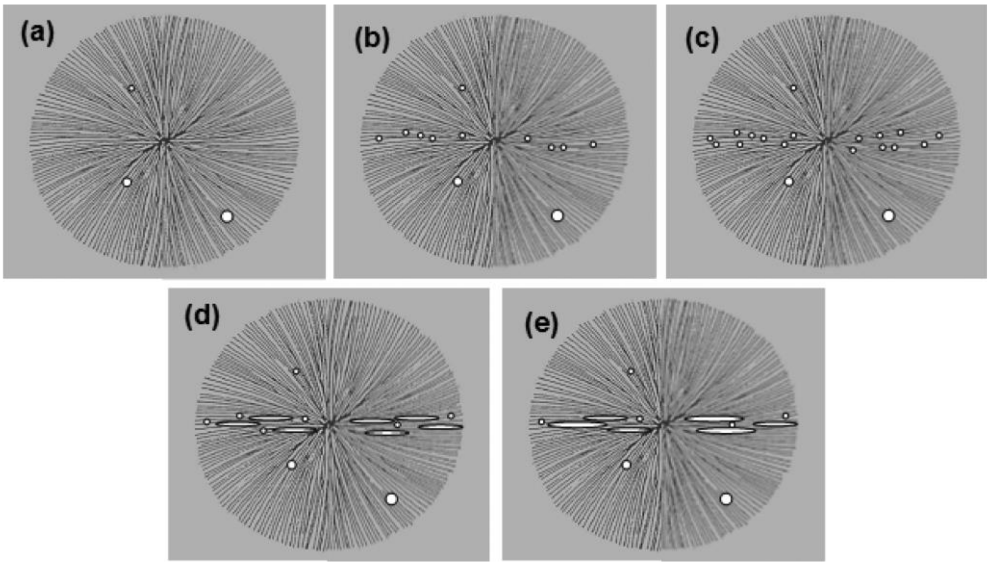

Figure 5.8: *Growth of submicrometer cavities in the amorphous phase between lamellae oriented in the direction normal to the applied stress. (a) Micrometer-sized cavities with broad distribution of size in the nonfatigued sample. (b) Nucleation of cavities in the amorphous phase with diameters comprised between 20 and 180 nm. (c) Increase of the number of the spherical cavities in the course of fatigue testing. (d, e) Growth of the cavities in the direction normal to the applied stress[38].*

At macroscale, a large number of cavities can induce the whitening of the material sample. Furthermore, the cavities lead to the volume increase (which can be characterized by Digital Image Correlation (DIC)[86] and/or dilatometric method[82]), thus the decrease of the density [68,87–90] (which can be characterized by density gradient column).

Several authors also believed that the cavitation is related to the mechanical deteriorations such as the decrease of modulus[54] and yield stress[74]. In particular, in the aforementioned work[38], the modulus evolution of a polyamide is linked with the cavitation during fatigue test (displayed in **Figure 5.9**). Regime 1 is associated with uncorrelated nucleation of cavities with characteristic dimension of about a few tens of nanometers. These cavities do not grow, only their number tends to increase. Regime 2 is ascribed to correlated nucleation of cavities near the already existing cavities. Regime 3 corresponds to crack propagation and the final breakage of the material.

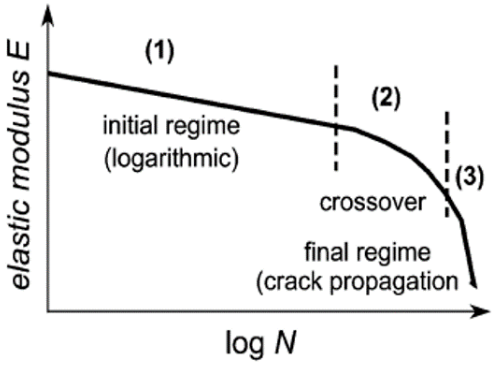

Figure 5.9: *Schematics of the modulus evolution with increasing cycles during fatigue tests[38].*

However, it has been found that several semi-crystalline polymers (such as low-density polyethylene) do not exhibit the cavitation behavior during the deformation. This phenomenon is related to the pristine microstructural properties of polymers. Xiong et al. developed a physical model based on thermally activated nucleation process for predicting the macroscopic stress needed to create cavities as well as the stress for initiating the plasticity (shearing/fragmentation of crystals). This model accounts for both the applied temperature and the microstructure of semi-crystalline polymers[91]. According to their results, in the temperature range 25°C-100°C 3 regimes could be distinguished: cavitation is observed prior to yielding for samples having thickness of crystallites L_c>20 nm, cavitation appears after yielding for samples having 12 nm<L_c<20 nm, and no cavitation was observed for samples having Lc < 12 nm, the plastic deformation being fairly homogeneous. Therefore, the macroscopic damage (deterioration of mechanical properties) cannot be always attributed to the cavitation

Moreover, it is well known that after the fibrillary transformation, the stiffness can even increase in the PEs who cavitate[8]. Therefore, the presence of cavities does not mean that the overall stiffness must decrease. Detrez et al believed that the cavitation should not be a *per se* damaging phenomenon[92].

1.5.3.2 Plasticity/damage coupling

In the work of Detrez et al.[92], macroscopic damage was evidenced through the gradual loss of elastic properties upon cyclic tensile tests and was already observed in the early stage of stretching in three different semi-crystalline polymers. However, no volume strain was measured up to the yield point. Such result suggested that the cavitation is negligible and another mechanism should be mentioned. The authors attributed the modulus deterioration to the fragmentation of crystalline lamellae in the pre-yield range (nominal strain inferior to 6%), which is observed by atomic force microscopy (AFM) as shown in **Figure 5.10**. This damage can be reasonably assigned to the reduction of the shape factor of the crystalline lamellae as a result of profuse fragmentation. However, the fragmentation of lamellae is not quantitatively described to date[80]. Moreover, it is also worth noting that, at large strain, altough the lamellae are crucially fragmented, the stiffness is possible to be higher than the one in the initial state.

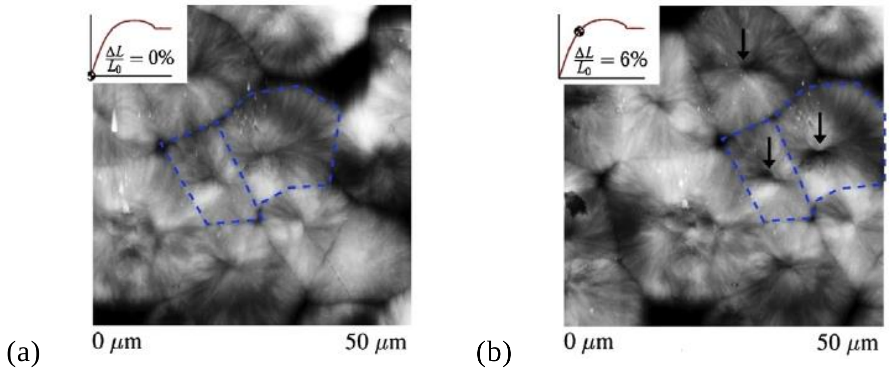

Figure 5.10: *AFM observation of fragmentation of lamellae in the pre-yield regime*[92]

1.5.3.3 *Mullins* phenomenon: stress softening

As mentioned in **section 1.4.3**, the mixed mode cyclic loading is mainly concerned in this work. During the cyclic deformation prescribed by this mode, a decrease of the stress at maximum strain and accumulation of residual strain at zero stress can be observed. They are generally considered as the main macroscopic features of the *so-called Mullins effect*, which was firstly observed and enacted in the filled and crystallizing rubbers[93,94]. It seems that the “heterogeneity” is the driving force of the *Mullins* phenomenon: in the unfilled rubbers, this behavior is almost negligible. Consequently, due to the heterogeneity induced by the crystalline/amorphous phases, this phenomenon has been also observed in the semi-crystalline polymers[57,58,60]. To distinguish with the classical behavior of rubbers, in our work, this phenomenon in semi-crystalline polymers is named as *Mullins-like* effect.

Due to the very few works that contributes to understand this phenomenon in the semi-crystalline polymers, several basic studies on the rubbers need to be mentioned here. Physically, Bueche et al. [95,96] explicated that the softening behavior in filled elastomers is related to the bond rupture. Moreover, the filler rupture was also taken into account by Kraus et al. [97]. In the macromolecular modeling, The *Mullins* stress softening has been often modeled by adopting a damage continuum mechanics approach[98–100]. Indeed, for the *Mullins-like* softening in the semi-crystalline polymers, Drozdov has also taken into account the accumulation of damage and its healing in the constitutive modeling[57].

However, according to Houwink[101], if chemical filler bonds and fillers break, the rupture would be permanent, which is not in accordance with the recoverable residual strain after relaxation. Hanson et al.[102] assumed that the entanglement density changes along with the extension and the removal of entanglements associated with stress softening. Fukahori et al. [103] proposed a double-layer model for explicating the physical mechanism of the *Mullins effect*. These physical mechanisms are reviewed in the work of Diani et al.[100] and are illustrated in **Figure 5.11**.

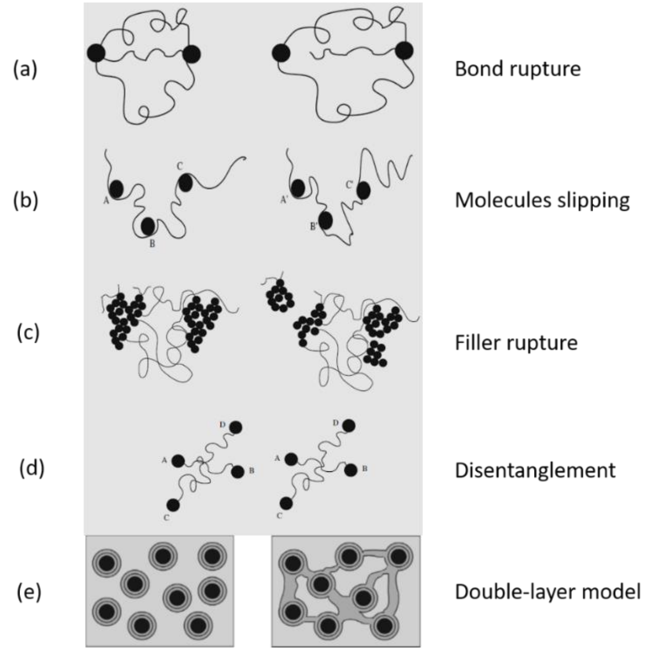

Figure 5.11: *Physical mechanisms to interpret the Mullins effect in filled rubbers: a) bond rupture; b)molecules slipping; c) filler rupture; d) disentanglement; e) double-layer model [100]*

More recently, Ayoub et al. proposed a new network alteration theory[104]. In their work, the evolution of stress at maximum strain as a function of the cycle number was used to identify three stages as shown in **Figure 5.12**: (i) The stress-softening stage is followed by (ii) a weak variation of the stress and finally (iii) a fast decrease of the stress prior to failure. The failure cycle number (lifetime decreases with increasing imposed maximum strain).

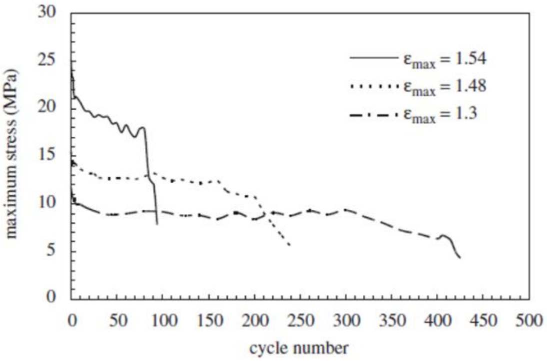

Figure 5.12: *Plot of maximum stress as a function of cycle number[104]*

The following **Figure 5.13** illustrates the associated mechanism related to the stage (i), stress softening stage: At maximum strain state of the cyclic loading, during the first stretching step, some chains reaching their extensibility limit cause the breakage of chains and weak bonds. Yet small chains being stucked between two entangled chains do not break after the first cycle. After being cycled, entanglement between chains split open and small chains stuck between them start to break down. The second zone is probably a consequence of the appearance of voids (due to cavitation in the rubber matrix and debonding between fillers and the rubber matrix) or micro-cracks and to their growing in the rubber matrix. Their rapid growth due to coalescence and breakage of ligaments leads to the manifestation of the third regime (a macro-crack occurs and propagates until complete failure).

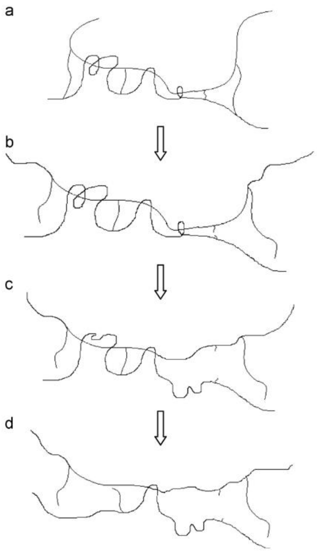

Figure 5.13: *Microstructure evolution associated with stress softening[104]*

In the filled rubbers, it is observed that the residual strain is not permanent, it can even be recovered rapidly. Diani et al.[105] reported an instantaneous residual stretch of 31%, which decreased to 13% after 20 min and remained to 12% after 48 h. Mullins[93] noticed that materials showing little softening also show little residual deformations. Moreover, though the residual strain depended on the type of fillers, it was simply related to the stiffening effect of the fillers. Several authors reported residual extensions increasing with the amount of fillers and with the amplitude of stretching applied to the materials[98]. In the model for predicting the *Mullins* behavior in semi-crystalline polymers, only the residual strain induced during the first cycle is non-recoverable [57,106].

Moreover, in the PE samples with different crystallinity, Makki et al.[58] have applied the same theory to interpret the *Mullins-like* effect in semi-crystalline polymers. As shown in **Figure 5.14.** The softening is related to the chains rupture as they reach their limit extensibility, whereas the residual strain is due to the new equilibrium state after unloading. The authors have also observed that Mullins stress-softening magnitude and strain accumulation are both related to the crystallinity and the maximum strain applied. However, they do not give any physical explication for these dependencies.

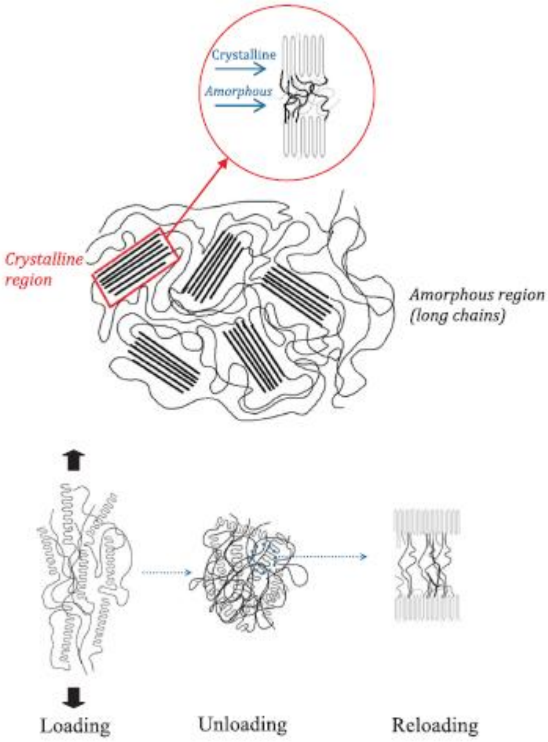

Figure 5.14: *Network alteration during loading-unloading-reloading[58].*

1.6 Conclusion and strategy

The aim of this thesis is to evaluate the influences of seismic events (modeled by mixed-mode oligo-cyclic tensile loading) on the mechanical properties and the associated microstructure evolutions in HDPE samples. Especially, the damage assessment should be carried out in those samples submitted to oligo-cyclic loading. Moreover, the relation between the effect of oligo-cyclic loading and the initial microstructure of HDPE samples are naturally of interest.
Thus, the following points will be mainly investigated in this thesis:

1. What microstructure evolutions are involved under oligo-cyclic loading conditions?
2. Does the oligo-cyclic loading change the lifetime, modulus, toughness and further deformation mechanisms?
3. What is the correlation between the microstructure evolutions and macroscopic changes?
4. Whether those mechanical/microstructure evolutions (including damage) have any relation with the initial material properties (especially the microstructural properties)
5. Is it possible to predict the materials' lifetime knowing the oligo-cyclic loading?

Experimental strategies were chosen in order to answer these scientific questions. They are listed below:

1. Implementation of a formatting protocol separating the different pristine microstructures of PE samples and generating a range of microstructural properties (crystallinity, geometry of crystallites, density of stress transmitters, etc.) by thermal treatments (quenching and isothermal treatment).
2. Selection and implementation of characterizing techniques allowing the evaluation of the initial microstructural and mechanical properties.
3. Implementation of an experimental protocol to conduct oligo-cyclic tests.
4. Characterization of the mechanical and microstructural evolutions including damage using both in-situ and ex-situ methods.

Reference

[1] Hideki Omuro, Tomokazu Himono, POLYETHYLENE PIPELINE PERFORMANCE AGAINST EARTHQUAKE, in: 2018.

[2] Angelo Masi, Giuseppe Santarsiero, Domenico Nigro, Cyclic tests on external RC beam-column joints: role of seismic design level and axial load value on the ultimate capacity, Journal of Earthquake Engineering. 17 (2013) 110–136.

[3] Paolino Cassese, Paolo Ricci, Gerardo M. Verderame, Experimental study on the seismic performance of existing reinforced concrete bridge piers with hollow rectangular section, Engineering Structures. 144 (2017) 88–106.

[4] Vincent Ji, Yong-Gang Zhang, Chang-Qi Chen, The non-destructive estimation of the superficial mechanical properties of components in the INCONEL 600 alloy by X-ray diffraction peak width, Surface and Coatings Technology. 130 (2000) 95–99.

[5] N. Nishonov, D. Bekmirzaev, E. An, Z. Urazmukhamedova, K. Turajonov, Behaviour and Calculation of Polymer Pipelines Under Real Earthquake Records, in: IOP Conference Series: Materials Science and Engineering, IOP Publishing, 2020: p. 052076.

[6] J. Shi, A. Hu, F. Yu, Y. Cui, R. Yang, J. Zheng, Finite element analysis of high-density polyethylene pipe in pipe gallery of nuclear power plants, Nuclear Engineering and Technology. (2020).

[7] C. W. Bunn, The crystal structure of long-chain normal paraffin hydrocarbons. The “shape” of the< CH2 group, Transactions of the Faraday Society. 35 (1939) 482–491.

[8] B. Xiong, Contribution to the study of elastic and plastic deformation mechanisms of polyethylene and polypropylene as a function of microstructure and temperature, Lyon, INSA, 2014.

[9] A. Peacock, Handbook of polyethylene: structures: properties, and applications, CRC press, 2000.

[10] Y.-L. Huang, N. Brown, The effect of molecular weight on slow crack growth in linear polyethylene homopolymers, Journal of Materials Science. 23 (1988) 3648–3655.

[11] N. Brown, X. Lu, Y.-L. Huang, R. Qian, Slow crack growth in polyethylene-a review, in: Makromolekulare Chemie. Macromolecular Symposia, Wiley Online Library, 1991: pp. 55–67.

[12] T. Seto, T. Hara, K. Tanaka, Phase transformation and deformation processes in oriented polyethylene, Japanese Journal of Applied Physics. 7 (1968) 31.

[13]J. Xu, B.-H. Guo, Z.-M. Zhang, J.-J. Zhou, Y. Jiang, S. Yan, L. Li, Q. Wu, G.-Q. Chen, J.M. Schultz, Direct AFM observation of crystal twisting and organization in banded spherulites of chiral poly (3-hydroxybutyrate-co-3-hydroxyhexanoate), Macromolecules. 37 (2004) 4118–4123.

[14] Y. Fujiwara, The superstructure of melt-crystallized polyethylene. I. Screwlike orientation of unit cell in polyethylene spherulites with periodic extinction rings, Journal of Applied Polymer Science. 4 (1960) 10–15.

[15] H.D. Keith, F.J. Padden Jr, Twisting orientation and the role of transient states in polymer crystallization, Polymer. 25 (1984) 28–42.

[16] K. Okano, Note on the lamellar twist is polymer spherulites, Japanese Journal of Applied Physics. 3 (1964) 351.

[17] B. Lotz, S.Z. Cheng, A critical assessment of unbalanced surface stresses as the mechanical origin of twisting and scrolling of polymer crystals, Polymer. 46 (2005) 577–610.

[18] S. Humbert, O. Lame, G. Vigier, Influence de la topologie moléculaire et de la microstructure sur les propriétés mécaniques des Polyéthylènes, Laboratoire de Recherche: MATEIS, INSA de Lyon. (2009).

[19] S. Kavesh, J.M. Schultz, Lamellar and interlamellar structure in melt-crystallized polyethylene. II. Lamellar spacing, interlamellar thickness, interlamellar density, and stacking disorder, Journal of Polymer Science Part A-2: Polymer Physics. 9 (1971) 85–114.

[20] A. Singhal, L.J. Fina, Dynamic two-dimensional infra-red spectroscopy of the crystal—amorphous interphase region in low-density polyethylene, Polymer. 37 (1996) 2335–2343.

[21] R. Seguela, Critical review of the molecular topology of semicrystalline polymers: The origin and assessment of intercrystalline tie molecules and chain entanglements, Journal of Polymer Science Part B: Polymer Physics. 43 (2005) 1729–1748.

[22] Frédéric Addiego, Stanislav Patlazhan, Kui Wang, Stéphane André, Sigrid Bernstorff, David Ruch, Time-resolved small-angle X-ray scattering study of void fraction evolution in high-density polyethylene during stress unloading and strain recovery, Polymer International. 64 (2015) 1513–1521.

[23] Frédéric Addiego, Abdesselam Dahoun, Christian G'Sell, Jean-Marie Hiver, Olivier Godard, Effect of microstructure on crazing onset in polyethylene under tension, Polymer Engineering & Science. 49 (2009) 1198–1205.

[24] H.-H. Kausch, R. Gensler, C. Grein, C.J.G. Plummer, P. Scaramuzzino, Crazing in semicrystalline thermoplastics, Journal of Macromolecular Science—Physics. 38 (1999) 803–815.

[25] S. Humbert, O. Lame, G. Vigier, Polyethylene yielding behaviour: What is behind the correlation between yield stress and crystallinity?, Polymer. 50 (2009) 3755–3761.

[26] Y.-L. Huang, N. Brown, Dependence of slow crack growth in polyethylene on butyl branch density: morphology and theory, Journal of Polymer Science Part B: Polymer Physics. 29 (1991) 129–137.

[27] J.T. Yeh, J. Runt, Fatigue crack propagation in high-density polyethylene, Journal of Polymer Science Part B: Polymer Physics. 29 (1991) 371–388.

[28] T. Deplancke, M. Fivel, O. Lame, 1D strain rate-dependent constitutive model of UHMWPE: From crystalline network to fibrillar structure behavior, Mechanics of Materials. 137 (2019) 103129.

[29] S. Humbert, O. Lame, R. Séguéla, G. Vigier, A re-examination of the elastic modulus dependence on crystallinity in semi-crystalline polymers, Polymer. 52 (2011) 4899–4909.

[30] S. Bensason, J. Minick, A. Moet, S. Chum, A. Hiltner, E. Baer, Classification of homogeneous ethylene-octene copolymers based on comonomer content, Journal of Polymer Science Part B: Polymer Physics. 34 (1996) 1301–1315.

[31] J.M. Schultz, Microstructural aspects of failure in semicrystalline polymers, Polymer Engineering & Science. 24 (1984) 770–785.

[32] T. Deplancke, Approche des mécanismes de frittage du UHMWPE: étude du comportement mécanique à l'état solide et à l'état fondu, 2013.

[33] P.-G. de Gennes, Reptation of a polymer chain in the presence of fixed obstacles, The Journal of Chemical Physics. 55 (1971) 572–579.

[34] J.D. Hoffman, R.L. Miller, Kinetic of crystallization from the melt and chain folding in polyethylene fractions revisited: theory and experiment, Polymer. 38 (1997) 3151–3212.

[35] B. Xiong, O. Lame, J.-M. Chenal, C. Rochas, R. Seguela, G. Vigier, Amorphous phase modulus and micro–macro scale relationship in polyethylene via in situ SAXS and WAXS, Macromolecules. 48 (2015) 2149–2160.

[36] Z. Cai, R.J. Bathurst, Seismic response analysis of geosynthetic reinforced soil segmental retaining walls by finite element method, Computers and Geotechnics. 17 (1995) 523–546.

[37] G. Hénaff, F. Morel, Fatigue des structures: endurance, critères de dimensionnement, propagation des fissures, rupture, 2005.

[38] Elodie Mourglia-Seignobos, Didier R. Long, Ludovic Odoni, Loïc Vanel, Paul Sotta, Cyrille Rochas, Physical mechanisms of fatigue in neat polyamide 6, 6, Macromolecules. 47 (2014) 3880–3894.

[39] Z. Qi, N. Hu, G. Li, D. Zeng, X. Su, Constitutive modeling for the elastic-viscoplastic behavior of high density polyethylene under cyclic loading, International Journal of Plasticity. 113 (2019) 125–144.

[40] Roel PM Janssen, Leon E. Govaert, Han EH Meijer, An analytical method to predict fatigue life of thermoplastics in uniaxial loading: sensitivity to wave type, frequency, and stress amplitude, Macromolecules. 41 (2008) 2531–2540.

[41] R.P. Janssen, D. de Kanter, L.E. Govaert, H.E. Meijer, Fatigue life predictions for glassy polymers: a constitutive approach, Macromolecules. 41 (2008) 2520–2530.

[42] N. Fouchier, C. Nadot-Martin, E. Conrado, A. Bernasconi, S. Castagnet, Fatigue life assessment of a Short Fibre Reinforced Thermoplastic at high temperature using a Through Process Modelling in a viscoelastic framework, International Journal of Fatigue. 124 (2019) 236–244.

[43] X.-M. Pan, X. Li, L. Chang, G.-D. Zhang, F. Xue, Y.-F. Zhao, C.-Y. Zhou, Thermal-mechanical fatigue behavior and lifetime prediction of P92 steel with different phase angles, International Journal of Fatigue. 109 (2018) 126–136.

[44] R. Khelif, A. Chateauneuf, K. Chaoui, Statistical analysis of HDPE fatigue lifetime, Meccanica. 43 (2008) 567–576.

[45] I. Constable, J.G. Williams, D.J. Burns, Fatigue and cyclic thermal softening of thermoplastics, Journal of Mechanical Engineering Science. 12 (1970) 20–29.

[46] M.N. Riddell, G.P. Koo, J.L. O'Toole, Fatigue mechanisms of thermoplastics, Polymer Engineering & Science. 6 (1966) 363–368.

[47] D. Rittel, Y. Rabin, An investigation of the heat generated during cyclic loading of two glassy polymers. Part II: Thermal analysis, Mechanics of Materials. 32 (2000) 149–159.

[48] T.R. Tauchert, S.M. Afzal, Heat generated during torsional oscillations of polymethylmethacrylate tubes, Journal of Applied Physics. 38 (1967) 4568–4572.

[49] B. Klimkeit, S. Castagnet, Y. Nadot, A. El Habib, G. Benoit, S. Bergamo, C. Dumas, S. Achard, Fatigue damage mechanisms in short fiber reinforced PBT+ PET GF30, Materials Science and Engineering: A. 528 (2011) 1577–1588.

[50] D. Kujawski, F. Ellyin, A unified approach to mean stress effect on fatigue threshold conditions, International Journal of Fatigue. 17 (1995) 101–106.

[51] W. Liu, Z. Gao, Z. Yue, Steady ratcheting strains accumulation in varying temperature fatigue tests of PMMA, Materials Science and Engineering: A. 492 (2008) 102–109.

[52] Song Thanh Thao Nguyen, Sylvie Castagnet, Jean-Claude Grandidier, Nonlinear viscoelastic contribution to the cyclic accommodation of high density polyethylene in tension: Experiments and modeling, International Journal of Fatigue. 55 (2013) 166–177.

[53] A.D. Drozdov, Cyclic viscoelastoplasticity and low-cycle fatigue of polymer composites, International Journal of Solids and Structures. 48 (2011) 2026–2040.

[54] A.D. Drozdov, Cyclic strengthening of polypropylene under strain-controlled loading, Materials Science and Engineering: A. 528 (2011) 8781–8789.

[55] A. Avanzini, Mechanical characterization and finite element modelling of cyclic stress–strain behaviour of ultra high molecular weight polyethylene, Materials & Design. 29 (2008) 330–343.

[56] A. Bezazi, N. Frioui, F. Scarpa, Tensile static, fatigue and relaxation behaviour of closed cell electret PVDF foams, Mechanics of Materials. 43 (2011) 459–466.

[57] A. D. Drozdov, Mullins' effect in semicrystalline polymers, International Journal of Solids and Structures. 46 (2009) 3336–3345.

[58] M. Makki, G. Ayoub, H. Abdul-Hameed, F. Zaïri, B. Mansoor, M. Naït-Abdelaziz, M. Ouederni, Mullins effect in polyethylene and its dependency on crystal content: a network alteration model, Journal of the Mechanical Behavior of Biomedical Materials. 75 (2017) 442–454.

[59] R.W. Meyer, L.A. Pruitt, The effect of cyclic true strain on the morphology, structure, and relaxation behavior of ultra high molecular weight polyethylene, Polymer. 42 (2001) 5293–5306.

[60] M. Wang, J. Shen, J. Li, S. Guo, Network alteration theory on Mullins effect in semicrystalline polymers, Polymer International. 64 (2015) 105–112.

[61] G. Capaccio, T.A. Crompton, I.M. Ward, Drawing behavior of linear polyethylene. II. Effect of draw temperature and molecular weight on draw ratio and modulus, Journal of Polymer Science: Polymer Physics Edition. 18 (1980) 301–309.

[62] G. Meinel, A. Peterlin, Plastic deformation of polyethylene II. Change of mechanical properties during drawing, Journal of Polymer Science Part A-2: Polymer Physics. 9 (1971) 67–83.

[63] R. Séguéla, On the Natural Draw Ratio of Semi-Crystalline Polymers: Review of the Mechanical, Physical and Molecular Aspects, Macromolecular Materials and Engineering. 292 (2007) 235–244.

[64] Bijin Xiong, Olivier Lame, Jean-Marc Chenal, Yongfeng Men, Roland Seguela, Gerard Vigier, Critical stress and thermal activation of crystal plasticity in polyethylene: Influence of crystal microstructure and chain topology, Polymer. 118 (2017) 192–200.

[65] B. Xiong, O. Lame, R. Seguela, Y. Men, Micro/macro-stress relationship and local stress distribution in polyethylene spherulites upon uniaxial stretching in the small strain domain, Polymer. 140 (2018) 215–224.

[66] L. Lin, A.S. Argon, Structure and plastic deformation of polyethylene, Journal of Materials Science. 29 (1994) 294–323.

[67] F. Addiego, A. Dahoun, C. G'Sell, J.-M. Hiver, Characterization of volume strain at large deformation under uniaxial tension in high-density polyethylene, Polymer. 47 (2006) 4387–4399.

[68] L. Cangemi, S. Elkoun, C. G'Sell, Y. Meimon, Volume strain changes of plasticized poly (vinylidene fluoride) during tensile and creep tests, Journal of Applied Polymer Science. 91 (2004) 1784–1791.

[69] V. Gaucher–Miri, C. Depecker, R. Séguéla, Reversible strain-induced order in the amorphous phase of a low-density ethylene/butene copolymer, Journal of Polymer Science Part B: Polymer Physics. 35 (1997) 2151–2159.

[70] A. Peterlin, Molecular model of drawing polyethylene and polypropylene, Journal of Materials Science. 6 (1971) 490–508.

[71] A. Peterlin, F.J. Balta-Calleja, Diffraction studies of plastically deformed polyethylene, Kolloid-Zeitschrift Und Zeitschrift Für Polymere. 242 (1970) 1093–1102.

[72] Zhiyong Jiang, Yujing Tang, Jens Rieger, Hans-Friedrich Enderle, Dieter Lilge, S.V. Roth, R. Gehrke, W. Heckmann, Y. Men, Two lamellar to fibrillar transitions in the tensile deformation of high-density polyethylene, Macromolecules. 43 (2010) 4727–4732.

[73] H.P. Wang, S.P. Chum, A. Hiltner, E. Baer, Deformation of elastomeric polyolefin spherulites, Journal of Polymer Science Part B: Polymer Physics. 47 (2009) 1313–1330.

[74] A. Peterlin, R. Corneliussen, Small-angle x-ray diffraction studies of plastically deformed polyethylene. II. Influence of draw temperature, draw ratio, annealing temperature, and time, Journal of Polymer Science Part A-2: Polymer Physics. 6 (1968) 1273–1282.

[75] B. Xiong, O. Lame, J. M. Chenal, C. Rochas, Roland Seguela, On the strain-induced fibrillar microstructure of polyethylene: Influence of chemical structure, initial morphology and draw temperature, Express Polymer Letters. 10 (2016) 311.

[76] S. Humbert, O. Lame, J.-M. Chenal, R. Seguela, G. Vigier, Memory effect of the molecular topology of lamellar polyethylene on the strain-induced fibrillar structure, European Polymer Journal. 48 (2012) 1093–1100.

[77] M.F. Butler, A.M. Donald, W. Bras, G.R. Mant, G.E. Derbyshire, A.J. Ryan, A real-time simultaneous small-and wide-angle X-ray scattering study of in-situ deformation of isotropic polyethylene, Macromolecules. 28 (1995) 6383–6393.

[78] M.F. Butler, A.M. Donald, A.J. Ryan, Time resolved simultaneous small-and wide-angle X-ray scattering during polyethylene deformation 3. Compression of polyethylene, Polymer. 39 (1998) 781–792.

[79] Michael F. Butler, Athene M. Donald, A real-time simultaneous small-and wide-angle X-ray scattering study of in situ polyethylene deformation at elevated temperatures, Macromolecules. 31 (1998) 6234–6249.

[80] Y. Zhang, P.-Y.B. Jar, S. Xue, L. Li, Quantification of strain-induced damage in semi-crystalline polymers: a review, Journal of Materials Science. 54 (2019) 62–82.

[81] A. Pawlak, A. Galeski, A. Rozanski, Cavitation during deformation of semicrystalline polymers, Progress in Polymer Science. 39 (2014) 921–958.

[82] S. Castagnet, S. Girault, J.L. Gacougnolle, P. Dang, Cavitation in strained polyvinylidene fluoride: mechanical and X-ray experimental studies, Polymer. 41 (2000) 7523–7530.

[83] A. Galeski, A.S. Argon, R.E. Cohen, Changes in the morphology of bulk spherulitic nylon 6 due to plastic deformation, Macromolecules. 21 (1988) 2761–2770.

[84] J.M. Brady, E.L. Thomas, Deformation of oriented high density polyethylene shish-kebab films, Journal of Materials Science. 24 (1989) 3311–3318.

[85] I. Raphael, N. Saintier, G. Robert, J. Béga, L. Laiarinandrasana, On the role of the spherulitic microstructure in fatigue damage of pure polymer and glass-fiber reinforced semi-crystalline polyamide 6.6, International Journal of Fatigue. 126 (2019) 44–54.

[86] M. Andersen, O.S. Hopperstad, A.H. Clausen, Volumetric strain measurement of polymeric materials subjected to uniaxial tension, Strain. 55 (2019) e12314.

[87] Sandrine Humbert, O. Lame, J. M. Chenal, C. Rochas, G. Vigier, New insight on initiation of cavitation in semicrystalline polymers: in-situ SAXS measurements, Macromolecules. 43 (2010) 7212–7221.

[88] C. G'sell, J.M. Hiver, A. Dahoun, Experimental characterization of deformation damage in solid polymers under tension, and its interrelation with necking, International Journal of Solids and Structures. 39 (2002) 3857–3872.

[89] A. Lazzeri, Y.S. Thio, R.E. Cohen, Volume strain measurements on CaCO3/polypropylene particulate composites: the effect of particle size, Journal of Applied Polymer Science. 91 (2004) 925–935.

[90] L.C. Cessna, Dilatometric studies of polymers undergoing high and low rate tensile deformation, Polymer Engineering & Science. 14 (1974) 696–701.

[91] B. Xiong, O. Lame, J. M. Chenal, C. Rochas, Roland Seguela, G. Vigier, In-situ SAXS study and modeling of the cavitation/crystal-shear competition in semi-crystalline polymers: Influence of temperature and microstructure in polyethylene, Polymer. 54 (2013) 5408–5418.

[92] F. Detrez, S. Cantournet, R. Seguela, Plasticity/damage coupling in semi-crystalline polymers prior to yielding: Micromechanisms and damage law identification, Polymer. 52 (2011) 1998–2008.

[93] L. Mullins, Permanent set in vulcanized rubber, Rubber Chemistry and Technology. 22 (1949) 1036–1044.

[94] Leonard Mullins, Softening of rubber by deformation, Rubber Chemistry and Technology. 42 (1969) 339–362.

[95] A.F. Blanchard, D. Parkinson, Breakage of carbon-rubber networks by applied stress, Industrial & Engineering Chemistry. 44 (1952) 799–812.

[96] F. Bueche, Molecular basis for the Mullins effect, Journal of Applied Polymer Science. 4 (1960) 107–114.

[97] G. Kraus, C.W. Childers, K.W. Rollmann, Stress softening in carbon black-reinforced vulcanizates. Strain rate and temperature effects, Journal of Applied Polymer Science. 10 (1966) 229–244.

[98] A. Dorfmann, R.W. Ogden, A constitutive model for the Mullins effect with permanent set in particle-reinforced rubber, International Journal of Solids and Structures. 41 (2004) 1855–1878.

[99] S. Govindjee, J. Simo, A micro-mechanically based continuum damage model for carbon black-filled rubbers incorporating Mullins' effect, Journal of the Mechanics and Physics of Solids. 39 (1991) 87–112.

[100] Julie Diani, Bruno Fayolle, Pierre Gilormini, A review on the Mullins effect, European Polymer Journal. 45 (2009) 601–612.

[101] Rubber Houwink, Slipping of molecules during the deformation of reinforced rubber, Rubber Chemistry and Technology. 29 (1956) 888–893.

[102] D.E. Hanson, M. Hawley, R. Houlton, K. Chitanvis, P. Rae, E.B. Orler, D.A. Wrobleski, Stress softening experiments in silica-filled polydimethylsiloxane provide insight into a mechanism for the Mullins effect, Polymer. 46 (2005) 10989–10995.

[103] Y. Fukahori, New progress in the theory and model of carbon black reinforcement of elastomers, Journal of Applied Polymer Science. 95 (2005) 60–67.

[104] G. Ayoub, F. Zaïri, M. Naït-Abdelaziz, J.M. Gloaguen, Modeling the low-cycle fatigue behavior of visco-hyperelastic elastomeric materials using a new network alteration theory: application to styrene-butadiene rubber, Journal of the Mechanics and Physics of Solids. 59 (2011) 473–495.

[105] J. Diani, M. Brieu, P. Gilormini, Observation and modeling of the anisotropic visco-hyperelastic behavior of a rubberlike material, International Journal of Solids and Structures. 43 (2006) 3044–3056.

[106] F.P.C. Gomes, M.R. Thompson, Analysis of Mullins effect in polyethylene using ultrasonic guided waves, Polymer Testing. 60 (2017) 351–356.

2 Materials and preliminary characterizations

2.1 Introduction

In this chapter, the protocol of sample preparation with different thermal treatments is introduced. Before and after the molding with HDPE pellets, various experimental techniques at both macro- and micro- scales are performed to characterize the initial pellets and molded sheets preliminarily. The principle and experimental conditions of each characterization are also presented.

2.2 Summary of HDPE materials

The industrial HDPE material for the piping application in the nuclear center (PE-100 and further labeled as PE-I) is provided by the industrial partner Electricity of France (*EDF*) in two forms: 1) a pipe model with internal and external diameters of 253 mm 315 mm respectively and 2) original pellets. This industrial HDPE material is filled with carbon black (CB). The pipe model is submitted to the same processing and molding as the real one supplied in the nuclear power plant. Because of its large dimensions (the one in the nuclear power plant), the microstructure of the pipe may be heterogeneous as a result of the varying thermal histories in different positions during the shaping process. The pipe model is thus provided to reproduce and probe the microstructural homogeneity of the real pipe. The pellets are used to prepare samples corresponding to different positions of the pipe via thermal treatments.

In order to broaden the field of investigations, two types of “natural” HDPE hereafter denoted as PE-A and PE-B were ordered from INEOS (Brussels, Belgium) and studied. The PE-B is also a commercial material used in PE-100 pipe application, whereas PE-A is a grade dedicated to blow-molding. These two materials contain only minimal additives that are necessary for processing, but no CB fillers. The molecular characteristics of the pellets were measured by INEOS group using gel permeation chromatography (GPC) (see **Table 1.1**). Although the M_n in PE-B is lower than PE-A, as for other averages of molecular weight and polydispersity (M_w/M_n), the ones in PE-B are all higher than PE-A. Due to the different molecular characteristics, the microstructure and morphology of these two materials submitted to the identical shaping protocol differ from each other. The procedure of the GPC tests and the molecular characteristics of PE-I are not displayed due to the confidential reasons.

Table 2.1: Molecular characteristics of the PE-A and PE-B materials.

Materials	M_n (g/mol)	M_w (g/mol)	M_z (g/mol)	M_w/M_n
PE-A	7 500	202 200	1 478 900	26.96
PE-B	6 700	270 800	1 589 400	40.42

M_n,, M_w and M_z are the number-average molar mass, the weight-average molar mass and z-average molar mass measured by gel permeation chromatography.

2.3 Thermogravimetric analysis (TGA)

2.3.1 Principle

Thermogravimetric analysis (TGA) consists of studying the material degradation by increasing its temperature while measuring its variation of mass. The technology requires an accurate measurement of the mass and temperature of the sample over time while controlling the atmosphere within the furnace. The obtained thermogram is related to the nature of the sample formulation. In this thesis, this technique can be used for measuring the CB content of PE-I and check the purity of PE-A and PE-B.

2.3.2 Experimental conditions

The aforementioned three PE pellets were tested with a machine PerkinElmer TGA Pyris. The experimental parameters were defined according to the ISO 6964 (Polyolefin pipes and fittings: Determination of carbon black content by calcination and pyrolysis) and ISO 11358-1 (Plastics-Thermogravimetry (TG) of polymers-Part 1: General principles). About 15-20 mg samples were placed into the crucible after taring the apparatus. The procedure was programed as follow:

Switch the gas to nitrogen flow at 50ml/min:

1. Hold for 2min at 25°C
2. Heat up from 25°C to 550°C at 10°C/min
3. Hold for 5min at 550°C
4. Cool down from 550°C to 500°C at 20°C/min

Switch the gas to oxygen flow at 50ml/min:

1. Heat up from 500°C to 800°C at 10°C/min
2. Hold for 15min at 800°C
3. Cool down from 800°C to 25°C at 20°C/min
4. Hold for 1min at 25°C

Each test was repeated three times and the results were averaged.

2.3.3 Preliminary results

Figure 3.1 displays the evolution of the mass weight of samples (%) as a function of temperature (°C). Under nitrogen flow, the three materials experience a significant loss of weight at about 480°C (±2°C). At 550°C or so, about 99.6% (±0.3%) of the PE-A and PE-B samples weight have been lost, whereas the PE-I sample lost about 97.1% (±0.1%) of its weight. During further temperature scan under oxygen flow, the variation of mass only occurs in the PE-I sample: in the vicinity of 600°C, the sample continually lost about the remaining 2.8% (±1%) of its initial mass. According to this finding, the CB content is only about 2.8% in the PE-I samples. Moreover, the PE-A and PE-B samples can be approximately considered as pure HDPE materials.

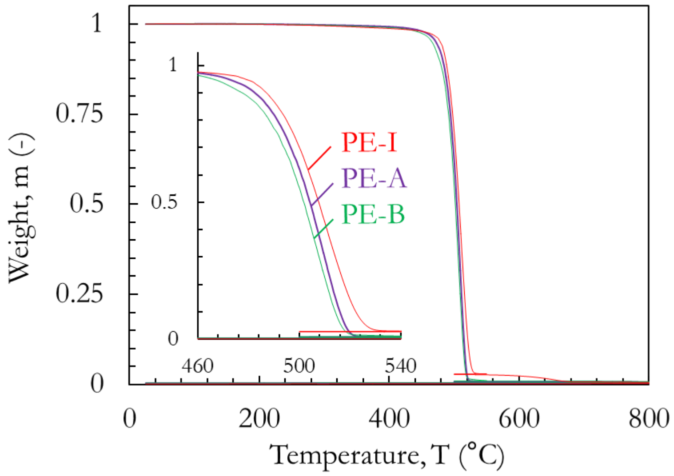

Figure 3.1: *TGA curves of HDPE samples.*

2.4 Molding with different thermal treatments (HDPE pellets)

It is known that the industrial pipe PE-100 was shaped by quenching, suggesting that a gradient of crystallizing rate along the radial direction happened during the molding (the high crystallizing rate at the exterior of the tube, which contacts the liquid, and the low crystallizing rate at interior due to the poor heat transfer). As mentioned in **Chapter 1.3.1**[1–3], the difference of thermal history is highly relevant to the regime of crystallization, thus the microstructural properties of semi-crystalline polymers. Therefore, the effect of thermal treatments should be taken into account during the sample preparation (the validation of this assumption is established in the next **subsection 2.5.3**).

The aforementioned crystallization regimes I and III in **Chapter 1.3.1** represent the two extreme conditions[1]. To approximate these two regimes, the so-called quenching (Regime III) and isothermal treatment (Regime I) are applied respectively.

Prior to the thermal treatments, the samples were firstly compression-molded at 10 MPa and 200°C for about 10 min in a designed aluminum-alloy mold that is displayed in **Figure 4.1**.

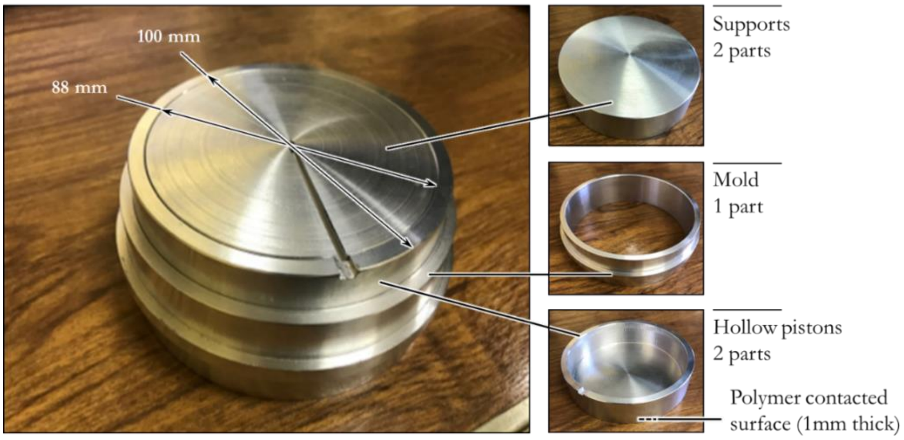

Figure 4.1: *Schematic of the assembled aluminum-alloy mold and its constitutive parts.*

The two supports were designed to increase the resistance against the compression of the mold. After the compression molding step, the two supports were removed, and the remaining components together with the molded polymer sheet were placed into the appropriate liquid of the desired thermal treatment. The polymer-contacted surface of the hollow pistons was quite thin (about 1mm) so that the thermal exchange associated with the crystallization could be effectively performed. **Figure 4.2** shows the schematic of the shaping process by pellets with different thermal treatments.

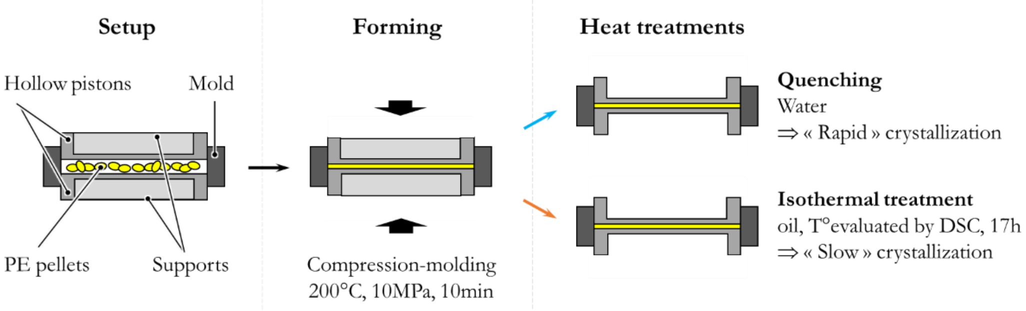

Figure 4.2: *Schematic of the shaping process with different thermal treatments.*

One group of samples was solidified in cold water so that the cooling rate was high. This procedure corresponded to the quenching process and the crystallization was potentially finished within just a few seconds thus following Regime III. The associated thermal program is shown in **Figure 4.3a.** Another group of samples was crystallized in an oil bath at a selected temperature T_{iso} in the vicinity of the crystallization temperature T_c. Details regarding the selection of T_{iso} will be provided in **subsection 2.5.3**. Here again, a schematic of the program of isothermal treatment is shown in **Figure 4.3b**.

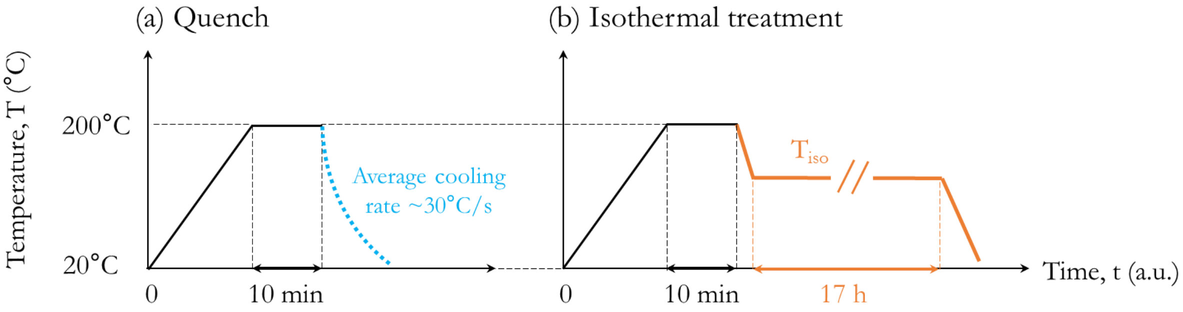

Figure 4.3: *Temperature profiles of the quenching and isothermal treatments: (a) quench; (b) isothermal treatment.*

2.5 Differential scanning calorimetry (DSC)

2.5.1 Principle

The phase transformations of the materials are along with the release or absorption of energy. These changes can be characterized by Differential Scanning Calorimetry (DSC), which measures the difference of the exchanged heat flux between a sample and a reference subjected to the same thermal history. The heat flux expressed in Wg^{-1} can be converted into specific heat C_p in $J.g^{-1}K^{-1}$.

Finally, the melting enthalpy ΔH_f can be determined as follow:

$$\Delta H_f = \int_{T_1}^{T_2} C_P dT \qquad (1)$$

Figure 5.1 displays the variation of specific heat (or heat flux) as a function of temperature (°C) where the solid sample is heated up to molten state and then cooled down back to room temperature: an endothermic peak relevant to melting of the crystallites and an exothermic peak associated with crystallization can be observed upon heating and cooling respectively.

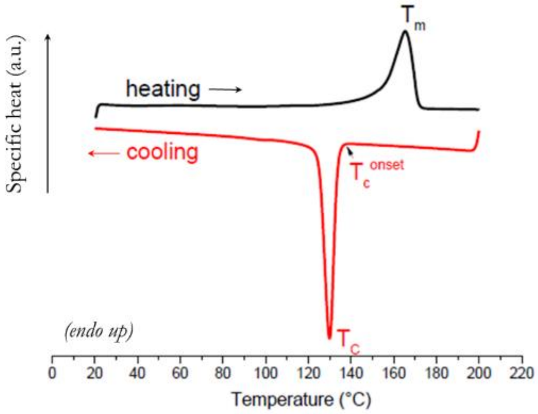

Figure 5.1: *Classical endothermic and exothermic DSC peaks in PE (figure adapted from Xiong[4]).*

The first aim of DSC characterization is to determine the temperature of isothermal treatment for the different PEs. And another important use of this technique is to measure the crystallinity of semi-crystalline polymers using relation (2).

$$X_c = \frac{\Delta H_f}{\Delta H_f^0} \qquad (2)$$

ΔH_f is the melting enthalpy calculated by equation (1). T_1 and T_2 are respectively the onset and end of the endothermic peak and ΔH_f^0 is the melting enthalpy of a theoretically perfect crystalline polymer. For the case of PE, ΔH_f^0 was set equal to 290 J/g[5].

2.5.2 Experimental conditions

The DSC measurements were conducted with an indium-calibrated Perkin-Elmer DSC7 machine (see **Figure 5.2**). About 6-8mg samples were heated up to 150°C at a heating rate of 10°C/min and stayed at 150°C for about 5 minutes, then cooled down to 30°C at the same rate under nitrogen flow.

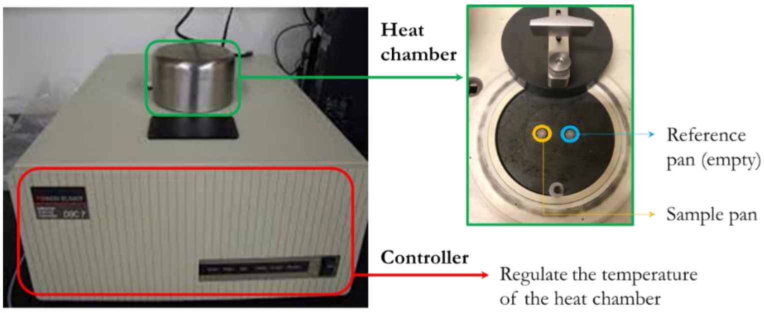

Figure 5.2: *Perkin-Elmer DSC7 apparatus.*

2.5.3 Preliminary results

2.5.3.1 Validation of the crystallinity heterogeneity in the industrial pipe

Figure 5.3 plots the crystallinity X_c as a function of radial position r (from inner to outer surfaces) of industrial tube PE100. r=0 mm corresponds to the internal surface whereas r=31 mm corresponds to the outer one. Each sample spans 3mm along this direction, which is considered by the horizontal error bar in **Figure 5.3** (right). Clearly, at the outer surface, where the rapid crystallization was expected, the crystallinity is at its lowest value (about 57%), and a gradient of crystallinity was found from r≈22mm to r=31mm. For the remaining part of the tube (from r=0mm to r≈22mm), the crystallinity remains almost constant at its highest (about 62.5%).

As evoked, the difference in crystallinity is attributed to the varying thermal history taking place during the molding and subsequent solidification. Therefore, the aforementioned assumption of the crystallinity heterogeneity is validated: during the sample preparation (with pellets), the influence of thermal treatments is important and necessary to be taken into account.

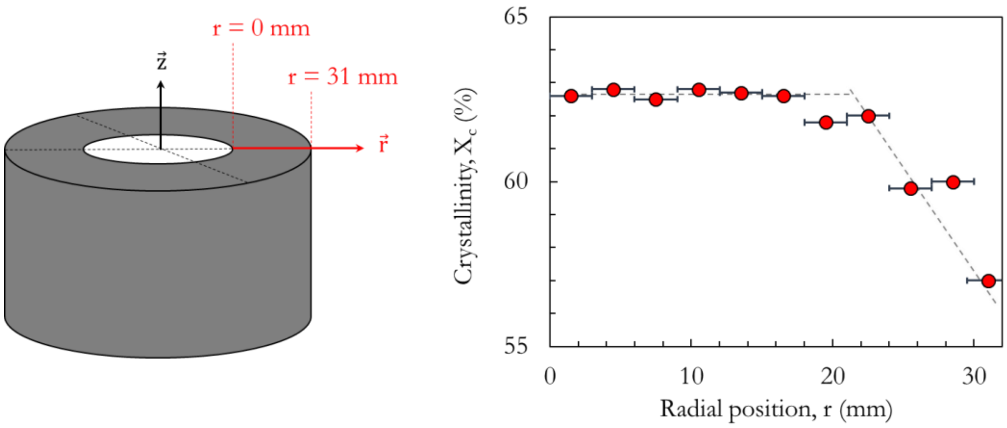

Figure 5.3: *The local crystallinity of industrial tube PE100 as a function of the radial position (N.B. the dashed grey lines are visual guidelines).*

It is worth noting that the crystallinity was also measured along the longitudinal direction (different location along z) at the inner free surface, and no significant variation was found. Therefore, it can be deduced that the crystallization rate is only as a function of the radial direction.

2.5.3.2 Selection of temperature for the isothermal treatment

The annealing temperature T_{iso} should meet two requirements:

1) T_{iso} should be a little bit higher than the minimum temperature for which the crystallization occurs T_c^{onset} so that the crystallization can take place "slowly" and approximately follows the Regime I introduced in **Chapter 1.3.1**. Following this procedure, the crystallinity should be the highest one for a prescribed material.

2) In the DSC curve, a smaller endothermic peak at a lower temperature is possible to be observed (see **Figure 5.4a**). In fact, above a critical T_{iso}, whatever the duration of the isothermal step, the crystallization is no longer complete, which leads to the creation of a significant proportion of small crystallites when the sample is cooled down to room temperature (after the isothermal treatment), designated as the second crystallization. The higher the annealing temperature, the more significant the second peak. Although it is not clarified in the literature, this second crystallization may potentially play a role in the microstructural and mechanical properties of polymers. Therefore, this phenomenon should be avoided and thus trigger the final choice of the annealing temperature.

As an example, the baseline-corrected heating DSC profiles in the 75°C-150°C temperature range of PE-I isothermal samples are displayed in **Figure 5.4a**. The corresponding crystallinity is plotted in **Figure 5.4b** as a function of the annealing temperature. With T_{iso} varying between 116 and 123°C limited influence was found on the crystallinity which was about 64%. Also, the second crystallization, with its peak occurring around 115°C, is seen to progressively decrease with the decrease of the annealing temperature. For T_{iso}= 116°C, it is almost ignored. Therefore, 116°C is chosen as the final T_{iso} for the PE-I material. The same method is applied to determine T_{iso} for the PE-A (121.5 °C) and PE-B (118°C) materials.

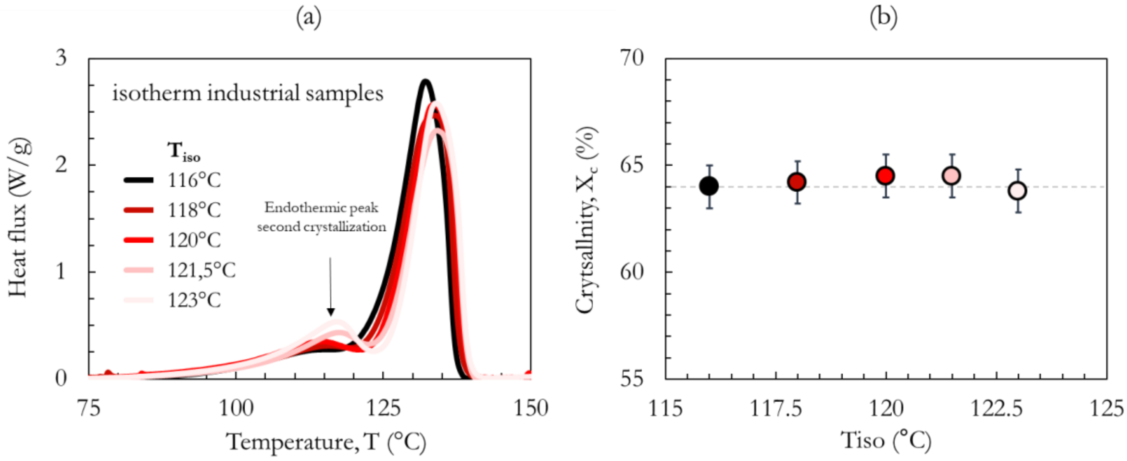

Figure 5.4: *(a) DSC curves for the isotherm industrial samples with different* T_{iso} *in the vicinity of the melting temperature (endo up); (b) crystallinity of isotherm samples as a function of treating temperature* T_{iso}.

2.5.3.3 Crystallinity and melting temperature

On the one hand, the DSC technique allows for the measurement of the melting enthalpy so that the crystallinity can be calculated by equation (2). On the other hand, the maximum temperature of the melting peak can be also measured. This parameter is relevant to the thickness of crystallites according to the following equation (3),

$$T_f = T_f^0 \times \left(1 - \frac{2\sigma_e}{\Delta H_f^0 \rho_c L_c}\right) \tag{3}$$

Where T_f is the melting temperature, T_f^0 the melting temperature of a perfect PE crystal (T_f^0 =141°C see [6]), ρ_c the density of PE crystal (1.003 g/cm^3) [7], σ_e the surface energy of the crystalline lamellae and L_c the thickness of crystallites. Ultimately, following the relation (3), the higher the melting temperature, the thicker the crystallites. The DSC curves of the materials resulting from the different thermal treatments are displayed in **Figure 5.5**. For each polymer, the isothermal sample has a relatively higher crystallinity and melting temperature than the quenched sample, indicating thicker crystals due to a better organization and arrangement of chains stacking during the crystallization process[8].

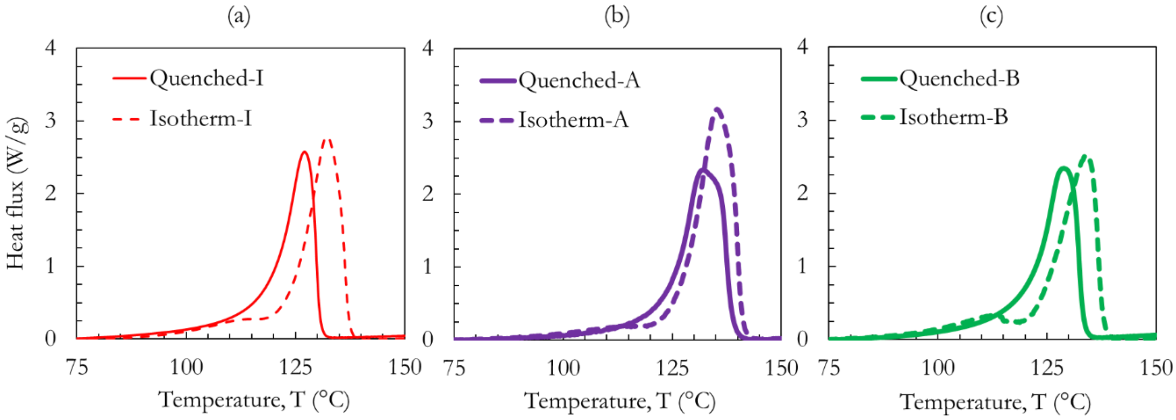

Figure 5.5: *DSC curves of the quenched and isotherm samples in the vicinity of the melting temperature (endo up): (a) PE-industrial; (b) PE-A; (c) PE-B.*

The summary of the microstructural indicators determined by these DSC profiles, namely the crystallinity (X_c) and the melting temperature (T_f), are listed in **Table 5.1**. It is found that the PE-I and PE-B show very similar sensitivity to experienced thermal histories: under identical shaping process (quench or isothermal treatment) both their crystallinity and melting temperature are very similar to each other, whereas the PE-A samples have a higher crystallinity and melting temperature.

Table 5.1: microstructural indicators based on DSC measurements.

Materials		X_c (%)	T_f (°C)
PE-A	Quenched	62	132.2
	Isotherm	73	135.4
PE-B	Quenched	57	129.7
	Isotherm	64	134
PE-I	Quenched	56	127.9
	Isotherm	64	134.2

2.6 X-ray scattering measurements

2.6.1 Principle

The X-ray scattering is a non-destructive technique well suited for characterizing the microstructure of semi-crystalline polymers. A schematic view of the experimental device with its principle is shown in **Figure 6.1.**

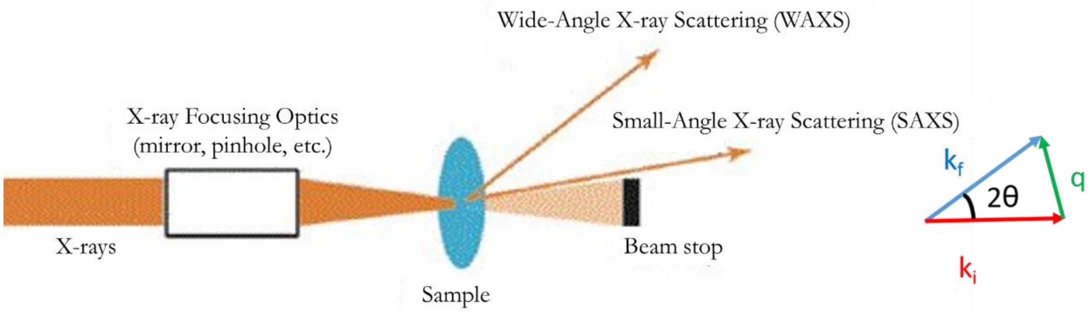

Figure 6.1: *Schematic of an experimental device of X-ray scattering[9].*

When the photons of X-ray meet the electrons of the sample, they are scattered due to the elastic interaction. The norm of the final wave vector $\mathbf{k}_f$ is same as the one of the initial wave vector $\mathbf{k}_i$. The relevant parameter to analyze the interaction is the scattering vector $\mathbf{q}=\mathbf{k}_i-\mathbf{k}_f$. The angle between the incident and scattered X-ray beams can either be defined by the scattering angle 2θ or the norm of the scattering vector q. The relation between the two parameters stands as follow:

$$q=|\mathbf{q}| = \frac{4\pi\sin(\theta)}{\lambda} \tag{4}$$

Where λ is the wavelength of X-ray.

The scattering intensity I(q) is determined as the Fourier Transform of the correlation function of the scattering electronic density at a specific q (or 2θ). Moreover, according to Bragg's law (5), the norm of scattering vector q can be further expressed as equation (6).

$$2d\sin\theta = \lambda \tag{5}$$

$$q= \frac{2\pi}{d} \tag{6}$$

Therefore, the q value is related to an observation window having a diameter d: the q-window at low/high value corresponds to respectively a large/small observation window. The X-ray scattering is thus divided into small-angle X-ray scattering (SAXS) and wide-angle X-ray scattering (WAXS) according to the experimental range of q value.

2.6.2 Experimental conditions

X-ray scattering tests were performed on the SWING beamline of the French SOLEIL synchrotron. To generate synchrotron radiation, the electrons are firstly accelerated in a linear accelerator then transmitted to a circular accelerator that allows them to reach the expected energy. These electrons are then injected into a large ring track, where they will travel at constant energy for several hours. The circular trajectory of the electrons is maintained by the magnets, which are inside the ring. Synchrotron radiation is emitted during the passage of the electrons in front of the bending magnets. The latter is then collected and directed to various beamlines (see **Figure 6.2a**).

On-site and as shown in **Figure 6.2b**, the samples were held in a homemade tensile machine to couple the X-ray measurements with the mechanical testing. The wavelength of the incident X-ray beam is equal to 1.03 Å. A WAXS detector is located 109 mm away from the sample, whereas the SAXS detector sits at the end of the detection tunnel, at a distance of about 2003 mm from the sample. Consequently, the q-range of observation lies between 0.036-0.52 Å^{-1} and 1.5-3.17 Å^{-1} for the SAXS and WAXS configurations respectively.

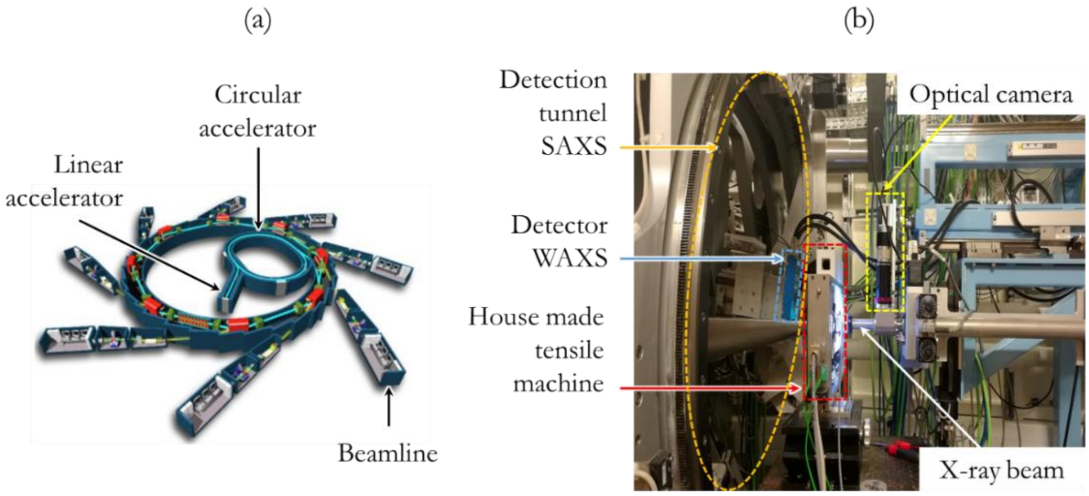

Figure 6.2: *(a) schematic of a synchrotron facility; (b) set-up for in-situ X-ray scattering measurements;*

2.6.3 Preliminary results

Pristine state

In the undeformed state, the scattering SAXS 2D patterns (*i.e.* the low q range) for all the PE samples are isotropic ring-shaped (as illustrated in **Figure 6.3a)** due to the randomly orientated crystalline lamellae in the spherulites**.** The smallest unit of repeated lamellar structure, whose value equals the sum of a single lamellar thickness plus the thickness of a single interlamellar amorphous layer, is defined as the long period L_p and can be determined from the SAXS patterns as follow:

$$\mathrm{L_p} = \frac{2\pi}{\mathrm{q_{max}}} \qquad (7)$$

Where q_{max} is the q value corresponding to the maximum diffuse intensity. It is directly obtained from the 1D plot such as the profile reported in **Figure 6.3b** which presents the Lorentz-corrected scattering intensity Iq^2 as a function of q value. This diagram can be obtained whatever the azimuthal angle ϕ and usually results from an azimuthal integration over few degrees (range arbitrarily set to ±5° in this work) surrounding the chosen angle. In the following, since the X-ray measurements will be coupled with tensile testing, preferred angles defined as H and V, and oriented parallel (0°) and perpendicular (90°) to the tensile direction respectively, will be specifically studied.

Referring to the crystallinity obtained by DSC, the thickness of a single crystalline layer can be computed by relations (8):

$$L_c = L_P \frac{\rho}{\rho_c} X_c \tag{8}$$

$$\frac{1}{\rho} = \frac{X_c}{\rho_c} + \frac{1-X_c}{\rho_a} \tag{9}$$

Where ρ, ρ_a, ρ_c are the densities of the material (calculated using relation (9)), the amorphous phase (0.850 g/cm^3) and the crystalline phase (1.003 g/cm^3) respectively[7].

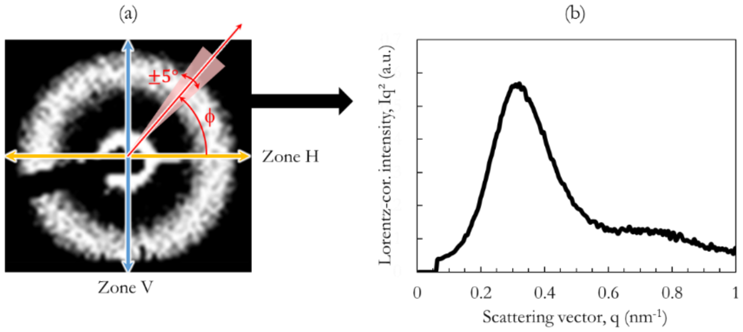

Figure 6.3: *(a) 2D SAXS pattern and (b) 1D plot of Lorentz-corrected intensity as a function of q*

At high q range, the inter-planar distances *d* in crystallographic unit cell can be determined by WAXS evaluation using the same equations (5) or (6). An example of the WAXS 2D pattern is shown in **Figure 6.4a**. It worth noting that the WAXS detector only captures the local information at Zone V due to the limit of dimension and position. Again, a 1D diagram of intensity against q value obtained by azimuthal integration of the 2D pattern for a given azimuthal angle is presented in **Figure 6.4b**. Thanks to the q range covered, numerous scattering peaks corresponding to different crystallographic planes are recorded.

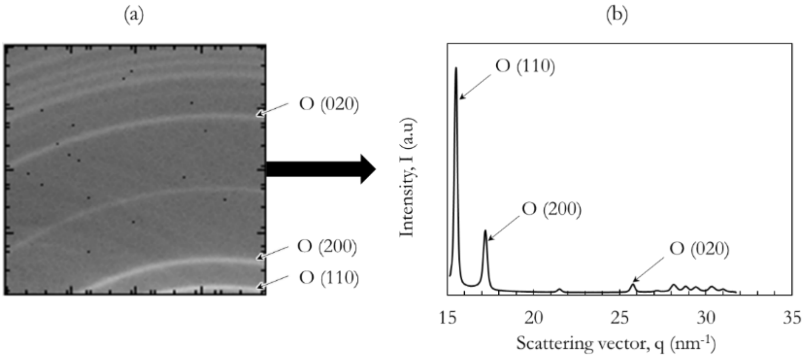

Figure 6.4: *(a) 2D WAXS pattern and (b) 1D plot of intensity as a function of q*

Using both the SAXS and WAXS measurements of the undeformed states, the initial lamellar and crystallographic structures of the different PE can thus be compared.

Focusing on the WAXS profiles, the peaks were found strictly located at the same position in each PE sample. Such results suggest that the crystallographic structure of the PE at room temperature is quasi constant and not affected by the thermal treatment. Although their evolution during the mechanical tests, are also of great interest, for example, to estimate the local stress, the inter-planar distances are not displayed in this chapter as microstructural characteristics of pristine samples.

Now looking at the SAXS profiles, the isotropic ring-shaped pattern was found in each PE sample yet the q position of the scattering peak differs, from each other. Hence, at nanoscale, their long period, *i.e.* the thickness of the lamellae, and/or the thickness of the amorphous layer vary. The microstructural indicators gathered from the SAXS patterns are listed in **Table 6.1.** For the same material, the isotherm sample has a higher long period and thickness of crystallites than the quenched one. Subjected to the same thermal treatment, relatively thicker crystallites can be observed in PE-A sample compared to the PE-B and PE-I samples which two show significant similarities. Noticeably, focusing on the thickness of crystallites L_c, the data obtained by SAXS measurements are in accordance with the result reduced from the DSC characterizations.

Table 6.1: Microstructural characteristics obtained by SAXS measurement

Materials		L_p (nm)	L_c (nm)	L_a (nm)
PE-A	Quenched	22	13	9
	Isotherm	35	24	11
PE-B	Quenched	20	11	9
	Isotherm	33	20	13
PE-I	Quenched	20	11	9
	Isotherm	35	21	14

2.7 Simple tensile characterization

2.7.1 Principle

Mechanical performances can be evaluated based on the stress-strain relation. For uniaxial tensile tests performed on a dedicated sample having a gauge of length L_0 and cross section A_0, assuming the deformation to be homogeneous and uniquely occurring within the gauge length, the axial nominal stress is defined as the ratio of loading force and pristine sample section, F/A_0, and the axial nominal strain is denoted as the ratio of current and initial gauge length $\Delta L/L_0$. Based on the initial geometry of the sample, the engineering formalism lacks providing a realistic description of the transformation experienced by the material submitted to moderate/large deformation (i.e. This description is suitable for $\Delta L << L_0$). Thus, the true stress-strain curves are often preferred to describe the mechanical behavior of a specimen heavily deformed. The true stress is defined as F/A, where A is the current section area at a certain moment. Under homogeneous isovolumetric assumption (i.e. $AL=A_0L_0$), the true stress and strain can be respectively determined by the following equations **(**10) and (11).

$$\sigma_{true} = \frac{F}{A} = \frac{(1+\varepsilon)F}{A_0} = (1+\varepsilon)\sigma_n \quad (10)$$

$$\varepsilon_{true} = \int_{l_0}^{l} \frac{dl}{l} = \ln(\frac{l}{l_0}) \quad (11)$$

However, it worth noting that for a semi-crystalline material exhibiting pronounced strain localization (necking), the above equations do only apply when the necking propagation is completed throughout the gauge length and is accurate for the samples without voids generated by deformation (i.e. volume change). Local determination of the strain field based on stereo correlation technique (or Digital Image Correlation) for instance is a way to enhance the characterization of the mechanical response of materials exhibiting this type of behavior.

In this PhD thesis, for the mechanical characterization of polymers, the nominal stress-strain curve is mainly employed. Several mechanical indicators such as the elastic modulus, yield stress, neck width and tensile toughness can be obtained based on the stress-strain relation, as highlighted in **Figure 7.1**.

-The stress-strain data points for ε_{nom}<0.01 are fitted by a linear regression and the slope of the fitting curve is denoted as the elastic modulus of material.

-the yield stress is the maximum value of stress prior to the load drop resulting from the initiation of necking.

- The neck width is designated as the difference in nominal strain between the threshold point of plastic deformation (where the nominal stress is about 80% of yield stress), and the “onset” of the constant-stress plateau coinciding with the necking propagation.
- The tensile toughness is defined as the area under the tensile stress-strain curves. This parameter is ascribed to the energy per unit volume absorbed by the sample when stretched till its failure.

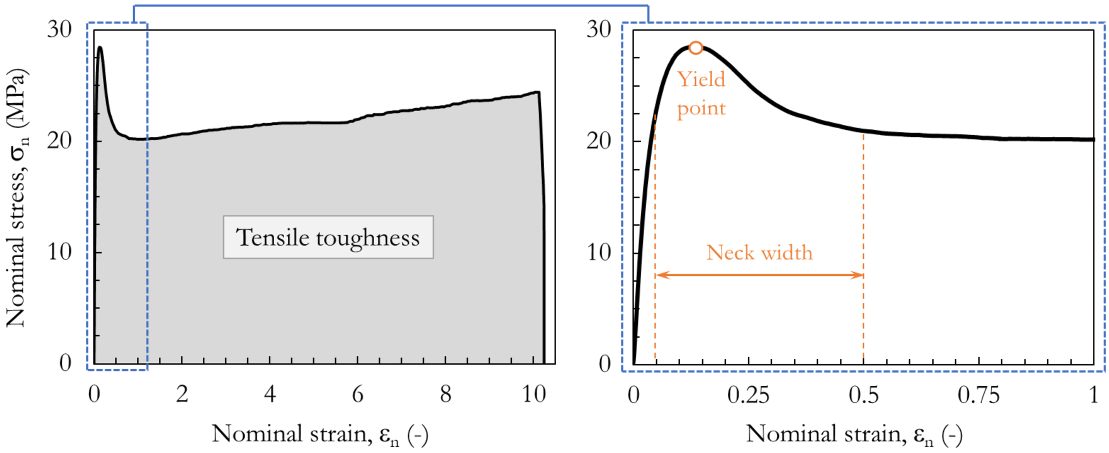

Figure 7.1: *Nominal stress-strain curves and some important mechanical indictors.*

2.7.2 Experimental conditions

Uniaxial tensile tests were conducted using an MTS 1/ME machine equipped with a 5kN load cell (see **Figure 7.2**). The samples were taken from the PE sheets subjected to different thermal treatments by dumbbell-shaped cutters. They are of 6.5 mm gauge length, 4 mm width and about 0.8 mm thickness. The tensile specimens were stretched until failure at a constant nominal strain rate $\dot{\varepsilon_n} = 5 \times 10^{-2}\ s^{-1}$ and at room temperature (about 23°C).

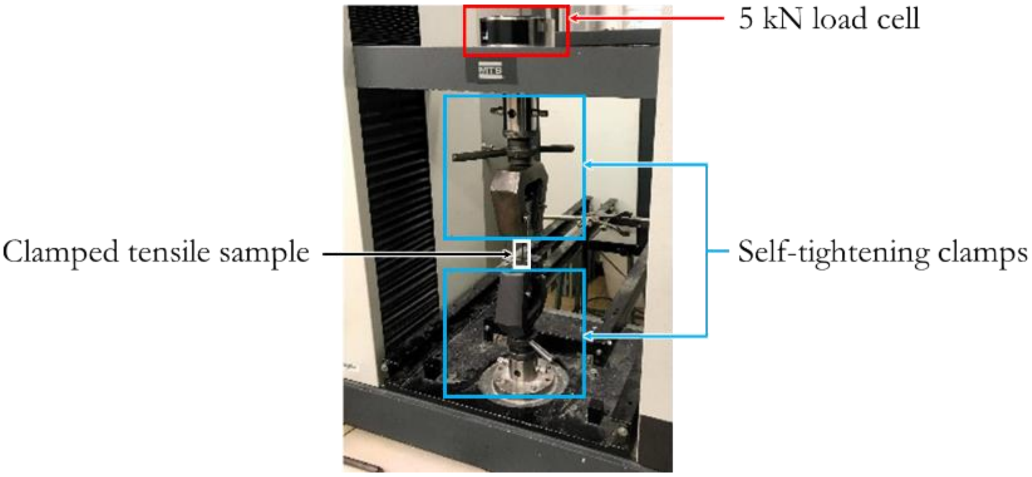

Figure 7.2: *MTS 1/ME machine equipped with 5kN load cell.*

2.7.3 Preliminary results

2.7.3.1 Summary of the results

The nominal tensile curves up to a nominal strain of 1 are displayed in **Figure 7.3** and **Table 7.1** summarizes the mechanical parameters of the 6 materials under consideration (by averaging the results of three repetitions). The deviations are shown in the following figures as the error bar.

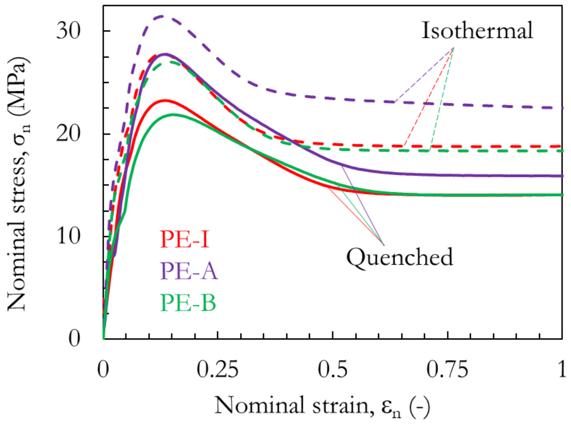

Figure 7.3: *Nominal stress-strain tensile curves (up to ε_n=1).*

Table 7.1: Elastic modulus, Yield stress, neck width and tensile toughness of the PE quenched/isotherm samples measured by uniaxial tensile test.

Materials		Elastic modulus (MPa)	Yield stress (MPa)	Neck width (-)	Tensile toughness (MPa)
PE-A	Quenched	595	24	0.5	202
	Isotherm	663	28	0.3	215
PE-B	Quenched	431	20	0.55	135
	Isotherm	526	24	0.35	154
PE-I	Quenched	437	21	0.55	130
	Isotherm	548	25	0.35	146

2.7.3.2 Micro-macro relations

As shown in **Figure 7.4**, a quasi-linear relation between the yield stress and PE crystallinity can be observed and physically interpreted by the dislocation model (related to the thickness of crystalline lamella) combined with the concentration of stress transmitters (STs) [10,11].

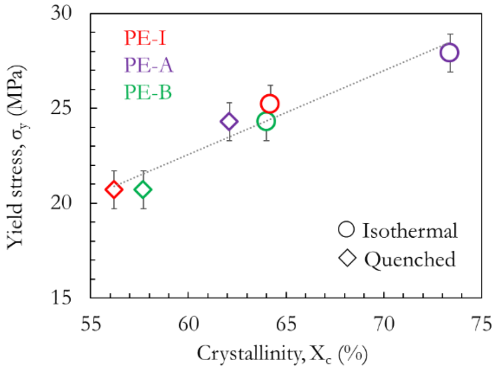

Figure 7.4: *Yield stress as a function of crystallinity.*

As mentioned in **Chapter 1.2.4**, the density of STs ([ST]) can be related to the neck width[10]. It is expected that the quenched samples exhibit a more diffused neck so that the ST density in these samples is higher than that in the isotherm samples due to the incomplete arrangement of chains during the crystallization. It is reported that the neck width follows a negative correlation with L_p[10], which is in accordance with our results (shown in **Figure 7.5a**). Moreover, Taking into account the Weight-Average Molecular Weight, M_w value, the ST density in PE-A and PE-B samples can be also estimated by Brown's model[12,13]. As shown in **Figure 7.5b**, the results obtained by these two methods are coherent.

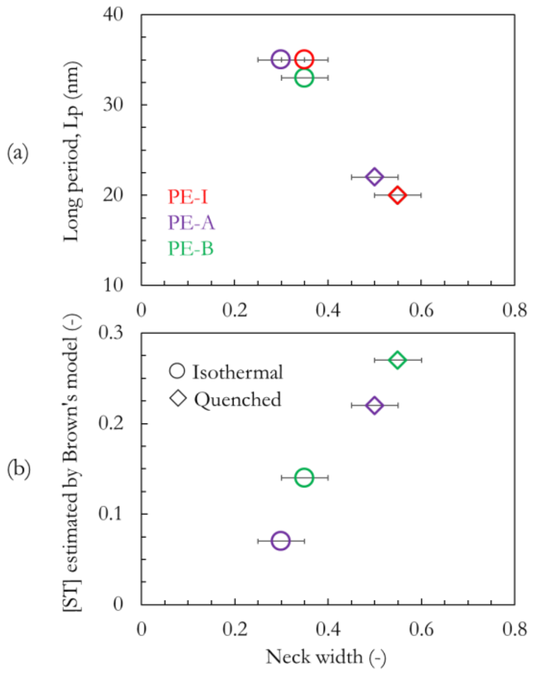

Figure 7.5: *(a) Long period and (b) [ST] value calculated by Brown's model as a function of neck width.*

Considering each material separately, the tensile toughness of the isotherm sample is slightly higher than that of the quenched samples (see **Figure 7.6**). However, it seems that this parameter strongly depends on the initial molecular properties and the influence of thermal treatment is too slight to compare with the material type. Indeed, both PE-A quenched and isotherm samples need to absorb more energy per unit volume during the tensile deformation until failure than other two PE materials.

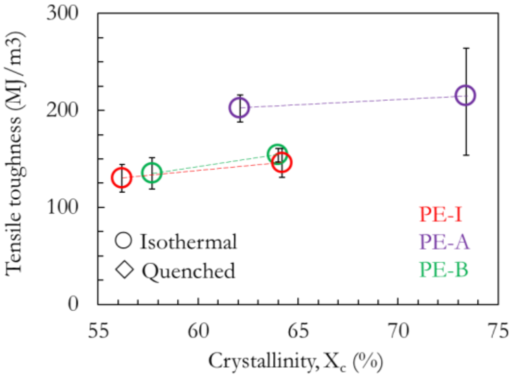

Figure 7.6: *Tensile toughness of PE samples as a function of crystallinity.*

It should mention that the tensile curve (i.e. the equipment used in this thesis) does not provide the required accuracy to evaluate the elastic response. Therefore, the aforementioned linear regression method is applied to obtain an equivalent tangent value for each sample, which can then be compared. As detailed elsewhere[14–16], the relation between the elastic modulus E and crystallinity is determined as follow:

$$E = \frac{E_s E_h (1-V_h+kV_h)}{(1-V_h)E_h+kV_h E_s} \tag{12}$$

Where E_h and E_s are respectively the modulus of hard and soft phases, *k* is a mechanical coupling parameter (the ratio σ_h/σ_s) and V_h is the volumetric fraction of hard phase. Here, the hard and soft phases can be simply assigned to the crystalline and amorphous phase by neglecting the effect of the interphase[16].

Following the relation (12), the kE_s product directly influences the elastic modulus: a high *k* value suggests that the material is assimilated to the "parallel-like coupling" whereas k~1 rather indicates that the "series-like coupling" applies. Physically, a higher *k* value can be interpreted as more percolated crystalline structure. Furthermore, a larger amorphous modulus E_s can be associated with a higher value of density of stress transmitters. Analyzing these two parameters separately remains tricky so that the evaluation of their product is preferred. As displayed in **Figure 7.7a and b**, although quenched samples have relatively lower modulus due to their crystallinity, these samples have a higher value of kE_s. The crystalline percolation should be more important in the isothermal sample[15] due to the higher crystallinity (*k* is higher), however, it seems that the amorphous modulus has a more important influence on their product: the higher density of stress transmitters (related to the neck width) can lead to a higher amorphous modulus, therefore, the product kE_s is more important in the quenched samples.

All in all, it is seen that the modulus is not only dependent on the crystallinity but also on the combination of the percolation and intrinsic property of the amorphous phases. These initial values are important for the further analysis on the evolution of modulus induced by oligo-cyclic loading in the following chapters.

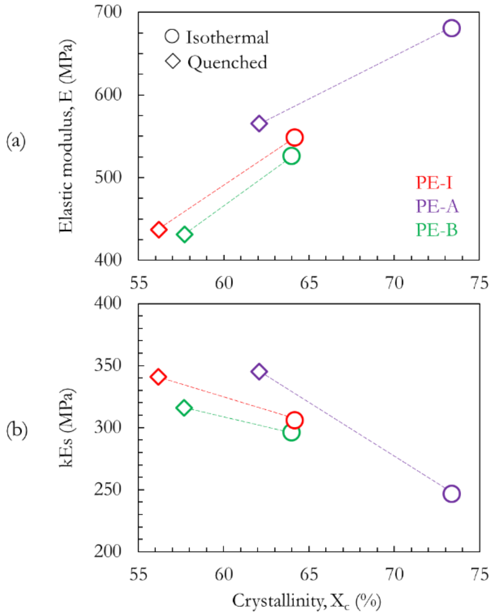

Figure 7.7: *(a) Elastic modulus E and (b) product kE_s as a function of crystallinity.*

2.8 Dynamic mechanical analysis (DMA)

2.8.1 Principle

Dynamic mechanical analysis (DMA) is a technique to characterize the visco-elastic properties of polymers. During this test, the sample is generally subjected to a periodic stress- or strain-controlled loading program. Using the complex formalism for sake of simplicity, if the material is loaded with a stress-controlled program as shown in relation (13), the corresponding strain is thus expressed using equation (14) and a phase lag designated as δ can be found between the applied and collected signals as shown in **Figure 8.1**. The complex modulus E^* (15) defined as the stress/strain ratio can be decomposed into a storage modulus E' and a loss modulus E'', which relate to the material ability to store and dissipate energy during deformation respectively. In addition, the ratio E''/E' or tan δ, is a damping parameter associated with the internal friction of chains due to molecular motions, relaxation processes, transitions, morphology and other structural heterogeneities[4].

$$\sigma^* = \sigma e^{i\omega t} \tag{13}$$

$$\varepsilon^* = \varepsilon e^{i(\omega t-\delta)} \tag{14}$$

$$E^* = \frac{\sigma^*}{\varepsilon^*} = \frac{\sigma}{\varepsilon}(\cos\delta + i\sin\delta) = E' + iE'' \tag{15}$$

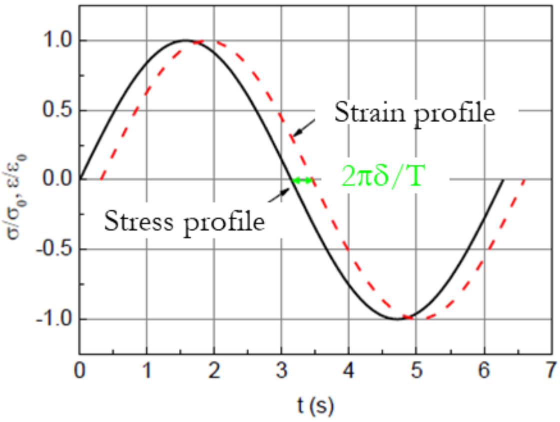

__Figure 8.1:__ Schematic of stress-controlled loading program and responded strain[4].

2.8.2 Experimental conditions

The DMA tests were carried out with a machine GABO EPLEXOR® equipped with a 150N load cell (see **Figure 8.2**). The dumbbell-shaped sample is of 6.5 mm gauge length, 4 mm width and about 0.5 mm thickness. A temperature-scanning program from -30°C-100°C at a heating rate 1K/min is applied. The loading mode is strain-controlled, the static strain is set to 0.1% whereas the dynamic strain amplitude is 0.2% with the frequency equals 1Hz.

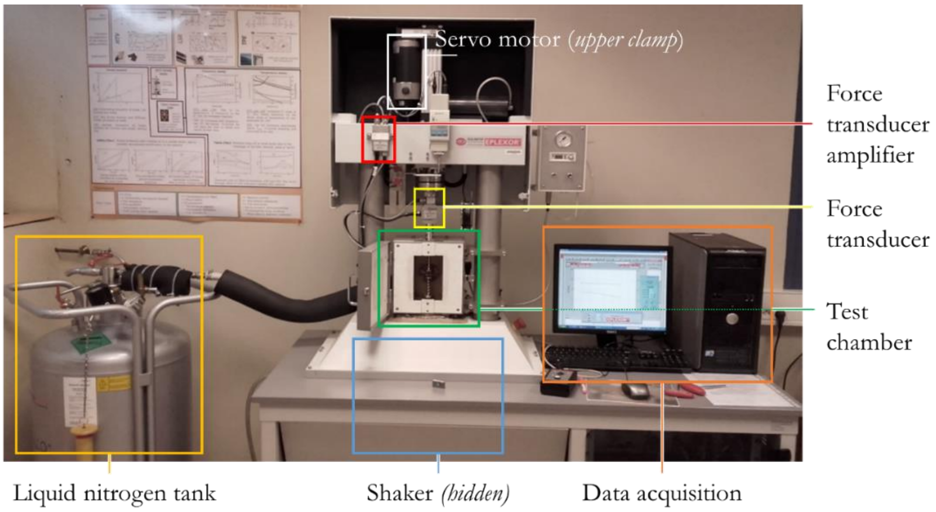

Figure 8.2: *Machine GABO EPLEXOR®*

2.8.3 Preliminary results

The dynamic mechanical responses including the evolutions of storage modulus $E^{'}$, loss modulus $E^{''}$ and loss factor *tan δ* in the six PE specimens are displayed in **Figure 8.3** as a function of the temperature.

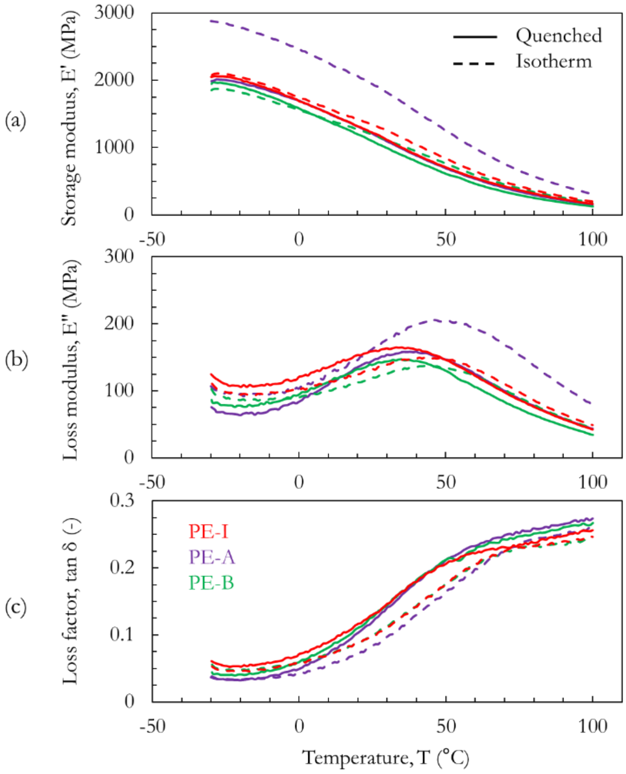

Figure 8.3: *Evolution of visco-elastic properties as a function of temperature.*

For a given temperature, the elastic (or storage) modulus of the PE-A isotherm sample is much higher than the others. Moreover, from 25°C to 100°C, for each material, the isotherm samples have a relatively higher *E'* value., whereas the quenched samples have a higher loss factor *tan δ*.

It worth noting that only α relaxation of PE can be observed at this temperature range. This relaxation is believed to be relevant to the motion within the crystalline phase along the c axis[17] or the movement at the interphase[18] . It is worth noting that the temperature of α relaxation indicated as the peak of the E'' curves, displays a clear dependency on thickness of crystallites (see **Figure 8.4**) and thus thermal treatment. This dependency is in accordance with the previous results reported in the literature[17–19].

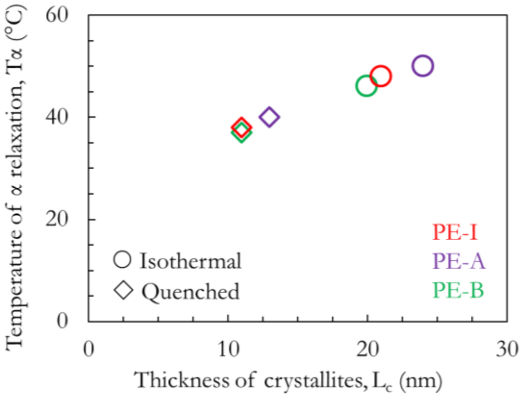

Figure 8.4: *Temperature of α relaxation as a function of thickness of crystallites.*

2.9 Conclusion

The three HDPE materials (PE-A, PE-B and PE-I) are characterized by various experimental techniques preliminarily. PE-B and PE-I are both the material for PE-100 pipe application, whereas PE-A is for blow-molding. According to the results of TGA analysis, PE-A and PE-B can be considered as the pure HDPE material models and PE-I is slightly filled with CB, whose weight content is about 2.8%.

According to the DSC characterization of the industrial PE-100 tube model, the difference of thermal history experienced during the shaping process (quenching) in the different regions of the pipe leads to the heterogeneity of crystallinity along its radial direction (from 57% to 62.5%). Therefore, two extreme crystallization conditions are requested to be taken into account during the sample preparation by PE pellets. During the quenching process, the material crystallizes rapidly in cold water, and during the isothermal treatment, the material crystallizes slowly in the oil bath, at selected annealing temperatures T_{iso}, where the second crystallization of samples is avoided.

Thanks to DSC and SAXS techniques, the crystallinity and geometry of the 2-phase structure at nanoscale (thickness of a single crystalline and amorphous layers) can be directly evaluated. In addition, with the aid of mechanical characterizations, additional microstructural information can be deduced.

Hence, it was found that for a given thermal treatment, the PE-A sample has a relatively higher crystallinity, and thicker crystallites than the PE-B and PE-I samples, which have similar microstructural properties. For the ST density, difference between the quenched samples cannot be exactly evidenced, whereas the PE-A isothermal sample has a lower density of STs compared to the two other isotherm materials.

Considering one material/grade at a time, the quenched sample has a lower crystallinity, thinner crystallites, along with a larger number of stress transmitters. This is due to the rapid and incomplete arrangement of the chains during the crystallization process.

Finally, both the microstructural and mechanical properties of the two HDPEs for PE-100 pipe application (namely PE-B and PE-I) show very similar sensitivity to the thermal treatments, and it seems that the low content of CB in PE-I does not influence their properties. However, in the following chapters, the X-ray scattering technique will be widely used for the microstructural characterization and even an extremely low quantity of CB can dramatically scatter the X-ray and consequently influence the quantitative analysis (i.e. lamellae and cavities). Therefore, the following chapters mainly focus on the PE-A and PE-B materials, and their microstructural evolution upon deformation.

Reference

[1] J.D. Hoffman, R.L. Miller, Kinetic of crystallization from the melt and chain folding in polyethylene fractions revisited: theory and experiment, Polymer. 38 (1997) 3151–3212.

[2] G. Strobl, Crystallization and melting of bulk polymers: New observations, conclusions and a thermodynamic scheme, Progress in Polymer Science. 31 (2006) 398–442.

[3] G.R. Strobl, G.R. Strobl, The physics of polymers, Springer, 1997.

[4] B. Xiong, Contribution to the study of elastic and plastic deformation mechanisms of polyethylene and polypropylene as a function of microstructure and temperature, Lyon, INSA, 2014.

[5] Laura Hubert, Laurent David, Roland Séguéla, Gérard Vigier, Small-angle X-ray scattering investigation of the deformation processes in the amorphous phase of high density polyethylene, Polymer International. 53 (2004) 582–585.

[6] L. Hubert, L. David, R. Seguela, G. Vigier, C. Degoulet, Y. Germain, Physical and mechanical properties of polyethylene for pipes in relation to molecular architecture. I. Microstructure and crystallisation kinetics, Polymer. 42 (2001) 8425–8434.

[7] Buckley Crist, Christopher J. Fisher, Paul R. Howard, Mechanical properties of model polyethylenes: tensile elastic modulus and yield stress, Macromolecules. 22 (1989) 1709–1718.

[8] S. Humbert, O. Lame, G. Vigier, Influence de la topologie moléculaire et de la microstructure sur les propriétés mécaniques des Polyéthylènes, Laboratoire de Recherche: MATEIS, INSA de Lyon. (2009).

[9] L. Austin, R. Kumar, B. Kousar, C.H. Lampadaris, M.M. Lucas, SAXS and WAXS measurements of PET, (2018).

[10] S. Humbert, O. Lame, G. Vigier, Polyethylene yielding behaviour: What is behind the correlation between yield stress and crystallinity?, Polymer. 50 (2009) 3755–3761.

[11] Bijin Xiong, Olivier Lame, Jean-Marc Chenal, Yongfeng Men, Roland Seguela, Gerard Vigier, Critical stress and thermal activation of crystal plasticity in polyethylene: Influence of crystal microstructure and chain topology, Polymer. 118 (2017) 192–200.

[12] Y.-L. Huang, N. Brown, The effect of molecular weight on slow crack growth in linear polyethylene homopolymers, Journal of Materials Science. 23 (1988) 3648–3655.

[13] Y.-L. Huang, N. Brown, Dependence of slow crack growth in polyethylene on butyl branch density: morphology and theory, Journal of Polymer Science Part B: Polymer Physics. 29 (1991) 129–137.

[14] S. Humbert, O. Lame, R. Séguéla, G. Vigier, A re-examination of the elastic modulus dependence on crystallinity in semi-crystalline polymers, Polymer. 52 (2011) 4899–4909.

[15] B. Xiong, O. Lame, J.-M. Chenal, C. Rochas, R. Seguela, G. Vigier, Amorphous phase modulus and micro–macro scale relationship in polyethylene via in situ SAXS and WAXS, Macromolecules. 48 (2015) 2149–2160.
[16] T. Deplancke, M. Fivel, O. Lame, 1D strain rate-dependent constitutive model of UHMWPE: From crystalline network to fibrillar structure behavior, Mechanics of Materials. 137 (2019) 103129.
[17] R. Popli, M. Glotin, L. Mandelkern, R.S. Benson, Dynamic mechanical studies of α and β relaxations of polyethylenes, Journal of Polymer Science: Polymer Physics Edition. 22 (1984) 407–448.
[18] Y.P. Khanna, E.A. Turi, T.J. Taylor, V.V. Vickroy, R.F. Abbott, Dynamic mechanical relaxations in polyethylene, Macromolecules. 18 (1985) 1302–1309.
[19] R.H. Boyd, Relaxation processes in crystalline polymers: molecular interpretation—a review, Polymer. 26 (1985) 1123–1133.

3 Microstructure evolutions in HDPE materials submitted to mixed-mode oligo-cyclic tensile loading

3.1 Abstract

The content of this chapter has been drafted as a research paper titled "*Characterization of the spherulitic deformation in equatorial region and cavitation in HDPE materials submitted to mixed-mode oligo-cyclic tensile loading*". In this chapter, the so-called "structural damage" reported in the literature (cavitation and fragmentation of lamellae) are mainly investigated.

HDPE materials of varying microstructures triggered via thermal treatments, are cycled to a prescribed strain in the vicinity yet beyond the elastic limit and then retracted to zero stress. Macroscopically, a Mullins-like effect can be observed. At the meso- and micro- scales, in-situ SAXS measurements have been carried out so that the local deformation of the equatorial region of the spherulites can be estimated along with the broad evolutions of the crystalline spherulitic structures and the cavitation. Upon loading, the local strain is found proportional to the macroscopic one in the equatorial region of the spherulites. The shearing of the crystallites initiates during the first cycle and slightly accumulates with increasing cycles. Moreover, nano-sized cavities are only observed in the isothermal samples exhibiting higher crystallinity and a lower density of stress transmitters. These micro-voids are nucleated during the first loading step. Assuming that the cavities do not merge, it is found that the accumulation-saturation of the cavity volume fraction is essentially resulting from their dimension increase, especially along the direction perpendicular to the macroscopic elongation.

3.2 Introduction

High-density polyethylene (HDPE) are often shaped to produce pipelines, since high ductility is pursued to sustain potential seismic activity[1–3]. The investigation of the materials performance under seismic episodes for industrial applications is thus of strong interest. Oligo-cyclic tests with large stress/strain (beyond the elastic limit) and limited number of cycles are commonly set to model seismic events and have been widely performed onto various materials[4–6]. Ultimately, it is worth investigating the corresponding microstructure evolution and the associated mechanisms induced in order to better anticipate the materials responses to potential seismic events and predict its lifetime.

In this work, special attention is paid to tensile loading. The stress-controlled cyclic tests[7–10] can induce only limited plasticity per cycle, the maximum applied strain cannot exceed the yield point due to the further softening effect associated with necking initiation. Moreover, the strain-controlled tests (cyclic loading between two fixed strains) may cause potential compression/buckling, which is not desired. To avoid these disadvantages, the mixed-mode (oligo-) cyclic tensile loading is selected, the semi-crystalline polymer samples are stretched to a fixed strain and retracted to zero force repeatedly. With this multi-cycle test, *Mullins-like* effect including the progressive stress softening at maximum applied strain and the accumulation of residual strain at zero stress with increasing cycle number could be observed in the semi-crystalline polymers. The *so-called* Mullins phenomenon was firstly discovered in the filled and crystallizing rubbers[11–13] and further investigations proved that a similar phenomenon, at least its macroscopic manifestation, also prevails in semi-crystalline polymers[14–16]. Various authors suggested physical interpretations to the stress softening and accumulation of residual strain such as bond rupture[17], molecular slip[18], disentanglements[19] and network alteration theories[20]. some of them being mentioned for semi-crystalline polymers[14–16]. Nevertheless, the physical origins of this phenomenon are still controversial. However, based on the observations of *Mullins(-like)* effect, the first loading cycle leads to a "significant" structural evolution yet differing from the remaining cycles associated to its progressive accumulation.

The structural evolutions of polyethylene (PE) or other semi-crystalline polymers submitted to simple loading such as uniaxial tension have been widely studied at the meso- and micro- scales. At mesoscale, where the HDPE material can be depicted as a media of interconnecting spherulites, the deformation mechanisms were shown to be highly heterogeneous along the tensile direction[21–23]. In semi-crystalline polymers, authors made use of four critical strains to describe the tensile deformation of semi-crystalline polymers and the interplay between the elastic and plastic strain contributions[24,25]. The elastic deformation is classically assigned to the amorphous phase and involves inter-lamellar separation, inter-lamellar shear and lamellar stack rotation[26,27]. During plastic deformation, various mechanisms may be involved, such as the shearing of the crystallites[27–33], cavitation[29,30,34–38], martensitic transformation[39,40] and fibrillation at large strain [41–43]. Among these, the cavitation and shearing of crystallites (also defined as the fragmentation of lamellae) are recognized as two competing mechanisms generated respectively in the crystalline and amorphous phases at small plastic strain ranges (in the vicinity of the neck initiation). The nucleation and growth of cavitation show a dependency on crystallization-related microstructural properties [44–46] such as the resulting thickness of crystalline lamellae and the density of stress transmitters (ST) including tie molecules and entanglements [29,30,47].

Several articles also discussed the microstructure evolutions in semi-crystalline polymers submitted to single loading-unloading path or fatigue tests. Focusing on cavitation, Addiego et al. have observed the partial reversibility of the cavitation in PE samples, distinguishing the total cavity volume fraction into a reversible part and a permanent part. The reversible contribution is further subdivided into an instantaneous elastic and a time-dependent viscoelastic one. Additionally, the permanent part depends on the applied strain level: for axial strain smaller than 4.1%, the cavities could be entirely reversible after relaxation[48]. Moreover, Raphael et al. reported the deformation and voiding of spherulitic microstructures in a pure polymer and glass-fiber reinforced polyamide 6.6 during fatigue tests by tomography analysis combined with SEM fractography observations[49]. In particular, they found that the cavity nucleation occurs firstly at equatorial plane of the spherulites, which is in accordance with the results reported by Mourglia-Seignobos et al. [9]. However, these classical fatigue tests are all conducted under stress-controlled loading conditions, and the imposed loading cycles (10^5-10^6 cycles) remain within the elastic regime. Moreover, Janssen et al. have reported that the failure mechanisms in the oligo-cyclic regime are different from the ones in high-cycle regime[8,50] in semi-crystalline polymers. Regarding the microstructure evolutions under mixed-mode cyclic conditions, beyond the elastic limit, only relevant studies performed on polymers other than semi-crystalline ones can be mentioned. Toki et al. performed a two-cycles *in-situ* SAXS/WAXS test to characterize the microstructure evolutions for a thermoplastic propylene-dominant ethylene-propylene copolymer. They noticed that the first cycle could destroy a fraction of the crystals and induce the reorientation of the other crystalline lamellae to form a "permanent set", which is thermally stable during the second loading[51].

The aim of this work is thus to further investigate the structural evolutions of semi-crystalline (HDPE) polymers under mixed-mode oligo-cyclic tensile loading conditions. Thermal treatments such as quenching and isothermal steps are applied to vary the initial microstructures, and *in-situ* SAXS measurements are performed to improve our understanding of the microstructural evolutions. Finally, the relation between the meso- and micro- structural evolutions and the aforementioned macro *Mullins-like* effect, if any, will also be discussed.

3.3 Experimental

3.3.1 Materials

Two types of commercial HDPE hereafter denoted as PE-A and PE-B are studied. These two materials were ordered from INEOS (Brussels, Belgium). It is worth noting that PE-B is a PE-100, widely used for tube applications, whereas PE-A is a HDPE for blow-molding applications. The two materials contain only minimal additives that are necessary for their shaping process: 1 to 1.5 g/kg of antioxidant and 1 g/kg of antacid. The two grades differ by their molecular topology and molar masses so that their microstructural and mechanical properties exhibit different sensitivity to thermal treatments. The molecular characteristics of the polyethylene pellets determined by gel permeation chromatography (GPC) are shown in **Table 1** (provided by INEOS Company).

Table 1: Molecular characteristics and isothermal treatment temperatures Tiso of PE pellets

Materials	Mn (g/mol)	Mw (g/mol)	Mz (g/mol)	Tiso (°C)
PE-A	7 500	202 200	1 478 900	121.5
PE-B	6 700	270 800	1 589 400	118

M_n,, M_w and M_z are the number-average molar mass, the weight-average molar mass and z-average molar mass measured by gel permeation chromatography.

3.3.2 Sample preparation

The PE pellets were molded at 200 °C for 10 min into 0.8 mm thick plates. Thermal treatments followed the compression molding step in order to modify the initial microstructure. On the one hand, plates were quenched in cold water and are further designated as “quenched” samples. On the other hand, some plates were wrapped and put into an oil bath at a constant temperature T_{iso} (shown in **Table 1**) for 17 h and are further defined as “isothermal” samples. The temperatures T_{iso} (121.5 °C and 118°C for PE-A and PE-B respectively) were chosen to meet two conditions: 1) the prescribed temperature should be close to the crystallization temperature so that the complete crystallization occur at a much lower rate[44,52]. 2) Furthermore, with this selected temperature, the isothermal treatments could hinder secondary crystallization, which may have affected the materials mechanical properties[52].

3.3.3 DSC (Differential Scanning Calorimetry) analysis

6 to 8 mg samples cut from the molded plates were heated up to 150°C at a heating rate 10°C/min under nitrogen flow with a DSC 7 PerkinElmer apparatus, which has been indium-calibrated. Equation (1) below was used to determine the crystallinity (Xc) of the pristine samples:

$$X_c = \frac{\Delta H_f}{\Delta H_f^0} \tag{1}$$

Where ΔH_f is the specific melting enthalpy and ΔH_f^0 is the melting enthalpy of a theoretically fully crystalline polyethylene. ΔH_f^0 was set equal to 290 J/g[53].

3.3.4 Tensile measurements

Tensile tests were conducted on dumbbell-shaped samples of 6.5 mm gauge length, 4 mm width and about 0.8 mm thickness. The specimen were punched from the processed plates then tested at room temperature (about 23°C) and a constant nominal strain rate of $\dot{\varepsilon} = 5 \times 10^{-2}\ s^{-1}$ with a MTS 1/ME machine equipped with a 5KN load cell. Single loading steps up to large strain were performed to measure the neck width, determined as the difference in nominal strain between the threshold point of plasticity (where the nominal stress is about 80% of the -maximum- yield stress σ_y) and the beginning of the constant-stress neck propagation. This indicator is qualitatively related to the density of stress transmitters (ST) including tie molecules and entanglements. More specifically, the greater the nominal strain difference, the higher the ST density[54]. For each condition, at least three samples were tested and the results were averaged.

3.3.5 Mixed-mode oligo-cyclic tensile tests coupled with in-situ SAXS (Small-angle X-ray scattering) measurements

The small-angle X-ray scattering measurements were performed on the SWING beamline of the French SOLEIL synchrotron with a wavelength of 0.78Å. The beam size is 100×40 μm^2. The distance between the samples and the detector was 2.08m, so that the corresponding range of observation (scattering vector q) spans from 0.06 to $5.5 nm^{-1}$. The long period (L_p) was computed from a scattering vector q_{max} corresponding to the maximum Lorentz-corrected diffuse intensity using equation (2):

$$L_P = \frac{2\pi}{q_{max}} \tag{2}$$

It is worth noting that the Gaussian fit of the Iq^2-q profile in the vicinity of the peak was used to determine q_{max}. In addition, the thickness (L_c) of the spherulite crystalline lamellae was estimated as follow:

$$L_c = L_P \frac{\rho}{\rho_c} X_c \tag{3}$$

$$\frac{1}{\rho} = \frac{X_c}{\rho_c} + \frac{1-X_c}{\rho_a} \tag{4}$$

Where ρ, ρ_a, ρ_c are the overall sample, the amorphous phase (0.850 g/cm^3) and the crystalline phase (1.003 g/cm^3) densities respectively[55]. X_c is the crystallinity measured by DSC (see Equation 1).

A homemade miniature apparatus was used to conduct the mixed-mode oligo-cyclic tensile tests consisting in 8 consecutive cycles at constant nominal strain rate $\dot{\varepsilon}_{oc}=10^{-3}s^{-1}$. The maximum applied strain was $\varepsilon_{oc}= 0.16$, beyond the elastic limit. The 2D SAXS patterns were recorded every 3 s in real time. With these settings, the SAXS patterns were acquired every 0.003 increment in macroscopic nominal strain. Finally, these *in-situ* measurements were carried out on samples identical to those shaped for the tensile tests.

3.4 Results and analysis

3.4.1 Microstructure characterization of the pristine materials

Table 2 lists some physical characteristics (crystallinity X_c, long period L_p, thickness of crystallites L_c and neck width connected to the density of ST) of the pristine materials studied. It is worth noting that the precision of the neck width measurement did not allow differentiating the densities of ST between the PE-A and PE-B samples subjected to the same thermal treatment. Yet, **Figure 1** displays the nominal stress-strain tensile responses up to an axial nominal strain of 1 for the 4 materials in which the influence of the thermal treatments is clearly emphasized. In comparison to the quenching process, the isothermal treatment promotes the formation of relatively thicker crystalline lamellae as well as higher crystallinity and a lower density of ST [54]. It is worth noting that the effect of thermal treatment on the measured microstructure markers is consistent with former studies[21,22,29,30].

Table 2. Physical characteristics of the HDPE pristine microstructures.

Materials		X_c (%)	L_p (nm)	L_c (nm)	Neck width (-)
Experimental method		DSC	SAXS	SAXS	Tensile test
PE-A	Quenched	62.1	22	13	0.55
	Isotherm	73.4	35	24	0.30
PE-B	Quenched	57.7	20	11	0.50
	Isotherm	64.0	33	20	0.35

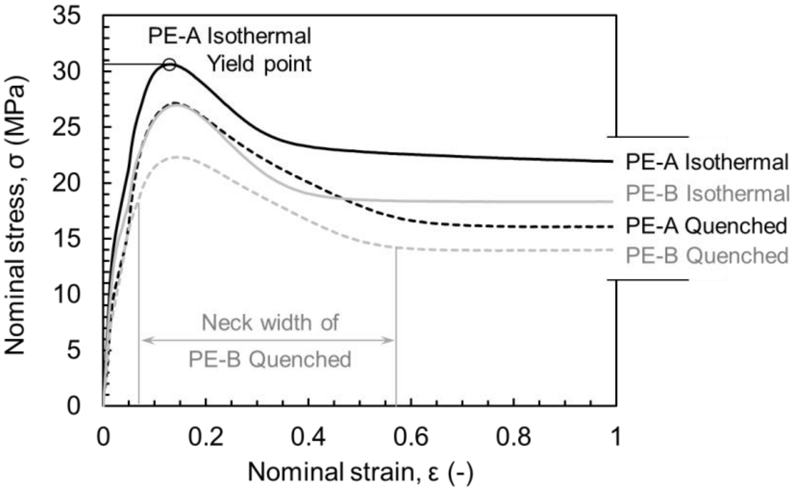

Figure 1: *Tensile curves and measurement of neck width.*

3.4.2 Structural evolutions of PE samples at different scales

The meso- and micro- structural evolutions of the HDPE samples submitted to mixed mode oligo-cyclic tests was evaluated by SAXS measurements. The 2D-SAXS patterns of either the two quenched or the two isothermal samples did reveal significant differences. Yet, few differences could be observed between the different HDPEs submitted to the same thermal treatment, hence suggesting similar “for the least qualitative” evolution. Consequently, the following focuses on the two PE-B materials (quenched and isothermal samples) and similar qualitative conclusions do apply for the PE-A materials. **Figure 2** presents the nominal stress-strain curves of the oligo-cyclic tests of the quenched (a) and isothermal (b) specimen respectively. It is worth noting that the loading path is seen to be stabilized after the 8th cycle. Therefore, only the first 8 cycles that involve the most significant evolutions (especially the first one) are investigated.

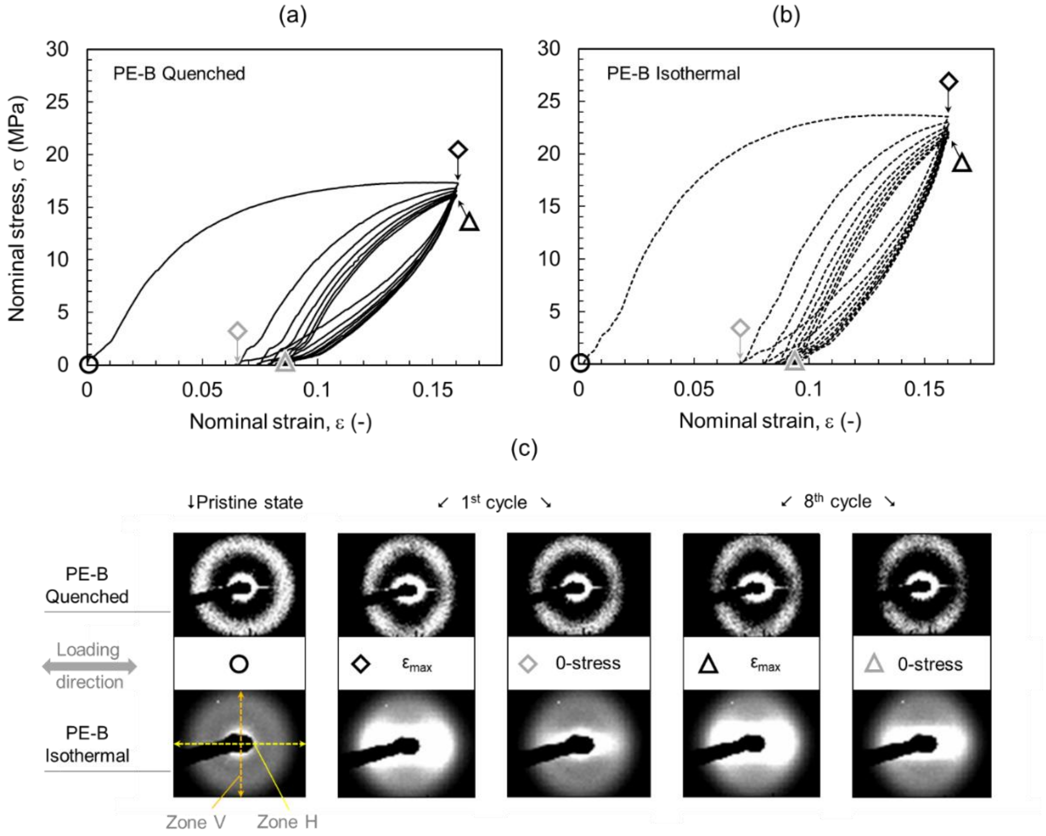

Figure 2: *Evolution of the SAXS patterns during the oligo-cyclic tests for the PE-B samples:*

(a) Quenched sample, (b) Isothermal sample. (c) 2D SAXS images for given deforming states (N.B. arbitrary gray scales).

2D-SAXS patterns corresponding to five precise deformed states were added onto the figure (**Figure 2c**). Precisely, the pristine states, the maximum-strain and the zero-stress states of the 1st cycle and 8th cycle are displayed. For both samples, the 2D-SAXS patterns in the pristine state exhibit a circular ring suggesting that the lamellar stacks of spherulite are randomly oriented and that the material is isotropic.

For additional analysis, preferential directions that are parallel and perpendicular to the macroscopic loading direction are investigated and correspond respectively to the horizontal (Zone H) and vertical (Zone V) regions of the 2D-SAXS patterns as evidenced onto the pristine image of PE-B Isothermal in **Figure 2c**. The azimuthal integrations are conducted with an angle of ±5°.

For quenched samples, with increasing strain during the first loading step, the ring-shaped pattern gradually becomes elliptical. The L_p at the equatorial region of the spherulite (corresponding to Zone H) increases upon stretching (the q-value decreases) as the equatorial crystalline lamellae of the spherulite are subjected to the local tensile load in the same direction as the macro sample and are thus pulled apart from one another. On the contrary, L_p at the pole (corresponding to Zone V) decreases (q-value increases) due to Poisson effect. When the applied strain reaches a critical value, the intensity in Zone H starts to decrease. Once unloaded to zero stress, the circular pattern is partly recovered and the scattering intensity of Zone H does not change significantly. At zero-stress states, the SAXS intensity of Zone H is seen to progressively decrease with increasing cycle number. Throughout the entire test, the evolution of the scattering intensity in the central part of the pattern is not remarkable meaning that the cavitation observed by SAXS is limited in these samples.

For isothermal samples, the deformation of the spherulites as well as the deformation of the crystalline lamellae can hardly be discussed because of the strong intensity scattered by cavities. The cavitation appears during the first loading step in the vicinity of the yield point in the central part of the pattern. The strong intensity scattered is more elongated within Zone H, suggesting that the cavities are elliptical with its long axis being normal to the tensile direction[29,30]. Throughout a full cycle of load/unload, the cavity intensity and shape are naturally seen to change. The evolution appears to be more pronounced in the horizontal region (Zone H) with a distinct difference between the zero-stress 2D-SAXS patterns of the 1st and 8th cycle. Comparing the pattern after each cycle, the intensity scattered by cavities shows yet again an accumulating behavior.

3.4.3 Local deformation of spherulite

Addressing the local deformation of the spherulites is challenging due to their complex morphology and their dependency on the unknown local stress. In the equatorial region of the spherulite, the lamellar stacks are simplified as the flat-on sheets and assumed to have the same orientation: the norm of these lamellae is parallel to the tensile loading. During the tensile deformation, although the interlamellar amorphous phase is subjected to a triaxial stress[56], the local axial strain along the tensile direction in the equatorial region can be estimated by the spacing changes between these lamellae. It is of prime importance for further meso-macro modeling. The average spacing changes in the SAXS irradiated volume is evaluated with billions of lamellar stacks in the equatorial region. As a consequence, the data are believed to be representative of the considered deformed zone. Compared to the interlamellar separation (spacing changes of the lamellar stacks), the slight plastic deformation in the crystalline phase should be neglected in the equatorial region since the yield point has just been reached.

The spacing changes of the equatorial lamellar stacks could be computed using the azimuthal integrations of the equatorial region (Zone H). The corresponding Lorentz-corrected intensity profiles of the PE-B quenched sample, normalized by the thickness of samples, are presented in **Figure 3**.

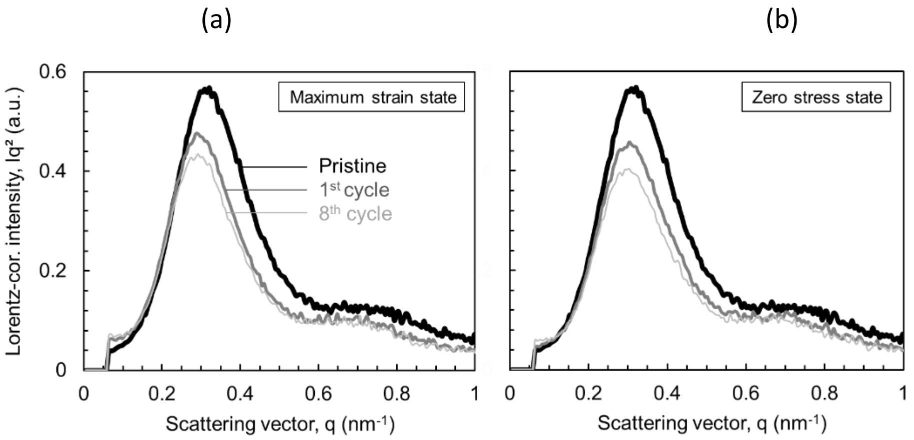

Figure 3: *Equatorial Lorentz-corrected intensity as a function of q (PE-B Quenched samples) in the equatorial region (Zone H). (a) At maximum-strain state. (b) At zero-stress state.*

The local strain at the equator of the spherulites could be calculated based on the evolution of the inter-lamellar long period L_p using relation (5):

$$\varepsilon_{\mathrm{local}}(t) = \frac{\triangle L_p(t)}{L_{p0}} = \frac{L_p(t) - L_{p0}}{L_{p0}} \qquad (5)$$

The end states of each cycle, corresponding to the maximum-strain (loading) and zero-stress (unloading) states are chosen to evaluate the relation between the local and the macroscopic strains. As previously discussed, the strong scattering intensity due to cavitation observed in the isothermal samples prevent the determination of L_p that is why only quenched samples are here studied. However, before the appearance of cavitation, the mechanisms leading to the deformation of the spherulites in both quenched and isothermal materials should be qualitatively similar[21,22]. **Figure 4a** illustrates the evolution of the local strain of the quenched samples as a function of cycle number. At maximum-strain states, both the macroscopic and the local strains remain mostly constant. Regarding the unloaded zero-stress states, both the macro and local residual strains exhibit an initiation-accumulation-stabilization behavior, and this spherulitic behavior is comparable to a Mullins-like phenomenon. The ratio of $\varepsilon_{local}/\varepsilon_{macro}$ at maximum-strain and minimum-stress states are plotted in **Figure 4b** as a function of cycle number. In both end states, a quasi-constant value of $\varepsilon_{local}/\varepsilon_{macro}$ of about 0.6 is observed, indicating that 1) the spherulitic deformation is directly (linearly) related to the macroscopic axial deformation throughout the entire test, 2) heterogeneity exists at the microscale and that the equatorial region of the spherulites is less deformed than other regions along the macroscopic loading direction[21,22]. The fact that an almost constant ratio $\varepsilon_{local}/\varepsilon_{macro}$ is observed in the unloaded states suggests that no significant rupture in the spherulites occurs during the oligo-cyclic test performed.

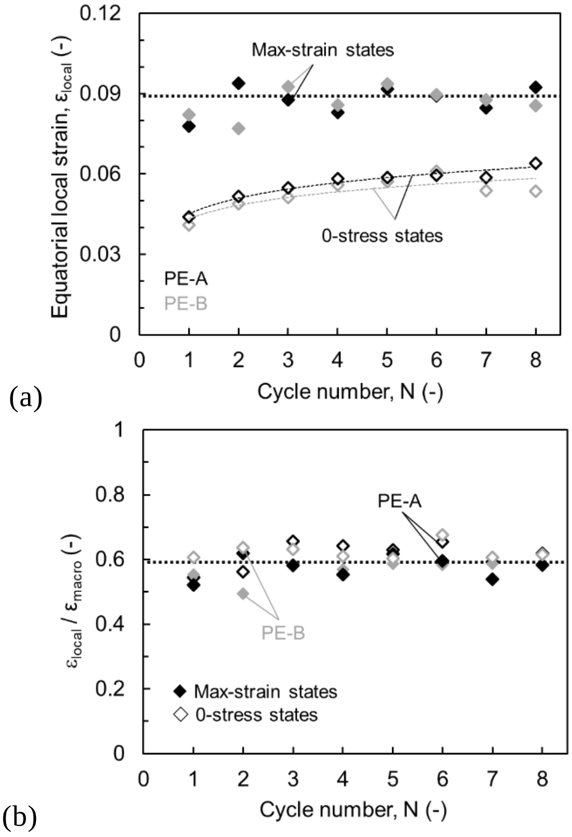

Figure 4: *(a) Local strain at maximum-strain and minimum-stress states. (b) Plot of ratio* ε_{local}/ ε_{macro} *as a function of cycle number (quenched samples).*

3.4.4 Evolution of the crystalline structure

Along with the spherulitic deformation, the crystalline structure of the spherulite also evolves. The structural alterations of the lamellar stacks are studied by monitoring the evolution of the intensity scattered $Q(\psi)$ that is defined as follow:

$$Q(\psi) = \int_0^{\infty} I^{\psi}(q)\, q^2 dq \tag{6}$$

Where ψ is the azimuthal angle and $I^{\psi}(q)$ is the scattering intensity of the crystalline structure in the ψ direction normalized by the thickness of the sample. Assuming that the difference of electronic density remains constant, $Q(\psi)$ should be related to the volume fraction of oriented crystalline lamellae in the ψ direction[29,30].

The intensity scattered for 3 preferred azimuthal angles ψ=0° (equatorial region of the lamellar stacks), 90° (polar region of the lamellar stacks) and 45° (lamellar stacks oriented into 45° to the loading direction) are determined by azimuthal integration with $\Delta\psi=\pm5°$. Taking into account the finite experimental q-range covered, and using the onset (q_1) and end (q_2) of the peak of the scattering intensity of the crystalline structure as experimental limits, relation (6) can then be decomposed as follow:

$$Q(\psi) = \int_0^{q_1} I_1{}^{\psi}(q)\, q^2 dq + \int_{q_1}^{q_2} I_2{}^{\psi}(q)\, q^2 dq + \int_{q_2}^{\infty} I_3{}^{\psi}(q)\, q^2 dq \tag{7}$$

In Equation 7 $I_2{}^{\psi}(q)$ is obtained experimentally for $q_1 \leq q \leq q_2$. $I_1{}^{\psi}(q)$ and $I_3{}^{\psi}(q)$ are extrapolated with a linear relation and the Porod's law respectively[29,30]. Finally, the evolution of the Q-value for the three preferred directions are presented in **Figure 5** as a function of time for the quenched samples. The evolution of the macroscopic axial strain with time is superimposed to better distinguish between the consecutive load/unload steps.

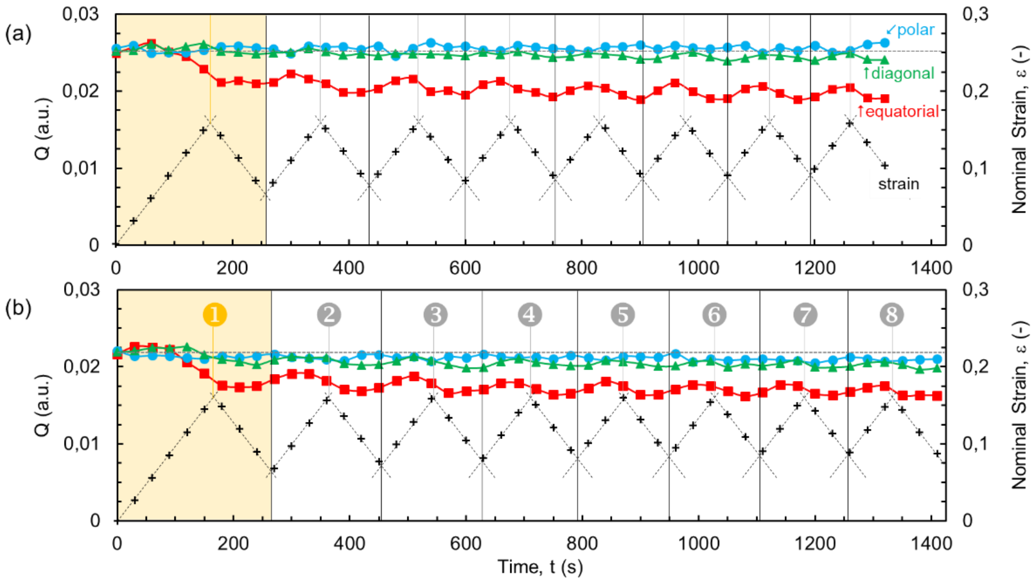

Figure 5: *Evolution of Q value at different region of spherulite/applied macro-strain as a function of time: (a) PE-A Quenched sample; (b) PE-B Quenched sample.*

For a given sample, the Q-value in the pristine state does not depend on the azimuthal angle which confirms the isotropy of the non-deformed state. During the deformation, the Q-values of the diagonal and polar regions do not exhibit an important variation, indicating that the local structures of the crystalline lamellae are i) not significantly modified and/or ii) sheared to large blocks with their orientation being nearly stable.

On the contrary, the Q-value focusing on the equatorial region of the spherulites evolves in an obvious periodic manner. During the first loading step, for macroscopic strain below the elastic limit ($\varepsilon \approx 0.1$), the Q-value scattered by the crystalline structure remains quasi-constant. Therefore, the spherulites are deformed with their lamellar structures being unaltered. For higher strain level, the scattering intensity begins to decrease, which means that the lamellar stacks at the equator are sheared or fragmented so that their preferential orientation (perpendicular to the tensile direction) is lost.

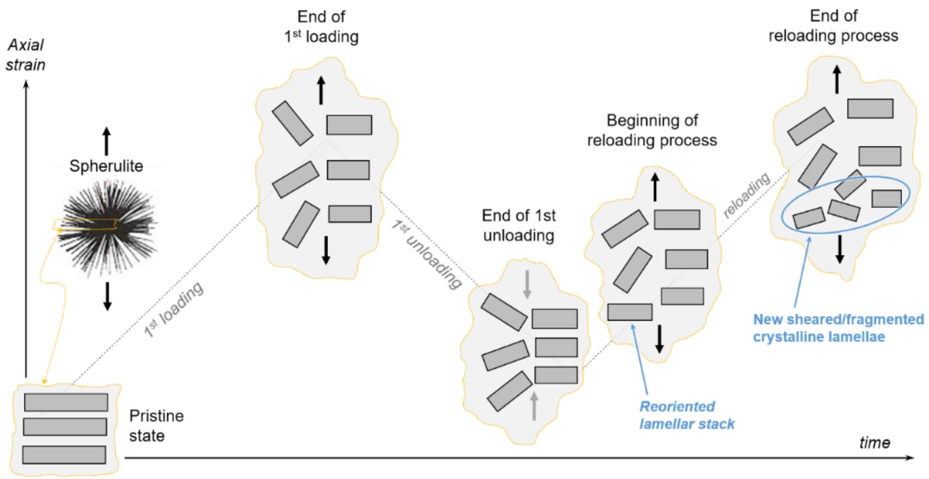

***Figure 6**: Evolution of the crystalline lamellae at the equator of the spherulite as function of oligo-cyclic loadings.*

It is worth mentioning that these sheared/fragmented crystalline lamellae do not form highly oriented chevron structure manifested by a four-point diagram in 2D-SAXS patterns[57] which would result in the increase of the intensity at ψ=45° direction. During the unloading step, Q-value remains almost constant, suggesting that the orientation of the previously sheared/fragmented crystalline lamellae are still disordered. The following loading steps are quite different from the first cycle: in the early stage of the second loading, reorientation of a fraction of the sheared/fragmented crystalline lamellae at the equator where the chains tend to be parallel to the tensile direction occurs. This phenomenon could lead to the increase of the Q-value. Nevertheless, the Q-value remains lower than its initial value, which means a large part of the previously sheared/fragmented lamellar stacks remains disordered. Moreover, as the strain overpasses a critical value, the Q-value begins to slightly decrease. This phenomenon is attributed to "weak" lamellar stacks that are sheared or fragmented. Throughout the consecutive deforming cycles, the scattering intensity of the equatorial region at the maximum-strain and zero-stress states first decreases then rapidly stabilizes. Finally, the schematic in **Figure 6** tends to summarize the evolution of the equatorial crystalline lamellae for representative states of the mixed-mode oligo-cyclic test.

3.4.5 Estimation of the observed cavity volume fraction and dissipation of energy due to cavities

Cavitation is an important micro-structural alteration also depicted as micro-damage that occurs in the amorphous phase of the polymer. In this work, the estimation of the cavitation volume fraction is based on an analytical method that has been initially proposed to calculate the volume fractions of a two-phase material with the aid to the equation (8).

$$2\pi^2\Delta\rho^2\Phi(1-\Phi)K_1 = \int_0^\infty I(q)q^2\,dq \tag{8}$$

$I(q)$ is computed by azimuthal integration in the $0^\circ \leq \psi \leq 360^\circ$ range and corrected by the sample thickness. $\Delta\rho$ is the electronic density difference between the two phases, Φ is the volume fraction of one phase, and K_1 is an amplification factor. It is worth noting that K_1 depends on the level of deformation endured by the material. However, the account for this evolution should have limited effect on the estimation of the cavities volume fraction due to the high electronic density contrast between the cavitation and the dense polymer matrix. Therefore, K_1 is further set to be constant and only depends on the samples. Its estimation is obtained in the pristine state using equation (8). More precisely, considering that the materials are fully dense without appearance of cavities, the phases under considerations are the crystalline and the amorphous phases so that K_1 is the only unknown of the problem. Indeed, $\Delta\rho$ is the difference between the crystalline and the amorphous phase densities (ρ_c=1.003 g/cm^3 and ρ_a=0.853 g/cm^3 respectively[55]), Φ is the volume fraction of crystalline (or amorphous) phase, and the right end term is obtained using the method previously described and obtained using equation (7).

Under deformation, the two phases under considerations are now the HDPE matrix (as a whole) and the cavities. Consequently, $\Delta\rho$ is assimilated to the density of the PE sample ρ since the density of the cavities is set to zero. It worth noting that this method only allows for the estimation of the volume fraction of the cavities that can be observed in the q-range of the SAXS measurement, later referred as V_{cav}^{SAXS}. However, this method provides a fair quantitative description of the evolution of the cavity volume fraction, which is representative and helpful to study the behavior of the cavities under oligo-cyclic loading conditions[29,30]. In addition, with the cavity volume fraction V_{cav}^{SAXS} being very small (<<1), Equation (8) can be rewritten as follow:

$$2\pi^2\rho^2 V_{\mathrm{cav}}^{\mathrm{SAXS}} K_1 = \int_0^\infty I(q) q^2\, dq \tag{9}$$

Again, the integral in the q-space is decomposed into 3 terms delimited by the 2 experimental extreme q-values: below q_1 ($0.05 nm^{-1}$) linear extrapolation is applied; between q_1 and q_2 ($0.1 nm^{-1}$) experimental data are processed; above q_2 the Porod's law is applied.

Figure 7 represents the volume fraction of the cavities V_{cav}^{SAXS}as a function of the applied axial nominal strain for all samples. For the quenched samples, having thinner crystalline lamellae and higher ST density, very little variation of V_{cav}^{SAXS} is observed upon loading suggesting that cavitation is not the driving structural phenomenon. Conversely, V_{cav}^{SAXS} shows significant hysteresis properties in isothermal samples. In the early stage of the first loading, prior to a critical strain ε_{onset}, no obvious evolution of cavitation is observed. ε_{onset} is graphically determined as the intersection of the two tangents (before and after cavity nucleation). Here, ε_{onset} equals 0.09 and 0.11 for the PE-A Isothermal and PE-B Isothermal samples respectively.

During unloading phase, V_{cav}^{SAXS}gradually decreases along a pathway differing from the loading one, with its minimum value at the zero-stress state being greater than the value observed during loading for the same macroscopic strain. The porosity can be thus partially decreased and it exhibits hysteretic behavior, which is in accordance with the finding of Addiego et al.[48]. During the consecutive loading steps, V_{cav}^{SAXS}evolution strongly differs from the first loading. Indeed, for stresses that have already been experienced by the sample, a gradual increase of V_{cav}^{SAXS} is observed with increasing strain. At any given strain, the value of V_{cav}^{SAXS} after N cycles is superior to the value after N-1 cycles, with the difference between the two decreasing as the number of cycles increases, suggesting eventual saturation. Therefore, throughout the oligo-cyclic tests, the volume fraction of the residual cavities accumulates at zero-stress state. Also, the hysteresis loops highlight that the evolution of cavities is time-dependent. Now comparing the different samples, the cavitation shows a great dependency on the microstructural properties: higher density of ST and thinner crystalline lamellae result in limited cavitation; this result is emphasized through the comparison between the quenched and isothermal samples, but also when comparing the two isothermal samples. Indeed, the nucleation and accumulation of cavities are more pronounced in PE-A isothermal sample having thicker crystals and lower density of ST.

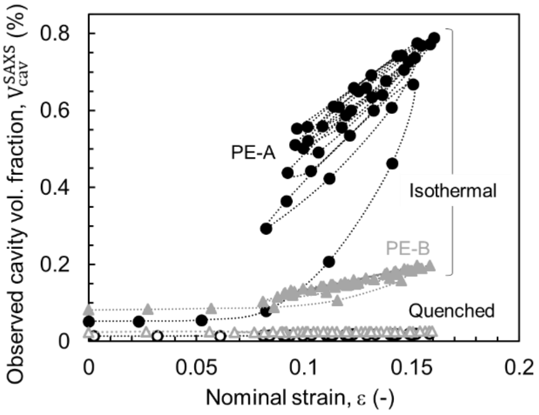

Figure 7: *Evolution of the observed cavity volume fraction V_{cav}^{SAXS} as a function of the imposed nominal axial strain during oligo-cyclic test.*

In the plastic regime, with the matrix deformation assumed to be isovolumetric, the macroscopic deformation ε_{vol} can be related to the volume fraction of cavities (the observed cavities generate only a part of the volumetric deformation $\varepsilon_{vol}^{SAXS} = V_{cav}^{SAXS}$). Also, the hydrostatic stress σ_H could be approximated by third of the axial nominal stress σ. The two quantities (ε_{vol}^{SAXS} and σ_H) are evaluated and plotted against one another in **Figure 8** for the PE-A isothermal sample. Hysteresis loops are clearly exhibited and can be related to the dissipated energy per unit volume attributed to the observed cavitation E_{cav}^{SAXS}.

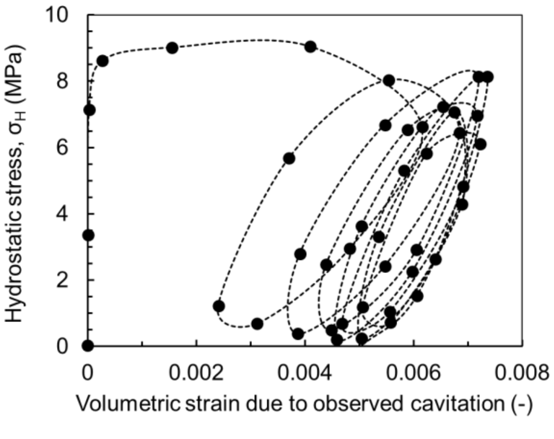

Figure 8: *Hydrostatic stress as a function of the volumetric deformation due to observed cavities in PE-A Isothermal sample.*

The total dissipated energy density (i.e. the energy dissipated per unit volume) occurring during the oligo-cyclic tests and denoted E_{total} is determined from the area of the hysteresis loops in the macroscopic nominal stress-strain curves (see **Figure 2**). Thus, the two dissipated energy densities E_{total} and E_{cav}^{SAXS} are presented in **Figure 9a** and **Figure 9b** respectively as a function of the cycle number for all materials.

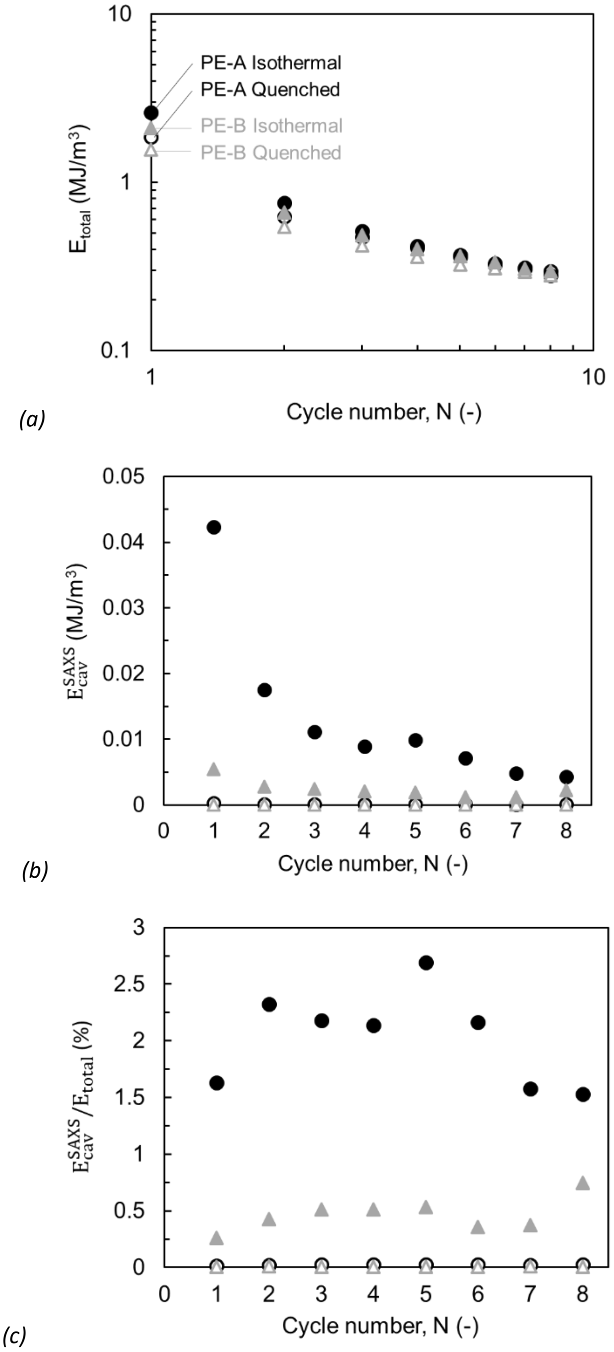

Figure 9: *Energy profiles plotted as a function of the cycle number: (a) Total dissipated energy per unit volume Etotal; (b) dissipated energy per unit volume due to cavitation* E_{cav}^{SAXS}*; (c)* E_{cav}^{SAXS} */ Etotal ratio as a function of cycle number.*

During the first load-unload cycle, ${}^{1}E_{total}$ shows a clear dependency on the microstructure: the sample with higher crystallinity exhibits a higher value of ${}^{1}E_{total}$. However, as the number of cycles increases, limited difference in ${}^{i}E_{total}$ (i>1) is observed, so that the dependency of E_{total} on the microstructure cannot be addressed. **Figure 9c** presents the corresponding $E_{cav}^{SAXS}/\ E_{total}$ ratio as a function of the cycle number. The results show that the energy dissipated due to observed cavitation only accounts for a limited part of the total dissipated energy. The observed cavitation contribution reaches about only 3% in the PE-A isothermal sample, with the higher observed cavity volume fraction (see **Figure 7**). Therefore, the evolution of these observed nano-sized cavities does not dominate the energy dissipation taking place during the oligo-cyclic tensile tests.

3.4.6 Evolution of observed cavity dimension and shape

The evolution of the shape and associated dimensions of these observed cavities are also worth being discussed in parallel with their volume fraction to better understand and characterize the nucleation and growth of cavities under oligo-cyclic loading conditions. These dimensions are averaged over billions of nano-sized cavities.

A quantitative method proposed by Humbert et al.[29] is further applied to characterize such morphological evolutions in the isothermal samples. First, the scattering intensity can be decomposed as follow:

$$\mathrm{I(q)} \propto \mathrm{F^2(q)S(q)} \tag{10}$$

F(q) and *S(q)* are the shape and interference factors respectively. Assuming the cavities to be distant from each other, *S(q)* can be set equal to 1. Also, $F^2(q)$ can be decomposed in two orthogonal parts, parallel and perpendicular to the loading direction. With the elliptical cavities being assimilated to cylindrical objects, $F^2(q)$ becomes:

$$\mathrm{F^2(q)} = \left[\frac{\sin\left(\frac{1}{2}\mathrm{q}_{\parallel}\mathrm{L}\right)}{\frac{1}{2}\mathrm{q}_{\parallel}\mathrm{L}}\right]^2 \left[2\frac{\mathrm{J}_1\left(\frac{1}{2}\mathrm{q}_{\perp}\mathrm{D}\right)}{\frac{1}{2}\mathrm{q}_{\perp}\mathrm{D}}\right]^2 \tag{11}$$

$$\mathrm{q}_{\parallel} = \mathrm{q}\cos\gamma \tag{12}$$

$$\mathrm{q}_{\perp} = \mathrm{q}\sin\gamma \tag{13}$$

D is the diameter (perpendicular to the loading direction) L is the height (parallel to the loading direction) and γ is the angle between the normal of the base of the cylinder and the wave vector q, J_1 is the first order Bessel function. The two orthogonal contributions can be studied separately. The calculation of D and L can be simplified using the following method: from the SAXS 2D patterns, the $I(q)$-q^2 profiles are obtained from the ±5° azimuthal integration in the Zone H (corresponding to γ=90°) and Zone V (corresponding to γ=0°) . The radius of gyration R_0 could be calculated using Guinier's law described by equation (14) where $q \leq 0.1nm^{-1}$. D and L are finally approximated by the spherical diameter D_{sp} using relation (15).

$$\mathrm{I(q)} = \mathrm{I(0)}e^{\left(-\frac{R_0^2q^2}{3}\right)} \tag{14}$$

$$\mathrm{D_{sp}} = 2 \times \frac{\mathrm{R_0}}{\sqrt{\frac{3}{5}}} \tag{15}$$

The average cavity dimensions are presented in **Figure 10** as a function of the macroscopic strain.

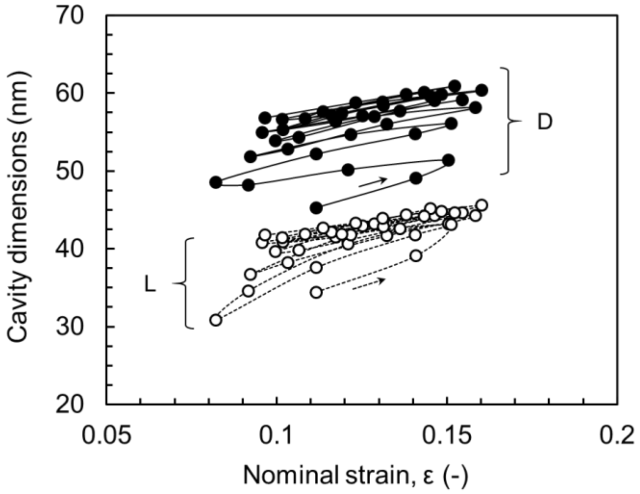

(a)

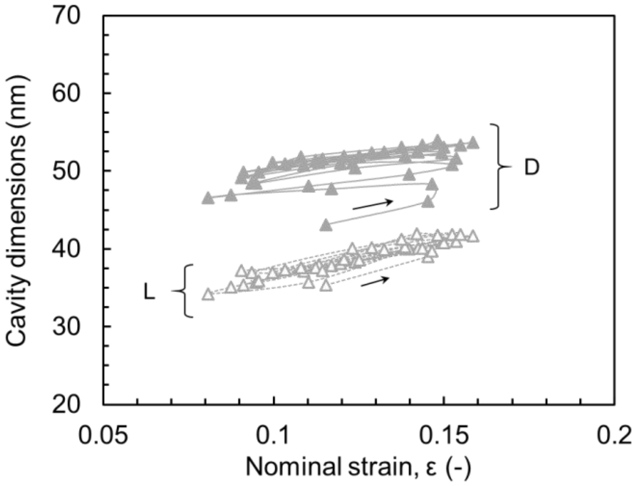

(b)

Figure 10: *Evolution of the cavity dimensions: (a) PE-A Isothermal sample; (b) PE-B Isothermal sample.*

The first estimation of the initial cavity dimensions in both PE-A and PE-B isothermal samples are obtained after nucleation during the first loading step. D=45 nm and L=35 nm are found. In the two samples, it worth noting that initial L values are larger than the thickness of a single amorphous layer, meaning that the onset of the cavity nucleation is not captured by SAXS as it is almost instantaneous[29,30]. The cavitation is considered to be firstly induced in the equatorial region of spherulite[9,36,37,49,58], the oriented crystalline lamellae in this region should strongly contribute to the limitation of cavity growth along tensile direction.

With additional stretching, the cavities begin to grow along both directions. In the literature, during uniaxial tensile stretching, the initial oblate cavities will further transform into the prolate one (L>D) accompanied with the fibrillary transformation at large strain[29,36,37,59]. These prolate cavities are located in the inter-fibrillary region, where the lateral propagation is limited thanks to the shish crystalline blocks within the microfibrils [36,60].

However, in our case, the overall spherulitic structure remains: despite the occurrence of fragmentation of lamellae, the growth of cavity in the equatorial region is still limited along the tensile direction thanks to the remaining lamellae. Therefore, the cavity dimension increases mainly along the direction perpendicular to the loading direction (D).

According to our measurement, upon unloading, the decrease is also more pronounced and rapid along the tensile direction (L) implying that the cavities tend to close primarily along the macroscopic loading direction. The cavities are not entirely closed at zero stress and the slight decrease of D should be related to the closure of the cavity tips. Taking PE-B isothermal sample as an example, **Figure 11a** summarizes the cavity's shape evolution throughout the test and **Figure 11b** and **c** focus on noticeable deformed states.

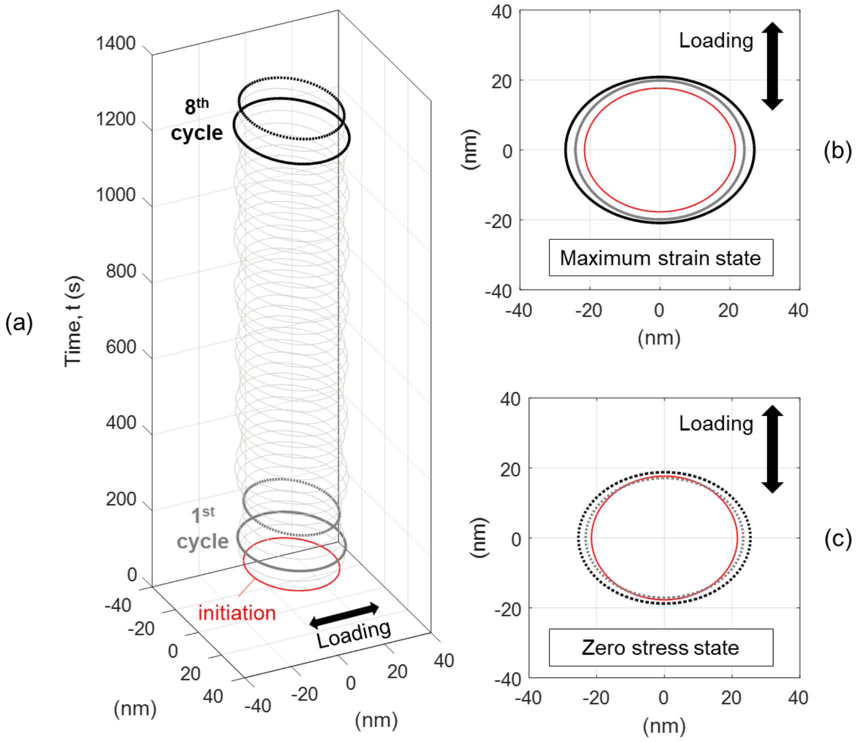

Figure 11: *Evolution of cavities under oligo-cyclic loading conditions (PE-B Isothermal sample): (a) time evolution; (b) maximum-strain state (loading); (c) zero-stress state (unloading).*

At the end of an oligo-cyclic test, the cavities in PE-A isothermal sample are in average larger than the ones in the PE-B isothermal sample with both D and L being greater. Previous results showed that the observed cavity volume fraction of PE-A isothermal sample is about 4 times higher than that of the PE-B isothermal sample (see **Figure 7**).

However, the difference in dimension is much smaller, implying that the amount of cavities in PE-A isothermal sample should also be higher in this q window. Assuming that the cavities are ellipsoid in shape, the average volume of the observed cavities, denoted A, could be estimated using relation (16):

$$\mathrm{A} = \frac{4}{3} \times \pi \times \mathrm{D}^2 \times \mathrm{L} \qquad (16)$$

The relative volume variation induced by the evolution of the cavity sizes could then be estimated. Moreover, according to the evolution of V_{cav}^{SAXS}, the relative volume variation of observed cavities induced by both the varying number of cavities and their growth (change of dimension) could be calculated. **Figure 12** compares the volume variation of a unit average cavity and the total cavities at zero-stress states as a function of the cycle number.

After the first cycle (nucleation), the relative volume variation of the observed cavities is considered to be 0. According to the results, at any given time, the relative volume variations of the cavities and the total number of observed cavities are about the same in both isothermal samples. This phenomenon indicates that after the first cycle, the subsequent evolution of the observed cavity volume fraction could be mainly attributed to the opening and closure of the previously nucleated cavities rather than the nucleation of new cavities.

Also, the "saturation" of the cavity dimension only suggests that the growth rate is significantly decreased within the following cycles (after the first few cycles). The lateral growth is mitigated by the stress transmitters, which are already strongly taut around the cavity. Also, it can be supposed that the remaining cycles mainly induce visco-elastic fatigue effects. Indeed, another study suggested that the further increase of D was related to the fatigue failure of semi-crystalline polymers[49].

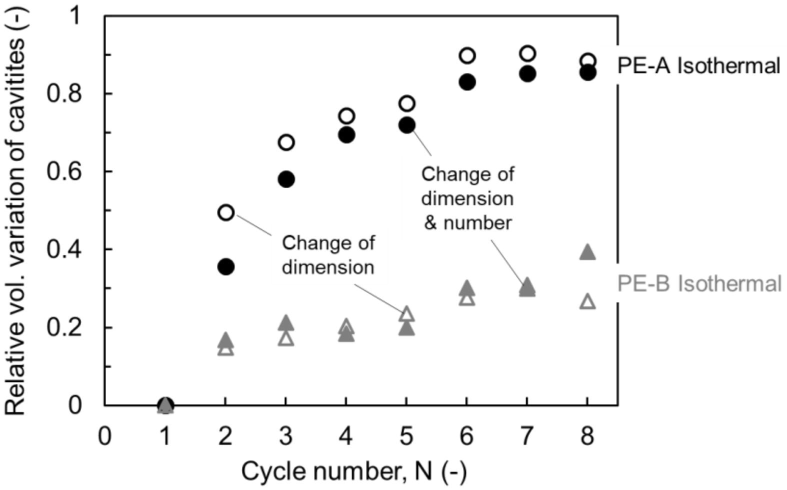

Figure 12: *Variation of unit/total cavity volume at zero stress states as a function of the cycle number.*

Figure 13 confronts the evolution of the aspect ratio (*D/L*) of these cavities along with the applied macroscopic axial strain of PE-B isothermal sample with respect to time: the aspect ratio (*D/L*) is seen to remain superior to unity at any given time confirming the elliptical shape of the cavities. Upon cycling, the aspect ratio reaches its minimum at the end of the loading steps and its maximum when the sample is fully unloaded. As time (and thus number of cycles) goes, the aspect ratio at zero-stress states increases progressively from 1.2 to 1.3, evidencing that the cavities become more and more elliptical as a consequence of the propagation of cavities along the direction perpendicular to the loading axis.

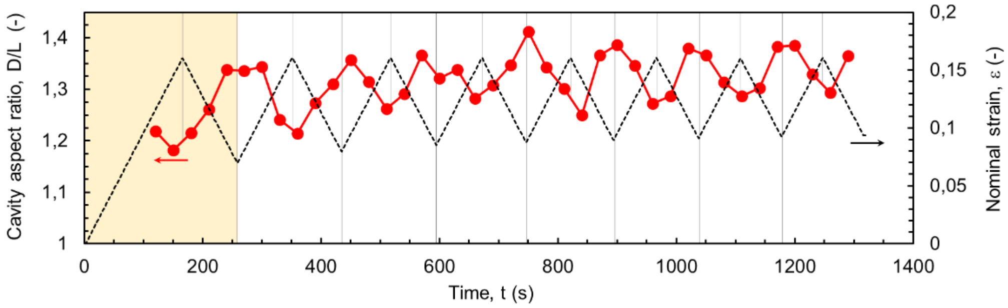

Figure 13: *Time evolution of the cavity aspect ratio and applied nominal strain in the PE-B Isothermal sample under mixed-mode oligo-cyclic test.*

3.5 Conclusion

Under mixed mode oligo-cyclic tensile loading conditions, meso- and micro- structural evolutions are shown in different HDPE samples obtained from varying thermal treatments. According to the macroscopic observation, the mechanical response strongly differs between the first and the consecutive loading cycles of the oligo-cyclic test. In-situ SAXS measurements allowed evidencing that: i) the deformations of nano-sized lamellar stacks located at the equatorial region of micron-sized spherulites remain proportional to the macroscopic ones. In addition, within this region of the spherulites, the first cycle induces the most important shearing/fragmentation of the crystallites and the remaining cycles cause the accumulating evolution and stabilization of the crystalline structure. ii) nano-sized cavities were observed in the isothermal samples, these micro-voids were nucleated during the first loading step, and partially closed upon the first unloading step. More importantly, with consecutive cycles, only the dimensions of the cavities evolve whereas no additional nucleation appears in the observation window. These cavities were found to grow primarily perpendicular to the loading/unloading direction. Focusing on the zero-stress states at each cycle, the initiated cavities progressively grew up to a saturated size. These results reveal that the oligo-cyclic tests cause significant structural evolutions during the first few cycles (especially the first one). Within the consecutive loading cycles, the stabilizing microstructure and the associated macroscopic mechanical behavior suggest that the additional loading-unloading processes mainly induce visco-elastic fatigue effects as the continuing accumulation of the initiated microstructure evolutions. Moreover, these structural evolutions (initiation-accumulation-stabilization) also suggest that the origin of the macroscopic Mullins behavior could be complex as several mechanisms could potentially interfere (plasticity, cavitation, phase transformation etc.). Ongoing investigations using in-situ SAXS measurements for varying maximum strains and applied to a larger range of microstructures should be helpful to better understand this complex phenomenon.

Also, the tendency for the PE to “cavitate” was highly dependent on the initial microstructure, as it was limited in quenched samples due to their high density of stress transmitters, lower crystallinity and thinner crystallites. This difference of cavitation behavior in these samples should be valuable for the further investigation on the origin of the dependency of the mechanical losses during oligo-cyclic deformation in HDPE materials on their pristine microstructures/morphologies so that it can make contribution to the design and selection of HDPE materials of pipeline systems combined with other mechanical evaluations.

Reference

[1] W.W. Chen, B. Shih, Y. Chen, J. Hung, H. H. Hwang, Seismic response of natural gas and water pipelines in the Ji-Ji earthquake, Soil Dyn. Earthq. Eng. 22 (2002) 1209–1214.

[2] T. H. Abdoun, D. Ha, Michael J. O’Rourke, M. D. Symans, T. D. O’Rourke, M. C. Palmer, H. E. Stewart, Factors influencing the behavior of buried pipelines subjected to earthquake faulting, Soil Dyn. Earthq. Eng. 29 (2009) 415–427.

[3] D. Ha, T. H. Abdoun, M. J. O’Rourke, M. D. Symans, T. D. O’Rourke, M. C. Palmer, H. E. Stewart, Centrifuge modeling of earthquake effects on buried high-density polyethylene (HDPE) pipelines crossing fault zones, J. Geotech. Geoenvironmental Eng. 134 (2008) 1501–1515.

[4] A. Masi, G. Santarsiero, D. Nigro, Cyclic tests on external RC beam-column joints: role of seismic design level and axial load value on the ultimate capacity, J. Earthq. Eng. 17 (2013) 110–136.

[5] P. Cassese, P. Ricci, G. M. Verderame, Experimental study on the seismic performance of existing reinforced concrete bridge piers with hollow rectangular section, Eng. Struct. 144 (2017) 88–106.

[6] V. Ji, Y. Zhang, C. Chen, The non-destructive estimation of the superficial mechanical properties of components in the INCONEL 600 alloy by X-ray diffraction peak width, Surf. Coat. Technol. 130 (2000) 95–99.

[7] M. J. W Kanters, T. Kurokawa, L. E. Govaert, Competition between plasticity-controlled and crack-growth controlled failure in static and cyclic fatigue of thermoplastic polymer systems, Polym. Test. 50 (2016) 101–110.

[8] R. P.M Janssen, L. E. Govaert, H. E. H Meijer, An analytical method to predict fatigue life of thermoplastics in uniaxial loading: sensitivity to wave type, frequency, and stress amplitude, Macromolecules. 41 (2008) 2531–2540.

[9] E. Mourglia-Seignobos, D. R. Long, L. Odoni, L. Vanel, P. Sotta, C. Rochas, Physical mechanisms of fatigue in neat polyamide 6, 6, Macromolecules. 47 (2014) 3880–3894.

[10] S. T. T. Nguyen, S. Castagnet, J.C. Grandidier, Nonlinear viscoelastic contribution to the cyclic accommodation of high density polyethylene in tension: Experiments and modeling, Int. J. Fatigue. 55 (2013) 166–177.

[11] L. Mullins, Permanent set in vulcanized rubber, Rubber Chem. Technol. 22 (1949) 1036–1044.

[12] L. Mullins, Softening of rubber by deformation, Rubber Chem. Technol. 42 (1969) 339–362.

[13] J. Diani, B. Fayolle, P. Gilormini, A review on the Mullins effect, Eur. Polym. J. 45 (2009) 601–612.

[14] A. D. Drozdov, Mullins’ effect in semicrystalline polymers, Int. J. Solids Struct. 46 (2009) 3336–3345.

[15] M. Makki, G. Ayoub, H. Abdul-Hameed, F. Zaïri, B. Mansoor, M. Naït-Abdelaziz, M. Ouederni, Mullins effect in polyethylene and its dependency on crystal content: a network alteration model, J. Mech. Behav. Biomed. Mater. 75 (2017) 442–454.

[16] M. Wang, J. Shen, J. Li, S. Guo, Network alteration theory on Mullins effect in semicrystalline polymers, Polym. Int. 64 (2015) 105–112.

[17] S. Govindjee, J. Simo, A micro-mechanically based continuum damage model for carbon black-filled rubbers incorporating Mullins' effect, J. Mech. Phys. Solids. 39 (1991) 87–112.

[18] R. Houwink, Slipping of molecules during the deformation of reinforced rubber, Rubber Chem. Technol. 29 (1956) 888–893.

[19] D. E. Hanson, M. Hawley, R. Houlton, K. Chitanvis, P. Rae, E. B. Orler, D. A. Wrobleski, Stress softening experiments in silica-filled polydimethylsiloxane provide insight into a mechanism for the Mullins effect, Polymer. 46 (2005) 10989–10995.

[20] G. Ayoub, F. Zaïri, M. Naït-Abdelaziz, J. M. Gloaguen, Modeling the low-cycle fatigue behavior of visco-hyperelastic elastomeric materials using a new network alteration theory: application to styrene-butadiene rubber, J. Mech. Phys. Solids. 59 (2011) 473–495.

[21] S. Humbert, O. Lame, J. M. Chenal, C. Rochas, G. Vigier, Small strain behavior of polyethylene: in situ SAXS measurements, J. Polym. Sci. Part B Polym. Phys. 48 (2010) 1535–1542.

[22] B. Xiong, O. Lame, J. M. Chenal, C. Rochas, R. Seguela, G. Vigier, In-situ SAXS study of the mesoscale deformation of polyethylene in the pre-yield strain domain: Influence of microstructure and temperature, Polymer. 55 (2014) 1223–1227.

[23] K. Nitta, A molecular theory of stress–strain relationship of spherulitic materials, Comput. Theor. Polym. Sci. 9 (1999) 19–26.

[24] Y. Men, Critical Strains Determine the Tensile Deformation Mechanism in Semicrystalline Polymers, ACS Publications, 2020.

[25] Y. Men, G. Strobl, Critical strains determining the yield behavior of s-PP, J. Macromol. Sci. Part B. 40 (2001) 775–796.

[26] L. Lin, A. S. Argon, Structure and plastic deformation of polyethylene, J. Mater. Sci. 29 (1994) 294–323.

[27] R. Hiss, S. Hobeika, C. Lynn, G. Strobl, Network stretching, slip processes, and fragmentation of crystallites during uniaxial drawing of polyethylene and related copolymers. A comparative study, Macromolecules. 32 (1999) 4390–4403.

[28] F. Addiego, A. Dahoun, C. G'Sell, J. M. Hiver, O. Godard, Effect of microstructure on crazing onset in polyethylene under tension, Polym. Eng. Sci. 49 (2009) 1198–1205.

[29] S. Humbert, O. Lame, J. M. Chenal, C. Rochas, G. Vigier, New insight on initiation of cavitation in semicrystalline polymers: in-situ SAXS measurements, Macromolecules. 43 (2010) 7212–7221.

[30] B. Xiong, O. Lame, J. M. Chenal, C. Rochas, R. Seguela, G. Vigier, In-situ SAXS study and modeling of the cavitation/crystal-shear competition in semi-crystalline polymers: Influence of temperature and microstructure in polyethylene, Polymer. 54 (2013) 5408–5418.

[31] B. Xiong, O. Lame, J. M. Chenal, Y. Men, R. Seguela, G. Vigier, Critical stress and thermal activation of crystal plasticity in polyethylene: Influence of crystal microstructure and chain topology, Polymer. 118 (2017) 192–200.

[32] K. Nitta, M. Takayanagi, Novel proposal of lamellar clustering process for elucidation of tensile yield behavior of linear polyethylenes, J. Macromol. Sci. Part B. 42 (2003) 107–126.

[33] Y. Men, J. Rieger, G. Strobl, Role of the entangled amorphous network in tensile deformation of semicrystalline polymers, Phys. Rev. Lett. 91 (2003) 095502.

[34] Y. Wang, Z. Jiang, L. Fu, Y. Lu, Y. Men, Lamellar thickness and stretching temperature dependency of cavitation in semicrystalline polymers, PLoS One. 9 (2014).

[35] M. F. Butler, A. M. Donald, A real-time simultaneous small-and wide-angle X-ray scattering study of in situ polyethylene deformation at elevated temperatures, Macromolecules. 31 (1998) 6234–6249.

[36] A. Pawlak, A. Galeski, Cavitation during tensile drawing of annealed high density polyethylene, Polymer. 51 (2010) 5771–5779.

[37]T.F. Morgeneyer, H. Proudhon, P. Cloetens, W. Ludwig, Q. Roirand, L. Laiarinandrasana, E. Maire, Nanovoid morphology and distribution in deformed HDPE studied by magnified synchrotron radiation holotomography, Polymer. 55 (2014) 6439–6443.

[38] N. Selles, P. Cloetens, H. Proudhon, T.F. Morgeneyer, O. Klinkova, N. Saintier, L. Laiarinandrasana, Voiding mechanisms in deformed polyamide 6 observed at the nanometric scale, Macromolecules. 50 (2017) 4372–4383.

[39] M.F. Butler, A.M. Donald, W. Bras, G.R. Mant, G.E. Derbyshire, A.J. Ryan, A real-time simultaneous small-and wide-angle X-ray scattering study of in-situ deformation of isotropic polyethylene, Macromolecules. 28 (1995) 6383–6393.

[40] M.F. Butler, A.M. Donald, A.J. Ryan, Time resolved simultaneous small-and wide-angle X-ray scattering during polyethylene deformation 3. Compression of polyethylene, Polymer. 39 (1998) 781–792.

[41] B. Xiong, O. Lame, J. M. Chenal, C. Rochas, R. Seguela, On the strain-induced fibrillar microstructure of polyethylene: Influence of chemical structure, initial morphology and draw temperature, Express Polym. Lett. 10 (2016) 311.

[42] Z. Jiang, Y. Tang, J. Rieger, H. F. Enderle, D. Lilge, S.V. Roth, R. Gehrke, W. Heckmann, Y. Men, Two lamellar to fibrillar transitions in the tensile deformation of high-density polyethylene, Macromolecules. 43 (2010) 4727–4732.

[43] S. André-Castagnet, S. Tencé-Girault, Relationships between mechanical tensile behavior and micro-mechanisms in poly (vinylidene fluoride) at high temperatures: Influence of the molecular weight distribution, J. Macromol. Sci. Part B. 41 (2002) 957–976.

[44] G. Strobl, Crystallization and melting of bulk polymers: New observations, conclusions and a thermodynamic scheme, Prog. Polym. Sci. 31 (2006) 398–442.

[45] G. Strobl, The physics of polymers, Springer, 1997.

[46] Y. Men, G. Strobl, From crystalline block slips to dominance of network stretching- Mechanisms of tensile deformation in semi-crystalline polymers, Chin. J. Polym. Sci. 20 (2002) 161–170.

[47] S. Tencé-Girault, S. Lebreton, O. Bunau, P. Dang, F. Bargain, Simultaneous SAXS-WAXS experiments on semi-crystalline polymers: Example of PA11 and its brill transition, Crystals. 9 (2019) 271.

[48] F. Addiego, S. Patlazhan, K. Wang, S. André, Sigrid Bernstorff, David Ruch, Time-resolved small-angle X-ray scattering study of void fraction evolution in high-density polyethylene during stress unloading and strain recovery, Polym. Int. 64 (2015) 1513–1521.

[49] I. Raphael, N. Saintier, G. Robert, J. Béga, L. Laiarinandrasana, On the role of the spherulitic microstructure in fatigue damage of pure polymer and glass-fiber reinforced semi-crystalline polyamide 6.6, Int. J. Fatigue. 126 (2019) 44–54.

[50] R.P. Janssen, D. de Kanter, L.E. Govaert, H.E. Meijer, Fatigue life predictions for glassy polymers: a constitutive approach, Macromolecules. 41 (2008) 2520–2530.

[51] S. Toki, Igors Sics, C. Burger, D. Fang, L. Liu, B.S. Hsiao, S. Datta, A.H. Tsou, Structure Evolution during Cyclic Deformation of an Elastic Propylene-Based Ethylene− Propylene Copolymer, Macromolecules. 39 (2006) 3588–3597.

[52] A. Alizadeh, L. Richardson, J. Xu, S. McCartney, H. Marand, Y. W. Cheung, S. Chum, Influence of structural and topological constraints on the crystallization and melting behavior of polymers. 1. Ethylene/1-octene copolymers, Macromolecules. 32 (1999) 6221–6235.

[53] L. Hubert, L. David, R. Séguéla, G. Vigier, Small-angle X-ray scattering investigation of the deformation processes in the amorphous phase of high density polyethylene, Polym. Int. 53 (2004) 582–585.

[54] S. Humbert, O. Lame, G. Vigier, Polyethylene yielding behaviour: What is behind the correlation between yield stress and crystallinity?, Polymer. 50 (2009) 3755–3761.

[55] B. Crist, C. J. Fisher, Paul R. Howard, Mechanical properties of model polyethylenes: tensile elastic modulus and yield stress, Macromolecules. 22 (1989) 1709–1718.

[56] B. Xiong, O. Lame, J. M. Chenal, C. Rochas, R. Seguela, G. Vigier, Amorphous phase modulus and micro–macro scale relationship in polyethylene via in situ SAXS and WAXS, Macromolecules. 48 (2015) 2149–2160.

[57] M. Krumova, S.Henning, G. H. Michler, Chevron morphology in deformed semicrystalline polymers, Philos. Mag. 86 (2006) 1689–1712.

[58] S. Castagnet, S. Girault, J. L. Gacougnolle, P. Dang, Cavitation in strained polyvinylidene fluoride: mechanical and X-ray experimental studies, Polymer. 41 (2000) 7523–7530.

[59] A. Blaise, C. Baravian, J. Dillet, L.J. Michot, S. André, Characterization of the mesostructure of HDPE under "in situ" uniaxial tensile test by incoherent polarized steady-light transport, J. Polym. Sci. Part B Polym. Phys. 50 (2012) 328–337.

[60] J. M. Brady, E. L. Thomas, Deformation of oriented high density polyethylene shish-kebab films, J. Mater. Sci. 24 (1989) 3311–3318.

4 Correlation between the mixed-mode cyclic loading induced mechanical/microstructure changes in HDPE

4.1 Abstract

The content of this chapter has been also drafted as a research paper titled "Correlation between the mixed-mode oligo-cyclic loading induced mechanical and microstructure changes in HDPE".

Two grades of HDPE (one is for PE-100 pipeline application and one is for blow molding) were processed to vary their crystallinity and molecular topology in order to investigate and understand the microstructural origin of the seismic performance of HDPE materials. For a given grade, the quenched sample exhibits a lower crystallinity, thinner crystallites, and a higher density of entanglement/tie molecules compared to the isothermal one. The HDPE samples are submitted to mixed-mode, oligo (plastic)-cyclic tensile deformation (that simulates the seism) with the applied maximum strain below or at the onset of necking propagation. The changes of numerous macroscopic mechanical metrics with increasing cycles were monitored (e.g. stress at maximum strain, residual strain at zero stress, secant modulus, and hysteresis loop area). These mechanical changes not only depend on the maximum imposed cyclic strain, but also the microstructure of HDPE. A physical scenario is proposed to describe the microstructural changes during the cyclic deformation and explicate the macro-micro correlations. Moreover, the post-cyclic tensile (reloading) curve can return to the original one rapidly for each sample, this phenomenon indicates the neglecting effect of the following cycles on the further loading path. It is also found that the material designed for the PE-100 pipeline shows limited variation between the initial and post-cyclic tensile toughness, indicating that the pre-loaded materials require nearly the same energy to rupture as the pristine ones. This is evidence that the material for PE-100 pipeline has a good resistance against the damage induced by seismic events.

4.2 Introduction

High-density polyethylene (HDPE) is widely used in industrial pipeline applications. PE 80 and PE 100 refer to common grades applied for gas and/or water pipelines. Among other benefits, pipelines made of HDPE exhibit a great resistance against seismic events[1,2], which are normally modeled by repeated loading-unloading cycles beyond the elastic limit (also defined as low cycle fatigue tests or oligo-cyclic tests)[3,4]. Therefore, it is valuable to carry out the investigations on the overall mechanical performances along with the deformation mechanisms and the damage evaluation in HDPE under (oligo-) cyclic loading conditions.

At the microscale, HDPE is a well-known semi-crystalline polymer consisting of crystalline and amorphous phases, connected by tie molecules/entanglement. The microstructural changes occurring throughout the small strain viscoelastic to the large strain plastic regimes during monotonic tensile tests in HDPE have been widely discussed for a long time[5–11]. The correlations between several mechanical indicators obtained from the stress-strain tensile profiles and the microstructure of HDPE are well established. In the elastic regime, the storage/elastic modulus is governed by the fraction of crystalline phase, apparent amorphous modulus, and percolation of the crystalline structure[9,12]. At the onset of plasticity, the quasi-linear relation between the threshold stress and crystallinity is associated with the dislocation model (thickness of crystalline lamellae) and the concept of stress transmitters (STs)[10,11]. It worth noting that insights regarding the amorphous chains topology or density of stress transmitters (ST density) were also obtained by mechanical measurements such as the neck width[11], natural draw ratio, and hardening[7,11,13]. The STs include the tie molecules and the entangled loops/chains, they are capable of transmitting the stress and they are also believed to play a crucial role in long-term properties such as creep, fatigue behaviors[14–17] as well as the crack propagation and cavitation [16,18–20].

In the literature, procedures can vary to perform (oligo-) cyclic tensile tests: for so-called stress-controlled[21–27] or strain-controlled modes[28,29], the cyclic paths are conducted between two prescribed forces (stresses) or displacements (strains) respectively. Besides these two modes, mixed-mode conditions can also be used[30–33], for which the sample is repeatedly stretched to a prescribed maximum strain and then retracted to zero force. During the cyclic tests, the mechanical indicators (e.g. stress, strain, modulus, hysteresis area) are seen to evolve with the increasing number of cycles suggesting microstructural modifications. The change of the elastic modulus has been attributed to two competing mechanisms. On the one hand, the modulus decrease is related to the cavitation (or micro-voids) and/or fragmentation of crystalline lamellae[24,29,34,35]. Generally, this mechanical loss is recognized as a macroscopic symbol of material damage[29,35]. On the other hand, the chain orientation might lead to an increase of the modulus along with the tensile deformation, also defined as "cyclic strengthening" as suggested by Drozdov[29]. Additionally, the density of dissipated energy of each stress-strain cycle, calculated as the hysteresis area, is ascribed to the generated heat by the plastic deformation and viscous loss mechanisms[36]. This parameter is related to the failure mode and lifetime of polymers[26,36,37].

Moreover, the accumulation of residual strain (by stress-controlled or mixed modes) and the stress softening (by strain-controlled or mixed modes) are also relevant features to probe the microstructural changes[21,23,25,29,31–33]. In particular, during mixed-mode cyclic tests, the semi-crystalline polymers display both stress softening at maximum strain and the accumulation of residual strain at zero stress with increasing cycles[31,32]. These two phenomena are largely considered as the macroscopic features of the *Mullins-like* effect, thus differing from the classically so-called *Mullins* effect enounced in the filled and crystallizing rubbers[38–40]. In detail, the first hysteresis loop is significantly different from the following ones, which is recognized as a primary property of the *Mullins-like* effect[32,41]. Although the mechanisms are complex and controversial, the network alteration theory has been successfully applied to explain this phenomenon. Makki et *al.*[32] described the microstructural changes of the *Mullins-like* effect in PE basing on a framework proposed for styrene-butadiene rubber[42]. In their work, the authors assign the difference in mechanical behaviors between the first cycle and the following ones to the rearrangement of the network. During the following cycles (after the first one), the additional rupture of chains reaching their limit extensibility is associated with the stress softening behavior. Moreover, a new equilibrium state at zero stress leads to an increase in the residual strain. Another striking manifestation of the *Mullins* phenomenon is that the post-cyclic reloading response for strain greater than the one already endured by the material coincides with the pristine response [38–40]. This phenomenon has been observed in polypropylene[31], with the maximum applied strain in the vicinity of the yield point. However, few studies discuss the post-cyclic behavior in PE, especially the properties related to the final rupture such as tensile toughness.

In this work, investigations of the *Mullins-like* stress softening/accumulation of residual strain in HDPE samples with different pristine microstructures and molecular topologies are carried out. Noticeably, mixed-mode oligo-cyclic tests with maximum strains preventing pronounced necking (below or at the onset of necking propagation phase) are performed. This strain range ascertains that the lamellar or spherulitic structure globally remains and the fibrillary structure[7,12,43,44] induced by large deformation is not completely formed. The relative changes of the secant modulus and hysteresis loop areas are also computed. A physical scenario is proposed to interpret the correlation between the mechanical changes and the pristine microstructure of the PE samples. Moreover, the post-cyclic mechanical behaviors are also discussed.

4.3 Experimental section

4.3.1 Materials

Two types of HDPE denoted PE-A and PE-B, are studied. PE-A refers to a blow molding grade and PE-B is a grade for the commercial PE-100 widely used in piping application. The molar masses were characterized and provided by the supplier INEOS (Brussels, Belgium) (see **Table 1**). The PE pellets were pressed into about 0.5 mm plates at 180°C in an aluminum-alloy mold. Once molded, quenching and isothermal thermal treatments were performed in order to vary the pristine microstructures of the two materials. The "quenched samples" were shaped in cold water whereas the "isothermal samples" were shaped in the oil bath for about 17h at a temperature T_{iso} around the crystallizing temperature, yet preventing the secondary crystallization[45,46].

Table 1: Initial molecular characteristics and T_{iso} of the polyethylene pellets

Materials	M_n (g/mol)	M_w (g/mol)	M_z (g/mol)	T_{iso} (°C)
PE-A	7500	202200	1478900	121.5
PE-B	6700	270800	1589400	118

M_n,, M_w and M_z are the number-average molar mass, the weight-average molar mass and z-average molar mass.

4.3.2 DSC (Differential Scanning Calorimetry) analysis

6 to 10 mg samples were taken from the HDPE plates and heated up to 150°C at 10°C/min with a DSC 7 PerkinElmer machine under nitrogen flow. The following equation (1) was used to estimate the material's crystallinity (X_c):

$$X_c = \frac{\Delta H_f}{\Delta H_f^0} \tag{1}$$

Where ΔH_f is the melting enthalpy calculated as the area under the DSC melting peak and ΔH_f^0 is the melting enthalpy of polyethylene of 100% crystallinity (290 J/g[47]). The overall density ρ could thus be estimated as follow:

$$\frac{1}{\rho} = \frac{X_c}{\rho_c} + \frac{1-X_c}{\rho_a} \tag{2}$$

Where ρ_c is the crystalline phase density (1.003 g/cm^3), ρ_a is the amorphous phase density (0.850 g/cm^3) [48]. X_c and ρ were also used for calculating the thickness of crystalline lamellae as shown in the next subsection.

4.3.3 SAXS (small-angle X-ray scattering) characterizations

The small-angle X-ray scattering experiments were performed on the SWING beamline of the French SOLEIL synchrotron with the X-ray wavelength of 0.103 nm. The sample-detector distance was 2003 mm so that the scattering vector q ranged between 0.036 and 0.52 $Å^{-1}$. The determination of the long period (*L_p*), the thicknesses of crystalline lamellae (*L_c*), and the amorphous layers (*L_a*) were obtained according to equations (3), (4) and (5).

$$L_p = \frac{2\pi}{q_{max}} \tag{3}$$

$$L_c = L_P \frac{\rho}{\rho_c} X_c \tag{4}$$

$$L_a = L_p - L_c \tag{5}$$

It worth noting that the scattering wave vector q_{max} corresponds to the maximum *Lorentz-corrected* scattering intensity. These nano-dimensions could be used for the estimation of the ST density by Brown's model[7,13,49,50] and for building the macro-micro correlations.

4.3.4 Mechanical tests: Uniaxial tensile, mixed-mode oligo-cyclic tensile and multi-step tests

Mechanical tests (uniaxial tensile, mixed-mode oligo-cyclic tensile, and multi-step tests) were performed on dumbbell-shaped samples of 8 mm gauge length, 4 mm width, and about 0.5 mm thickness punched out of the polymer sheets at room temperature. The tests were conducted using an MTS 1/ME machine equipped with a 100N load cell at a nominal strain rate $\dot{\varepsilon} = 3 \times 10^{-3} s^{-1}$.

Uniaxial tensile tests were conducted till failure to guide the selection of the oligo-cyclic strain ε_{OC} (the maximum imposed strain in each cycle). These tests also allow characterizing the mechanical properties such as the neck width[11] and initial tensile toughness defined as the area under the stress-strain profile until failure. 100 mixed-mode cycles with ε_{OC}= 0.08/0.16/0.24/0.5 were performed. In multi-steps tests, the samples were initially subjected to 10 mixed oligo-cycles with the same ε_{OC}= 0.08/0.16/0.24/0.5 and then immediately stretched up to failure, special attention is drawn to the post-cyclic behavior in each sample.

4.4 Results and discussion

4.4.1 Pristine microstructural characteristics

The microstructural properties (crystallinity X_c, long period L_p, thickness of crystallites L_c, and thickness of amorphous layers L_a) of the PE materials are listed in **Table 2**. It worth noting that L_c and L_a are precisely obtained according to the results of SAXS, the deviation is too small to present. As for crystallinity measurement, the deviation is ±1%. The density of STs has been approximated by both the statistic approach (Brown's model)[7,13,49,50] and the neck width[11] (with deviation ±0.05) measured from the nominal uniaxial tensile stress-strain curves reported in **Figure 1**. The PE having enhanced ST density tends to exhibit a more diffuse neck indicating a more homogenous deformation[8,11]. The results obtained by these two methods are consistent with each other. For a given grade (PE-A or PE-B), the isothermal sample has a relatively higher crystallinity, thicker crystallites, and lower ST density[5,11,51] thanks to its slower crystallization process[45] compared to the quenched sample.

Table 2. Crystallinity X_c, long period L_p, thickness of crystallites L_c and amorphous layers L_a, [ST] value estimated by Brown's model and neck width of PE plates subjected to different thermal treatments.

Methods		DSC	SAXS			Brown's model	Neck width
Material characteristics		X_c (%)	L_p (nm)	L_c (nm)	L_a (nm)	[ST]	
PE-A	Quenched	62	22	13	9	0.22	0.55
	Isothermal	73	35	24	11	0.07	0.27
PE-B	Quenched	57	20	11	9	0.27	0.65
	Isothermal	64	33	20	13	0.14	0.32

4.4.2 Mixed-mode oligo-cyclic tensile behaviors

Figure 1 superimposes the nominal uniaxial (up to a nominal strain $\varepsilon = 1$) and the oligo-cyclic tensile stress-strain profiles (maximum applied strain $\varepsilon_{OC} = 0.08$, 0.16, 0.24 and 0.5) of all four PE samples. The 2nd and 100th cycles are highlighted for better reading of the overall change of the mechanical loops. Throughout the mixed-mode oligo-cyclic tests, the stress at maximum strain, the residual strain at zero stress, the tangent modulus and the hysteresis response are seen to evolve and progressively saturate as the cycle number increases.

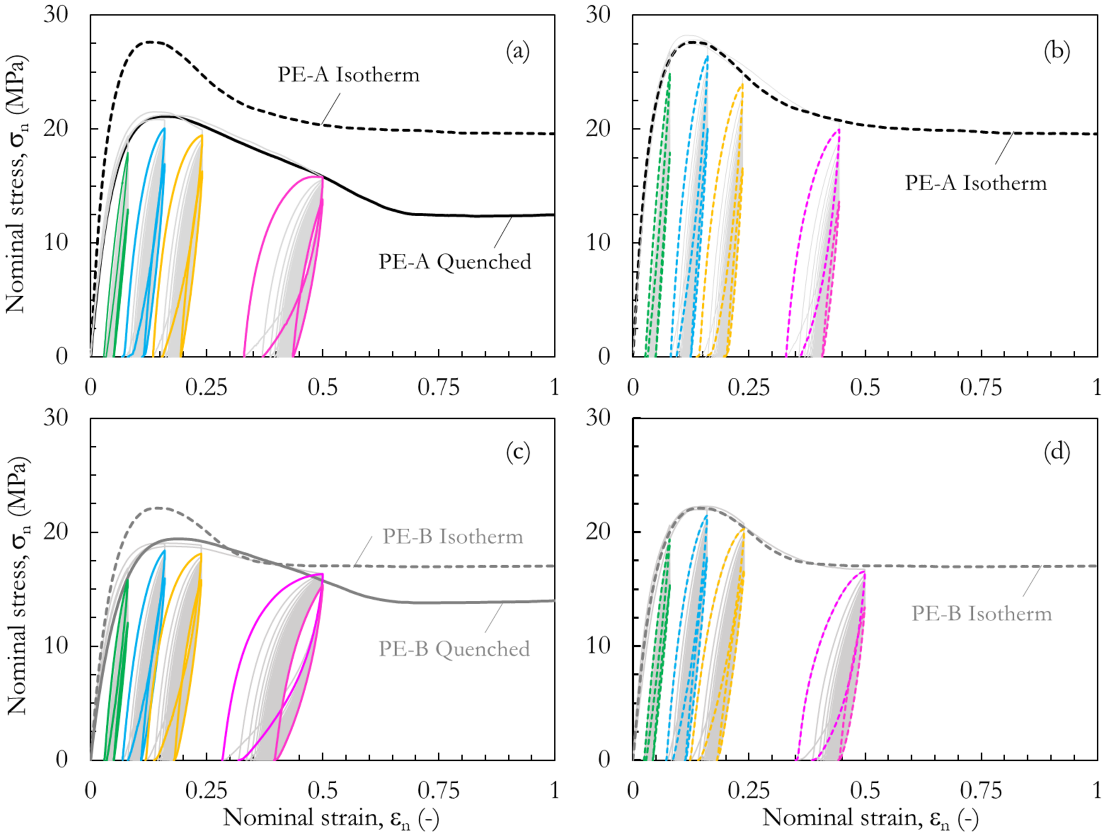

***Figure 1**: Nominal uniaxial and oligo-cyclic tensile stress-strain profiles.*

(ε_{OC} = 0.08, 0.16, 0.24 and 0.5).

In order to quantify the mechanical alterations during the oligo-cyclic tests and tend to express their dependencies on the pristine sample microstructure and/or ε_{OC} values, several mechanical indicators are monitored. They are illustrated in **Figure 2** and defined as follow:

- σ_{oc}^{i}: The nominal stress corresponding to the maximum-strain state at ith cycle ($1 \leq i \leq 100$).
- $\Delta\sigma^{i-1}$: The magnitude of stress softening between 1st and ith cycle ($2 \leq i \leq 100$).
- ε_{res}^{i}: The residual strain at zero-stress state at ith cycle ($1 \leq i \leq 100$).
- $\varepsilon_{res}^{2-100}$: The residual strain at zero-stress state induced by the following cycles (from 2nd to 100th).
- ε_{OC}: The applied maximum strain in oligo-cyclic tests.
- W_{d}^{i}: The hysteresis energy corresponding to the dissipated energy per unit volume at ith cycle ($1 \leq i \leq 100$).
- E^{i}: Secant modulus of ith cycle determined as $E^{i} = \frac{\sigma_{oc}^{i}}{\varepsilon_{1}^{i}}$, where $\varepsilon_{1}^{i} = \varepsilon_{OC}^{i} - \varepsilon_{res}^{i-1}$ ($2 \leq i \leq 100$).
- E_{1}^{i}: Comparative modulus measured in the first cycle within the same span of strain ε_{1}^{i} as E^{i}($2 \leq i \leq 100$). It is used for evaluating the relative change of modulus from the 1st to the ith cycle. The detail of the calculation will be introduced in the following section *Change of modulus*.

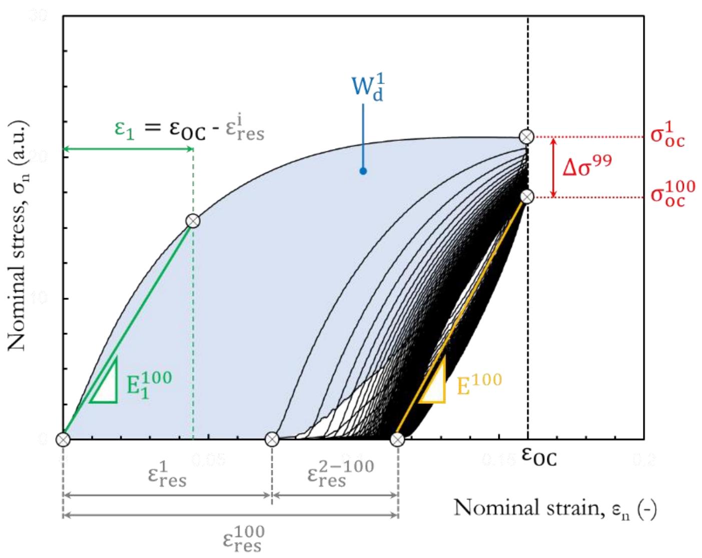

Figure 2: *Oligo-cyclic curve with the description of the evaluated mechanical changes.*

4.4.3 Mechanical alterations and associated mechanisms

Stress softening

As shown in **Figure 3**, the stress-softening magnitude (Δσ) decreases as ε_{OC} increases for all the four samples whatever the cycle number. The negative correlation between the total stress softening magnitudes $\Delta\sigma^{99}$ and ε_{OC} is further displayed, in **Figure 4a**.

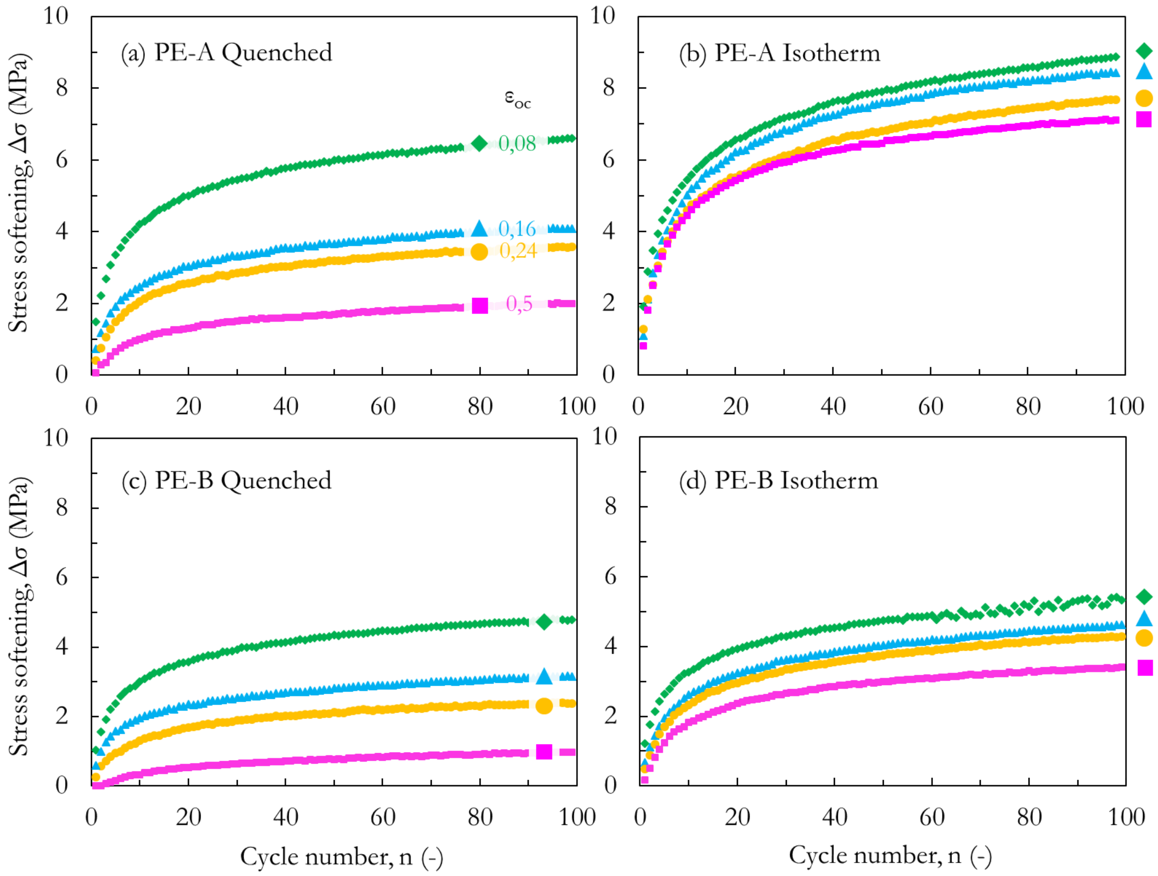

Figure 3: Stress-softening magnitude in different samples as a function of cycle number: (a) PE-A Quenched; (b) PE-A Isothermal; (c) PE-B Quenched and (d) PE-B Isothermal

For a given grade, it worth noting that more pronounced stress softening is observed in the isothermal sample when ε_{OC} is identical. Moreover, an indicator $\Delta\sigma^*$ determined by **equation (6)** is evoked for evaluating the improvement of the stress-softening resistance with increasing ε_{OC} in each sample (from $\varepsilon_{OC} = 0.08$ to $\varepsilon_{OC} = 0.5$). In particular, when $\varepsilon_{OC} = 0.08$, $\Delta\sigma^*$ is set as zero.

$$\Delta\sigma^*(\varepsilon_{OC}) = \frac{\Delta\sigma^{99}(0.08) - \Delta\sigma^{99}(\varepsilon_{OC})}{\Delta\sigma^{99}(0.08)} \qquad (6)$$

As shown in **Figure 4b,** it has been found that $\Delta\sigma^*$ also depends on the PE initial microstructure. A more significant increase of $\Delta\sigma^*$ is observed in the sample with lower crystallinity and higher ST density.

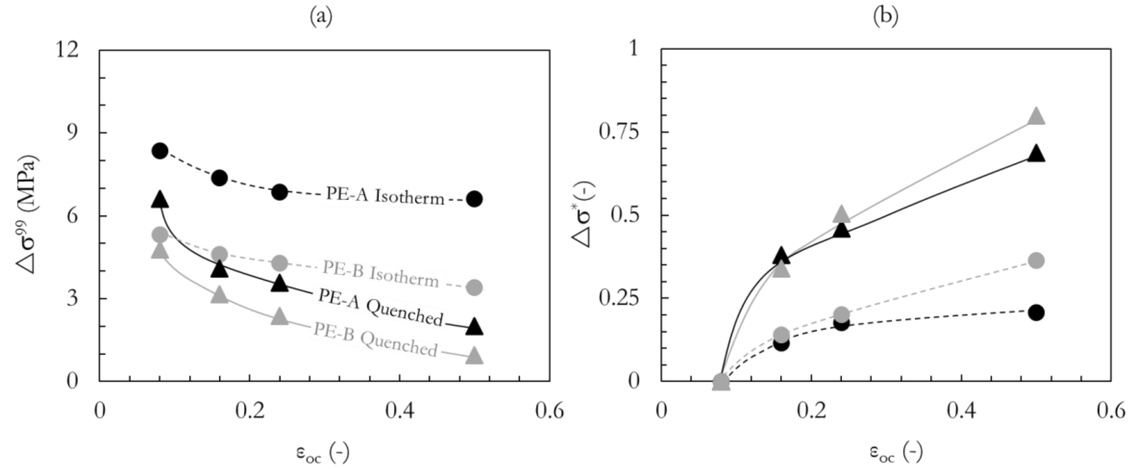

Figure 4: a) Total stress-softening magnitudes between 1st and 100th loading; b) Relative decrease of stress softening as a function of ε_{OC} in different samples

Various authors have attempted to figure out the physical interpretation of the cyclic stress-softening phenomenon in semi-crystalline polymers. However, the mechanisms remain disputable. Firstly, the rupture of short chains reaching their limit of extensibility, along with the disentanglement and breakdown of chains being stuck between two entanglement/crystallites are raised[32,42]. These mechanisms occurring in the amorphous phase could also potentially induce cavitation[35]. Furthermore, when a semi-crystalline polymer is deformed beyond yielding, the fragmentation of crystallites can also be considered as an origin of the macroscopic material softening[35]. This phenomenon could also be related to the elimination of the crystalline percolation.

The aforementioned dependencies of stress softening on ε_{OC} and PE microstructure can be explicated as follow: i) the stress-softening-related microstructure changes are mainly induced by the first cycle. And the higher ε_{OC}, the more important these structural changes. As these phenomena could induce the softening, they are thus globally named as “structural deteriorations” in the following sections. As the ε_{OC} increases, the microstructure after the 1st cycle tends to become an “extreme state” where the crystalline percolation is all eliminated and the remained STs are difficult to be disentangled/ruptured by the following cycles, the progressive stress-softening is thus more limited. ii) It has another compensating mechanism being stronger with increasing ε_{OC}. Also, its enhancement with increasing ε_{OC} should be more pronounced in the samples with lower crystallinity but higher ST density due to the lower value of stress softening. As mentioned in the introduction, under uniaxial tensile loading, the stress transmitters can be highly stretched, oriented along the loading direction, and induce recrystallization[52]. This phenomenon is related to the strengthening effect and should compensate for the stress softening[29,53]. Also, it is reasonable that this compensating phenomenon is more important in the samples with more STs [10,11] that promote their stretching and strain-induced recrystallization.

Residual strain accumulation

The residual strain (or inelastic strain) ε_{res} in semi-crystalline polymers can be divided into two parts, one being associated with the plastic deformation whereas the other one is due to the viscous effect of the amorphous phase that can be recovered after relaxation[31,40,41]. The residual strain accumulation-saturation behavior in each sample is displayed in **Figure 5.** The first-cycle-induced residual strain is the most important one.

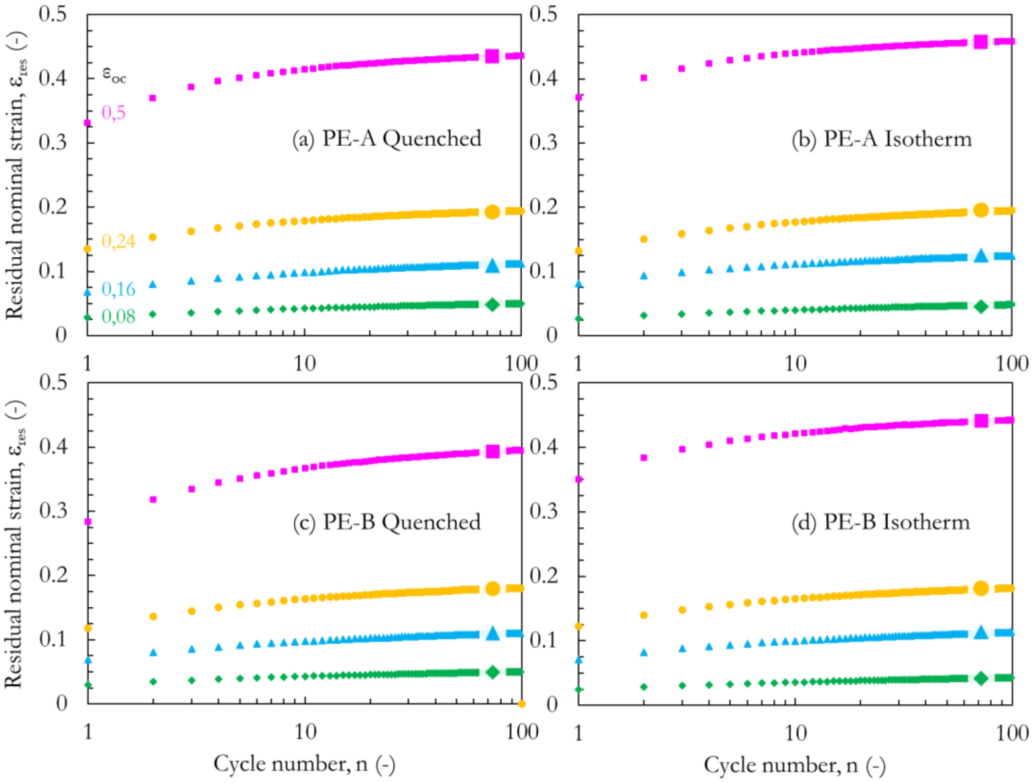

Figure 5: Residual strain in different samples as a function of cycle number: (a) PE-A Quenched; (b) PE-A Isothermal; (c) PE-B Quenched and (d) PE-B Isothermal

Moreover, ε_{res}^{1} and $\varepsilon_{res}^{2-100}$ as a function of ε_{OC} are shown in **Figure 6a** and **6b** respectively. For all samples, with increasing ε_{OC}, the inelastic strains induced by the first and the remaining cycles are both seen to increase. For ε_{OC} = 0.08, 0.16, and 0.24, the difference in residual strains between the four materials is not clearly measurable. However, when ε_{OC} = 0.5, the ε_{res}^{1} is larger in the samples with higher crystallinity, whereas the tendency is the opposite for $\varepsilon_{res}^{2-100}$.

As a physical interpretation, when the imposed strain in the first cycle is high enough (i.e. ε_{OC} = 0.5), The percolation of the crystalline network is most likely ruptured in numerous locations during the first cycle, and the majority of the residual strain can be considered as the irreversible/plastic one. The plasticity is thus stronger in the sample with higher crystallinity. However, the residual strain induced by the following cycles could be mainly attributed to the deformation in the amorphous phase. Therefore, the sample with lower crystallinity should have a macromolecular network more “inelastically” deformable due to the larger quantity of STs. However, in the lower strain range (ε_{OC} = 0.08, 0.16 and 0.24), the crystalline network is not completely broken by the first loading, the following cycles may continually and slightly induce the residual strains in both the crystalline and amorphous phases, thus, the magnitudes of ε_{res}^{1} and $\varepsilon_{res}^{2-100}$ are not clearly differed.

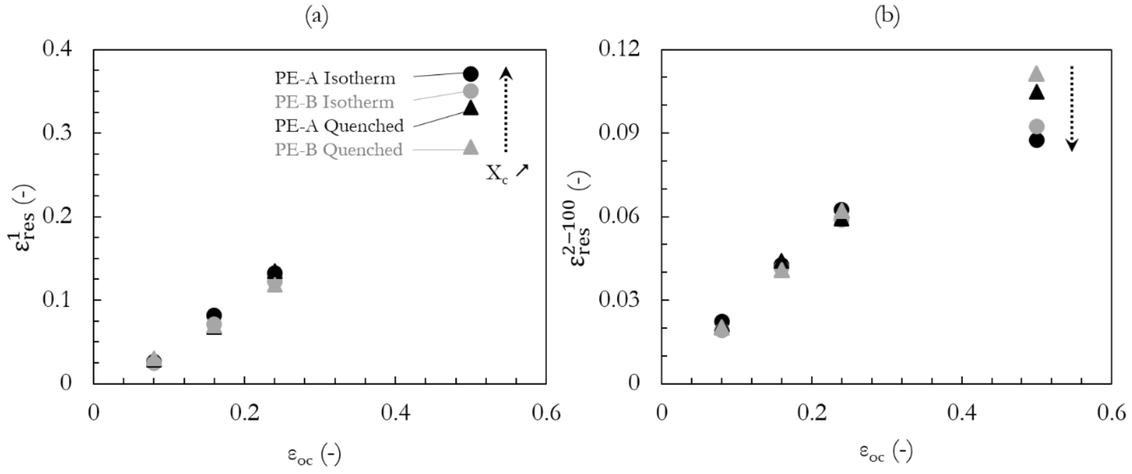

Figure 6: Change of the residual strains as a function of the prescribed maximum strain a) after the 1st cycle, b) from 2nd to 100th cycle

Density of energy dissipated

The hysteresis area W_d^i represents the density of energy dissipated during the i^{th} loading-unloading cycle. The dissipated energy can be ascribed to several mechanisms: for example, the friction between the chains (viscosity), and potential plastic mechanisms such as lamellae fragmentation and/or cavitation[36,37]. The changes of W_d as a function of the cycle number are shown in **Figure 7.** Similar to the residual strain profiles, W_d^1 is much higher than W_d^i (with i >1), confirming major differences between the first and the remaining cycles.

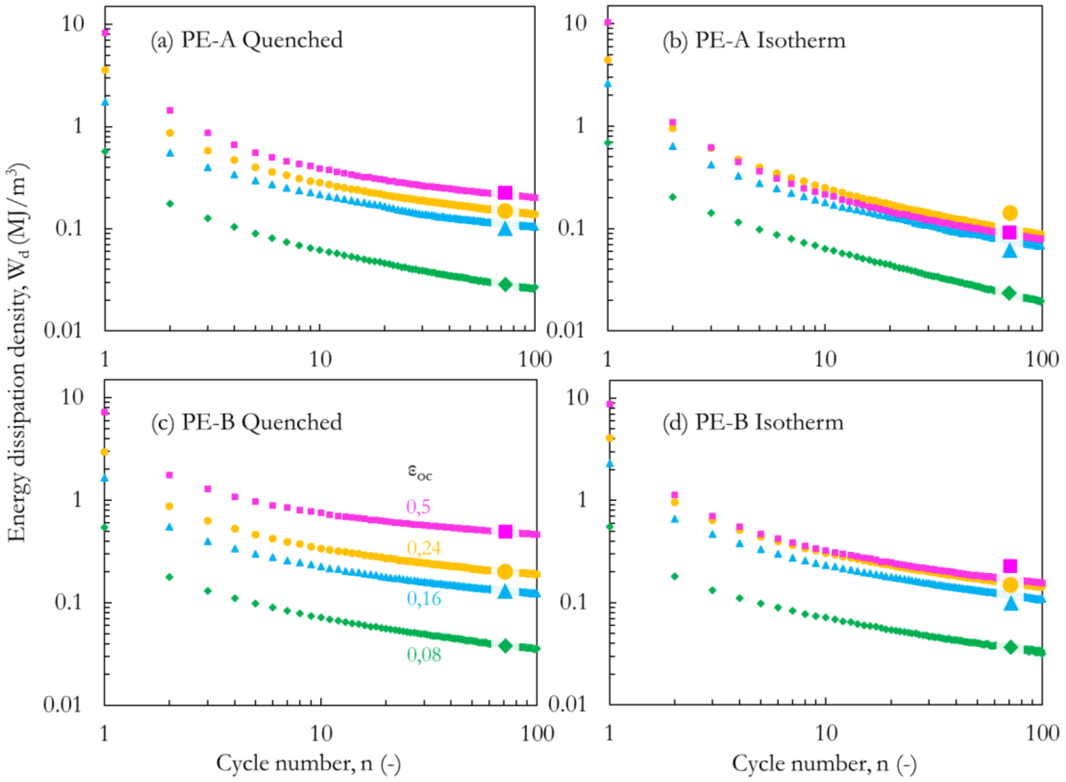

Figure 7: Density of energy dissipation W_d as a function of cycle number in PE samples with different applied oligo-cyclic strains ε_{OC}: (a) PE-A Quenched; (b) PE-A Isothermal; (c) PE-B Quenched and (d) PE-B Isothermal

In **Figure 8a**, for a prescribed ε_{OC}, the isothermal samples tend to dissipate the higher amount of energy per unit volume during the first cycle compared to the quenched ones. The relation between W_d^1 and ε_{OC} is quasi-linear. A simple elastoplastic theory (no hardening) can be used to approximate and explain their relation, the approximated density of energy dissipation of the first cycle W_d^{1*} is calculated using **equation (7)**.

$$\mathrm{W_d^{1*}} = \sigma_{\mathrm{th}}(\varepsilon_{\mathrm{OC}} - \varepsilon_{\mathrm{th}}) \tag{7}$$

Where σ_{th} and ε_{th} are the threshold stress and strain corresponding to the initiation of plasticity (where the stress σ_{th} is set to be 80% of yield stress σ_y obtained by uniaxial tensile curves). The approximated relations are also displayed in **Figure 8a**. Such approximation seems adapted so that the first-cycle induced energy dissipation can be mainly ascribed to the plasticity, it is consistent with the conclusion obtained by residual strain analysis.

The consumed energy per cycle is progressively saturated and approximately identical from the 90th-100th cycle. The energy dissipation during a whole saturated cycle (W_d^{100}) increases as the crystallinity decreases (or ST density increases). This relation is following the aforementioned assumption that the sample deformation remains primarily visco-elastic so that the energy dissipation is mainly caused by the additional viscous effect. W_d^{100}as a function of ε_{OC} of each sample is displayed in **Figure 8b.** The PE-B quenched samples exhibit the highest W_d^{100} value, indicating that this material has a superior energy dissipating capacity in the visco-elastic regime during cyclic deformation due to the more important friction between the chains.

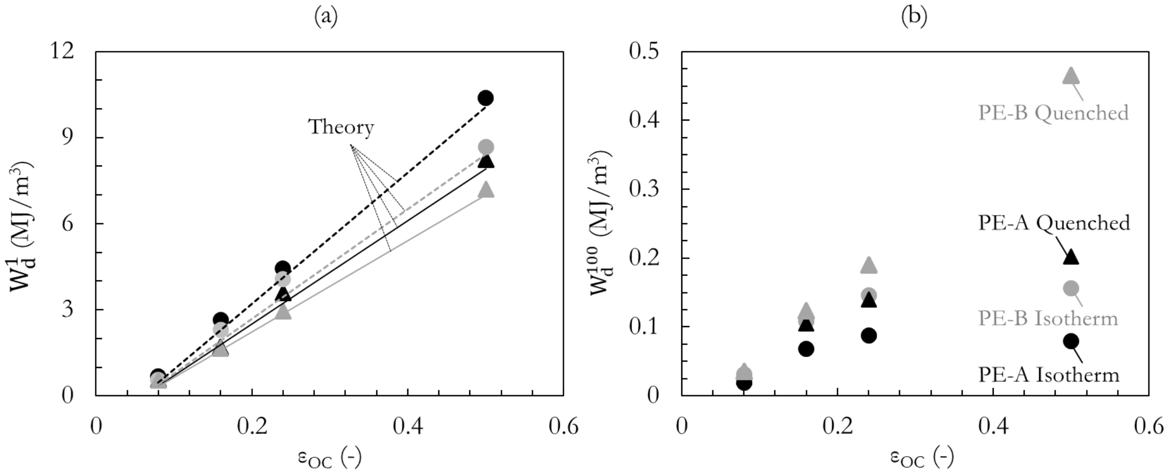

Figure 8: Dissipated energy density of PE samples at different applied oligo-cyclic strains a) after the first loading cycle (W_d^1) and b) after the 100nd loading cycle (W_d^{100})

Change of modulus

As evidenced in **Figure 1**, the experimental stress-strain curves are highly non-linear, therefore, the secant method is widely used to evaluate the modulus at the beginning of each cycle (zero-stress state) [24,26,27,29]. However, to our knowledge, this method has been yet applied to characterize the mixed-mode oligo-cyclic responses of polymers. Indeed, the secant modulus should be measured in the “cycle” with constant stress or strain range, so that the non-linearity effect can be ignored. Yet, by mixed-mode, neither the stress nor the strain amplitude is constant in different cycles. Therefore, an indicator D_E is proposed to evaluate the relative change of the secant modulus is defined as follow. The modulus of each following cycle (2nd-100th cycle) is compared with the modulus of the first cycle respectively. $\mathrm{E^i}$ and $\mathrm{E_1^i}$ are already defined in the last section **“Description of oligo-cyclic tensile behaviors”**:

$$\mathrm{D_E^{i-1}} = 1 - \mathrm{E^i} / \mathrm{E_1^i} \qquad (2 \leq i \leq 100) \qquad (8)$$

Although this mechanical indicator D_E is commonly used to evaluate the material damage at macroscale in semi-crystalline polymers[19,24,35], which means that a positive indicator D_E^{i-1} reflecting the decrease of secant modulus is expected. In this work, the negative value is also observed under certain condition and suggest that the modulus of the i^{th} cycle is superior to the initial modulus and indicating a strengthening effect. The changes of D_E in all four PE samples are shown in **Figure 9** as a function of the cycle number. In each sample, it is found that D_E^1 is negative (modulus increases) when $\varepsilon_{OC} = 0.08$ and 0.16. However, D_E^1 becomes positive (modulus decreases) when $\varepsilon_{OC} = 0.24$ and 0.5. From negative to positive, D_E^1 tends to be higher with increasing ε_{OC}. However, during the remaining cycles, D_E values decrease monotonically, indicating the growth of modulus with increasing cycles prior to progressively stabilizing.

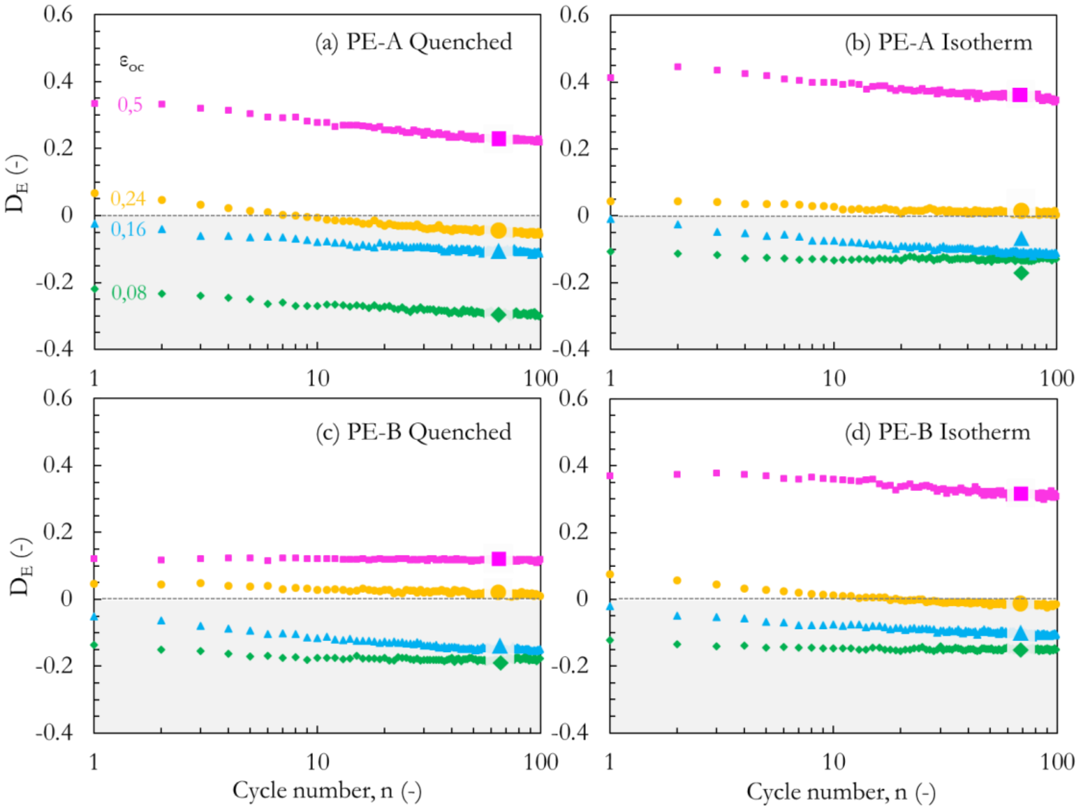

Figure 9: Relative change of the secant modulus evaluated by D_E as a function of cycle number in PE samples with different applied oligo-cyclic strains: (a) PE-A Quenched; (b) PE-A Isothermal; (c) PE-B Quenched and (d) PE-B Isothermal

As mentioned in the introduction, Humbert et *al*. used a model to predict the relation between the elastic modulus and the microstructure of PE [9,12], introducing the use of a mechanical coupling parameter k (the ratio between the stresses concentrated in hard phase and soft phase, σ_h/σ_s), which is physically related to the percolation level of the crystalline phase. The more percolated crystalline structure, the higher k value. The modulus is estimated using relation (9) where φ_h is the volume fraction of hard phase and E_s is the modulus of the soft phase.

$$E \approx k\mathrm{E_s} \times \frac{\mathrm{\varphi_h}}{1-\mathrm{\varphi_h}} \qquad (9)$$

Neglecting the influence of the interphase, the hard and soft phases are simply considered as the crystalline and amorphous phases[12]. Within this theoretical framework, three microstructural parameters (k, E_s, and φ_h) can directly determine the macroscopic modulus. Therefore, the modulus change can be related to different mechanisms that modify these parameters.

Firstly, the plastic deformation can provoke the decrease of E_s and k due to the disentanglement/rupture of weak chains (they may also induce cavitation) and fragmentation of the percolated crystalline structure respectively. However, to interpret the initial negative values of D_E (the first-cycle induced increase of modulus) under certain loading conditions (ε_{OC} = 0.08 and 0.16) and the decrease of D_E in the subsequent cycles (rest-cycles induced increase of modulus), the aforementioned competing mechanism should be mentioned again. As it compensates the stress softening, the orientation/alignment of chains and the stretching of stress transmitters can result in partial recrystallization, potentially increasing both the fraction of hard phase φ_h, amorphous modulus E_s. Also, the recrystallization may bridge the fragmented crystalline network and increase the k value.

Regarding D_E^1, with increasing ε_{OC}, the effect of "structural deteriorations" on the modulus becomes more and more dominant compared to the recrystallization at the zero-stress state. However, differing from the first cycle, the chain orientation/recrystallization governs the modulus of the consecutive cycles.

Figure 10 shows that the values of D_E^1 in all four samples increase as a function of ε_{OC}. For the relatively lower ε_{OC} (0.08/0.16/0.24), the dependency of D_E^1 on the microstructural properties remains unclear. However, when ε_{OC} = 0.5, D_E^1 value becomes higher as the sample crystallinity increases or ST density decreases. Indeed, the sample with higher crystallinity should have a more percolated crystalline structure, when the imposed strain is high enough, the crystalline network is nearly all broken, so it shows a more important loss of percolation, k decreases from a very high value to almost 1[12]. Additionally, the lower ST density promotes the disentanglement and chain rupture that could also induce a more important loss of amorphous modulus.

Physically, it seems reasonable that under a given loading condition, the recrystallization at zero-stress state should be more effective in the quenched samples during the following cycles due to their larger number of STs and higher residual strain in the amorphous phase (the chains are more stretched). However, the relation between the following-cycles-induced strengthening effect (decrease of D_E as a function of cycle number) and pristine PE microstructure is not clear. It may be interpreted as the complicated relations between the orientation of chains/recrystallization and the relative evolutions of the three parameters (k, E_s, and φ_h).

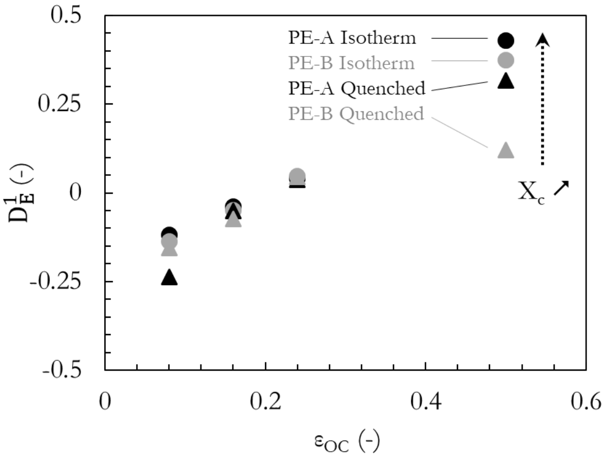

Figure 10: a) D_E^1 of PE samples at different applied oligo-cyclic strains εOC; b) kE_s product as a function of crystallinity

Physical scenario

According to all the aforementioned changes of the mechanical indicators, and the microscopic interpretations, a physical scenario describing the microstructural deformation mechanisms is proposed. The schematic is shown in **Figure 11.** It worth noting that the cavitation is not mentioned here, indeed, the origin of this phenomenon is related to the disentanglement/rupture of chains[35,41].

The pristine HDPE microstructure is composed of spherulites with radially oriented crystalline lamellae within the amorphous matrix. Several lamellae are percolated. Considering the ε_{OC} range under investigation, STs have different resistance against the deformation. The "strong" tie molecules can continually act without rupture, whereas the “weak” entanglement or loops, can be unfolded due to the slip of chains.

During the first loading, the very weak active entanglement/loops slip and unfold even at low macroscopic strain, followed by the elimination of percolation and shearing of crystals when the imposed strain reaches the plastic regime. The higher imposed strain, the more complete breakage of the crystalline network and disentanglement. In particular, the elimination of crystalline percolation tends to activate the confined STs that do not transmit the stress during the first cycle due to the percolated crystalline structure. The tie molecules with high deformation capacity can be aligned and may lead to the recrystallization, which can partially disappear during the unloading. Comparing the pristine (undeformed) state and the 1st zero-stress state, the orientation of chains/recrystallization competes with the structural deteriorations (disentanglement/rupture of STs and breakage of the crystalline network): in the low strain range (ε_{OC} = 0.08 and 0.16), the recrystallization dominates and results in a higher apparent modulus whereas in the high strain range (ε_{OC} = 0.24 and 0.5), the structural deteriorations prevail, the modulus after the first cycle is inferior to the initial one.

During the following cycles, the main deformation is ascribed to the amorphous phase. At the maximum-strain state, the level of chain orientation/recrystallization does not change with increasing cycles due to the constant imposed strain (ε_{OC}), therefore, the progressive stress softening is governed by the disentanglement occurring in the pre-confined regions and successive breakage of the crystalline network (if it is not completely broken by the first loading). With increasing ε_{OC}, the first cycle can induce more important structural deteriorations, which means that fewer STs that can be potentially disentangled, and less crystalline percolation remains after the first cycle. Regarding the zero-stress state, due to the accumulation of residual strain, the effect of recrystallization increases crucially as a function of cycle number. And the successive structural deteriorations cannot counteract this effect on modulus, the modulus thus tends to be a higher value with increasing cycles.

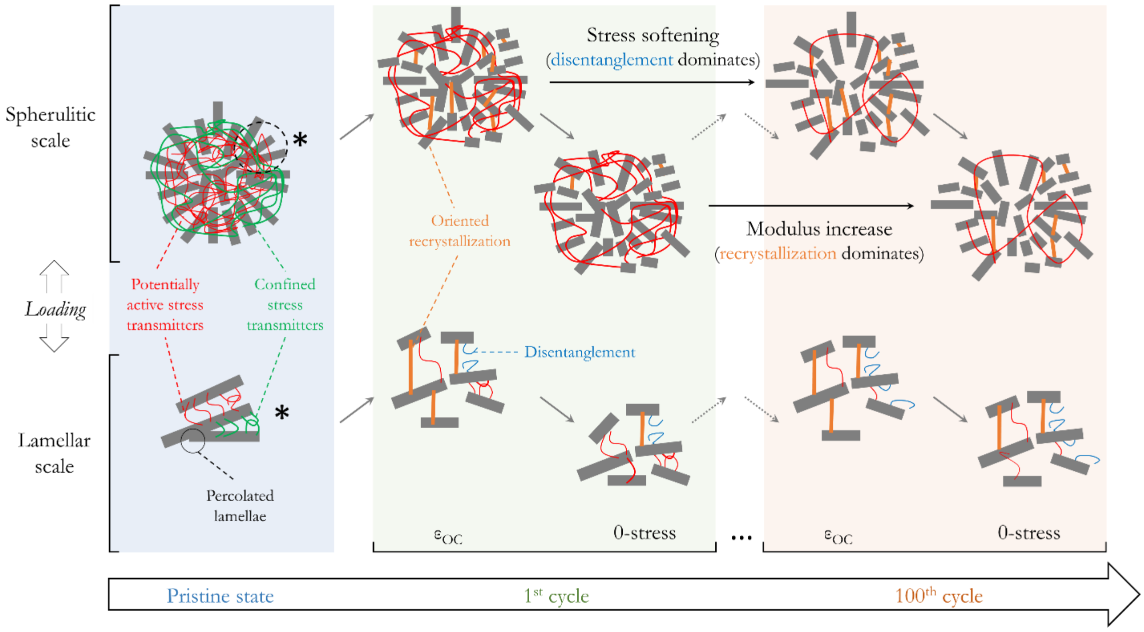

Figure 11: The physical scenario of HDPE under mixed-mode oligo-cyclic loading conditions (spherulitic scale and lamellar scale)

4.4.3 Post-cyclic tensile behavior

Uniaxial tension until failure was achieved after a series of 10 cycles as most of the microstructure changes were proven to occur within this period. All the PE samples show the *Mullins-like* behavior, as an example, the post-cyclic tensile behaviors of the PE-A isothermal sample are superimposed in **Figure 12a**: the post-cyclic curves tend to match the pristine one for strain larger than the ones endured during the oligo-cyclic test ($\varepsilon > \varepsilon_{OC}$), suggesting that all the changes occurring in the following cycles (2nd-100th) have a limited influence on the overall short-term mechanical performance. However, regarding fracture performance, the remaining toughness, W_f was then estimated as indicated in **Figure 12b**, where the multi-step stress-strain profile of PE-A isothermal sample with $\varepsilon_{OC} = 0.5$ is displayed as an example. Within this method, the first-cycle-induced damage (related to the loss of tensile toughness) is also taken into account. **Figure 12c** gives the relation between W_f and ε_{OC}. W_f for $\varepsilon_{OC} = 0$ naturally corresponds to the tensile toughness of the pristine PE samples, and the error bar indicates the difference between the maximum/minimum values. For a given grade (PE-A or PE-B), the value W_f does not significantly differ by the heat treatments, the isothermal samples require just slightly more energy until fracture (10% for PE-B and 8% for PE-A). However, between PE-A and PE-B samples, the difference is important (about 30%), which means that pristine W_f shows a more crucial dependency on the molecular characteristics than thermal treatment. Also, it is found that the W_f values of all four samples remain almost constant indicating that the change of energy required to failure is not measurable when ε_{OC} does not exceed 0.24. However, when $\varepsilon_{OC} = 0.5$, in the PE-A isothermal sample, which has the lowest ST density and highest crystallinity, the W_f decreases about 25%. This result tends to confirm that the resistance to failure decreases so that the mechanical damage should be relatively more important in PE-A isothermal sample than others.

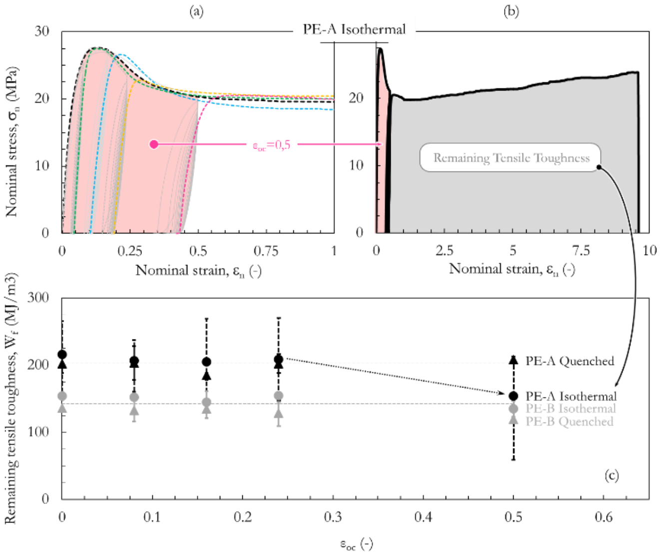

Figure 12: a) Mullins-like behavior of PE-A isothermal sample; b) Definition of remaining tensile toughness (ex. PE A isothermal sample, with ε_{OC}=0.5), c) Remaining tensile toughness in different samples as function ε_{OC}

4.5 Conclusion

The performance of varying HDPE samples under oligo-cyclic loading conditions was evaluated and a physical scenario is proposed for the interpretation of the measured macro-micro correlations: the structural deteriorations, such as chain rupture/disentanglement and breakage of lamellae/percolation are mainly induced by the first cycle. These structural deteriorations can induce the loss of modulus and compete with the orientation of stress transmitters/recrystallization associated with the strengthening effect. When the imposed cyclic strain is high enough (ε_{OC}=0.5), during the following cycles, the structural deteriorations are mainly assigned to the pre-confined disentanglement in the amorphous phase, dominating the stress change (decrease) at maximum strain state. However, at the zero-stress state, the chain orientation/recrystallization plays a more crucial role as illustrated by the increase of apparent modulus. Noticeably, the mechanical losses during the cyclic deformation including the stress softening and the decrease of the apparent modulus are more crucial in the isothermal samples, especially the PE-A grade, having higher crystallinity and lower ST density. However, it seems that the microstructural/mechanical changes during the following cycles have a limited effect on the further tensile loading path. As for the tensile toughness, considering the effect of the complete loading process including the first cycle, there is a loss only in the PE-A isothermal sample with the “extreme” microstructural parameters.

Compared to the other HDPE, the one for PE-100 pipeline (PE-B in this study) has relatively lower yield stress, modulus and tensile toughness. However, this material shows a better resistance against the mechanical losses under oligo-cyclic loading conditions. Regarding the tensile toughness, even when $\varepsilon_{OC} = 0.5$, the variation/decrease is limited in either the quenched or the isothermal PE-B sample. It means that the pre-loaded PE-B samples also require the same energy to rupture as the pristine ones. This can evidence the good resistance against seismic damage in PE-100 material under these loading conditions. Also, the modulus decrease is not sufficient for the damage evaluation in HDPE material, especially, its reversibility should be further investigated.

Reference

[1] N. Nishonov, D. Bekmirzaev, E. An, Z. Urazmukhamedova, K. Turajonov, Behaviour and Calculation of Polymer Pipelines Under Real Earthquake Records, in: IOP Conf. Ser. Mater. Sci. Eng., IOP Publishing, 2020: p. 052076.

[2] Hideki Omuro, Tomokazu Himono, POLYETHYLENE PIPELINE PERFORMANCE AGAINST EARTHQUAKE, in: 2018.

[3] Angelo Masi, Giuseppe Santarsiero, Domenico Nigro, Cyclic tests on external RC beam-column joints: role of seismic design level and axial load value on the ultimate capacity, J. Earthq. Eng. 17 (2013) 110–136.

[4] Paolino Cassese, Paolo Ricci, Gerardo M. Verderame, Experimental study on the seismic performance of existing reinforced concrete bridge piers with hollow rectangular section, Eng. Struct. 144 (2017) 88–106.

[5] B. Xiong, O. Lame, J. M. Chenal, C. Rochas, Roland Seguela, G. Vigier, In-situ SAXS study and modeling of the cavitation/crystal-shear competition in semi-crystalline polymers: Influence of temperature and microstructure in polyethylene, Polymer. 54 (2013) 5408–5418.

[6] Bijin Xiong, Olivier Lame, Jean-Marc Chenal, Cyrille Rochas, Roland Seguela, Gerard Vigier, In-situ SAXS study of the mesoscale deformation of polyethylene in the pre-yield strain domain: Influence of microstructure and temperature, Polymer. 55 (2014) 1223–1227.

[7] B. Xiong, O. Lame, J. M. Chenal, C. Rochas, Roland Seguela, On the strain-induced fibrillar microstructure of polyethylene: Influence of chemical structure, initial morphology and draw temperature, Express Polym. Lett. 10 (2016) 311.

[8] R. Séguéla, On the Natural Draw Ratio of Semi-Crystalline Polymers: Review of the Mechanical, Physical and Molecular Aspects, Macromol. Mater. Eng. 292 (2007) 235–244.

[9] S. Humbert, O. Lame, R. Séguéla, G. Vigier, A re-examination of the elastic modulus dependence on crystallinity in semi-crystalline polymers, Polymer. 52 (2011) 4899–4909.

[10] Bijin Xiong, Olivier Lame, Jean-Marc Chenal, Yongfeng Men, Roland Seguela, Gerard Vigier, Critical stress and thermal activation of crystal plasticity in polyethylene: Influence of crystal microstructure and chain topology, Polymer. 118 (2017) 192–200.

[11] S. Humbert, O. Lame, G. Vigier, Polyethylene yielding behaviour: What is behind the correlation between yield stress and crystallinity?, Polymer. 50 (2009) 3755–3761.

[12] T. Deplancke, M. Fivel, O. Lame, 1D strain rate-dependent constitutive model of UHMWPE: From crystalline network to fibrillar structure behavior, Mech. Mater. 137 (2019) 103129.

[13] B. Xiong, O. Lame, J.-M. Chenal, C. Rochas, R. Seguela, G. Vigier, Amorphous phase modulus and micro–macro scale relationship in polyethylene via in situ SAXS and WAXS, Macromolecules. 48 (2015) 2149–2160.

[14] Y.-Q. Zhou, N. Brown, The mechanism of fatigue failure in a polyethylene copolymer, J. Polym. Sci. Part B Polym. Phys. 30 (1992) 477–487.

[15] J. Runt, M. Jacq, Effect of crystalline morphology on fatigue crack propagation in polyethylene, J. Mater. Sci. 24 (1989) 1421–1428.

[16] J.T. Yeh, J. Runt, Fatigue crack propagation in high-density polyethylene, J. Polym. Sci. Part B Polym. Phys. 29 (1991) 371–388.

[17] M. Niinomi, L. Wang, T. Enjitsu, K.-I. Fukunaga, Fatigue characteristics of ultra high molecular weight polyethylene with different molecular weight for implant material, J. Mater. Sci. Mater. Med. 12 (2001) 267–272.

[18] N. Brown, X. Lu, Y.-L. Huang, R. Qian, Slow crack growth in polyethylene-a review, in: Makromol. Chem. Macromol. Symp., Wiley Online Library, 1991: pp. 55–67.

[19] Y. Zhang, P.-Y.B. Jar, S. Xue, L. Li, Quantification of strain-induced damage in semi-crystalline polymers: a review, J. Mater. Sci. 54 (2019) 62–82.

[20] Sandrine Humbert, O. Lame, J. M. Chenal, C. Rochas, G. Vigier, New insight on initiation of cavitation in semicrystalline polymers: in-situ SAXS measurements, Macromolecules. 43 (2010) 7212–7221.

[21] W. Liu, Z. Gao, Z. Yue, Steady ratcheting strains accumulation in varying temperature fatigue tests of PMMA, Mater. Sci. Eng. A. 492 (2008) 102–109.

[22] G. Tao, Z. Xia, Fatigue behavior of an epoxy polymer subjected to cyclic shear loading, Mater. Sci. Eng. A. 486 (2008) 38–44.

[23] G. Kang, Y. Liu, Y. Wang, Z. Chen, W. Xu, Uniaxial ratchetting of polymer and polymer matrix composites: time-dependent experimental observations, Mater. Sci. Eng. A. 523 (2009) 13–20.

[24] Elodie Mourglia-Seignobos, Didier R. Long, Ludovic Odoni, Loïc Vanel, Paul Sotta, Cyrille Rochas, Physical mechanisms of fatigue in neat polyamide 6, 6, Macromolecules. 47 (2014) 3880–3894.

[25] A.D. Drozdov, Cyclic viscoelastoplasticity and low-cycle fatigue of polymer composites, Int. J. Solids Struct. 48 (2011) 2026–2040.

[26] N. Fouchier, C. Nadot-Martin, E. Conrado, A. Bernasconi, S. Castagnet, Fatigue life assessment of a Short Fibre Reinforced Thermoplastic at high temperature using a Through Process Modelling in a viscoelastic framework, Int. J. Fatigue. 124 (2019) 236–244.

[27] B. Klimkeit, S. Castagnet, Y. Nadot, A. El Habib, G. Benoit, S. Bergamo, C. Dumas, S. Achard, Fatigue damage mechanisms in short fiber reinforced PBT+ PET GF30, Mater. Sci. Eng. A. 528 (2011) 1577–1588.

[28] A. Avanzini, Mechanical characterization and finite element modelling of cyclic stress–strain behaviour of ultra high molecular weight polyethylene, Mater. Des. 29 (2008) 330–343.

[29] A.D. Drozdov, Cyclic strengthening of polypropylene under strain-controlled loading, Mater. Sci. Eng. A. 528 (2011) 8781–8789.

[30] A.D. Drozdov, J. deC Christiansen, Cyclic viscoplasticity of high-density polyethylene: experiments and modeling, Comput. Mater. Sci. 39 (2007) 465–480.

[31] A. D. Drozdov, Mullins' effect in semicrystalline polymers, Int. J. Solids Struct. 46 (2009) 3336–3345.

[32] M. Makki, G. Ayoub, H. Abdul-Hameed, F. Zaïri, B. Mansoor, M. Naït-Abdelaziz, M. Ouederni, Mullins effect in polyethylene and its dependency on crystal content: a network alteration model, J. Mech. Behav. Biomed. Mater. 75 (2017) 442–454.

[33] R.W. Meyer, L.A. Pruitt, The effect of cyclic true strain on the morphology, structure, and relaxation behavior of ultra high molecular weight polyethylene, Polymer. 42 (2001) 5293–5306.

[34] F. Xu, N. Aravas, P. Sofronis, Constitutive modeling of solid propellant materials with evolving microstructural damage, J. Mech. Phys. Solids. 56 (2008) 2050–2073.

[35] F. Detrez, S. Cantournet, R. Seguela, Plasticity/damage coupling in semi-crystalline polymers prior to yielding: Micromechanisms and damage law identification, Polymer. 52 (2011) 1998–2008.

[36] Z. Qi, N. Hu, D. Zeng, X. Su, Failure of high density polyethylene under cyclic loading: Mechanism analysis and mode prediction, Int. J. Mech. Sci. 156 (2019) 46–58.

[37] R.P. Janssen, D. de Kanter, L.E. Govaert, H.E. Meijer, Fatigue life predictions for glassy polymers: a constitutive approach, Macromolecules. 41 (2008) 2520–2530.

[38] L. Mullins, Permanent set in vulcanized rubber, Rubber Chem. Technol. 22 (1949) 1036–1044.

[39] Leonard Mullins, Softening of rubber by deformation, Rubber Chem. Technol. 42 (1969) 339–362.

[40] Julie Diani, Bruno Fayolle, Pierre Gilormini, A review on the Mullins effect, Eur. Polym. J. 45 (2009) 601–612.

[41] F.P.C. Gomes, M.R. Thompson, Analysis of Mullins effect in polyethylene using ultrasonic guided waves, Polym. Test. 60 (2017) 351–356.

[42] G. Ayoub, F. Zaïri, M. Naït-Abdelaziz, J.M. Gloaguen, Modeling the low-cycle fatigue behavior of visco-hyperelastic elastomeric materials using a new network alteration theory: application to styrene-butadiene rubber, J. Mech. Phys. Solids. 59 (2011) 473–495.

[43] S. Humbert, O. Lame, J.-M. Chenal, R. Seguela, G. Vigier, Memory effect of the molecular topology of lamellar polyethylene on the strain-induced fibrillar structure, Eur. Polym. J. 48 (2012) 1093–1100.

[44] Z. Jiang, Y. Tang, J. Rieger, H.-F. Enderle, D. Lilge, S.V. Roth, R. Gehrke, W. Heckmann, Y. Men, Two lamellar to fibrillar transitions in the tensile deformation of high-density polyethylene, Macromolecules. 43 (2010) 4727–4732.

[45] A. Alizadeh, L. Richardson, J. Xu, S. McCartney, H. Marand, Y. W. Cheung, S. Chum, Influence of structural and topological constraints on the crystallization and melting behavior of polymers. 1. Ethylene/1-octene copolymers, Macromolecules. 32 (1999) 6221–6235.

[46] S. Humbert, O. Lame, G. Vigier, Influence de la topologie moléculaire et de la microstructure sur les propriétés mécaniques des Polyéthylènes, Lab. Rech. MATEIS INSA Lyon. (2009).

[47] L. Hubert, L. David, R. Seguela, G. Vigier, C. Degoulet, Y. Germain, Physical and mechanical properties of polyethylene for pipes in relation to molecular architecture. I. Microstructure and crystallisation kinetics, Polymer. 42 (2001) 8425–8434.

[48] B. Crist, C.J. Fisher, P.R. Howard, Mechanical properties of model polyethylenes: tensile elastic modulus and yield stress, Macromolecules. 22 (1989) 1709–1718.

[49] Y.-L. Huang, N. Brown, The effect of molecular weight on slow crack growth in linear polyethylene homopolymers, J. Mater. Sci. 23 (1988) 3648–3655.

[50] Y.-L. Huang, N. Brown, Dependence of slow crack growth in polyethylene on butyl branch density: morphology and theory, J. Polym. Sci. Part B Polym. Phys. 29 (1991) 129–137.

[51] Séverine Humbert, Olivier Lame, Jean-Marc Chenal, Cyrille Rochas, Gérard Vigier, Small strain behavior of polyethylene: in situ SAXS measurements, J. Polym. Sci. Part B Polym. Phys. 48 (2010) 1535–1542.

[52] V. Gaucher–Miri, C. Depecker, R. Séguéla, Reversible strain-induced order in the amorphous phase of a low-density ethylene/butene copolymer, J. Polym. Sci. Part B Polym. Phys. 35 (1997) 2151–2159.

[53] W.W. Adams, D. Yang, E.L. Thomas, Direct visualization of microstructural deformation processes in polyethylene, J. Mater. Sci. 21 (1986) 2239–2253.

5 Anisotropic deformation behavior of necked HDPE materials induced by oligo-cyclic loading

5.1 Abstract

In this chapter, the necking behavior during the oligo-cyclic deformation and the post-cyclic deformation behavior of the necked High-Density Polyethylene (HDPE) materials are characterized. Along with the large-strain oligo-cyclic deformation by mixed mode in four HDPE samples with a range of crystallinity (from 57% to 73%), simultaneous Digital Image Correlation (DIC) is carried out to determine the evolution of surface local strains along both longitudinal and transversal directions. The final volumetric strain (after the whole oligo-cyclic test), physically related to the voids generated throughout the test, is estimated by measuring the reduction of thickness in addition to the surface strain measurements. The axial strain significantly localizes when the macroscopic strain exceeds a threshold, indicating the necking behavior during the first loading path. Upon the consecutive cycles, the accumulation of longitudinal residual strain in the zero-stress state mainly occurs in the necked region as the other part remains in the elastic regime approximately. In the necked region, the microstructure is transformed from spherulites to oriented fibrillary structures and the deformation behavior becomes strongly anisotropic according to post-cyclic tensile characterization combined with *in-situ* Small Angel X-ray Scattering (SAXS) observation. Along both longitudinal and transversal directions, the deformation is mainly ascribed to the inter-fibrillary chains, which are more extended along the pre-orientation and more flexible along the transversal direction. Due to the anisotropic structure, the end-of-life (failure) stresses differ between the orthogonal directions. The loss in failure stress indicates that the pre-loaded samples are damaged during the cyclic pre-loading, this damage only occurring in the sample with the highest crystallinity and the lowest density of stress transmitters, and in particular along the transversal direction. Moreover, the influences of the initial microstructure of HDPE materials on the strain localization, post-cyclic deformation behavior, and anisotropic failure stress in the necked materials are also discussed. This chapter is drafted as a research paper that is under review and will be published later.

5.2 Introduction

The use of High-Density Polyethylene (HDPE) as constitutive material to design pipelines is now widely spread. One of their advantages compared to conventional metal-based pipes is their convincing capability to resist seismic-like events. Indeed, in 2018, according to the report of Polyethylene Piping System Integrated Technology & Engineering Center in Japan, HDPE pipelines remained almost undamaged consecutive to the seismic activity[1]. Therefore, the origin of their impressive seismic performance deserves an investigation at different length scales thus possibly to optimize the material design. In order to model a seismic event, oligo-cyclic testing conditions involving plastic deformation and a limited amount of loading cycles[2–4] are often used. Notwithstanding, under a real seismic condition, the loading mode for a certain pipeline in a global architecture can be complex due to the complicated connection between each other[4]. Nevertheless, in this work, efforts are limited exclusively to the tensile loading conditions in order to simplify the macro-micro correlation/interpretation.

When HDPE and/or other semi-crystalline polymers are submitted to plastic deformation, they potentially exhibit various macroscopic phenomena, such as necking[5–10], whitening (cavitation)[11–16] and buckling[9], etc. In particular, under uniaxial tensile deformation, necking is recognized as the manifestation of plastic instability[6,7,17,18] and a failure mode[9]. The necking (strain localization) is initiated due to pre-existing “weak points”, such as a structural defect or a geometrical artifact for instance. When the strain along tensile direction locally reaches a critical value, designated as natural draw ratio, λ_n, the growth of local strain is somehow completed and similar mechanisms then occur in the nearby regions[6,18], so the neck finally propagates throughout the entire gauge length of the tensile specimen. Occurring within a sample of constant cross-section, the propagation phase is seen to develop at quasi-constant force. Also, as the neck propagates, the local strain within the necked region may also slightly increase due to the potential plastic creep[19,20]. At the end of propagation, the axial strain is almost spatially homogenous within the entire gauge length of the sample.

As for the macroscopic evaluation and characterization of necking behavior, the neck width and natural draw ratio obtained from nominal stress-strain profiles are often recognized as the relevant indicators[7,21]. Moreover, infrared imaging[22], local strain measurement by Electronic Speckle Pattern Interferometry (ESPI)[23], and full-field displacement measurement by Digital Image Correlation (DIC) technique[5,8,24,25] have also been applied. Among these techniques, DIC measurement deserves particular attention due to its high accuracy and immediacy. This technique allows for tracking of the displacement field of a speckled pattern (subdivided into subsets) added onto the surface of a sample. Real-time image recording of the specimen is performed, and a subsequent image analysis leads to the determination of the surface or volumetric[26] (for the case of the sample with cylindrical cross-section) strain fields.

At the microscopic scale, the necking behavior depends on the density of stress transmitters (STs) as ties, entanglements and loops that link the crystalline/amorphous phases. PE with lower ST density tend to exhibit enhanced deformation heterogeneity[7,27]. Whatever the pristine microstructures, within the already-necked region, the original isotropic spherulites in PE material change into highly oriented microfibrils composed of fragmented/oriented crystalline blocks connected by stretched STs in the amorphous phase. These fibrils play an important role in preventing the crack/craze propagation[13,28–30] . The *so-called* fibrillary transformation[31–34] is physically interpreted as destruction-recrystallization or melting/recrystallization mechanisms[31,32].

Despite the aforementioned contributions, the macroscopic necking behavior of semi-crystalline polymers was mainly studied and discussed under uniaxial stretching conditions. However, Janssen et al.[35,36] also referred to necking as one of the fatigue failures (ductile type) in the oligo-cyclic regime (or thermally-dominated domain), differing from the brittle failure as cracking in the high-cycle regime (or mechanically-dominated domain). Some authors have also drawn the similar conclusion in their works[9,37]. Therefore, it is worth investigating the necking/strain heterogeneities taking place under the oligo-cyclic loading conditions with the objective to improve the understanding of the seismic performance of HDPE. In addition, the material within the necked region being in an “extreme” deformed state, the characterizations of its further mechanical properties and associated deformation behaviors are important for the qualification of the pre-loaded HDPE pipelines by the earthquake and material design considering the seismic requirements. In particular, due to the cyclic-loading induced orientation of the microstructure, the anisotropy evaluation should also be of great interest.

5.3 Experimental section

5.3.1 Shaping process and microstructure characterizations

Two groups of commercial HDPE pellets were ordered from INEOS (Brussels, Belgium), and denoted as PE-A and PE-B, they are used for blow-molding and pipeline application (PE-100) respectively. These two materials were compression-molded into 0.8 mm thick sheets. Different thermal treatments (quenching in cold water and isothermal treatment in the oil bath at a selected temperature in the vicinity of the crystallizing one) were imposed in order to generate the samples with a range of microstructural properties (e.g varying crystallinity and density of stress transmitters) thanks to the different regimes of crystallization[38]. Once shaped, the pristine microstructures were characterized: the crystallinity was measured by Differential Scanning Calorimetry (DSC) technique, the long period and thickness of lamellar stacks were characterized by SAXS, the ST density was estimated by both tensile characterization (neck width[7,21]) and Brown's model[39,40] (see our previous work for further details[21]). The results are summarized in the following **Table 1.** The four samples under consideration show a range of crystallinity varying from 57% to 73%. Relatively lower value of ST density is observed in the samples having higher crystallinity. All in all, under identical processing condition, the PE-B material has lower crystallinity and more ST elements than the PE-A. For a given grade, isothermal sample has higher crystallinity but lower ST concentration.

Table 1. Microstructure characteristics of HDPE after shaping process.

Methods		DSC	SAXS			Brown's model	Neck width
Microstructure characteristics		X_c (%)	L_p (nm)	L_c (nm)	L_a (nm)	[ST]	
PE-A	Quenched	62	22	13	9	0.22	0.55
	Isothermal	73	35	24	11	0.07	0.27
PE-B	Quenched	57	20	11	9	0.27	0.65
	Isothermal	64	33	20	13	0.14	0.32

5.3.2 Mixed-mode oligo-cyclic tests with simultaneous Digital Image Correlation (DIC)

Dumbbell-shaped specimens of 14 mm gauge length, 12 mm width, and 0.8 mm thickness were punched from the shaped sheets. Spray paint was used for the speckled pattern in DIC analysis. At least 15min separated the painting from the test to leave sufficient time for the paint to dry. The specimens were subjected to 10 repeated loading-unloading cycles at a constant nominal strain rate $\dot{\varepsilon}$=$1 \times 10^{-2} s^{-1}$ using an MTS 1/ME machine with a 5KN load cell. For each test, the specimens were stretched up to a selected macroscopic strain ε_{OC} = 1.5 and unloaded till reaching the zero-stress state. Simultaneously, CCD camera was installed to capture the sample images every 0.5s. The commercial software VIC-3D from correlated solutions® was employed to perform the correlation process and strain mapping generation in the painted surface. After the tests, all pre-loaded specimens were stored at room temperature for about 1 month, to ensure sufficient relaxation before the following tests.

5.3.3 Post tensile tests combined with in-situ SAXS characterizations

To compare the deformation behaviors at both macro- and micro- scales of the pristine and necked materials, three specimens were prepared for each material listed in **Table 1:** 1) a "Pristine" sample was directly punched from the sheet, 2) a "L-necked" sample was cut out from the necked region of the sample that beforehand experienced oligo-cyclic loading, 3) Following the same procedure, the "T-necked" specimen was cut perpendicular to the tensile loading direction of another pre-conditioned sample. A small dumbbell-shaped cutter with a gauge length of 3.5 mm in length and 2 mm in width was used for the sample preparation.

Uniaxial loading tests up to failure were performed with a homemade uniaxial testing machine at room temperature (about 25°C). The nominal strain rate was 3×10^{-3} s^{-1}. *In-situ* SAXS characterizations were carried out on the SWING beamline at the SOLEIL synchrotron in France. The wavelength of the X-ray was 1.03 Å and the specimen-detector distance was 2003 mm so that the scattering information could be observed in a 2D q-window with the range 0.036-0.52 $Å^{-1}$. The time interval between two consecutive SAXS acquisitions is 3s.

Moreover, to consolidate the investigation of the pre- and post- oligo-cyclic loading end of life properties, especially the failure stress, additional tensile characterizations were performed using an MTS 1/ME machine equipped with a 100N load cell. The testing conditions were replicated and each test was repeated at least three times, with the average values and standard deviations being recorded. **Figure 1** illustrates the overall mechanical testing procedure**.**

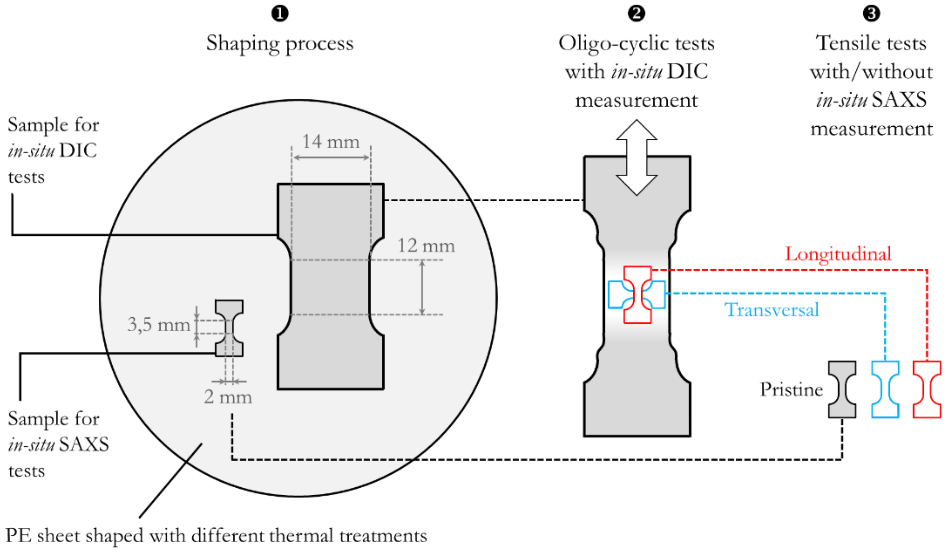

Figure 1: *Overview of the mechanical testing procedure.*

5.4 Results and discussion

5.4.1 Strain localization and accumulation

The strain localization is evaluated by DIC analysis. For instance, **Figure 2a** plots the evolution of the macroscopic nominal strain with respect to the time in PE-A quenched material during the mixed-mode cyclic test. The residual strain at zero stress evolves as the cycle number increases during a test (see the values reported in **Figure 2a** for the 1st and 10th unloaded states). The spatial distribution of the X-oriented (longitudinal, i.e. parallel to the loading direction) and Y-oriented (transversal) nominal strain components can be recorded along with the time/macroscopic strain evolution. As an example, **Figure 2b and c** illustrate the longitudinal and transverse strain mappings at the end of the first loading process (in the maximum-strain state), clearly, the strain components are heterogeneous and a clear necked region is observed.

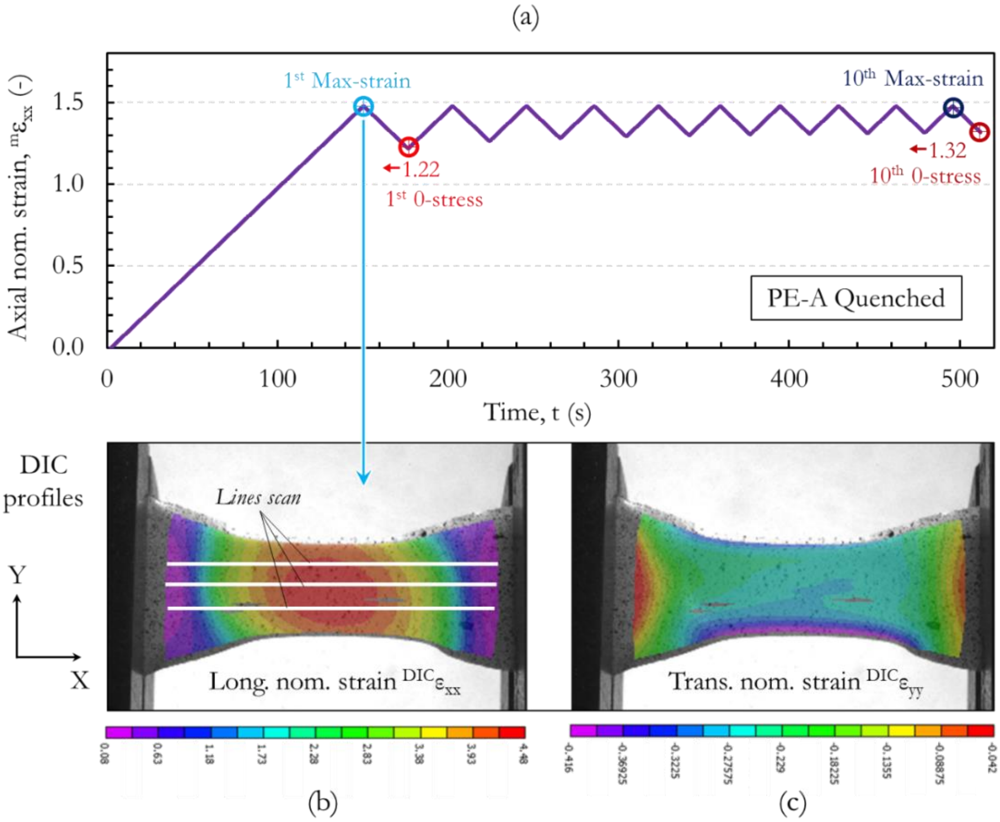

Figure 2: *Results of in-situ DIC measurement of PE-A quenched sample: (a) strain loading profile prescribed by the testing machine; (b) longitudinal strain mapping at the end of the first loading; (c) transversal strain mapping at the end of the first loading.*

Further quantitative data reductions are pursued: to simplify and highlight the evolution of strain localization with increasing cycles, the potential through-width variations are omitted and the longitudinal and transverse strain components are now determined as a function of the X-position. The values obtained from three line-scans are displayed in **Figure 2b:** each line is discretized into 200 elements and the local strains for a given X-position is determined by averaging the values collected by the three lines. The X- and Y-oriented strain profiles with respect to the X-position are presented in **Figure 3**.

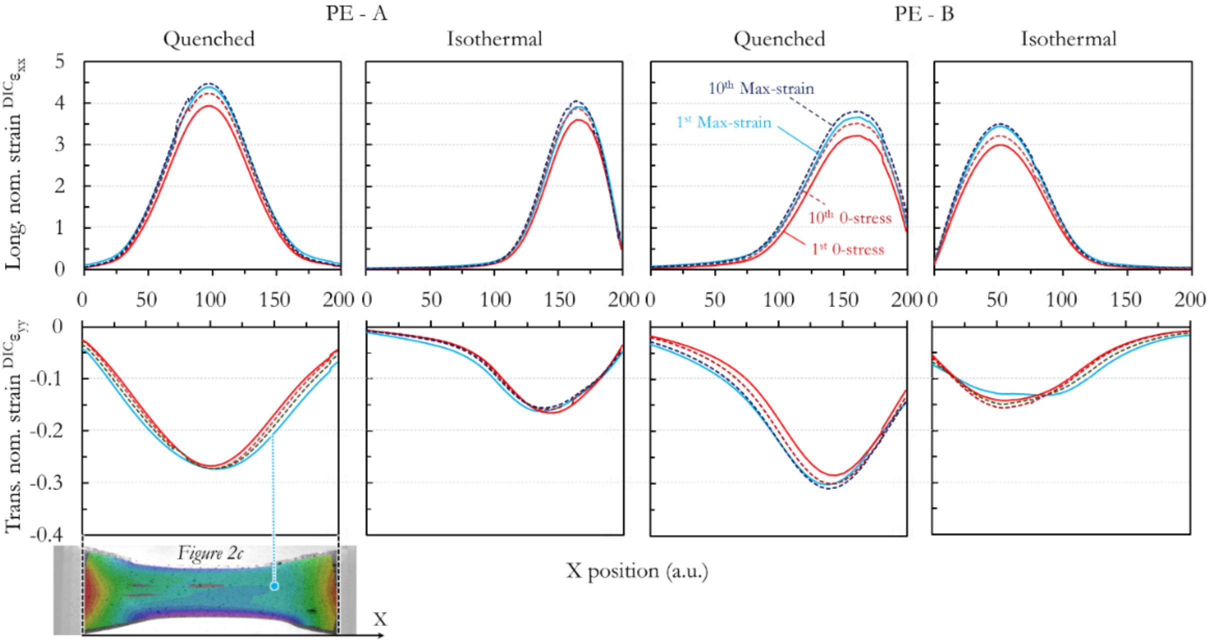

***Figure 3**: Longitudinal (L.) and transversal (T.) nominal strain distributions as a function of X-position at 4 stages during the oligo-cyclic test (N.B. the bottom left image recalls the transverse nominal strain field at the end of the first loading step).*

Data for all four materials in the maximum-strain and zero-stress states of the 1st and 10th cycles are plotted. Considering the aforementioned remarks regarding the neck initiation and its sensitivity to "weak points", it is not surprising that the X-position of the maximum local strain differs within these samples. Focusing on the first maximum-strain state, the maximum local longitudinal strains range between 3.5 and 4.5 in all samples (i.e. taking the smaller value as the reference, the relative difference is within 15% in different samples), yet being much higher than the prescribed macroscopic one (1.5). Along the transversal direction, the local strain value shows a great dependency on thermal treatment: the quenched samples exhibit a remarkable reduction of width in the necked region (local strains are about -0.3), whereas the peak values of the transverse strain in isothermal samples are only about -0.2. The relative difference is thus about 50%.

In the zero-stress state, by comparing the local strain profiles between the 1st and the 10th cycles, it can be observed that the longitudinal strain accumulation is still localized in the necked region. However, along the transverse direction, limited accumulation effect can be observed.

Beyond the elastic limit, a semi-crystalline material is supposed to undergo isovolumetric deformation when voids generation does not occur. Therefore, a volumetric strain differing from 0, yet positive can be attributed to the voids/cavitation[12,14]. The dimension evolution along z-axis (direction of thickness) could not be measured in real-time with the experiment setup available. However, by comparing the sample thicknesses in the undeformed and the 10th zero-stress state (measured in the necked region), the strain along z-axis after 10 cycles (the whole test) can be approximately obtained. The contraction (strain) along z-axis ε_{zz} (about -0.7 in every sample) is significantly different from that along the y-axis, ε_{yy}. This lateral anisotropy could be related to the compression-molding and different initial dimensions. The volumetric strain can be thus estimated using **equation (1)** below:

$$\frac{\Delta V}{V_0} = (1 + \varepsilon_{xx})(1 + \varepsilon_{yy})(1 + \varepsilon_{zz}) - 1 \tag{1}$$

To estimate the maximum local volumetric strain, the peak values of ε_{xx} and ε_{yy} are taken into account for this calculation. The results of the four materials are presented in **Figure 4** as a function of the crystallinity and a good correlation is observed between the maximum local volumetric strain and the microstructure of the samples.

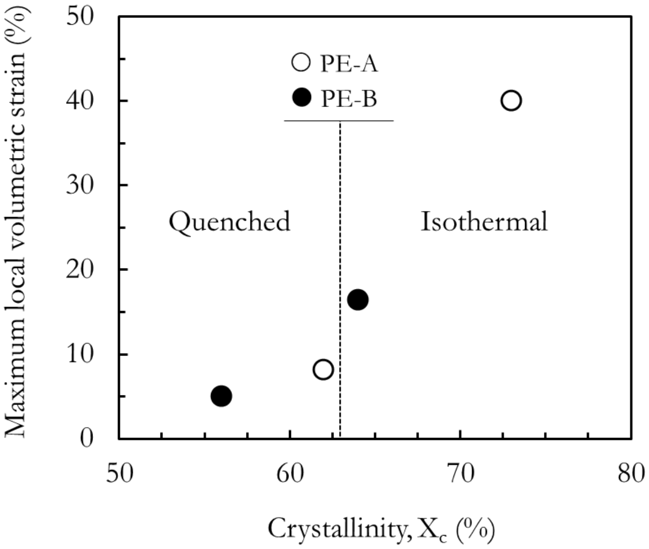

Figure 4: *Maximum local volumetric strain at the final zero-stress state as a function of sample crystallinity*

More precisely, the isothermal samples with higher crystallinity and lower ST density show a stronger volumetric variation after the same loading history, in particular, the PE-A one. Conversely, the two quenched samples show only slight volumetric variation (inferior to 10%). This dependency is in accordance with our previous conclusions drawn for volumetric fraction of cavities by *in-situ* SAXS characterizations, the cavitation in the quenched samples being limited[41].

5.4.2 Anisotropy in the necked region

Qualitative descriptions at macroscale

Although the mechanical/deformation behaviors undoubtedly differ with respect to the thermal treatment (as shown in **Figure 5**) and material type, in the following, the qualitative descriptions and discussions are mainly focused on the differences among the pristine, L- and T-necked samples of the same grade to highlight the changes and anisotropy induced by the oligo-cyclic loading. Only the results of PE-B samples are presented due to the similar qualitative observations for the PE-A samples.

The nominal stress-strain responses of the Pristine, L- and T-necked samples submitted to uniaxial elongation up to macroscopic strain ε=1.5 are presented in **Figure 5a**. They strongly differ in terms of nominal stress magnitude and profile. Different macroscopic deformation behaviors are also explored as the test proceeded by recording simultaneous 2D images of the samples using a CCD camera as illustrated in **Figure 5b and 5c** (PE-B samples). Four representative deformation states (ε=0, 0.15, 0.5, and 1) are presented for each sample. According to the results, the L-necked samples show limited necking and stress softening during elongation. However, both the pristine and T-necked samples present strain localization behaviors, especially the T-necked samples for which the width reduction is highly pronounced. Consequently, the nominal stress softening in T-necked samples is much more significant (the stress softening is about 45%-50%, taking the yield stress as the reference) than the pristine ones (20%-25%).

Due to the different strain localization (necking) levels until ε=1.5, the nominal stress values are not representative and comparable during this phase, it is worth considering the true stress instead. Taking into account the potential voids, especially for the pristine isothermal samples, the traditional isovolumetric assumption is not suitable for the true stress calculation. However, the failure stress can still be estimated in the vicinity of the failure/fracture point, where the section of specimen can be measured after the fracture in tensile test (the neck propagation is finished at this moment). The analysis of the failure true stress will be further discussed in the next section combined with the micro-mechanism.

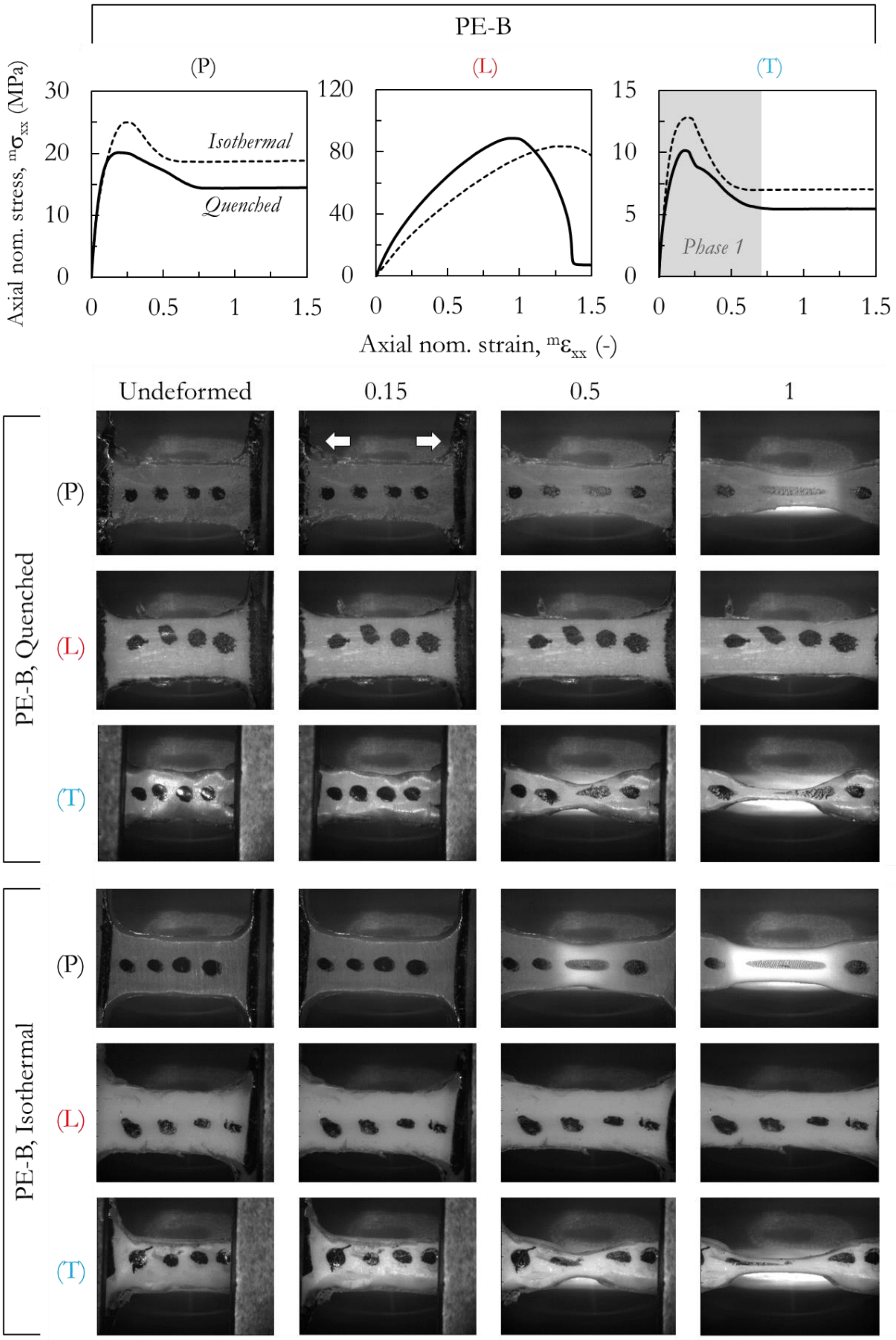

Figure 5: *Tensile nom. stress - nom. strain profiles in the pristine (P), L-necked (L) and T-necked (T) samples of PE-B materials (on top). Companion pictures of the specimen for four stages (on bottom).*

Quantitative analysis at microscale

At microscale, *in-situ* SAXS measurement allows coupling the macroscopic deformation behavior with the evolution of the material microstructure. The SAXS 2D patterns obtained for the same four deformation stages as the 2D sample images are presented in **Figure 6**.

Focusing on the pristine samples composed of the spherulites, they display the isotropic ring-shaped 2D SAXS patterns in the undeformed state, confirming the presence of randomly oriented lamellae in the spherulite, which are then progressively transformed to the *lobe-like* shapes indicating the fibrillary structure[31,32] with increasing macroscopic strain. The stronger scattering intensity in the center of the SAXS patterns suggests a pronounced cavitation phenomenon in the isothermal sample. It is in accordance with the macroscopic sample whitening observed in the necked region (see **Figure 5**). As for necked samples (L and T), the initial *lobe-like* patterns indicate that the microstructures of both quenched and isothermal samples have already transformed into the fibrillary structure during the oligo-cyclic pre-loading process. In the L-necked samples, the configuration of the SAXS pattern remains constant qualitatively, whereas, in the T-necked samples, a 90° re-orientation of the structures can be observed with increasing strain up to 1. The deformation behaviors of fibrillary structures in L- and T-necked samples can be quantitatively described based on the evolution of two microstructural dimensions: the long period and the average width of micro-fibrils.

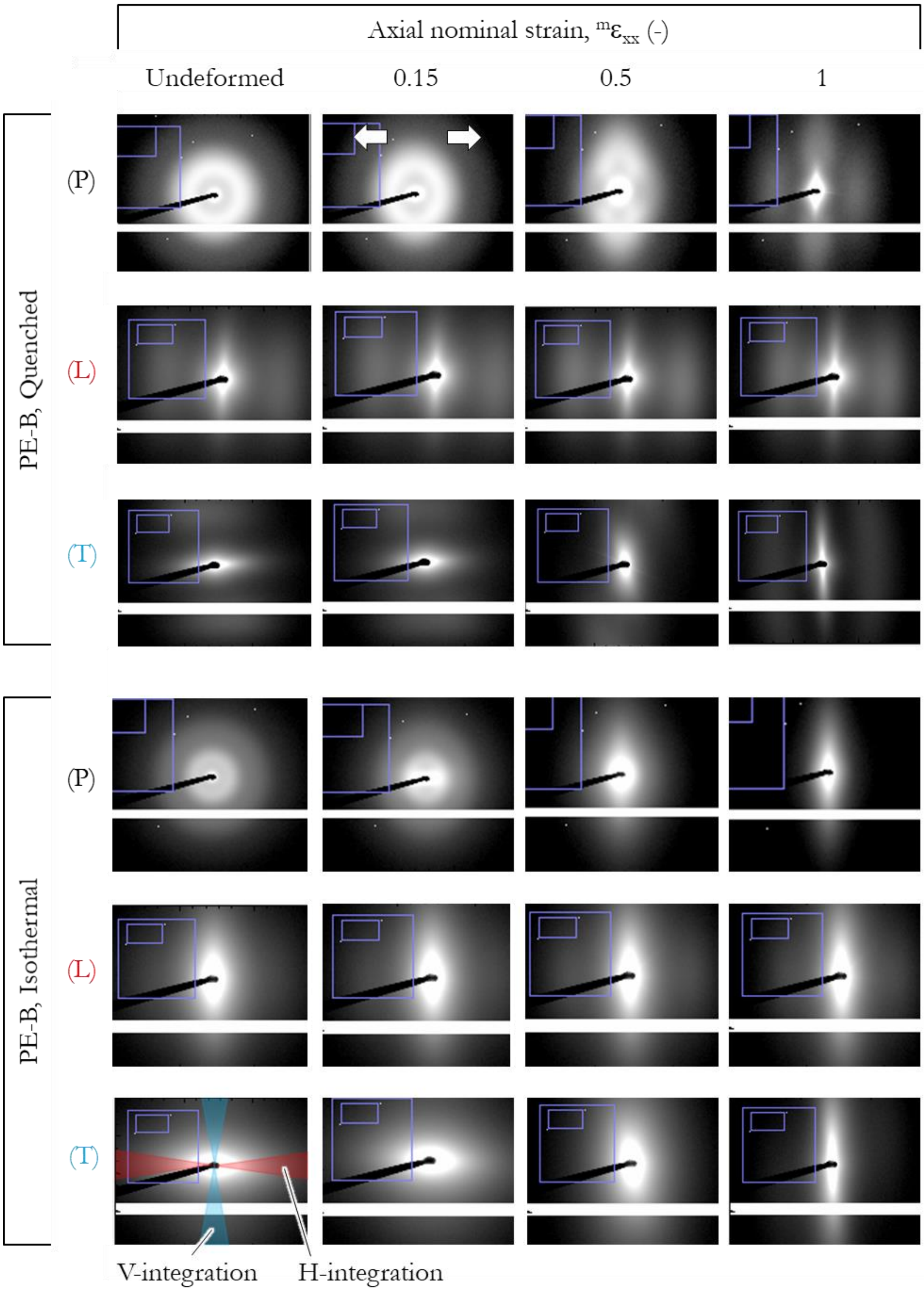

Figure 6: *Evolution of the SAXS patterns along with the deformation in Pristine (P), L-necked (L) and T-necked (T) PE-B samples.*

L-necked samples:

Firstly, the deformation behavior of the L-necked samples is analyzed, it is also compared with the behavior in pristine samples in the elastic regime.

For measuring local long periods, the azimuthal integrations within ±5° at horizontal (0°) and vertical (90°) regions of each SAXS pattern are conducted, they are denoted respectively as H- and V-integrations. Keeping in mind that the loading direction is "horizontal", the H and V regions of the SAXS pattern provide information of a subgroup of specifically orientated crystalline lamellae or blocks. Considering the PE-B quenched material as an example, the integrated *Lorentz-corrected* intensities (Iq^2) are plotted in **Figure 7** as a function of the norm of the scattering vector q.

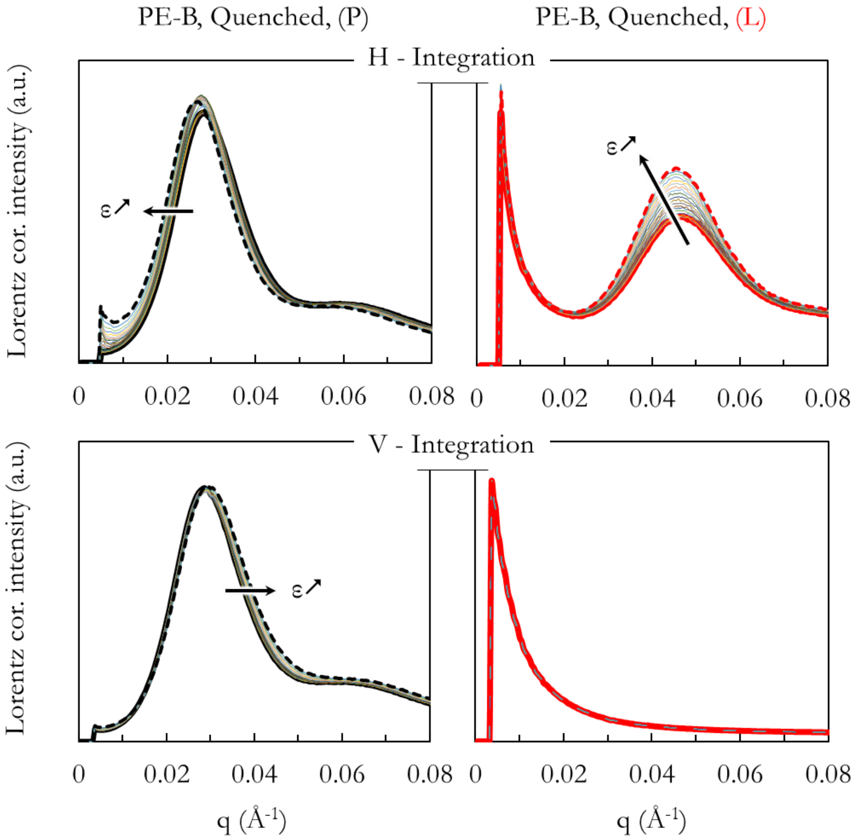

Figure 7: *Lorentz-corrected intensities (Iq^2) as a function of the norm of the scattering vector q in horizontal (H) and vertical (V) regions of the SAXS pattern for the Pristine (P) and L- necked (L) samples of the PE-B quenched material.*

The q-position of a scattering peak (q_{max}) allows calculating the long period with **equation (2).**

$$L_P = \frac{2\pi}{q_{max}} \tag{2}$$

For pristine materials (**Figure 7** left), spherulitic structure consists of randomly oriented lamellae so that the profiles are identical by H- and V- integrations prior to deformation. Under uniaxial elongation, the q_{max} values of the scattering peaks in the horizontal zone 0° and vertical zone 90° tend to be lower and higher respectively: the equatorial lamellae (corresponding to horizontal

SAXS zone) are subjected to tensile force and separate from one another, whereas the polar lamellae (corresponding to the vertical SAXS zone) get closer due to the Poisson's effect[42].

Focusing on the profiles obtained for the L-necked PE-B quenched sample (right in **Figure 7**) in the undeformed state, a scattering peak can only be observed by H-integration due to the orientation of the fibrils. At this stage, the long periods of the microfibrils (L_p^f) are listed in **Table 2** to compare with the long periods of pristine spherulitic structures (L_p^{sp}). For PE-A isothermal sample, L_p^f cannot be measured as the strong cavitation prohibits the observation of the scattering peak of lamellae. In other materials, it is found that $L_p^f < \mathrm{L}_p^{sp}$, and the smaller long period values in the L-necked samples than the pristine ones can be explicated by the melting-recrystallization or destruction-reconstruction [31,32] during fibrillary transformation. In details, the initial crystalline lamellae are fragmented and thinned due to the destruction and/or local melting whereas the small new crystalline bocks are created due to the strain-induced orientation of chains. Furthermore, L_p^f is seen to have limited dependency on the thermal treatment.

Table 2. Long periods of pristine samples and L-necked samples

	PE-A Quenched	PE-A Isothermal	PE-B Quenched	PE-B Isothermal
L_p^{sp} (nm)	22	35	20	33
L_p^f (nm)	15	-	13	13

Upon elongation, with increasing strain, the $q_{\max}$ value slightly decreases in the horizontal zone of SAXS pattern of the L-necked samples, indicating the same mechanism as the equatorial lamellae in the pristine samples. Due to the constant orientation of the crystalline structure, the evolution of $q_{\max}$ in the horizontal region along the deformation can be translated as the relative L_p^{sp} and L_p^f variations in order to calculate the local strain in the spherulitic equatorial and intra-fibrillary regions (marked in **Figure 8**) respectively using **equation (3)**. It is worth noting that this calculation is only adapted in the elastic regime (ε<0.05 is taken in this work).

$$\varepsilon_{\mathrm{local}}(\mathrm{t}) = \frac{\triangle \mathrm{L_p(t)}}{\mathrm{L_{po}}} = \frac{\mathrm{L_p(t)} - \mathrm{L_{po}}}{\mathrm{L_{po}}} \quad (3)$$

As shown in **Figure 8,** the local/macro strain ratios in equatorial/polar regions of pristine spherulites are about 0.4 ~ 0.5 and -0.25 ~ -0.17 respectively in all samples.

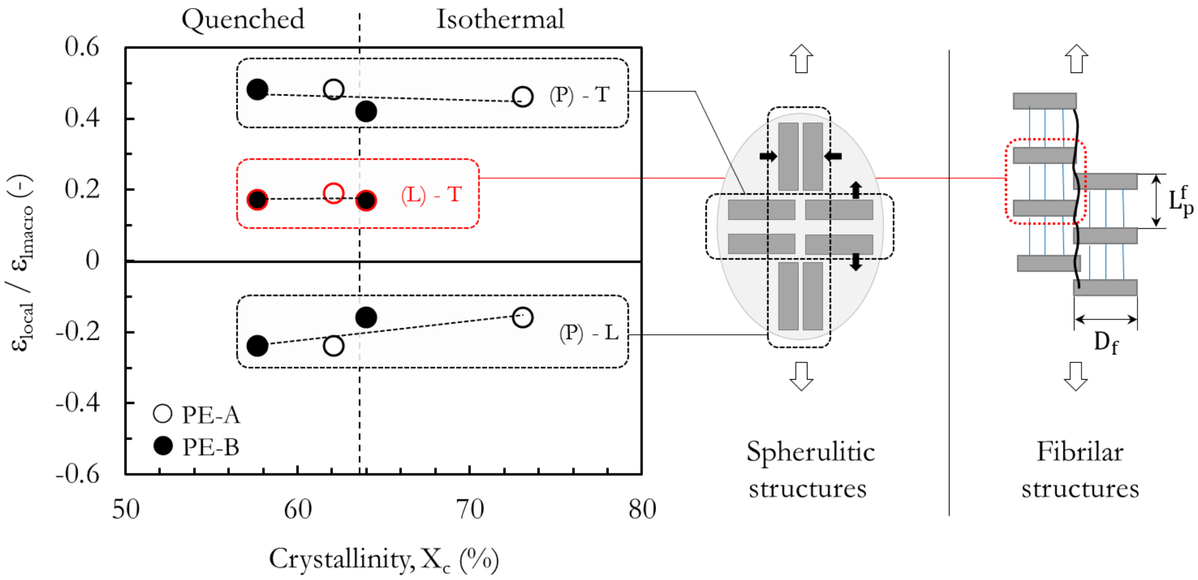

Figure 8: *Local/macro strain ratios in Pristine (P) and L-necked (L) samples.*

The low ratio (<1) at the equator is an evidence of the heterogeneous distribution of the stress triaxiality within the spherulitic structure[41,42]. The even lower local/macro strain ratio in the L-necked samples (about 0.17), suggests that the intra-fibrillary region should be more difficult to deform due to the stretched chains. The concept of the inter-fibrillary region is thus introduced. These chains are relatively more deformable than the intra-fibrillary ones along the pre-orientation. Thus, the macroscopic deformation of L-necked sample is mainly ascribed to the inter-fibrillary slide.

The measurement of the second microstructural parameter, the average width of micro-fibrils (D_f in **Figure 8** right) or crystalline blocks, is performed following a method proposed by Xiong et al.[26]. The scattering objects are assumed to be individually located in a medium of lower electron density without interference, D_f can thus be estimated by Guinier's law using a cylinder model (see **equation (4)**).

$$I(\mathrm{q}) = I_0 e^{\left(\frac{-q^2 R_g^2}{4}\right)} \qquad (4)$$

Where R_g is the radius of gyration, the width of the crystalline blocks D_f=2R_g. In this case, the integration is performed at the center of the scattering patterns (where $qR_g \ll 1$). The maximum deviation of D_f is 0.6 nm. It is worth noting that the variations of D_f during the tensile tests are all lower than the deviation value, indicating the stability of the crystalline width of micro-fibrils and suggesting that the fragmentation of lamellae can be neglected. In **Figure 9,** a correlation is found between the D_f and the stress transmitter density [ST] estimated by Brown's model: ST elements can generate the local stress concentration and induce the fragmentation of crystalline lamellae prior to the fibrillary transformation[31]. Therefore, with the higher ST concentration, the initial crystalline lamellae tend to be fragmented as the crystalline blocks with smaller width in the fibrillary state. Consequently, the tensile deformation of L-necked is mainly assigned to the inter-fibrillary slide, and no further fragmentation is observed.

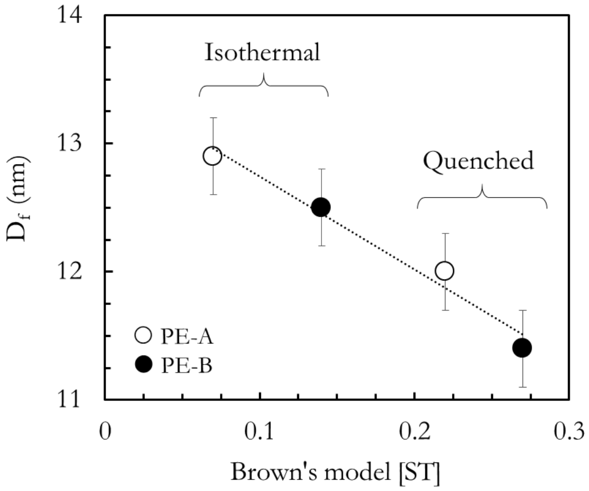

Figure 9: *Correlation between the width of micro-fibrils D_f and initial [ST] value estimated by Brown's model. D_f does not change during the tensile loading.*

T-necked samples:

For T-necked samples, the deformation behavior is quite different from the others: the gradual appearance and disappearance of scattering peaks can be observed respectively by H- and V-integrations with increasing strain (see **Figure 10a**). This evolution of pattern suggests a progressive 90° reorientation of crystalline blocks. The reorientation phase is finished approximately at the onset of the neck propagation (denoted as phase 1 in the mechanical profile, see **Figure 5**). **Figure 10b** displays the schematic of the reorientation of the crystalline blocks. Indeed, the inter-fibrillary chains not being confined should mainly contribute to the motion of crystalline blocks, and during this phase, the local deformation cannot be determined.

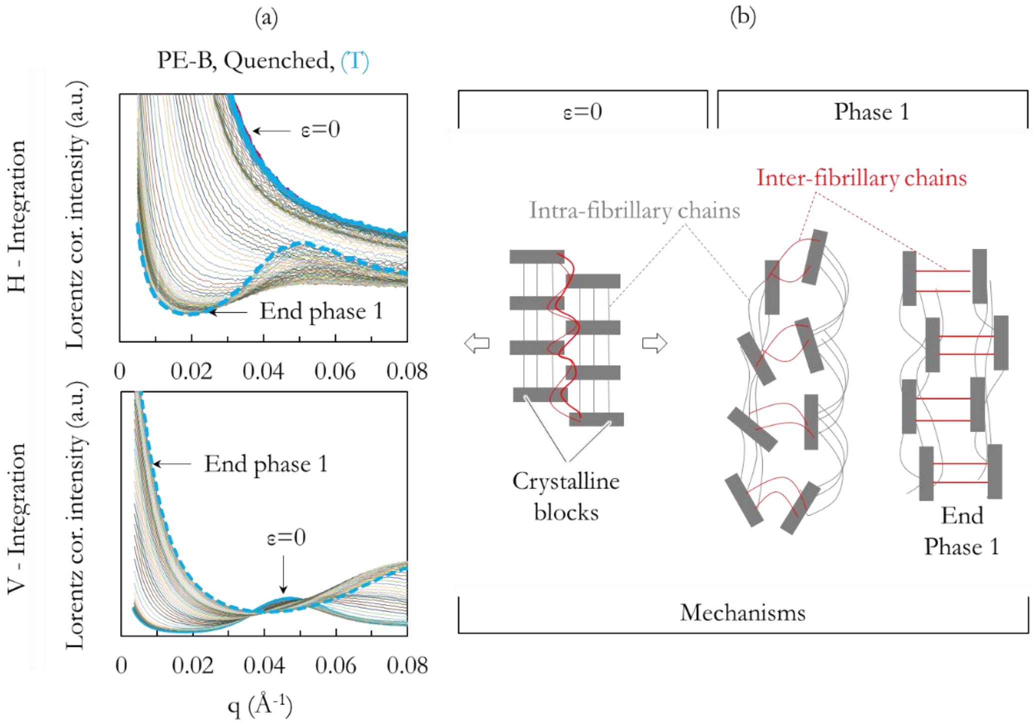

Figure 10: a) Lorentz-corrected intensities (Iq^2) as a function of the norm of the scattering vector q at horizontal and vertical zones of the SAXS pattern for the T-necked PE-B quenched sample; b) Schematic of the reorientation of crystalline blocks during the tensile deformation of T-necked samples.

However, during the neck propagation, which means that after the reorientation of the crystalline blocks, the configuration and dimension of the new fibrillary structure can be measured, as shown in **Table 3**, both the long period and width of crystalline blocks are stable before/after reorientation. According to these observations, it seems that the crystalline blocks only be rotated without measurable fragmentation during the necking initiation phase. Moreover, at the end of rotation, the same long period value suggests that the initial intra- and inter-fibrillary chains have the approaching ability of extension until being stretched.

Concludingly, the deformation of T-necked samples is also assigned to the inter-fibrillary chains. The final dimensions of the microfibrils after the reorientation is identical to the initial one before rotation.

Table 3. Long periods and average width of microfibrils before and after reorientation

	PE-A Quenched	PE-A Isothermal	PE-B Quenched	PE-B Isothermal
Before rotation: L_p^{f1} (nm)	15	-	13	13
After rotation: L_p^{f2} (nm)	14	-	13	13
Before rotation: D_f^{intra} (nm)	12	13	11	12
After rotation: D_f^2 (nm)	12	13	11	13

5.4.3 Failure properties of pristine, L-necked and T-necked samples

In the vicinity of fracture/failure point, the neck propagation is completed within the entire constant gauge of the sample so that the axial sample deformation is assumed to be homogenous. The specimens having the same initial geometry (value of thickness aside), so the difference in the ultimate failure stress between the pristine and necked samples are only related to the microstructural differences and potential damage.

Figure 11a gathers the true failure stress of the pristine and necked samples of the four materials under study as a function of the initial crystallinity. The black, red and blue symbols correspond to the pristine, L-necked, and T-necked samples respectively. Due to the appearance of the cavities, especially, in the isothermal samples, the final section of each specimen should be measured after the fracture in the nearby region, the traditional isovolumetric assumption is not adapted. Despite uncertainties (see the error bar in **Figure 11a**), several important observations are valuable to be discussed. First, the failure stresses of the pristine and L-necked samples are similar, it means that, except the first loading, the influence of the consecutive cycles on the failure stress is neglected. Moreover, for a given material, these values are mainly related to the material type (or molecular structure), the PE-A samples exhibit higher values. The thermal treatments show limited influence.

Variation of the failure stress between the pristine (or L-necked) and T-necked samples is also evaluated in each material. Only in the PE-A isothermal samples having the highest crystallinity and the lowest ST density, about 34% decrease of the failure stress is observed, indicating a significantly anisotropic failure stress of the fibrillary structure. However, this anisotropy in other pre-necked materials are limited.

Just before the failure, the stress is transmitted by the stretched STs: in the pristine and L-necked samples, the active stress transmitters are mainly in the intra-fibrillary region, whereas in the T-necked samples, the active stress transmitters are those in the initial inter-fibrillary region.

For a given material, it has been found that the final dimensions of the microfibrils (D_f and L_p^f) are similar in all the pristine and necked samples (no matter along which direction) thanks to *in-situ* SAXS characterization. Therefore, the different failure stresses should be related to the difference in the density/number of the active STs.

Regarding the PE-A isothermal material, the STs in the inter-fibrillary region should be much fewer than the intra-fibrillary STs. Indeed, for the PE who strongly cavitates, the voids are believed to be highly localized between the fibrillary structure, the assembly of the cavities and microfibrils is recognized as the craze[12] (see **Figure 11b**). The formation of craze is consistent with the heterogenous of ST distribution in the intra- and inter-fibrillary regions: fewer STs exist in the inter-fibrillary region. However, it is worth noting that, the cavitation is not the origin of the decrease of failure stress, but an associated phenomenon to the low amounts of STs.

Especially, for other samples with higher initial ST density (including the PE-B isothermal sample), after the cyclic pre-loading induced fibrillation, the ST distributions are almost homogenous in the intra- and inter- fibrillary regions (in accordance with the low cavity volume). Thus, the variation of stress and the anisotropy are both not obvious.

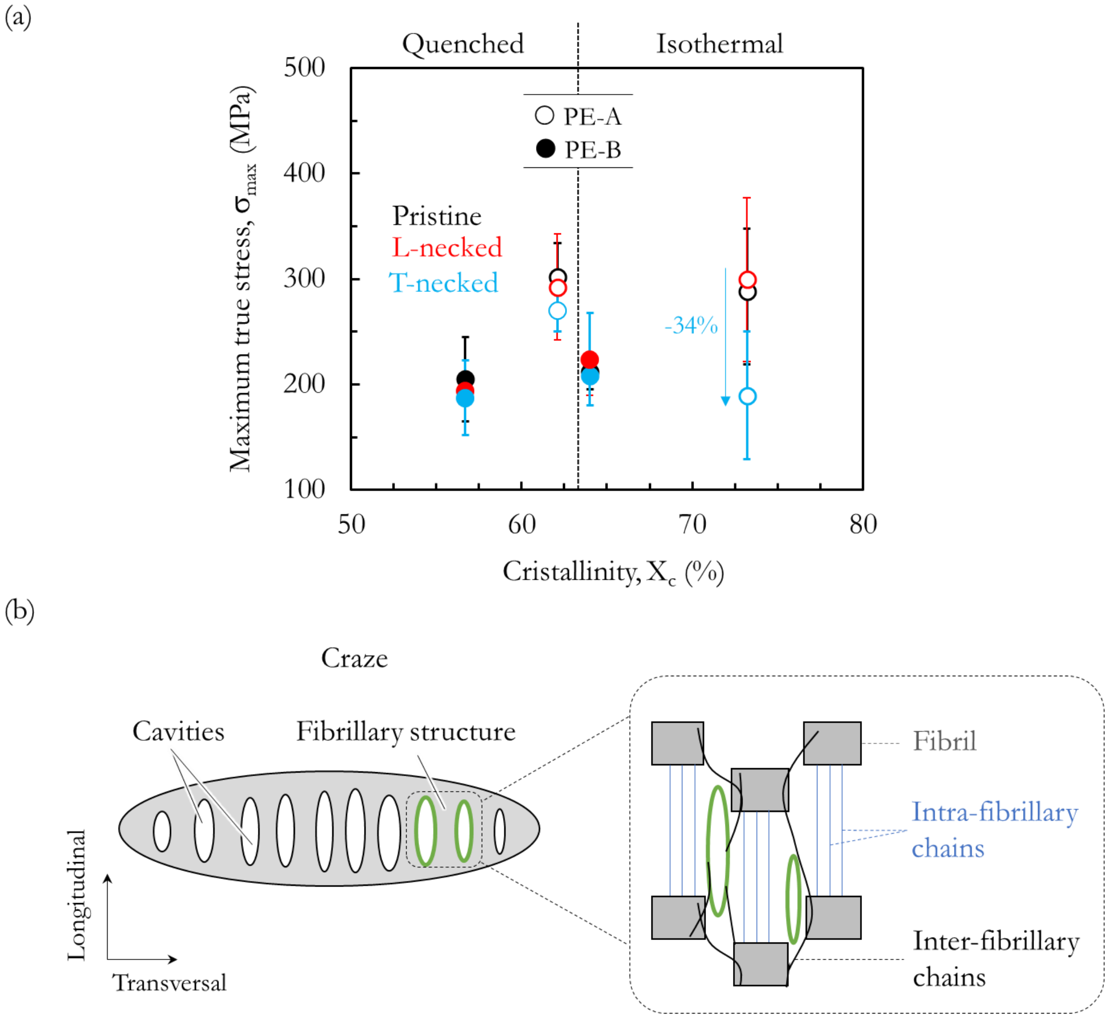

Figure 11: *a) Failure stress in different samples; b) schematic of craze and the heterogeneous ST distribution in the intra- and inter-fibrillary regions in PE-A isothermal sample who strongly cavitates.*

5.5 Conclusion

Being an important failure mode in semi-crystalline polymers, the evolution of necking during the mixed-mode oligo-cyclic deformation and the post-cyclic deformation behavior in the pre-necked HDPEs were investigated. According to the surface strain mappings generated by DIC, the local longitudinal strain (3.5 ~ 4.5) is much higher than the macroscopic one (1.5) in each material, indicating a remarkable strain localization (necking) initiated during the first loading. Moreover, the lateral reduction of dimension is more evident in the quenched samples with higher ST density. During the consecutive cycles, the strain accumulation is continually localized in the necked region, and mainly along the longitudinal direction, while the lateral contraction in the necked region remains almost constant. The maximum local volumetric strain after the 10th cycle depends on the microstructural properties. The quenched samples show limited volumetric variation whereas the two isothermal samples exhibit about 16% and 40% local variation (higher value for PE-A isothermal sample with higher crystallinity and less stress transmitters).

After being pre-loaded by oligo-cyclic deformation, the mechanical behaviors of the necked samples are strongly anisotropic due to the orientation of fibrillary structure. Along the chain orientation, stress transmitters in the intra-fibrillary region are stretched. The deformation mode is mainly related to the inter-fibrillary slide. In addition, along the transversal direction, the material is still deformable, the crystalline blocks are rotated thanks to the inter-fibrillary STs. Along both the orthogonal directions, the final microstructural dimension (long period and average width of microfibrils) remain identical. The true failure stress is thus associated with the ST distribution in the intra- and inter- fibrillary regions. Only in the PE-A isothermal samples, the STs in the inter-fibrillary region are fewer than in the intra-fibrillary region, this result is in accordance with the assumption that amounts of oriented cavities are located between the microfibrils. It is worth noting that the cavitation is not simply recognized as the origin of the decrease of failure stress (damage), but a symbol of important heterogeneity of ST distribution between the intra- and inter- fibrillary regions.

In the industrial application, although PE-A samples show stronger initial ultimate stress, the one of isothermal sample is significantly deteriorated (in particular, along the transverse direction) after the oligo-cyclic tests. However, the PE-B samples conceived for pipeline application (PE-100), show relatively better stability during the oligo-cyclic deformation in both quenched and isothermal samples. These results are helpful to confirm the good oligo-cyclic performance of PE-B materials, even under extreme crystallizing (isothermal) and cyclic (large strain) loading conditions, the most deformed part of the sample (necking) is still competent regarding the stress criterion.

Reference

(1) O. Hideki, H. Tomokazu. POLYETHYLENE PIPELINE PERFORMANCE AGAINST EARTHQUAKE; 2018.

(2) A. Masi, G. Santarsiero, D. Nigro. Cyclic Tests on External RC Beam-Column Joints: Role of Seismic Design Level and Axial Load Value on the Ultimate Capacity. *Journal of Earthquake Engineering* **2013**, *17* (1), 110–136.

(3) P. Cassese, P. Ricci, G. M. Verderame. Experimental Study on the Seismic Performance of Existing Reinforced Concrete Bridge Piers with Hollow Rectangular Section. *Engineering Structures* **2017**, *144*, 88–106.

(4) N. Nishonov, D. Bekmirzaev, E. An, Z. Urazmukhamedova, K. Turajonov, Behaviour and Calculation of Polymer Pipelines Under Real Earthquake Records. In *IOP Conference Series: Materials Science and Engineering*; IOP Publishing, 2020; Vol. 869, p 052076.

(5) L. Farge, J. Boisse, I. Bihannic, A. Diaz, S. André. Anisotropy Development during HDPE Necking Studied at the Microscale with in Situ Continuous 1D SAXS Scans. *Journal of Polymer Science Part B: Polymer Physics* **2018**, *56* (2), 170–181.

(6) R. Séguéla, On the Natural Draw Ratio of Semi-Crystalline Polymers: Review of the Mechanical, Physical and Molecular Aspects. *Macromolecular Materials and Engineering* **2007**, *292* (3), 235–244.

(7) S. Humbert; O. Lame; G. Vigier. Polyethylene Yielding Behaviour: What Is behind the Correlation between Yield Stress and Crystallinity? *Polymer* **2009**, *50* (15), 3755–3761.

(8) J. Ye, S. André, L. Farge, Kinematic Study of Necking in a Semi-Crystalline Polymer through 3D Digital Image Correlation. *International Journal of Solids and Structures* **2015**, *59*, 58–72.

(9) Z. Qi, N. Hu, D. Zeng, X. Su, Failure of High Density Polyethylene under Cyclic Loading: Mechanism Analysis and Mode Prediction. *International Journal of Mechanical Sciences* **2019**, *156*, 46–58.

(10) L. Laiarinandrasana, N. Selles, O. Klinkova, T. F. Morgeneyer, H. Proudhon, L. Helfen, Structural versus Microstructural Evolution of Semi-Crystalline Polymers during Necking under Tension: Influence of the Skin-Core Effects, the Relative Humidity and the Strain Rate. *Polymer Testing* **2016**, *55*, 297–309.

(11) B. Xiong; O. Lame; J. M. Chenal; C. Rochas; R. Seguela; G. Vigier. In-Situ SAXS Study and Modeling of the Cavitation/Crystal-Shear Competition in Semi-Crystalline Polymers: Influence of Temperature and Microstructure in Polyethylene. *Polymer* **2013**, *54* (20), 5408–5418.

(12) A. Pawlak; A. Galeski. Cavitation during Tensile Drawing of Annealed High Density Polyethylene. *Polymer* **2010**, *51* (24), 5771–5779.

(13) A. Pawlak, A. Galeski, A. Rozanski, Cavitation during Deformation of Semicrystalline Polymers. *Progress in polymer science* **2014**, *39* (5), 921–958.

(14) S. Humbert; O. Lame; J. M. Chenal; C. Rochas; G. Vigier. New Insight on Initiation of Cavitation in Semicrystalline Polymers: In-Situ SAXS Measurements. *Macromolecules* **2010**, *43* (17), 7212–7221.

(15) N. Selles, P. Cloetens, H. Proudhon, T. F. Morgeneyer, O. Klinkova, N. Saintier, L. Laiarinandrasana, Voiding Mechanisms in Deformed Polyamide 6 Observed at the Nanometric Scale. *Macromolecules* **2017**, *50* (11), 4372–4383.

(16) T. F. Morgeneyer, H. Proudhon, P. Cloetens, W. Ludwig, Q. Roirand, L. Laiarinandrasana, Maire, E. Nanovoid Morphology and Distribution in Deformed HDPE Studied by Magnified Synchrotron Radiation Holotomography. *Polymer* **2014**, *55* (25), 6439–6443.

(17) B. Xiong; O. Lame; J. M. Chenal; Y. Men; R. Seguela; G. Vigier. Critical Stress and Thermal Activation of Crystal Plasticity in Polyethylene: Influence of Crystal Microstructure and Chain Topology. *Polymer* **2017**, *118*, 192–200.

(18) Y. Men, *Critical Strains Determine the Tensile Deformation Mechanism in Semicrystalline Polymers*; ACS Publications, 2020.

(19) G. Capaccio, T. A. Crompton, I. M. Ward, Drawing Behavior of Linear Polyethylene. II. Effect of Draw Temperature and Molecular Weight on Draw Ratio and Modulus. *Journal of Polymer Science: Polymer Physics Edition* **1980**, *18* (2), 301–309.

(20) G. Meinel, A. Peterlin, Plastic Deformation of Polyethylene II. Change of Mechanical Properties during Drawing. *Journal of Polymer Science Part A-2: Polymer Physics* **1971**, *9* (1), 67–83.

(21) H. Guo, R. G. Rinaldi, S. Tayakout, M. Broudin, O. Lame, The Correlation between the Mixed-Mode Oligo-Cyclic Loading Induced Mechanical and Microstructure Changes in HDPE. *Polymer* **2021**, 123706. https://doi.org/10.1016/j.polymer.2021.123706.

(22) A. Chrysochoos, H. Louche, An Infrared Image Processing to Analyse the Calorific Effects Accompanying Strain Localisation. *International journal of engineering science* **2000**, *38* (16), 1759–1788.

(23) B. Guelorget, M. François, G. Montay, Strain Localization Band Width Evolution by Electronic Speckle Pattern Interferometry Strain Rate Measurement. *Scripta Materialia* **2009**, *60* (8), 647–650.

(24) X. Poulain, L. W. Kohlman, W. Binienda, G. D. Roberts, R. K. Goldberg, A. A. Benzerga, Determination of the Intrinsic Behavior of Polymers Using Digital Image Correlation Combined with Video-Monitored Testing. *International Journal of Solids and Structures* **2013**, *50* (11–12), 1869–1878.

(25) M. Uchida, N. Tada, Sequential Evaluation of Continuous Deformation Field of Semi-Crystalline Polymers during Tensile Deformation Accompanied by Neck Propagation. *International journal of plasticity* **2011**, *27* (12), 2085–2102.

(26) M. Andersen, O. S. Hopperstad, A. H. Clausen, Volumetric Strain Measurement of Polymeric Materials Subjected to Uniaxial Tension. *Strain* **2019**, *55* (4), e12314.

(27) A. Peterlin, Molecular Model of Drawing Polyethylene and Polypropylene. *Journal of materials science* **1971**, *6* (6), 490–508.

(28) F. Addiego; S. Patlazhan; K. Wang; S. André; Sigrid Bernstorff; David Ruch. Time-resolved Small-angle X-ray Scattering Study of Void Fraction Evolution in High-density Polyethylene during Stress Unloading and Strain Recovery. *Polymer International* **2015**, *64* (11), 1513–1521.

(29) F. Addiego, A. Dahoun; C. G'Sell; J. M. Hiver; O. Godard. Effect of Microstructure on Crazing Onset in Polyethylene under Tension. *Polymer Engineering & Science* **2009**, *49* (6), 1198–1205.

(30) H. H. Kausch, R. Gensler, C. Grein, C. J. G. Plummer, P. Scaramuzzino, Crazing in Semicrystalline Thermoplastics. *Journal of Macromolecular Science—Physics* **1999**, *38* (5–6), 803–815.

(31) S. Humbert, O. Lame, J. M. Chenal, R. Seguela, G. Vigier, Memory Effect of the Molecular Topology of Lamellar Polyethylene on the Strain-Induced Fibrillar Structure. *European polymer journal* **2012**, *48* (6), 1093–1100.

(32) B. Xiong; O. Lame; J. M. Chenal; C. Rochas; R. Seguela. On the Strain-Induced Fibrillar Microstructure of Polyethylene: Influence of Chemical Structure, Initial Morphology and Draw Temperature. *Express Polymer Letters* **2016**, *10* (4), 311.

(33) Z. Jiang, Y. Tang, J. Rieger, H. F. Enderle, D. Lilge, S. V. Roth, R. Gehrke, W. Heckmann, Y. Men, Two Lamellar to Fibrillar Transitions in the Tensile Deformation of High-Density Polyethylene. *Macromolecules* **2010**, *43* (10), 4727–4732.

(34) T. Deplancke, M. Fivel, O. Lame, 1D Strain Rate-Dependent Constitutive Model of UHMWPE: From Crystalline Network to Fibrillar Structure Behavior. *Mechanics of Materials* **2019**, *137*, 103129.

(35) R. P. Janssen, D. de Kanter, L. E. Govaert, H. E. Meijer, Fatigue Life Predictions for Glassy Polymers: A Constitutive Approach. *Macromolecules* **2008**, *41* (7), 2520–2530.

(36) R. P. Janssen; L. E. Govaert; H. E. Meijer. An Analytical Method to Predict Fatigue Life of Thermoplastics in Uniaxial Loading: Sensitivity to Wave Type, Frequency, and Stress Amplitude. *Macromolecules* **2008**, *41* (7), 2531–2540.

(37) S. Lampman, B. B. Sanders, N. Hrivnak, J. Kinson, C. Polakowski, Characterization and Failure Analysis of Plastics: ASM International. *Materials Park, OH, USA* **2003**.

(38) J. D. Hoffman, R. L. Miller, Kinetic of Crystallization from the Melt and Chain Folding in Polyethylene Fractions Revisited: Theory and Experiment. *Polymer* **1997**, *38* (13), 3151–3212.

(39) Y. L. Huang, N. Brown, The Effect of Molecular Weight on Slow Crack Growth in Linear Polyethylene Homopolymers. *Journal of materials science* **1988**, *23* (10), 3648–3655.

(40) Y. L. Huang, N. Brown, Dependence of Slow Crack Growth in Polyethylene on Butyl Branch Density: Morphology and Theory. *Journal of Polymer Science Part B: Polymer Physics* **1991**, *29* (1), 129–137.

(41) H. Guo, R. G. Rinaldi, S. Tayakout, M. Broudin, O. Lame, Characterization of the Spherulitic Deformation in Equatorial Region and Cavitation in HDPE Materials Submitted to Mixed-Mode Oligo-Cyclic Tensile Loading. Polymer testing 2021, 107208. https://doi.org/10.1016/j.polymertesting.2021.107208.

(42) B. Xiong, O. Lame, J. M. Chenal, C. Rochas, R.Seguela, G. Vigier. In-Situ SAXS Study of the Mesoscale Deformation of Polyethylene in the Pre-Yield Strain Domain: Influence of Microstructure and Temperature. *Polymer* **2014**, *55* (5), 1223–1227.

6 Estimation of amorphous modulus in the fibrillary HDPE materials induced by oligo-cyclic loading

6.1 Abstract

This chapter shows some complementary and preliminary results for Chapter 5. Nevertheless, it is also drafted as a research paper.

To estimate the resistance against an earthquake of HDPE materials with different microstructures, the pre- and post-oligo cyclic micro-mechanical characterizations are carried out thanks to tensile tests and simultaneous *in-situ* small- and wide- angle X-ray scattering (SAXS/WAXS) measurements. At microscale, the crystalline structure can be considered as stress gauges, the local stress estimation being based on both the displacement of the crystallographic planes measured by *in-situ* WAXS and the intrinsic properties of crystalline phase reported in the literature. For the spherulitic structure, the local stress distribution is heterogeneous: the polar region is submitted to a higher local stress ($2<\sigma_{local}/\sigma_{macro}<3.5$) than the equatorial region ($\sigma_{local}/\sigma_{macro}<1$). As for the fibrillary structure resulting from the oligo-cyclic pre-loading, even larger local-macro stress ratio ($5<\sigma_{local}/\sigma_{macro}<8$) suggests that the stress is strongly concentrated in the intra-fibrillary region. The pronounced stress heterogeneous distribution suggests the very high contrast of stiffness between intra- and inter-fibrillary regions. In the elastic regime, the apparent modulus of the amorphous phase in the prescribed regions can be estimated by taking into account the local strain evaluated by simultaneous *in-situ* SAXS measurements. The amorphous modulus was found to vary from 71-106 MPa in the equatorial region of spherulite to 2000-7000 MPa in the intra-fibrillary region. This variation indicates that the evolution of the amorphous chain topology can significantly alter its stiffness. In addition, the amorphous modulus was found to depend on both the prescribed thermal history (crystallization conditions) and the molecular structure (molecular weight), with the molecular structure having the major effect on the spherulitic/fibrillary amorphous modulus. Additionally, for a given grade, the quenched sample exhibits a higher value than the isothermal one.

6.2 Introduction

High-density polyethylene (HDPE) pipelines are widely used for the transportation of gas or water. As an example, in the nuclear plant, several institutes and organizations have used HDPE materials to replace traditional steel pipelines as a result of its low cost and good resistance against corrosion and earthquake[1–3]. In laboratory, a seismic event is commonly modeled by oligo-cyclic test, involving high level of imposed stress/strain and a limited number of cycles[4–8]. Despite complex setups and loading programs, the investigations mainly focus on the seismic response of the structures at macroscale. However, the microstructural characterizations are undoubtedly valuable, especially for the improvement of macro-micro constitutive modeling, damage assessment, and material design strategies accounting for the potential seismic effects and anticipating risk of fracture.

The micro-evaluations are generally carried out on a relatively simple loading mode e.g. the uniaxial tensile mode. Regarding the oligo-cyclic regime, the necking is recognized as a main manifestation of failure[9–11] in HDPE or other semi-crystalline polymers. In the already necked region, the HDPE is composed of oriented fibrillary structure, which differs from the initial spherulitic one in the undeformed state. This structural transformation includes not only the fragmentation of lamellae but also the evolution of the chain configurations manifested by the disentanglement, unfold, stretching, and orientation[12–16]. For predicting the post-cyclic constitutive relation of HDPE materials, and the post-cyclic mechanical properties. it is important to consider these microstructural evolutions, in particular, the changes of intrinsic properties in both crystalline and amorphous phases, as well as the mechanical coupling. Deplancke et al. proposed a 1D strain rate-dependent model for the fibrillary structure of polyethylene with ultra-high molecular weight[14]. In this model, the transformation from spherulitic to fibrillary structures is simulated by the variation of the mechanical coupling between the amorphous and crystalline phases. The spherulitic structure is modeled by an approach proposed by Humbert et al.[17] that is close to the Halpin's model[18]. The crystalline/amorphous stress ratio k is decreased to 1, coinciding with the *series-like (i.e. Reuss)* model, when the spherulites completely transform into fibrillary structures depicted as non-percolated crystalline blocks and amorphous chains.

Besides the mechanical coupling, the evolutions of the intrinsic properties of the two phases are also important features to account for. Due to the regular arrangement of the chains, the crystalline phase is known to exhibit anisotropic yet constant modulus, the values are reported in the literature [19–23]. On the contrary, the amorphous modulus varies and depends on the chain topology and configuration. Some authors also give the order of magnitude. In the molten state, the pre-existing stress transmitters (STs), namely the entanglements, loops and tie molecules, are preserved during the crystallization, so that the Young's modulus of purely amorphous PE is about 3-10MPa[24–27]. Several authors demonstrated that the structural confinement and the shape factor of the crystalline lamellae can result in the increase of the amorphous modulus. Using the Halpin's model to fit their data collected from mechanical tests at the macroscale, Boyd et al. for instance reported a shear modulus of 130-200 MPa as the temperature decreased from room temperature to 0°C[28]. Xiong et al. also reported that the structural confinement led to the increase of the amorphous modulus up to a maximum value of 300 MPa. The results were determined in the equatorial region of the spherulite on PE samples with crystallinity, $X_c = 50\%$, tested at room temperature. Furthermore, a monotonic drop of the modulus down to about 230 MPa with increasing crystallinity (80%) and to about 160 MPa with increasing temperature (100°C) were observed[27]. Based on their approach, the local strain and stress values were respectively measured by *in-situ* SAXS and WAXS characterizations[29–32].

The aforementioned works only focused on the modulus of the purely amorphous material[24-27] or the amorphous phase within the spherulite[27-28]. To our knowledge, few authors studied the amorphous modulus in the fibrillary state of the material. This value should be different and associated with the change of the chain topology as well as the potential rupture/disentanglement of chains. In our previous work[16], the existence of the highly oriented and stretched macromolecules was reported, especially the intra-fibrillary ones. The deformation along the chain pre-orientation is mainly assigned to the inter-fibrillary regions, and limited deformation tends to develop in the intra-fibrillary ones, suggesting significantly different stiffnesses/stress concentrations between these two regions. Moreover, the strain-induced rupture/disentanglement of chains could also induce the cavitation, highly localized in the necked region and oriented along the loading direction. These phenomena potentially contribute to the modulus reduction recognized as a symbol of material damage[33–35].

In this work, pre- and post-cyclic tensile tests with simultaneous *in-situ* SAXS/WAXS measurements are performed in two HDPE samples, one being widely used for pipeline application. The materials are subjected to different thermal histories to vary the range of pristine microstructures. The apparent amorphous modulus in the intra-fibrillary region of the samples pre-loaded by oligo-cyclic deformation is estimated and compared with the original amorphous modulus in the equatorial region of spherulite.

6.3 Experimental section

6.3.1 Sample molding with different thermal treatments

Two types of HDPE pellets were ordered from INEOS (Brussels, Belgium) and renamed as PE-A and PE-B respectively. PE-A is commonly for blow-molding, whereas PE-B is a commercial grade for PE-100 pipelines. The two materials initially available as pellets were compression-molded at about 180°C and 10MPa in an aluminum-alloy mold to form PE sheets of about 0.8mm thickness, two different crystallizing processes were then performed: quenching in the cold water and isothermal crystallization at a selected temperature in the vicinity of the crystallizing temperature as mentioned in our previous works[16,36]. Thanks to the great capacity of thermal transfer of the thin elements of the mold in contact with the polymer sheet free surfaces (about 1mm), significantly different crystallization regimes could be achieved.

6.3.2 Oligo-cyclic loading process

A dogbone-shaped sample cutter of 12mm length and 14mm width was used for punching the specimens from the shaped PE sheets (Figure 1). Oligo-cyclic tensile tests were performed to precondition the punched samples and somehow simulate a severe seismic event. The tests were performed on an MTS 1/ME machine equipped with 5KN load cell on mixed-mode[37] at a nominal strain rate 0.01 s^{-1}: each specimen was elongated up to a nominal strain 1.5 (coinciding with the neck propagation stage), and then retracted to zero force for 10 cycles. The pre-loaded samples were then relaxed at room temperature for about 1 month. Mini-samples were then punched from the necked region for further Differential scanning calorimetry (DSC) analysis and tensile tests coupled with *in-situ* SAXS/WAXS measurements, as described in the following sections.

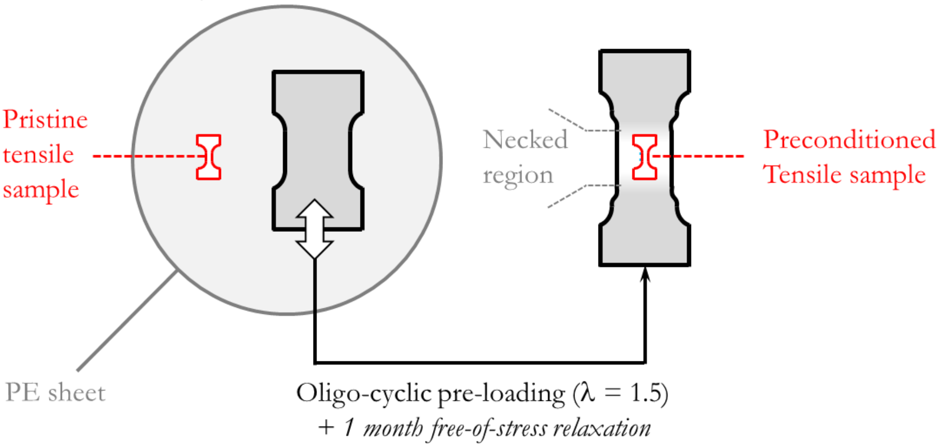

Figure 1: *Pristine and pre-loaded sample preparations*

6.3.3 Differential Scanning Calorimetry (DSC) measurements

Differential scanning calorimetry (DSC) tests were performed to evaluate the crystallinity (X_c) using equation (1). ΔH_f, the melting enthalpy, was measured as the peak area integrated above the baseline of the DSC curve, and ΔH_f^0 corresponds to the melting enthalpy of a theoretical 100% crystalline PE (290 J/mg[24])

$$X_c = \frac{\Delta H_f}{\Delta H_f^0} \tag{1}$$

The measurements were carried out using a DSC 7 PerkinElmer apparatus under nitrogen flow. About 6-8 mg samples were taken from the pristine PE sheets and the necked region of pre-loaded specimens, and then submitted to a thermal scan from room temperature up to 150°C at 10°C/min. Each test was repeated three times, so that the results correspond to the arithmetic average. Noticeably the standard deviation remained within ±1%.

6.3.4 Tensile tests with simultaneous SAXS/WAXS characterizations

As shown in **Figure 1**, for each material, two samples were prepared using a mini sample-cutter of 3.5 mm length and 2 mm width. Along with the one obtained from the necked region of the pre-loaded sample and already mentioned, one sample was directly punched from the pristine PE sheet so that the effect of the pre-loading could be studied. The tensile tests with simultaneous *in-situ* SAXS/WAXS measurements were performed on the SWING beamline of the SOLEIL synchrotron with a homemade mechanical apparatus. The nominal strain rate was set to 3×10^{-3} s^{-1}. The q-window is of 0.036-0.52 $Å^{-1}$ for SAXS observation. Long period (L_p) and thickness of crystalline lamellae (L_c) were calculated using relation (2) and (3) respectively:

$$L_P = \frac{2\pi}{q_{max}} \tag{2}$$

$$L_c = L_P \frac{\rho}{\rho_c} X_c \tag{3}$$

$$\frac{1}{\rho} = \frac{X_c}{\rho_c} + \frac{1-X_c}{\rho_a} \tag{4}$$

q_{max} corresponded to the norm of scattering vector at the peak of Gaussian-fitted Iq^2-q. ρ_a, and ρ_c are the amorphous phase (0.850 g/cm^3) and the crystalline phase (1.003 g/cm^3) densities respectively[38]. X_c is the crystallinity (measured by DSC). ρ designates the sample density, and was estimated by equation (4).

As a complementary analysis, a 3 × 3 cm^2 WAXS detector was positioned 109 mm from the sample to capture the scattering intensity within the q-window of 1.5-3.17 $Å^{-1}$. The time interval between two consecutive WAXS acquisitions was equal and synched with the SAXS and sample images acquisitions (3s). It is worth noting that unlike the SAXS pattern, the WAXS pattern is not complete and only the vertical zone was monitored.

6.4 Results and discussion

6.4.1 Pre- and post- cyclic microstructure characterizations

Table 1 summarizes the original molecular properties of HDPE pellets provided by supplier, and the microstructural characteristics of the HDPE materials processed by two thermal treatments in their pristine and deformed states (i.e. in the necked region of the pre-loaded specimens):
M_n, M_w and M_z are the number-average molar mass, the weight-average molar mass and z-average molar mass respectively. X_c is the crystallinity measured by DSC. L_p, L_c and L_a are the long period, thickness of the crystalline phase and amorphous phase respectively.
According to the SAXS results in the previous work[16], mini-samples punched from the necked region of pre-loaded samples can be approximately recognized as an anisotropic yet homogenous fibrillary structure material which differs from the spherulitic structure in the pristine samples. During the fibrillary transformation phase, a melting/recrystallization process is generally evoked in order to interpret the thinner crystallites and lower long period identified in the fibrillary state[12,13] compared to the pristine one. It is worth noting that the post-cyclic SAXS characterization of PE-A isothermal sample cannot be performed due to cavitation, the SAXS signal of the lamellae being prevented by the strong scattering intensity of the cavities. Regarding the crystallinity (with the deviation ±1%, the variation is less than 5% in absolute value), a slight decrease, increase of crystallinity is observed in PE-A isotherm and PE-B quenched samples

respectively (the two extreme materials). These variations can be interpreted as the imbalance between melting and recrystallization. Indeed, the lower crystallinity and higher density of stress transmitters should promote the stretching of chains in the amorphous phase and potentially induce more recrystallization[36].

Table 1. Molecular properties of HDPE pellets and pre- and post- cyclic and microstructural characteristics.

State	**Characteristics**	**Materials**			
		PE-A Quenched	**PE-A Isotherm**	**PE-B Quenched**	**PE-B Isotherm**
Original pellets	M_n (g/mol)	7500		6700	
	M_w (g/mol)	202200		270800	
	M_z (g/mol)	1478900		1589400	
Pre- cyclic (pristine/spherulitic)	X_c (%)	62	73	57	64
	L_p (nm)	22	35	20	33
	L_c (nm)	13	24	11	20
	L_a (nm)	9	11	9	13
Post- cyclic (pre-loaded/fibrillary)	X_c (%)	61	68	60	64
	L_p (nm)	15	-	13	13
	L_c (nm)	8	-	7	8
	L_a (nm)	7	-	6	5

6.4.2 Local stress estimation

Spherulite

Ahead of the quantitative analysis, several points need to be enounced:

(i) In the literature, the crystalline lamellae in the spherulite are twisted due to the surface stress and consecutive formation of screw dislocations[39–41]. However, the deformation of the twisted structure is too complex to evaluate, thus all the crystalline lamellae in this work are simplified as flat sheets.

(ii) As shown in **Figure 2**, the crystallographic strains along *a*, *b* and *c* axes should relate to the changes of the inter-planar distances of (200), (020), (002) respectively. They can be measured as the shift in q-values of designated WAXS scattering peaks.

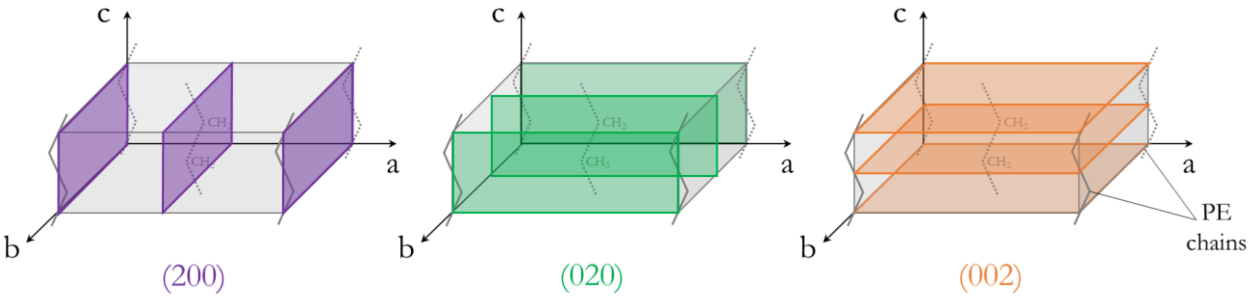

Figure 2: Illustration of prescribed planes in a PE crystal orthorhombic cell related to crystallographic strains along *a, b* and *c* axes.

Noticeably, the crystals exhibit large stiffness along the *c*-axis[19–21,23] so that the corresponding strain, or inter-planar distance change of (002), is too small to be characterized experimentally. Also, the intensity of this scattering peak is extremely low. Therefore, the experimental measurements can only be used for calculating the local strains along the *a* and *b* axes using equation (5) and (6) respectively.

$$\varepsilon_a^{crystalline} = \frac{\Delta d_{200}}{d_{200}^0} \tag{5}$$

$$\varepsilon_b^{crystalline} = \frac{\Delta d_{020}}{d_{020}^0} \tag{6}$$

Δd is the variation of inter-planar distance and d^0 is the initial inter-planar distance. Additionally, the strain along *c*-axis will be computed based on these two crystallographic strains, following a procedure that will be later detailed.

(iii) In this work, the structure of crystallographic planes having the normal vector parallel/perpendicular to the loading direction can be characterized in the H (Ψ=0°) and V (Ψ=90°) regions of the WAXS pattern respectively (the loading direction is horizontal). Ψ is assigned to the azimuthal angle (see the illustration of WAXS pattern in the right of **Figure 3**). In particular, the (200) and (020) plans corresponding to Zone V of the WAXS pattern are highlighted in the schematic of the spherulite in purple and green respectively (Figure 3 left).

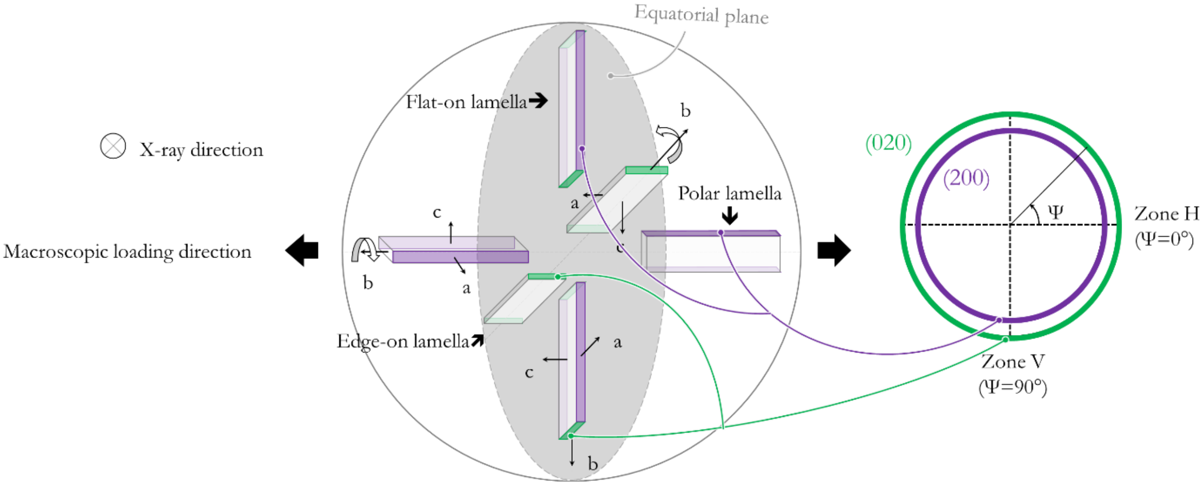

Figure 3: *Location of equatorial and polar lamellae in spherulite and identification of the WAXS scattering patterns.*

The formation of spherulites has been observed by microscopy technique[42,43], and the growth of the lamellae during the crystallization proceeds along the *b*-axis. Thus, for each lamella, the *b* axis corresponds to the radial direction. Yet, considering aforementioned point (iii), the following investigation focuses on the lamellae located in the equatorial and polar regions. In the polar region, the *b*-axis coincides with the tensile direction whereas *a* and *c* axes are perpendicular to the loading direction. In the equatorial region, the *b*-axis remains perpendicular to the loading direction whereas the *a* and *c* axes may form any admissible angle (from 0°-90°) with the loading direction. In particular, regarding *a*-axis, a 0° angle found for edge-on lamella and 90° angle refers to flat-on lamella. Thus, the X-ray scattered by (200) and (020) planes in Zone H correspond to edge-on and polar lamellae respectively. However, in Zone V, the X-ray scattered by plane (200) comes from both the flat-on and polar lamellae (it is worth noting that other locations may also contain the lamella, whose (200) plane is normal to the tensile direction). Also, the scattering information of the plane (020) corresponds to all the lamellae located in the equatorial region, suggesting that the spacing changes of planes (200) and (020) in Zone V correspond to average values. These averages are assumed to be representative of the lamellae under investigation (i.e. plane (200) of polar lamella and plane (020) of edge-on lamella).

In the elastic regime, the stress distribution in the equatorial region is assumed to be homogenous, which means that the axial stress (along the tensile direction) is the same for all the randomly oriented equatorial lamellae. Therefore, only the stress state of edge-on lamella is further analyzed. Indeed, for this type of lamella, the crystallographic strain along the a-axis is directly related to the local stress parallel to the macroscopic loading and can be measured experimentally (providing that the full 2D WAXS pattern is available). Also, assuming that the crystalline lamellae are located within the amorphous matrix. The great difference of the Poisson's ratio between the two phases can lead to the reciprocal stress inducing the contraction in the crystalline surfaces. This effect is determined by the shape factor: a larger surface can be contracted significantly. Therefore, the loading conditions of both the edge-on lamella in the equatorial region and polar lamella are close to the plane-stress assumption: the thickness of lamella is much lower than other two dimensions.

The calculation of the crystallographic strains using equation (5) and (6), requires the determination of the inter-planar distances at any time i, namely d_{200}^{i} and d_{020}^{i} which can be obtained by equations (7) and (8) respectively:

$$d_{200}^{i} = \frac{2\pi}{q_{200}^{i}} \tag{7}$$

$$d_{020}^{i} = \frac{2\pi}{q_{020}^{i}} \tag{8}$$

q_{200}^{i} and q_{020}^{i} correspond to the peak values of intensity scattered by (200) and (020) planes respectively. The shifts of the scattering peaks (200) and (020) in Zone V are shown in **Figure 4a** and **b** respectively**.**

As mentioned above, only the polar and edge-on lamella are concerned. Their axial local stresses are representative for the stress-state of the pole and equator of spherulite. According to the evolutions of scattering peaks at Zone V, due to the Poisson's effect, both d_{200} of polar lamella and d_{020} of edge-on equatorial lamella decrease. They are related to ε_a^{polar} and $\varepsilon_b^{equator}$ respectively.

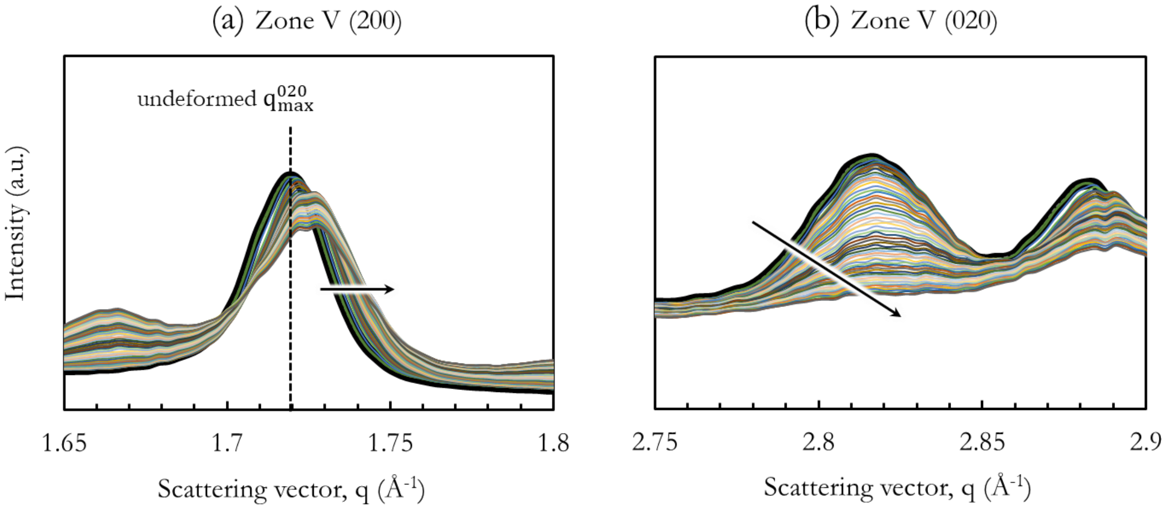

Figure 4*: Shift of WAXS peaks in Zone V under macroscopic tension (a) (200) peak; (b) (020) peak.*

As mentioned above, due to the experimental limitations, the information in Zone H are missing. Therefore, the $\varepsilon_a^{equator}$ and ε_b^{polar} cannot be directly measured. Nevertheless, two important ratio values in the literature should be raised as follow[30]: By using the same method to characterize the local stress. The authors reported that for these two types of lamella in a series of polyethylene with different microstructures and crystallinities, $\frac{-\varepsilon_b^{equator}}{\varepsilon_a^{equator}}$=1.2 and $\frac{-\varepsilon_b^{polar}}{\varepsilon_a^{polar}}$=0.38. According to this result, the $\varepsilon_a^{equator}$ and ε_b^{polar} can be deduced. In the work of Choy et al.[23], the axial stresses can be calculated using the following equation (9).

$$\begin{bmatrix}\sigma_a\\ \sigma_b\\ \sigma_c\\ \tau_{ab}\\ \tau_{ac}\\ \tau_{bc}\end{bmatrix}=\begin{bmatrix}7 & 3.8 & 4.7 & 0 & 0 & 0\\ 3.8 & 7 & 3.8 & 0 & 0 & 0\\ 4.7 & 3.8 & 81 & 0 & 0 & 0\\ 0 & 0 & 0 & 1.6 & 0 & 0\\ 0 & 0 & 0 & 0 & 1.6 & 0\\ 0 & 0 & 0 & 0 & 0 & 1.6\end{bmatrix}\begin{bmatrix}\varepsilon_a\\ \varepsilon_b\\ \varepsilon_c\\ \gamma_{ab}\\ \gamma_{ac}\\ \gamma_{bc}\end{bmatrix} \qquad (9)$$

The local stress components to be estimated in this work are the ones colinear with the macroscopic tensile force so that macro-micro correlations can be attempted. Therefore, only the σ_b^{polar} and $\sigma_a^{equator}$ are evaluated. They are plotted in **Figure 5** as a function of the macroscopic strain and compared with the nominal macroscopic stress.

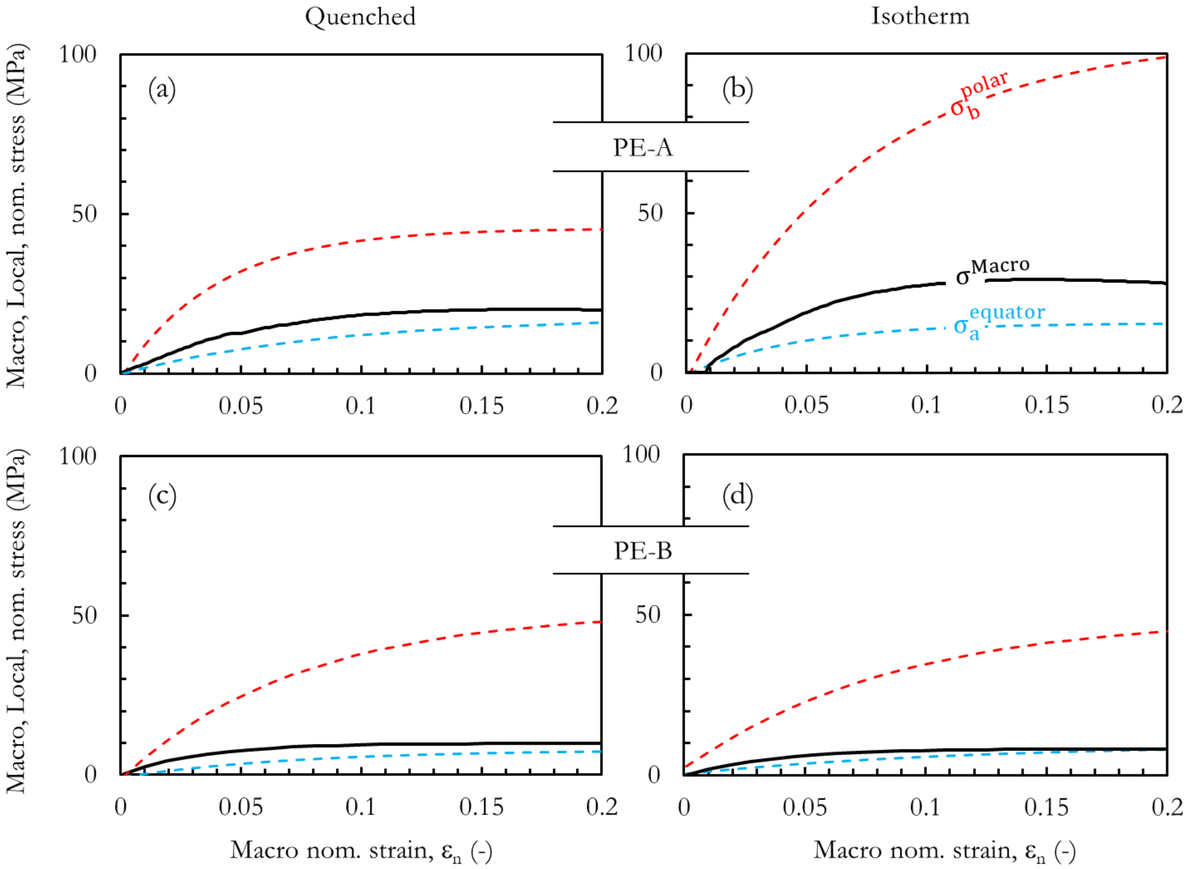

Figure 5: *Macro and local stresses in (a) PE-A Quenched, (b) PE-A Isotherm, (c) PE-B Quenched and (d) PE-B Isotherm samples.*

The data are fitted by the Levenberg–Marquardt relation, and the focus is paid on the onset of the elastic regime (for macroscopic strain ε≤0.01), where the shearing of crystallites should not occur. Clearly, in all four samples, the local stress in the polar region along the tensile direction is much higher than the macroscopic stress, whereas the local stress in the equatorial region is similar to (slightly smaller than) the macroscopic one.

Fibrillary structure

As for the samples punched within the necked region induced by cyclic loading, their microstructures are fibrillar[16]. The initial crystalline lamellae in the spherulite were fragmented and orientated, and the chain orientation is now mainly parallel to the loading direction. The crystalline structure in fibrillary structure is not a "lamella" but a "block" separated by inter- and intra- fibrillary regions (see **Figure 6**). As a consequence of the chain orientation, the *c*-axis is along the pre-loading direction so that the planes (200) and (020) can be only detected in Zone V of the WAXS pattern. Also, only the local stress in the intra-fibrillary region can be estimated. It can be assumed that the dimensions along *a* and *b* axes are similar to each other in crystalline blocks. Regarding equation (9), this assumption is equivalent to $\sigma_a=\sigma_b$. Also, with ε_a and ε_b being experimentally measured, σ_c can then be deduced.

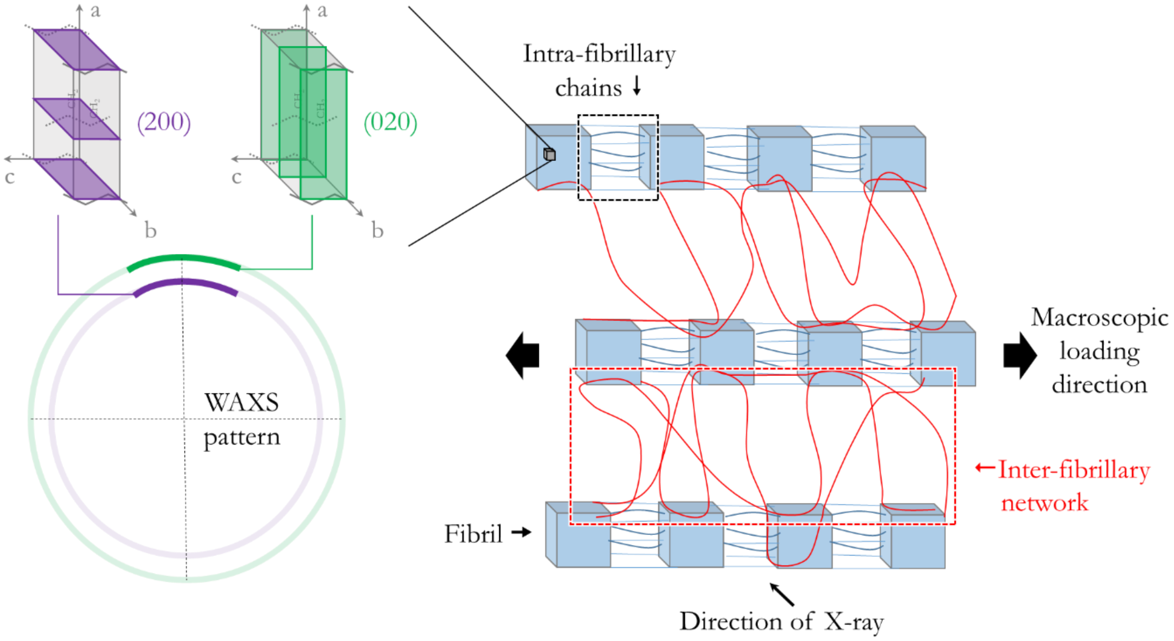

Figure 6: *Fibrillary structure in HDPE and corresponding location onto the WAXS pattern.*

Although the fragmentation of lamellae and martensitic transformation may potentially occur in the necked region during the pre-loading, there is no work indicating that these phenomena are related to any change of the intrinsic properties of the crystalline phase. Therefore, in this work, it is assumed that the intrinsic elastic properties of the crystalline structures in both pristine (spherulite) and preconditioned (fibrillary) HDPE materials are constant. This assumption suggests that the intrinsic parameters of the crystalline phase shown in equation (9) are still available in the fibrillary structure and the local stress calculated. The local and macro stresses are displayed in **Figure 7**. The local stress in the intra-fibrillary region is much higher than the macroscopic axial stress within the spherulite.

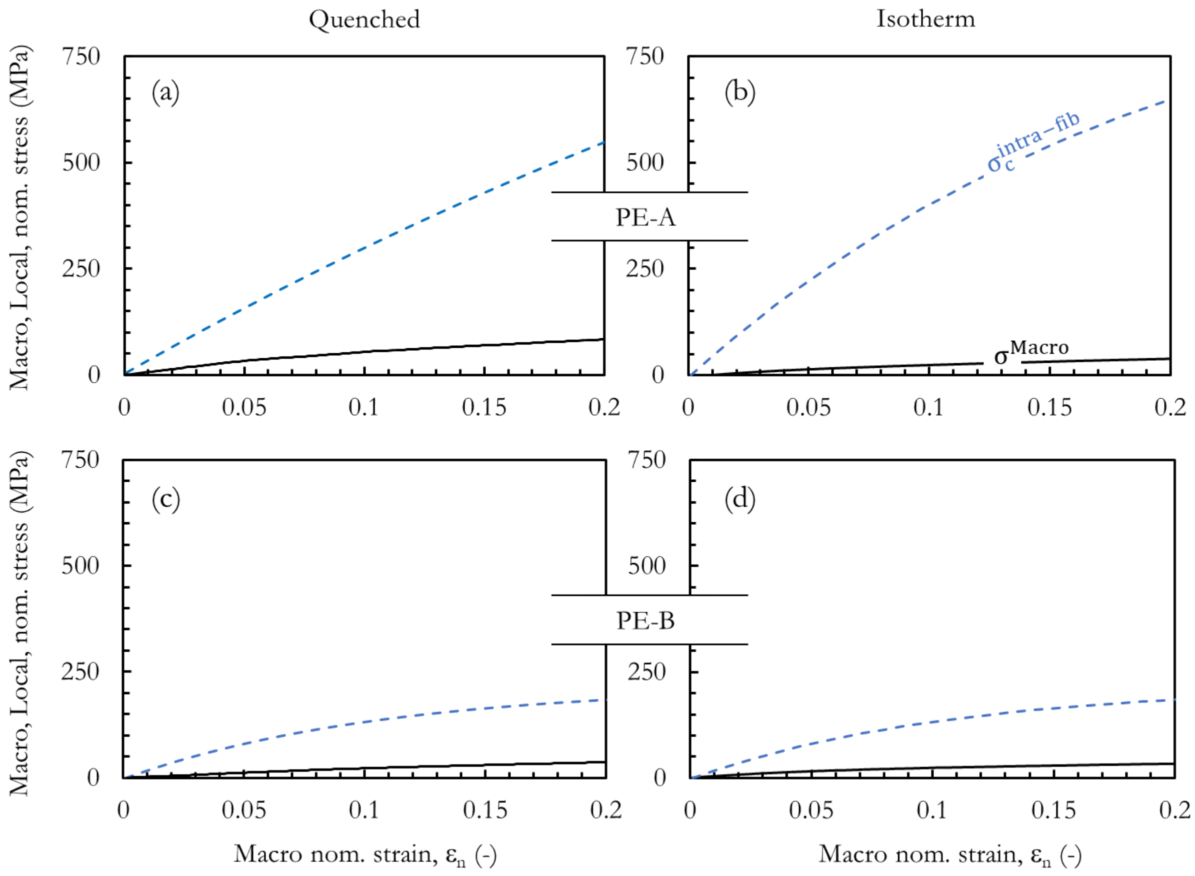

Figure 7: *Macro and local stresses in fibrillary structure of (a) PE-A Quenched, (b) PE-A Isotherm, (c) PE-B Quenched and (d) PE-B Isotherm samples.*

Local-macro stress relationship

In **Figure 8** presenting the local/macro stress ratio ($\sigma_{local}/\sigma_{macro}$) as a function of the pristine material crystallinity, X_c, a higher $\sigma_{local}/\sigma_{macro}$ value is found in the polar region of spherulite than in the equatorial region, indicating a heterogeneous mechanical coupling within the spherulite[30]. As for fibrillary structure, an even higher $\sigma_{local}/\sigma_{macro}$ value in the intra-fibrillary region was found suggesting a pronounced stress concentration. In addition, the stiffness contrast between the intra- and inter- fibrillary regions are even stronger than that between the polar and equatorial regions of spherulite. Moreover, for each material, a higher value is observed in the isothermal sample. Two interpretations can be attempted: on the one hand, this dependency can be ascribed to a more confined structure due to the higher crystallinity and larger crystalline blocks. On the other hand, the inter-fibrillary structure in the isothermal samples may contain more cavities, thus a weaker ability to transmit the stress and a higher contrast between these two regions.

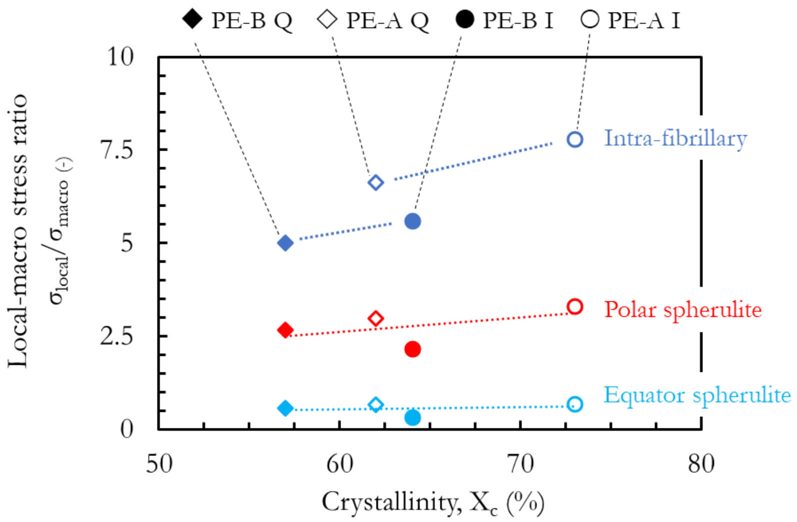

Figure 8: *Local-macro stress ratio in the different regions and samples.*

6.4.3 Amorphous modulus estimation

Under uniaxial loading conditions, the local amorphous modulus can be estimated as the ratio between local stress and local strain in the amorphous phase. A particular attention is paid to the spherulitic equator and intra-fibrillary regions. Indeed, the amorphous phases of these two regions are subjected to elongation along the macroscopic tensile direction. The local axial stress in the amorphous phase should be identical to the one in the crystalline phase. Moreover, the local axial strain in amorphous phase can be computed as the relative variation of L_a (see equation 10). It is worth noting that at the onset of the elastic strain, the variation of the long period could be approximately assigned to the amorphous phase alone (see equation 11).

$$\varepsilon_{amorphous}^{equator/intra-fib} = \frac{\Delta L_a}{L_a} \tag{10}$$

$$\Delta L_a = \Delta L_p \tag{11}$$

In our previous work[16], the local/macro strain relations in the elastic regime in the equatorial region of spherulite ($\varepsilon_{local}^{equator}/\varepsilon_{macro}$) and intra-fibrillary regions ($\varepsilon_{local}^{\text{intra-fibrillary}}/\varepsilon_{macro}$) have been evaluated by *in-situ* SAXS measurements. It is worth noting than these local strains are considered equivalent to the relative variation of L_p, $\varepsilon_{local}=\Delta L_p/L_p$. These important results are quoted as shown in **Figure 9.**

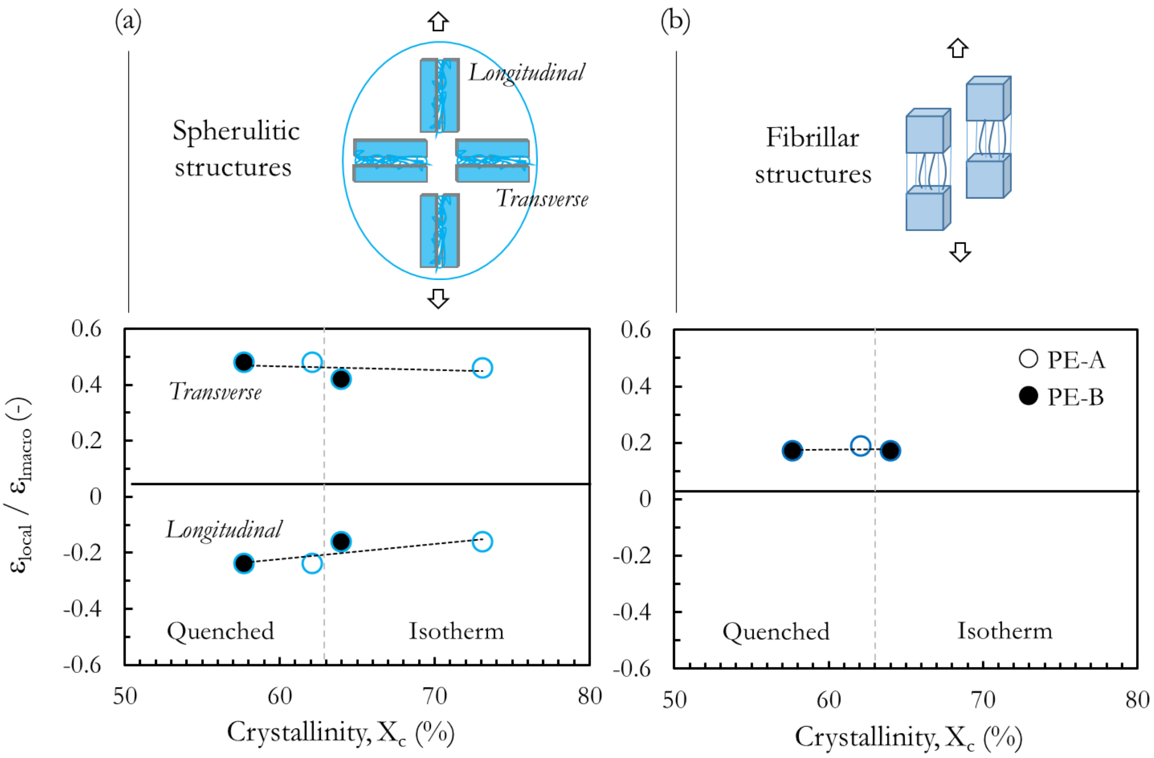

Figure 9: *local/macro strain ratios in pristine and pre-loaded samples*[16].

As evoked already, the local strain in the pre-loaded PE-A isotherm sample is not measurable because of the strong intensity scattered by cavities. However, due to the quasi-constant relation found in other studied materials, the local-macro strain value can be also supposed to be about 0.17. Under this assumption, the local strain in the amorphous phase, $\varepsilon_{amorphous}$ can be straightforwardly estimated.

All in all, the estimation of the local stress and strain in the elastic regime obtained by simultaneous *in-situ* SAXS/WAXS measurements, allow for the computation of the local apparent modulus in each sample (see **Figure 10**).

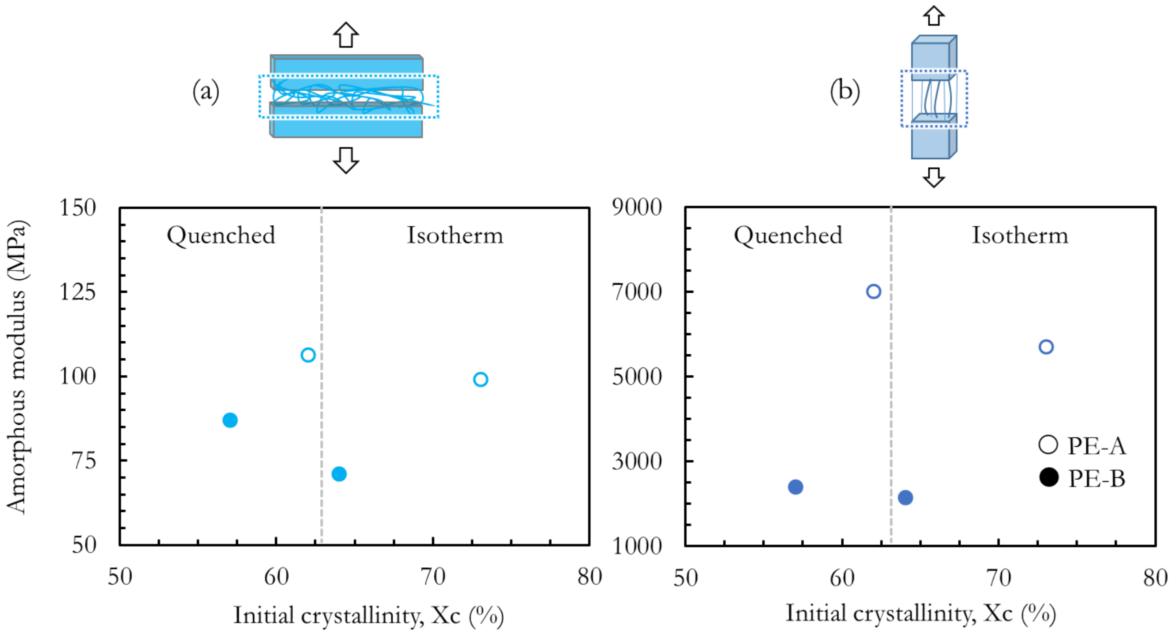

Figure 10: *(a) Amorphous modulus in equatorial region of spherulite in the pristine samples; (b) Amorphous modulus in the intra-fibrillary region in the pre-loaded samples.*

Figure 10a displays the amorphous modulus in the equatorial region of spherulite in the pristine samples and the values are seen to vary from 71 MPa to 106 MPa. These values are very similar to the order of magnitude reported in the literature[27,28]. It is reasonable to state that they are much higher than the modulus values estimated in the purely amorphous polyethylene due to the structural confinement caused by the crystalline lamellae[25,26,38]. Regarding the amorphous modulus of the intra-fibrillary region (see **Figure 10b**), the values vary from 2000 MPa to 7000 MPa. This surprising increase by an order of magnitude should be related to the chain orientation and possible strain-induced recrystallization. According to the DSC results, this strain-induced recrystallization during the fibrillary transformation just slightly influences the crystallinity, however, the lower long period values of the fibrillary structure indicates that the stretched amorphous chains are effectively confined between two neighboring crystalline blocks. Thus, this enhancement of structural confinement may largely contribute to the increase of the amorphous modulus. In addition, the increase of stiffness also indicates that the rupture of chains/disentanglement, might not occur in this region or just play a much weaker effect than the chains orientation on the amorphous modulus.

Also, it seems that in both the spherulitic and fibrillary structures, the material type (or the initial molecular characteristic/structure) exhibits a major influence on the amorphous modulus. In particular, for the intra-fibrillary amorphous modulus, the PE-A materials (about 6000-7000 MPa) are significantly different from the PE-B materials (about 2000 MPa). This dependency may be assigned to the shape factor of crystalline lamellae/blocks or geometry of the microfibrils. As for the same grade, the amorphous modulus of these two regions are always higher in the quenched samples. This dependency can be associated to the higher density of stress transmitters in the pristine material which most likely remained in the pre-loaded microfibrils[44–46].

6.5 Conclusion

In HDPE materials, the initial spherulitic structure transform into a fibrillary structure after being submitted to a mixed-mode oligo-cyclic deformation (maximum macroscopic strain ε_{max}=1.5). The post-cyclic macro- and micro-characterizations are important to evaluate the HDPE materials properties potentially submitted to a severe earthquake. Simultaneous *in-situ* SAXS/WAXS techniques allow estimating the micro-macro stress relations and amorphous modulus in each sample. As for spherulitic structure of pristine samples, the local stress distribution is heterogeneous, it suggests that the local stress is more concentrated in the polar region than equatorial region and different mechanical couplings in these two regions. As for the fibrillary structure, the heterogeneity of local stress distribution is even stronger between the intra- and inter- fibrillary regions. The stiffness contrast in the two regions of fibrillary structure should be more significant. A surprising increase of amorphous modulus is found from the equatorial region of spherulite to intra-fibrillary region due to the chain orientation and potential strain-induced recrystallization. When the stress transmitters are confined between the equatorial lamellae, the apparent amorphous modulus is about 71-106 MPa. The order of magnitude of amorphous modulus can be improved to 2000-7000 MPa in the intra-fibrillary region when the chain is stretched, the strain-induced recrystallization can also lead to the decrease of long period, the smaller and more stretched amorphous segmentations are thus confined between the crystalline blocks and should increase the local modulus. Although the potential disentanglement, rupture of chains may compete with the effect of chain orientation and recrystallization on the amorphous modulus, it seems that in the intra-fibrillary region, the final intrinsic properties is dominated by the strengthening effect. However, it is hard to evaluate the situation in the inter-fibrillary region.

Finally yet importantly, in the fibrillary state, it seems that both the amorphous modulus and local stress distribution are mainly dependent on the molecular structure (or material type). The thermal treatments have less important effects on these micro-mechanical properties. However, regarding the same grade, with the isothermal treatment, the larger crystalline blocks (both width and thickness) can also slightly increase the local stress concentration, and the amorphous modulus is relatively lower in these samples because of a lower quantity of stress transmitters.

Reference

(1) Haddad, A. N. Modern Bimodal High-Density Polyethylene for the Nuclear Power Plant Piping System. In *International Conference on Nuclear Engineering*; 2009; Vol. 43543, pp 213–218.

(2) Kim, Y. S.; Yoon, J. K.; Kim, Y. H. Analysis of ASME Class 3 Buried HDPE Piping Systems Related to Code Case N-755-1. In *Pressure Vessels and Piping Conference*; American Society of Mechanical Engineers, 2013; Vol. 55676, p V003T03A011.

(3) Zheng, J.; Hou, D.; Guo, W.; Miao, X.; Zhou, Y.; Shi, J. Ultrasonic Inspection of Electrofusion Joints of Large Polyethylene Pipes in Nuclear Power Plants. *J. Press. Vessel Technol.* **2016**, *138* (6).

(4) Angelo Masi; Giuseppe Santarsiero; Domenico Nigro. Cyclic Tests on External RC Beam-Column Joints: Role of Seismic Design Level and Axial Load Value on the Ultimate Capacity. *J. Earthq. Eng.* **2013**, *17* (1), 110–136.

(5) Paolino Cassese; Paolo Ricci; Gerardo M. Verderame. Experimental Study on the Seismic Performance of Existing Reinforced Concrete Bridge Piers with Hollow Rectangular Section. *Eng. Struct.* **2017**, *144*, 88–106.

(6) Vincent Ji; Yong-Gang Zhang; Chang-Qi Chen. The Non-Destructive Estimation of the Superficial Mechanical Properties of Components in the INCONEL 600 Alloy by X-Ray Diffraction Peak Width. *Surf. Coat. Technol.* **2000**, *130* (1), 95–99.

(7) Nishonov, N.; Bekmirzaev, D.; An, E.; Urazmukhamedova, Z.; Turajonov, K. Behaviour and Calculation of Polymer Pipelines Under Real Earthquake Records. In *IOP Conference Series: Materials Science and Engineering*; IOP Publishing, 2020; Vol. 869, p 052076.

(8) Shi, J.; Hu, A.; Yu, F.; Cui, Y.; Yang, R.; Zheng, J. Finite Element Analysis of High-Density Polyethylene Pipe in Pipe Gallery of Nuclear Power Plants. *Nucl. Eng. Technol.* **2020**.

(9) Roel PM Janssen; Leon E. Govaert; Han EH Meijer. An Analytical Method to Predict Fatigue Life of Thermoplastics in Uniaxial Loading: Sensitivity to Wave Type, Frequency, and Stress Amplitude. *Macromolecules* **2008**, *41* (7), 2531–2540.

(10) Janssen, R. P.; de Kanter, D.; Govaert, L. E.; Meijer, H. E. Fatigue Life Predictions for Glassy Polymers: A Constitutive Approach. *Macromolecules* **2008**, *41* (7), 2520–2530.

(11) Qi, Z.; Hu, N.; Zeng, D.; Su, X. Failure of High Density Polyethylene under Cyclic Loading: Mechanism Analysis and Mode Prediction. *Int. J. Mech. Sci.* **2019**, *156*, 46–58.

(12) B. Xiong; O. Lame; J. M. Chenal; C. Rochas; Roland Seguela. On the Strain-Induced Fibrillar Microstructure of Polyethylene: Influence of Chemical Structure, Initial Morphology and Draw Temperature. *Express Polym. Lett.* **2016**, *10* (4), 311.

(13) Humbert, S.; Lame, O.; Chenal, J.-M.; Seguela, R.; Vigier, G. Memory Effect of the Molecular Topology of Lamellar Polyethylene on the Strain-Induced Fibrillar Structure. *Eur. Polym. J.* **2012**, *48* (6), 1093–1100.

(14) Deplancke, T.; Fivel, M.; Lame, O. 1D Strain Rate-Dependent Constitutive Model of UHMWPE: From Crystalline Network to Fibrillar Structure Behavior. *Mech. Mater.* **2019**, *137*, 103129.

(15) Jiang, Z.; Tang, Y.; Rieger, J.; Enderle, H.-F.; Lilge, D.; Roth, S. V.; Gehrke, R.; Heckmann, W.; Men, Y. Two Lamellar to Fibrillar Transitions in the Tensile Deformation of High-Density Polyethylene. *Macromolecules* **2010**, *43* (10), 4727–4732.

(16) Guo, H.; Rinaldi, R.; Tayakout, S.; Broudin, M.; Lame, O. Strain Localization in HDPEs during Oligo-Cyclic Deformation and Anisotropic Deformation behaviors in Necked Region. *under review*.

(17) Humbert, S.; Lame, O.; Séguéla, R.; Vigier, G. A Re-Examination of the Elastic Modulus Dependence on Crystallinity in Semi-Crystalline Polymers. *Polymer* **2011**, *52* (21), 4899–4909.

(18) Affdl, J. H.; Kardos, J. L. The Halpin-Tsai Equations: A Review. *Polym. Eng. Sci.* **1976**, *16* (5), 344–352.

(19) Satcurada, I.; Ito, T.; Nakamae, K. Elastic Moduli of the Crystal Lattices of Polymers. In *Journal of Polymer Science Part C: Polymer Symposia*; Wiley Online Library, 1967; Vol. 15, pp 75–91.

(20) Strobl, G. R.; Eckel, R. A Raman Spectroscopic Determination of the Interlamellar Forces in Crystalline N-alkanes and of the Limiting Elastic Modulus Ec of Polyethylene. *J. Polym. Sci. Polym. Phys. Ed.* **1976**, *14* (5), 913–920.

(21) Holliday, L. The Stiffness of Polymers in Relation to Their Structure. In *Structure and properties of oriented polymers*; Springer, 1975; pp 242–263.

(22) Lacks, D. J.; Rutledge, G. C. Simulation of the Temperature Dependence of Mechanical Properties of Polyethylene. *J. Phys. Chem.* **1994**, *98* (4), 1222–1231.

(23) Choy, C. L.; Leung, W. P. Elastic Moduli of Ultradrawn Polyethylene. *J. Polym. Sci. Polym. Phys. Ed.* **1985**, *23* (9), 1759–1780.

(24) Crist, B.; Fisher, C. J.; Howard, P. R. Mechanical Properties of Model Polyethylenes: Tensile Elastic Modulus and Yield Stress. *Macromolecules* **1989**, *22* (4), 1709–1718.

(25) Krigas, T. M.; Carella, J. M.; Struglinski, M. J.; Crist, B.; Graessley, W. W.; Schilling, F. C. Model Copolymers of Ethylene with Butene-1 Made by Hydrogenation of Polybutadiene: Chemical Composition and Selected Physical Properties. *J. Polym. Sci. Polym. Phys. Ed.* **1985**, *23* (3), 509–520.

(26) Liu, C.; He, J.; Van Ruymbeke, E.; Keunings, R.; Bailly, C. Evaluation of Different Methods for the Determination of the Plateau Modulus and the Entanglement Molecular Weight. *Polymer* **2006**, *47* (13), 4461–4479.

(27) Xiong, B.; Lame, O.; Chenal, J.-M.; Rochas, C.; Seguela, R.; Vigier, G. Amorphous Phase Modulus and Micro–Macro Scale Relationship in Polyethylene via in Situ SAXS and WAXS. *Macromolecules* **2015**, *48* (7), 2149–2160.

(28) Boyd, R. H. The Modulus of the Amorphous Component in Polyethylenes. *Polym. Eng. Sci.* **1979**, *19* (14), 1010–1016.

(29) Bijin Xiong; Olivier Lame; Jean-Marc Chenal; Yongfeng Men; Roland Seguela; Gerard Vigier. Critical Stress and Thermal Activation of Crystal Plasticity in Polyethylene: Influence of Crystal Microstructure and Chain Topology. *Polymer* **2017**, *118*, 192–200.

(30) Xiong, B.; Lame, O.; Seguela, R.; Men, Y. Micro/Macro-Stress Relationship and Local Stress Distribution in Polyethylene Spherulites upon Uniaxial Stretching in the Small Strain Domain. *Polymer* **2018**, *140*, 215–224.

(31) Bijin Xiong; Olivier Lame; Jean-Marc Chenal; Cyrille Rochas; Roland Seguela; Gerard Vigier. In-Situ SAXS Study of the Mesoscale Deformation of Polyethylene in the Pre-Yield Strain Domain: Influence of Microstructure and Temperature. *Polymer* **2014**, *55* (5), 1223–1227.

(32) Séverine Humbert; Olivier Lame; Jean-Marc Chenal; Cyrille Rochas; Gérard Vigier. Small Strain Behavior of Polyethylene: In Situ SAXS Measurements. *J. Polym. Sci. Part B Polym. Phys.* **2010**, *48* (13), 1535–1542.

(33) Drozdov, A. D. Cyclic Strengthening of Polypropylene under Strain-Controlled Loading. *Mater. Sci. Eng. A* **2011**, *528* (29–30), 8781–8789.

(34) Pawlak, A.; Galeski, A.; Rozanski, A. Cavitation during Deformation of Semicrystalline Polymers. *Prog. Polym. Sci.* **2014**, *39* (5), 921–958.
(35) Frédéric Addiego; Stanislav Patlazhan; Kui Wang; Stéphane André; Sigrid Bernstorff; David Ruch. Time-resolved Small-angle X-ray Scattering Study of Void Fraction Evolution in High-density Polyethylene during Stress Unloading and Strain Recovery. *Polym. Int.* **2015**, *64* (11), 1513–1521.
(36) Guo, H.; Rinaldi, R.; Tayakout, S.; Broudin, M.; Lame, O. The Correlation between the Mixed-Mode Oligo-Cyclic Loading Induced Mechanical/Microstructure Evolutions in HDPE. *under review*.
(37) A. D. Drozdov. Mullins' Effect in Semicrystalline Polymers. *Int. J. Solids Struct.* **2009**, *46* (18–19), 3336–3345.
(38) Buckley Crist; Christopher J. Fisher; Paul R. Howard. Mechanical Properties of Model Polyethylenes: Tensile Elastic Modulus and Yield Stress. *Macromolecules* **1989**, *22* (4), 1709–1718.
(39) Xu, J.; Guo, B.-H.; Zhang, Z.-M.; Zhou, J.-J.; Jiang, Y.; Yan, S.; Li, L.; Wu, Q.; Chen, G.-Q.; Schultz, J. M. Direct AFM Observation of Crystal Twisting and Organization in Banded Spherulites of Chiral Poly (3-Hydroxybutyrate-Co-3-Hydroxyhexanoate). *Macromolecules* **2004**, *37* (11), 4118–4123.
(40) Fujiwara, Y. The Superstructure of Melt-crystallized Polyethylene. I. Screwlike Orientation of Unit Cell in Polyethylene Spherulites with Periodic Extinction Rings. *J. Appl. Polym. Sci.* **1960**, *4* (10), 10–15.
(41) Keith, H. D.; Padden Jr, F. J.; Vadimsky, R. G. Intercrystalline Links in Polyethylene Crystallized from the Melt. *J. Polym. Sci. Part A-2 Polym. Phys.* **1966**, *4* (2), 267–281.
(42) Strobl, G. Crystallization and Melting of Bulk Polymers: New Observations, Conclusions and a Thermodynamic Scheme. *Prog. Polym. Sci.* **2006**, *31* (4), 398–442.
(43) Bassett, D. C. Polymer Spherulites: A Modern Assessment. *J. Macromol. Sci. Part B* **2003**, *42* (2), 227–256.
(44) Xiong, B. Contribution to the Study of Elastic and Plastic Deformation Mechanisms of Polyethylene and Polypropylene as a Function of Microstructure and Temperature, Lyon, INSA, 2014.
(45) Yeh, J. T.; Runt, J. Fatigue Crack Propagation in High-density Polyethylene. *J. Polym. Sci. Part B Polym. Phys.* **1991**, *29* (3), 371–388.
(46) Seguela, R. Critical Review of the Molecular Topology of Semicrystalline Polymers: The Origin and Assessment of Intercrystalline Tie Molecules and Chain Entanglements. *J. Polym. Sci. Part B Polym. Phys.* **2005**, *43* (14), 1729–1748.

General conclusions

The thesis aims at studying the mechanical/microstructure evolutions, especially the potential damage induced by seismic events in the industrial HDPE pipes. Two HDPE materials are under investigation, one is for blow-molding whereas another is designed for commercial PE-100 pipelines (denoted as PE-B). The industrial pipe contains a heterogenous microstructure due to the thermal gradient during the molding. Therefore, for the sample preparation of each grade, two different thermal treatments (quenching and isothermal treatment) are applied so that a wide range of microstructures could be obtained.

In the literature, the damage is determined as the deterioration of material properties (such as modulus, stress, and toughness, etc.), they are also believed to be related to several structural deteriorations such as disentanglement/chain rupture, cavitation, and fragmentation of lamellae/percolation. Therefore, in this work, we tried to evaluate both the mechanical/microstructure changes under oligo-cyclic loading conditions (that simulates the seismic signal) and establish the macro-micro correlation.

Under mixed-mode oligo-cyclic loading conditions, the fragmentation of lamellae is induced in all the samples whereas the cavitation is only obvious in those isothermal samples. These microstructure evolutions are characterized by *in-situ* SAXS measurement. The results suggest that higher crystallinity and lower density of stress transmitters (STs) including the entanglements, tie molecules, and tie loops, promote the generation of cavities. Both of them obey the initiation-accumulation-saturation with increasing cycles. However, regarding the mechanical indicators (stress, modulus, and toughness), the modulus is even possible to increase after the oligo-cyclic loading despite the presence of the *so-called* structural deteriorations. Thus, it can be deduced that a compensating mechanism must exist, this mechanism is related to the chain orientation/recrystallization. Indeed, by tensile tests coupled with the simultaneous in-situ SAXS/WAXS measurement, we found that the intra-fibrillary amorphous region is much stiffer than the original equatorial amorphous region thanks to the stretching of STs. Therefore, due to the co-existence of this competing mechanism, it is unfair to indicate that the material is damaged simply by the appearance of the structural changes in the plastic regime. Moreover, under certain loading conditions, although the decrease of modulus can be found, and more important in the samples with higher crystallinity and lower ST density. Some pre-loaded samples still require almost the same energy to rupture as the pristine ones. This result suggests that the modulus decrease might be insufficient to determine the damage in HDPE materials. The reversibility of the modulus change remains to be further investigated. Also, although all the materials exhibit stress softening, it seems that this mechanical loss is not permanent, this effect of the cyclic loading (after the first one) has totally vanished upon additional loading when the imposed strain is higher than the maximum strain previously experienced by the sample. It means that the consecutive cycles (following the first one) do not influence the further short-term stress level of material.

For a given grade, only when the imposed cyclic strain is very high (DIC spatial measurements evidenced that the maximum local axial strain within the necked section is about 3-4), the structural and mechanical deteriorations are correlated with each other in the PE-A isothermal sample. Thus, this material pre-loaded by oligo-cyclic deformation can be determined as damaged. This damage (deterioration of failure stress) is anisotropic, which is mainly along the transversal direction. The quenched samples exhibit not only limited volume change but also constant failure properties before and after the oligo-cyclic pre-loading. It seems that the higher ST density in these samples induces the stronger resistance against the seismic damage.

Compared to another material, after the same processing, the one for PE-100 (PE-B) shows lower crystallinity, and thus lower overall modulus, yield stress, and even toughness. However, regarding the PE-A and PE-B isothermal samples, we found that the PE-B exhibits a much stronger resistance against the cavitation and mechanical deteriorations so that it confirms the good seismic performance of PE-100 material. According to the aforementioned macro- and micro- characterizations, this great property can be attributed to the relatively higher ST density in PE-B.

Perspectives

Some concepts deserve to be deepened:

1. (1) The results presented in the manuscript are all obtained at room temperature. That being said and according to the industrial requirements, the influence of the testing temperature (from -10°C up to 60°C) are valuable to be investigated. Some in-situ SAXS/WAXS tests are already carried out. The results are still under treatment and analysis.
2. (2) When the cycle number is inferior to 100, it seems that the first few cycles show the most important influences on the tensile properties. However, it is also interesting to investigate the influences of both the first few cycles and the saturated ones on the long-term (such as creep and fatigue) properties. ultimately, the evaluation of the lifetime of pre-loaded materials is of importance
3. (3) The macro-micro correlations are discussed only upon uniaxial tensile loading. Now considering a real earthquake, the pipelines will undoubtedly experience a complex (3D) loading mode. for instance, coupled tension, compression, and shearing can be envisioned. Therefore, these correlations need to be deepened by taking into account the different loading modes.
4. (4) The experimental results are valuable ingredients for the development of constitutive modeling. The consideration / integration of these microstructure evolutions and potential damage in the modeling is a key challenge for future studies.

FOLIO ADMINISTRATIF

THESE DE L’UNIVERSITE DE LYON OPEREE AU SEIN DE L’INSA LYON

NOM : GUO

DATE de SOUTENANCE : 25/03/2021

Prénoms : Hang

TITRE : Evaluation des propriétés mécaniques et de l’endommagement de polyéthylènes soumis à des sollicitations oligo-cycliques en relation avec leurs microstructures

NATURE : Doctorat

Numéro d'ordre : 2021LYSEI020

Ecole doctorale : ED34 Matériaux

Spécialité : Matériaux

RESUME : En tant que représentant de la polyoléfine, le polyéthylène (PE) est l'un des thermoplastiques les plus populaires appliqués dans divers domaines industriels en raison de sa excellente performance mécanique. En particulier, en tant que matériau utilisé dans les systèmes de tuyauterie, le polyéthylène haute densité (PEHD) présente une grande résistance sismique.

En général, les tests oligo-cycliques consistant en un processus de chargement-déchargement répété et plastique, sont mis en place pour simuler des événements sismiques, et ainsi étudier les performances sismiques du matériau. Les performances mécaniques sont fortement liées à la microstructure et à la morphologie du PE.

Cette recherche vise à étudier les origines de la bonne résistance sismique des matériaux PEHD, les points d'investigation suivants sont principalement concernés : 1) les évolutions mécaniques et microstructurales y compris l'endommagement lors de la déformation oligo-cyclique. Et la corrélation macro-micro. 2) L'influence de la microstructure et de la morphologie du PEHD vierge sur les réponses mécaniques et les évolutions de la microstructure lors des essais oligo-cycliques. 3) Les différences de comportements mécaniques et de micro-mécanismes associés entre les matériaux d'origine et préchargés.

MOTS-CLÉS : polyéthylène haute densité - essais oligo-cycliques - endommagement - évolutions mécaniques et microstructurales – corrélation macro-micro

Laboratoire (s) de recherche : MATEIS

Directeur de thèse: Olivier LAME

Président de jury : Valérie Gaucher

Composition du jury :

Cantournet, Sabine	Directeur de Recherche	Mines ParisTech	Rapporteur
Laiarinandrasana, Lucien	Professeur	Mines ParisTech	Rapporteur
Govaert, Leon	Professeur	Eindhoven University of Technology	Examinateur
Gaucher, Valérie	Professeur	Université de Lille	Examinatrice
Rinaldi, Renaud	Maître de Conférences	INSA-Lyon	Co-encadrant
LAME, Olivier	Professeur	INSA-Lyon	Directeur de thèse
Broudin, Morgane	Ingénieur-Chercheur	EDF – R&D	Examinatrice